PROCESS DESIGN AND ANALYSIS OF A CRYOGENIC FREEZE-OUT HEAT EXCHANGER FOR HELIUM PURIFICATION

By

Duncan Kroll

A DISSERTATION

Submitted to
Michigan State University
in partial fulfillment of the requirements
for the degree of

Mechanical Engineering – Doctor of Philosophy

2024

ABSTRACT

Purification systems are necessary to support commissioning and operation of medium to large-scale cryogenic refrigeration systems using various cryogenic working fluids. The present research focuses on helium refrigeration systems that operate at 4.5 K (which is just above the normal boiling point of helium), down to 1.8 K (which requires helium with a vapor pressure of 16 mbar). At these very low temperatures, the presence of any substances except helium (contaminants) will result in solidification. Even trace amounts of these impurities in the process fluid can block and/or change the flow distribution in a refrigerator's heat exchangers and potentially damage rotating equipment operating at high speeds. Therefore, helium purifiers for these refrigerators are typically designed for a low level of impurity (i.e., 1-100 ppm_v) removal of moisture and air components, since gross impurities are removed during the initial clean-up and commissioning of the system.

Purification of the process gas (helium) is typically achieved by molecular sieve adsorption beds at room temperature for moisture removal and liquid nitrogen (LN) cooled activated carbon adsorption bed for air (nitrogen/oxygen/argon) removal. However, past studies and operational experience show that molecular sieves are unable to remove low level moisture contamination effectively. Freeze-out purification has great potential to reliably remove low-level moisture contamination, but requires careful design. Typical commercially available freeze-out purifiers have a much shorter operating time in between regenerations than should be achievable, are not optimized for low pressure operation, and require large amount of utilities like liquid nitrogen. Furthermore, frost formation in a purifier heat exchanger is not well understood. Developing an understanding of this process and studying the design and process parameters that can improve the process for this critical sub-system is the focus of this research.

This work begins with an experimental study of a commercially available helium freeze-out purifier. It is tested under practical operating conditions and controlled operating conditions, under different contamination levels and flow capacity imbalances. Auxiliary equipment was designed, fabricated, tested, and operated to achieve controlled and tunable low-level moisture contamination in the helium stream. The performance and moisture capacity of the purifier heat exchanger was characterized. Following the experimental study, a series of theoretical studies were carried out. First, a heat and mass transfer model on an isothermal surface was developed to establish a base-level understanding of frost formation and relate to the existing literature. This model was used to study the effects of gas pressure, wall temperature difference, reduced temperature differential, absolute humidity, and carrier gas on the frost growth and mass transfer. A simplified estimation to predict frost thickness was developed and found to be accurate within 1%. Second, this model was extended to a heat exchanger surface. This model was validated using test data and used to study the effects of flow imbalance and inlet moisture contamination level. Through this study, it was found that flow mal-distribution within the heat exchanger caused a significant rift between many of the experimental results and the simulation results. Third, in order to eliminate the effects of flow mal-distribution and reduce utility usage, a novel purifier design is studied. It considers a coiled finned-tube design to maximize surface area for heat exchange and mass collection. An initial exergy analysis was done to determine a reasonable reference design geometry. The effects of fin density and heat exchanger mandrel diameter on frost formation and heat exchanger performance were studied. It was found that the novel purifier can hold approximately as much frost as the commercially available purifier, while using significantly less nitrogen for cooling.

ACKNOWLEDGEMENTS

First, I would like to thank my primary advisor, Dr. Abraham Engeda, for his support of my graduate studies. He initially connected me with FRIB and handled the interfacing between FRIB and the MSU mechanical engineering department. Without Dr. Engeda, I would never have been connected to the cryogenic field, which I have found to be an interesting and meaningful field of study. He has supported and encouraged me throughout my educational and career aspirations and achievements.

I would also like to thank Dr. Nusair Hasan, Dr. Rao Ganni, Dr. Andre Benard, and Dr. Wei Liao, for their willingness to be a part of my dissertation committee. They offered me a wealth of knowledge inside and outside of my field of research. Their feedback at several stages throughout the formulation of my dissertation was invaluable.

My colleagues at FRIB played an enormous part in my education and research. Nusair Hasan, Rao Ganni, and Peter Knudsen have a wealth of experience and depth of knowledge of cryogenic systems that is unparalleled. I have benefitted greatly through their teaching in cryogenics classes, advising in my research, and encouragement in my career aspirations. They assisted in the interfacing between FRIB and the mechanical engineering department, allowing me to focus on my education. Rao Ganni's past work in helium purification developed the foundation for my work in this area. His vast experience and insight in helium cryogenic systems was an incredible resource through my education. Nusair Hasan functioned as my primary research advisor for the day to day challenges, and helped formulate and guide my research direction. He provided very valuable feedback and directly shaped the researcher and academic I am today. They empowered me to see my projects from both global and hyper-specific points of view. They, along with my fellow graduate students at FRIB, Jon Howard, Scott Anthony, Austin Grake, and Tasha Williams, created a collaborative and helpful environment which assisted me in achieving my

goals. Mathew Wright was always willing to help me understand any of the systems at FRIB and connect me with the groups I needed to work with at FRIB. Brandon Laumer and Alex Dolehanty assisted in the operation and testing of the helium purifiers at FRIB. Adam Fila and Shelly Jones facilitated the fabrication and commissioning of testing equipment that I designed. Special thanks to Fabio Casagrande (Cryogenic Department Manager, FRIB), Thomas Glasmacher (Laboratory Director, FRIB), and the Accelerator Science and Engineering Traineeship program for providing me with the opportunity to work at FRIB. I am deeply grateful to the entire FRIB team for providing me such a unique and diverse education.

Finally, I would like to thank my family and friends for supporting me through the long and challenging process of completing my PhD. My parents, Kevin and Suzanne, and my sister, Sydney, have shown unwavering faith and assurance in my abilities, believing I would achieve any goal I set for myself. I would like to thank my family and friends for understanding the commitment, focus, and time it took to achieve my goals. Without that support network, my PhD would not have been possible.

This material is based upon work supported by the U.S. Department of Energy Office of Science under Cooperative Agreement DE-SC0000661, the State of Michigan and Michigan State University. Michigan State University designs and establishes FRIB as a DOE Office of Science National User Facility in support of the mission of the Office of Nuclear Physics.

TABLE OF CONTENTS

Chapter 1 : Introduction

1.1 Background and Motivation

In 2015, more than one-third of the total helium consumption in the United States was in the cryogenic refrigeration sector [1]. Cryogenic helium refrigeration systems are used in facilities ranging from small university or medical / industrial laboratories to large government sponsored research facilities. The latter are mostly particle accelerators, which use superconducting devices cooled to cryogenic temperatures [2]. These refrigeration systems take advantage of helium's very low normal boiling temperature and operate at 4.5 K or lower. Since everything else will freeze at these temperatures, everything but helium is considered a contaminant. However, normally these contaminants in the helium inventory in a helium refrigerator are air (i.e., oxygen, nitrogen, argon) and moisture. Presumably, care is taken during system commissioning to remove bulk contamination from the system. Assuming this is the case, the performance and reliability of components used in these refrigeration systems can still be strongly influenced by the low-level contamination. Persistent low-level contamination, as low as on the order of 1 to 100 ppm_v (parts per million, by volume), will degrade the performance of the refrigerator heat exchangers by freezing out on the heat transfer surfaces [3], as well as freezing out on other localized areas such as valves and turbo-expanders. The source of this low-level contamination can be residual left from commissioning. However, persistent contamination can often come from several sources [4], such as the make-up helium '*charge*'. Typically, better than industrial Grade A purity helium, which is also known as Grade 4.7 (or 99.997% pure helium, which has 30 ppm_v impurity content) is obtained from vendors for this purpose and then further purified before being added to the refrigeration system [5]. The low-level contamination can also stem from the refrigerator's compressor system, since it is very difficult to completely remove air and moisture contamination from the compressor oil (used for lubricating and cooling). Superconducting magnets with their relatively large surface area and high hydraulic tortuosity are another common source of persistent low-level contamination. Their manufacturing process involves using volatile fluids, which are adsorbed into the magnet coils, and diffuse out into the coolant (refrigerant) helium very slowly during operation [6]. For helium refrigeration systems that operate below 4.5 K, that is, those operating at sub-atmospheric pressures, the ability to handle air and moisture intrusion is a practical necessity. To maintain refrigerator system performance and reliability, while reducing unnecessary helium waste, the helium recovered from these sources are decontaminated using a helium purifier before it is returned into the refrigerator system.

Helium is commonly recovered from natural gas using cryogenic distillation processes [7]. The recovered helium can then be *upgraded* (above 90% purity) and *purified* (above 99% purity) using either an adsorption process or a membrane separation process [8]. The helium recovery and (gross level) purification process is discussed in detail in Chapter 2. Removal of low-level impurities (purity below 1 ppm_v or less) is critically important for cryogenic applications as discussed above. The industrial helium purification systems in this application commonly use adsorption processes [9]. However, these processes are not efficient. Shortcomings of these processes are discussed in the following section.

1.2 Challenges in Helium Purification

Low-level contamination removal from a helium stream for cryogenic applications, involves mainly the removal of the constituents of air (oxygen, nitrogen and trace amounts of carbon dioxide), moisture, and volatile organic compounds (VOCs, either leaked in from ambient atmosphere in case of sub-atmospheric systems or outgassed from cryogenic equipment). In some cases, there might be trace amounts of oil (migrated from the warm compressor system). However, removal of this oil is performed in a separate system (specifically designed for oil removal) and it is not within the scope of the present research. Out of the major constituents described (nitrogen, oxygen, moisture and VOCs), the major obstacle in low-level purification is the moisture removal. Nitrogen, oxygen and VOCs are typically removed by an adsorption process (carried out at 80 K), using an activated charcoal or silica bed. The regeneration process of these adsorber beds is rather simple and involves a hybrid process (both temperature and pressure swing) [10]. Moreover, the contaminations (nitrogen, oxygen and VOCs) are desorped in gaseous phase and removal of these contaminants from the purification system can be relatively easily performed. However, this is not the case for moisture removal. Removal of low-level moisture from the contaminated stream by adsorption process typically uses molecular sieve beds. However, this process doesn't perform well in practice [11] compared to the theoretical estimations. Over a long operating period (many operation and regeneration cycles), the low-level contamination (<100 ppm_v) typically passes through the molecular sieve bed [11] and freezes out downstream of the purification system (in refrigeration recovery heat exchangers, etc.). The regeneration process of these molecular sieve beds is rather complicated and time consuming as well [12-14], resulting in the beds being regenerated improperly and a corresponding reduction in the operating time of the purifier.

The freeze-out purification process for low-level moisture removal is an alternative to the adsorption process. These systems, when properly designed, can remove very low-level moisture contamination (up to fraction of a ppm_v) due to the low partial pressures of the moisture (at correspondingly low solid-vapor saturation temperatures). Optimal design of the freeze-out heat exchanger in these systems is a significant factor. The heat exchanger must be designed to retain a large amount of moisture, without significantly impacting heat exchange, flow distribution and pressure drop. The design should also support easier removal of the contaminants for a quicker regeneration process. However, design procedure and associated fundamental correlations (*e.g.,* heat and mass transfer) for these heat exchangers are very limited in the literature. Frost deposition from humid air streams with relatively high humidity (>10% relative humidity) has been studied extensively [15-18], but that from a helium stream with low levels of impurity is not available in the literature. Gas purifiers with the capability to remove low levels of contamination are used in very specific industries (*e.g.,* medical, cryogenic) and are not very common. Optimal process design of such system can be challenging, but poses a potential to carry out novel research in this field.

1.3 Scope and Research Objectives

In low level contaminant purifiers, the moisture removal is the dominant and more challenging aspect. Therefore, the present research is focused on the moisture removal from the helium.

The overall objective of the present research is to develop a better understanding of freeze-out helium purification, and especially frost deposition in a freeze-out heat exchanger. The crucial understanding is on the driving forces for how frost deposits. This allows for better design and operation of a purifier to capture a maximum amount of frost. In order to develop this understanding, the design process and performance characterization for a moisture freeze-out heat exchanger was developed. Special consideration was given in the characterization of frost formation over the heat exchanger surface and the associated performance degradation.

Experiments were performed to characterize the existing commercially available helium purifier at FRIB. A one-dimensional transient computational heat and mass transfer model of the conjugate heat exchange and frost formation process over the freeze-out heat exchanger surface was developed. The experimental results were used to validate the computational model. This computational model, and the information learned from the characterization of the FRIB purifier, were used to optimize the design of a freeze-out purifier and evaluate the performance (frost collection capacity and associated heat exchanger performance degradation) of a proposed freeze-out helium purifier design. The overall research objective can be divided into several segments. Each of these segments and their corresponding scopes are presented below –

a) *Characterization of an industrial freeze-out helium purifier*

The performance of an existing industrial freeze-out helium purifier was characterized. The performance characterization involves measuring the utility consumption (*i.e.,* nitrogen usage for cooling and regeneration, helium loss due to regeneration) during nominal operation and regeneration. Contamination collection capacity (*i.e.,* moisture capacity of freeze-out heat exchanger) was measured during nominal operation and several different controlled conditions. To carry out this controlled test, equipment was designed and fabricated to control the low level of moisture contamination in a helium gas stream. This equipment allows for testing with controlled amounts of constant moisture addition to the helium supply stream to the purifier to study the effect of certain input variables. The input variables of interest for this study are supply moisture contamination level and heat exchanger flow capacity ratio of the supply and return helium streams of the heat exchanger. The measured characteristics from the tests will be compared to the characteristics of the proposed freeze-out helium purifier design.

b) *Modeling frost formation on an iso-thermal surface*

Before modeling a heat exchanger surface, a fundamental understanding of frost formation must be established. A transient, zero-dimensional heat and mass transfer model for a simple, flat-plate geometry was developed. The model was validated with existing experimental and simulation results from literature at atmospheric temperature and pressure and high humidity with air as the moisture carrier gas. The model was expanded to include the purifier operating conditions of lower temperature, higher pressure, low humidity, and more carrier gases. The impacts of these parameters were studied.

c) Modeling frost formation in a heat exchanger

A transient, one-dimensional computational model to predict the frost collection characteristics from a helium stream with low-level moisture contamination was developed. It takes the geometry of a heat exchanger and the conditions under which it operates and predicts the frost collection profile, heat transfer, mass transfer, and heat exchanger performance parameters over the course of its operation. The experimental results during controlled operating conditions were used to validate the computational model. This model will serve as a design and optimization tool for freeze-out helium purifiers using similar configurations.

d) Design and performance estimation of a cryogenic freeze-out heat exchanger

The thermodynamic design of a freeze-out helium purifier was proposed. The mechanical design and configuration of this purifier is based on the process and mechanical design by Kroll [19, 20] for low-level contamination removal from a helium stream at FRIB experimental systems [19-21].

A quasi-steady process model for the overall freeze-out helium purifier was developed. The model includes geometric modeling of the heat exchanger and process modeling of the conjugate heat and mass (frost) transfer processes. The process model is able to predict the stream outlet temperatures, heat exchanger performance parameters (NTU, effectiveness), cooling curves, and frost collection characteristics from simplified assumptions. A preliminary exergetic optimization was carried out to obtain a better understanding of the heat exchanger sizing and overall utility consumption.

The proposed freeze-out helium purifier design and configuration was input into the computational model in order to predict its transient moisture collection capacity and heat exchanger performance parameters. The improvements that this analysis and simulation make to the existing purifier operated at FRIB were discussed. Design and operation improvements were suggested based on this discussion.

REFERENCES

[1] J.E. Hamak, Minerals Handbook, United States Geological Survey, 2015

[2] V. Ganni, J. Fesmire, Cryogenics for superconductors: Refrigeration, delivery, and preservation of the cold, in, 2012, pp. 15

[3] R.B. Hinkley, J.C. Burke, F.E. Ruccia, R.P. Berthiaume, R.C. Reid, E.M. Drake, I.W. Dingwell, M.E. Weber, Contaminant Freeze-Out In Heat Exchangers. Volume II - Basic Investigation Of Contaminant Freeze-Out, ASD-TDR-63-508, United States Air Force Systems Command, Wright-Patterson Air Force Base, OH, 1963

[4] I.I. Abrikosova, A.I. Shal'nikov, The purity of liquid helium, Cryogenics, 11(2) (1971) 137-138

[5] N. Hasan, P. Knudsen, M. Wright, Online helium inventory monitoring of JLab cryogenic systems, IOP Conference Series: Materials Science and Engineering, 278 (2017) 012113

[6] R.C. Duckworth, J.A. Demko, A. Lumsdaine, J. Rapp, T. Bjorholm, R.H. Goulding, J.B.O. Caughman, W.D. McGinnis, Cryogenic considerations for superconducting magnet design for the material plasma exposure experiment, IOP Conference Series: Materials Science and Engineering, 101 (2015) 012143

[7] P. Häussinger, R. Glatthaar, W. Rhode, H. Kick, C. Benkmann, J. Weber, H.-J. Wunschel, V. Stenke, E. Leicht, H. Stenger, Noble Gases, in: Ullmann's Encyclopedia of Industrial Chemistry, Wiley-VCH, Weinheim, Germany, 2001

[8] T.E. Rufford, K.I. Chan, S.H. Huang, E.F. May, A Review of Conventional and Emerging Process Technologies for the Recovery of Helium from Natural Gas, Adsorption Science & Technology, 32(1) (2014) 49-72

[9] J.G. Weisend II, Cryogenic Technology, in: Kirk-Othmer Encyclopedia of Chemical Technology, John Wiley & Sons, Hoboken, NJ, 2012, pp. 1-29

[10] M. Wright, Design and Development of a Helium Purifier, Old Dominion University, Norfolk, VA, 2009

[11] V.P. Singh, D.M. Ruthven, Adsorption of moisture on molecular sieve adsorbents at low humidity, F84026, Canadian Fusion Fuels Technology Project, Canada, 1984

[12] S.A. Stern, F.S. DiPaolo, The Adsorption of Atmospheric Gases on Molecular Sieves at Low Pressures and Temperatures. The Effect of Preadsorbed Water, Journal of Vacuum Science and Technology, 4(6) (1967) 347-355

[13] S. Da-Ming, An experimental study of the adsorption characteristics of 13X molecular sieves, Journal of Physics E: Scientific Instruments, 22(3) (1989) 159-162

[14] R.S. Voleti, N. Singhal, R.S. Pant, Critical Review of Helium Purification Techniques for Lighter-than-Air Systems, in: AIAA Balloon Systems Conference, Denver, CO, 2017

[15] M. Kandula, Frost growth and densification on a flat surface in laminar flow with variable humidity, International Communications in Heat and Mass Transfer, 39(8) (2012) 1030-1034

[16] K.-S. Lee, W.-S. Kim, T.-H. Lee, A one-dimensional model for frost formation on a cold flat surface, Int. J. Heat Mass Transfer, 40(18) (1997) 4359-4365

[17] K.-S. Lee, W.-S. Kim, The effects of design and operating factors on the frost growth and thermal performance of a flat plate fin-tube heat exchanger under the frosting condition, KSME International Journal, 13(12) (1999) 973-981

[18] A. El Cheikh, A. Jacobi, A mathematical model for frost growth and densification on flat surfaces, Int. J. Heat Mass Transfer, 77 (2014) 604-611

[19] D. Kroll, N. Hasan, V. Ganni, A. Fila, A. Engeda, Freeze-out purifier for helium refrigeration system applications, IOP Conference Series: Materials Science and Engineering, 755 (2020) 012056

[20] D. Kroll, Development of the mechanical design for a freeze-out purifier, Michigan State University, East Lansing, MI, 2020

[21] N. Hasan, M. Wright, V. Ganni, F. Casagrande, S. Jones, C. Nguyen, A. Fila, N. Joseph, Design, Fabrication, and Installation of the Cryogenic Distribution System from FRIB Target and Fragment Pre-Separator Superconducting Magnets, IOP Conference Series: Materials Science and Engineering, 756 (2021)

Chapter 2 : Literature Review of Relevant Work

The overall objective of the present research work is to develop the design process for a thermodynamically optimal and higher capacity freeze-out helium purifier. A detailed literature review was carried out on the topics of gas purification (especially that of helium), industrial helium purifiers, freeze-out heat exchangers, and frost collection from a contaminated gas stream. A summary of the literature review on each of these topics are presented below.

2.1 Gas / Helium Purification

The first instance of successful air separation (and purification) was in 1902, by Carl von Linde [1]. He used a cryogenic fractionating distillation column to produce ~98% pure oxygen and ~99% pure nitrogen from air. Once separated, these gases (oxygen, nitrogen etc.) are typically purified using adsorption process, especially molecular sieves, and pressure swing adsorption. Specialty gases like hydrogen, helium, argon etc., are produced from different other sources and their separation and purification process can be considerably different (based on the source and purity needed). Production and purification of helium are discussed in the following sections.

Helium is typically extracted and recovered from natural gas. The decay of uranium and thorium in pre-Cambrian crystalline basement rocks produces helium [2]. Helium diffuses vertically through faults and porous sedimentary rock, eventually getting trapped with natural gas under 'salt domes' made of anhydrite. Helium is found in natural gas reservoirs in very low concentrations (nominally 0.1%, and rarely up to 10%) [2]. Conventional helium extraction from natural gas is a multi-stage process, as discussed in detail by Rufford [3]. There are several processes that lead to the output of crude helium (50-70% helium). These include compression, acid gas removal, dehydration, mercury removal, methane liquefaction, and nitrogen rejection by fractionated distillation. The simplified steps for helium recovery process from natural gas and their byproducts are shown in Figure 2-1.

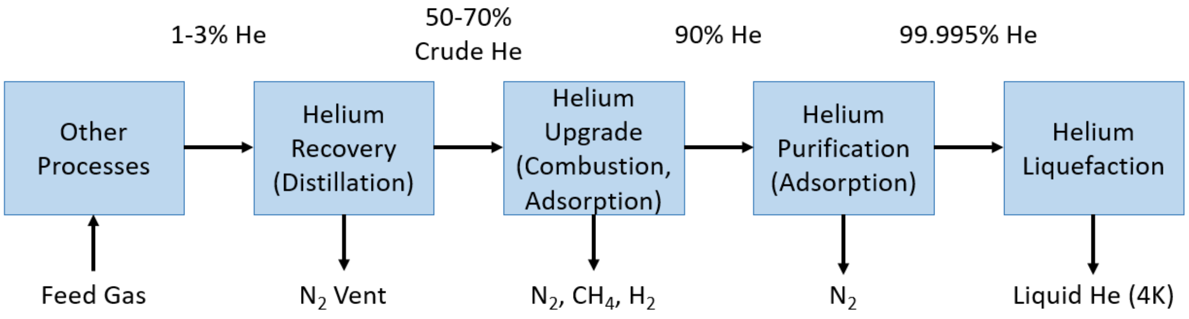

Figure 2-1 Overview of helium recovery processes from natural gas

Helium recovery involves a two-column distillation process, carried out at two different operating pressures. It outputs '*crude*' helium, which is usually 50-70% pure. The next step in the process is helium upgrading. Air is added to the helium to facilitate combustion of any remaining methane (from natural gas) and hydrogen. Bulk components (mainly nitrogen) are condensed and removed. Any remaining gases are removed using a pressure swing adsorption process. The resulting helium stream is approximately 90% pure. This step in the process is often performed by cryogenic distillation instead. The next step, helium purification, is carried out by another nitrogen condensation process or pressure swing adsorption. This results in helium at 99.995% purity (50 ppm_v of nitrogen). The final step is helium liquefaction, which allows it to be efficiently stored and shipped. This process ignores potential low-level moisture contamination, focusing on removing higher-level nitrogen contamination and other contaminants found in natural gas.

Flash distillation processes are often used in the beginning steps of helium extraction from natural gas [4]. A two-stage membrane process has been used for a direct removal of helium from natural gas, achieving 59% purity with 95% yield [5]. These processes discussed, are used for gross level contamination (gases from source, constituents of air, moisture, oil and lubricants from mining/processing equipment etc.) removal from helium.

Removal of low-level impurities (100 ppm_v or below) from helium is very important for cryogenic applications, especially in helium liquefiers and refrigerators for particle accelerators. Although, usually, better than industrial Grade-A (also Grade 4.7) purity helium is used in cryogenic helium refrigerators, contaminants are inadvertently introduced to the system through residuals leftover from a clean-up, air in-leaks to systems operating below 4.5 K, and out-gassing from cooled devices (*e.g.*, superconducting magnets). The constituents from the first two are oxygen, nitrogen, and moisture. After the initial clean-up, these constituents are present in relatively low concentrations, of the order of 10 ppm or less. Although, this seems small, it can (and does) build up over time and consequently pose threat to the reliable and efficient operation of the equipment. These low-level contaminations can be removed from helium using either adsorption or freeze-out. Lozano [6] examined two methods of purification - liquid nitrogen traps (freeze-out) and heated getter materials (adsorption). He found both methods to be effective for the test system and of similar cost. The heated getter purifier reached a lower oxygen content (the main contaminant used in this experiment) than the liquid nitrogen trap purifier. A detailed review of low-level contamination removal by filtration (using membranes) was carried out by Scholes [7]. Due to the smaller molecular size, many membranes have selectivity for helium and can offer relatively higher purity. Membrane technologies are often combined with another separation method, such as pressure swing adsorption, to achieve high purity helium. Saberimoghaddam [8] designed a pressure swing adsorption process to purify helium from 99.95% to 99.99999% (0.1 ppm_v). It uses granular activated carbon adsorbent at 60 bar to achieve this purity. However, low-level contamination removal from helium using present filtration (membrane) techniques is not suitable for industrial applications with high flow capacities [7].

2.2 Industrial Helium Purifiers

For industrial helium purification systems, adsorption and freeze-out are the two major methods employed in low-level contamination removal. Helium purification systems using adsorption processes are very common and widely used [9]. This can be a pressure-swing adsorption (PSA) process, a temperature-swing adsorption process (TSA) or a hybrid of these two [8]. Many helium purification systems designed for large-scale cryogenic refrigerator applications use a hybrid adsorption process; namely, a molecular sieve bed for moisture removal and an activated carbon bed cooled with liquid nitrogen (LN) to remove air contaminants [10, 11]. From a theoretical perspective, helium purification systems using molecular sieve beds are considered to be very effective for low-level contamination removal [6]. However from experience, molecular sieves do not perform well in removing the low-level moisture contamination (< 100 ppm_v) over long periods [12], and the contamination instead ends up freezing out in the purifier's heat exchanger used for the activated carbon bed, which is usually at 80 K [13]. In addition, sufficiently regenerating the molecular sieve beds is time consuming and often not done properly. As such, the moisture contamination holding capacity of this type of helium purifier tends to deteriorate over time [14, 15].

Wright [10] designed an industrial helium purifier using such hybrid adsorption process. A schematic diagram of the helium purifier is shown in Figure 2-2. Liquid nitrogen (LN) is used as the primary cooling medium for the purifier. A brazed-aluminum plate-fin heat exchanger is used to recover the refrigeration from the 'clean' gas (from adsorber) and the nitrogen boil-off. Molecular sieve is used to adsorb moisture from the contaminated stream (at ambient temperature), and a refrigerated (at 80 K) activated charcoal bed is used to adsorb oxygen and nitrogen. This purifier was designed to continuously operate up to 30 days with 40 g/s of contaminated helium flow (at 13.0 bar, 10 ppm_v of nitrogen and 10 ppm_v moisture at inlet).

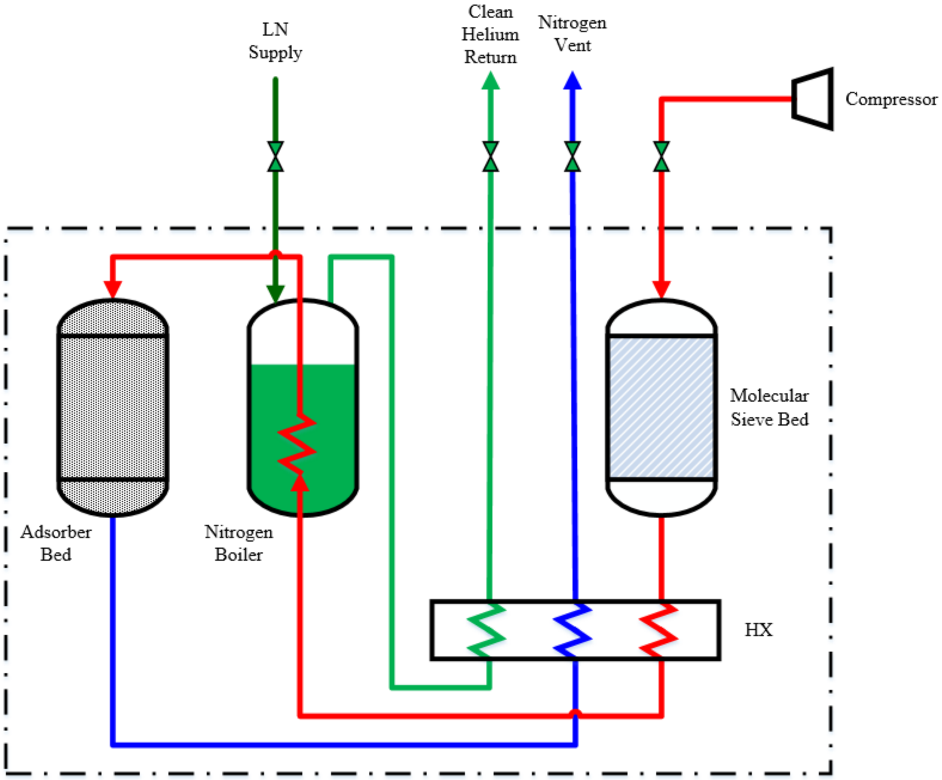

Figure 2-2 Schematic diagram of the helium purifier designed by Wright [10]

As an alternative to these helium purification systems using molecular sieve for moisture removal, helium purification by freeze-out / refrigeration has been proposed in the past [16-18]. Collins [16] first proposed the design of a freeze-out helium purifier. The piping and instrumentation diagram for this purifier is presented in Figure 2-3. Cold, pure helium cools the contaminated helium stream to approximately 30 K during operation. This operating temperature allows the moisture, air (oxygen and nitrogen), and carbon dioxide in the contaminant stream to freeze-out. Liquid helium as well as recovered refrigeration from the purified helium stream is used to achieve these low operating temperatures. This purifier, although very effective in low level impurity removal, can be significantly energy intensive due to the use of very cold or liquid helium as the primary refrigerant for the freeze-out process.

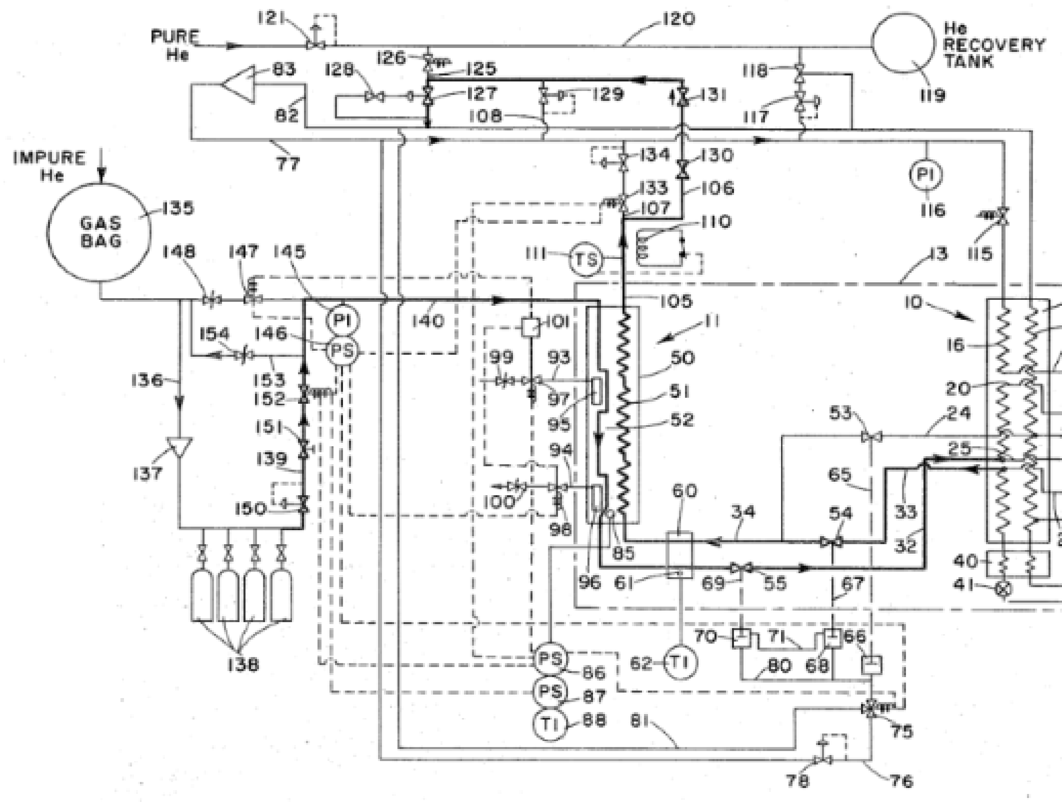

Figure 2-3 Piping and instrumentation diagram of the helium freeze-out purifier developed by Collins [16]

Dauvergne *et al.* [17] developed a helium freeze-out purifier for CERN. It was designed for a sub-atmospheric refrigerator operation to eliminate the contaminants that sub-atmospheric pumping systems introduce. The freeze-out heat exchanger cools the helium down to 33 K to assure that the contaminant (mainly nitrogen) concentration is less than 1 ppm_v (at outlet). This purifier was designed to remove gross levels of contamination (up to 13000 ppm) at low flow rates (~0.7 g/s) as well.

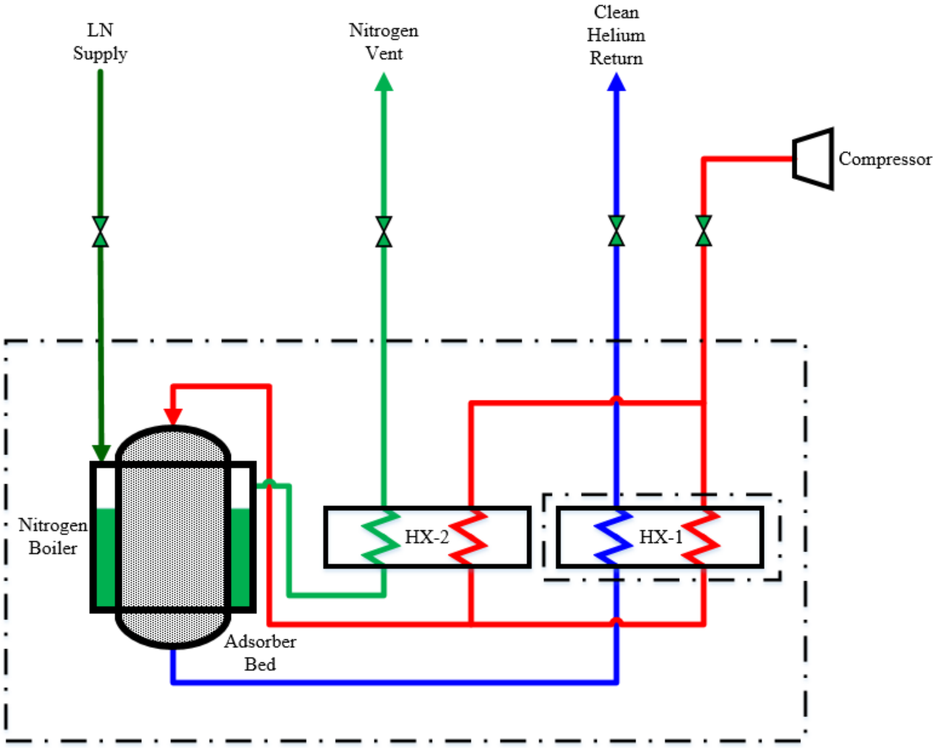

Figure 2-4 Schematic diagram of a commercially available freeze-out helium purifier

Apart from purifiers using a complete freeze-out process for contaminant removal, a hybrid process using freeze-out for moisture removal, and adsorption for air (oxygen and nitrogen) removal can be more efficiently used. A hybrid purification process can be less energy intensive compared to those discussed in [16, 17]. Such a purifier using freeze-out moisture removal is available commercially [19]. This design consists of two freeze-out heat exchangers - one for utilizes refrigeration from 'clean' helium stream (out of the adsorber bed), and the other utilizes the boil-off nitrogen. Moisture is removed from the contaminated helium streams from these two heat exchangers by freezing at solid-vapor saturation temperatures corresponding to the partial pressure. These streams are then recombined, cooled to 80 K in a nitrogen boiler vessel, and further purified (from oxygen and nitrogen) by passing through an activated charcoal bed. A schematic diagram of this commercially available purifier is shown in Figure 2-4.

2.3 Freeze-Out Heat Exchangers

A properly designed freeze-out heat exchanger is of primary importance for an efficient (and effective) freeze-out purification system. Deposition of a solid (frost / moisture) over a heat exchanger surface may pose several performance issues, namely loss of effectiveness, flow mal-distribution, development of additional stresses due to growth of frost layer. A freeze-out heat exchanger needs to be naturally adjusting and tolerant to these issues.

Typically, several types of heat exchangers have been used for this application. These include brazed-aluminum plate-fin heat exchangers (BAHX) [10], coiled heat exchangers [19], and finned tube heat exchangers [16, 20]. Freeze-out heat exchange involves sublimating a vapor (moisture) onto a heat exchanger surface. In general, the frost deposition process is highly localized within the heat exchanger (depending on the partial pressure of moisture in the contaminated stream) and results in a localized blockage (and pressure drop) of the flow. Hence, the moisture collection capacity, as well as the operating period of the heat exchanger is limited by the flow pressure drop.

For the design of such heat exchangers, pressure drop (and heat transfer) correlations are important design information, allowing the prediction of freeze-out heat exchanger performance. Hilz [21] and Hausen [22] suggests that in pure turbulence, contaminants may freeze to a surface with which heat transfer is occurring. During laminar flow, the solid contaminants often detach. This is counterproductive for a freeze-out heat exchanger, so designing a heat exchanger that maintains turbulent flow is necessary. Working with this objective, Bailey *et al.* [23] studied the freeze-out of nitrogen from a hydrogen stream, focusing on predicting the pressure drop. It resulted in the following equation for pressure drop through a tube in which frost is depositing on the inside surface (as in a shell-and-tube heat exchanger).

$$\Delta p = \frac{m_t^2}{2g\pi^2\bar{\rho}}\left[\frac{fL}{8}\frac{(R_i+r_o)\left(R_1^2+r_o^2\right)}{R_i^4 r_o^4} + \frac{K_c}{r_o^4}\right] \qquad 2.1$$

In which,

m_t = mass flow

$\bar{\rho}$ = gas density at mean temperature of the affected zone

f = friction factor

r_o = deposit profile radius

g = gravitational constant

Hinkley *et al.* [24] performed a broad study of water and carbon dioxide freeze-out from an air stream in heat exchangers. These tests were carried out with super-saturated inlet streams. It was reported that mass transfer to the cold walls of a heat exchanger is the dominant mode of phase change when the contaminated stream has a low relative humidity. With higher relative humidity, nucleation can proliferate, potentially causing solids to escape the heat exchanger. They also found that Woodside's [25] correlation for frost density (and thermal conductivity) is relatively accurate at low frost densities. It was also reported that frost density is primarily dependent on flow velocity at low temperatures (below 255.0 K). The pressure drop through the frost layer is related to the flow rate, frost thickness, and fluid density by the following equation.

$$\frac{\Delta p/\Delta p_o}{(W/W_o)^2} = \left[\frac{1}{1-t/\delta_o}\right]^2 \frac{\rho_o}{\rho} \qquad 2.2$$

Frost distribution is a large contributing factor to the pressure drop. As discussed previously, localized pressure drop is a significant issue in these heat exchangers. Therefore, understanding frost distribution could be extremely helpful in understanding where and why pressure drops occur. Chang [26] investigated mass transfer from a helium stream in a round tube, with the objective of predicting the distribution of frost formation in a cryogenic heat exchanger. The helium stream was supersaturated with water. The test apparatus included a propane heater, nitrogen bath and test column (for helium flow and frost formation) and is shown in Figure 2-5a. This experiment showed two different mechanisms of frost formation (per unit length) on the surface. First, molecular diffusion causes frost formation. Second, frost is collected from snow in the helium flow. This snow is formed by homogeneous nucleation in the supersaturated regions. The differences between frost formation without snow, with only snow, and with both are shown in Figure 2-5b.

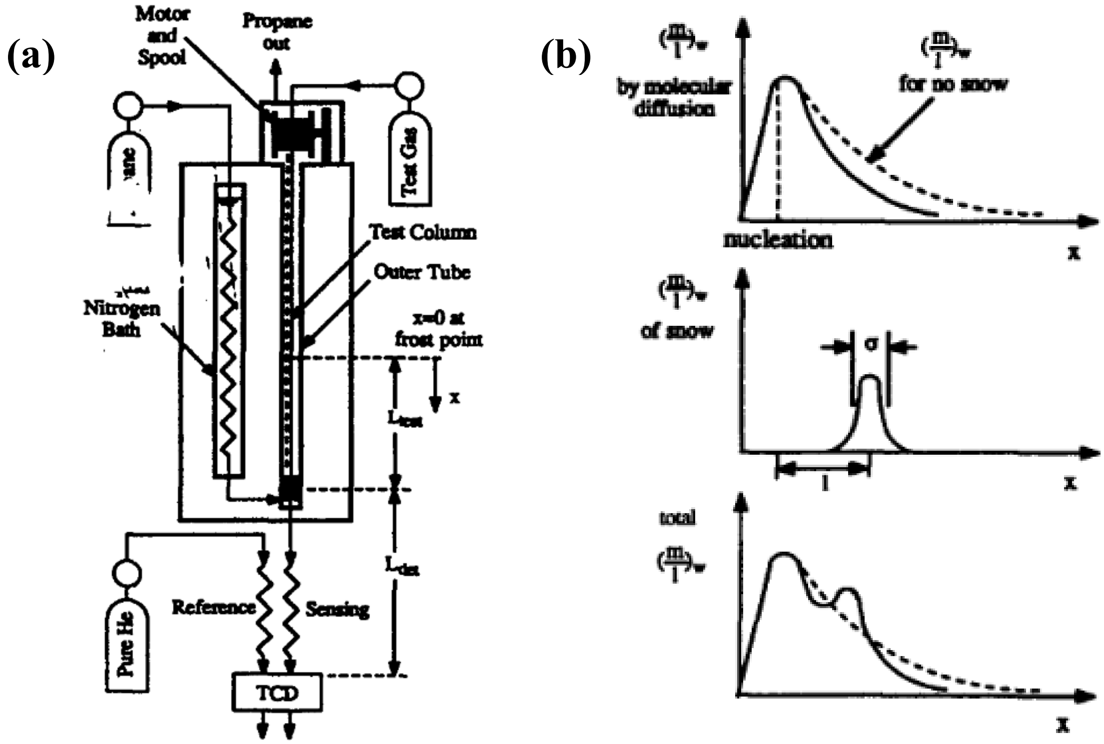

Figure 2-5 (a) Test apparatus to study frost formation inside a round tube and (b) corresponding results from the experimentation by Chang [26]

2.4 Frost Collection from a Contaminated Stream

Frost collection / deposition over a heat exchanger surface has been extensively investigated in the past [27-30]. However, almost all these studies consider air as the carrier gas with gross levels (1000 ppm_v or more) of moisture contamination. Frost deposition characteristics over a heat exchanger surface from a helium stream (with low levels of contaminant / moisture) is not available in the literature. Moreover, most of these studies are performed considering a flat plat as the heat exchanger surface. Frost deposition characteristics over extended surfaces (fins) are not common in the literature.

Kandula [31] has developed a numerical model to study frost growth over a flat plate in one dimension (frost thickness) from a humid air stream. This quasi-steady numerical model [31] is based on energy and mass balances around and inside the frost layer, as depicted in Figure 2-6. For frost deposition from humid air flow over a flat plate, the numerical model can accurately predict the deposition characteristics (Figure 2-6).

More commonly, the frost thermal conductivity is correlated to the frost density. The correlation developed by Yonko and Sepsy [32] (equation below) is widely used.

$$k_{ef} = 0.024248 + 0.7231x10^{-3}\rho_f + 0.1183x10^{-5}\rho_f^2 \qquad 2.3$$

However, an analytical model to predict the frost density and thermal conductivity for a wide temperature range has also been reported [33]. The frost density is calculated using a correlation based on the flow Reynolds number (*Re*) and frost surface temperature. The frost thermal conductivity is calculated from the frost shape factor (porosity), the thermal conductivity of ice, and the effective thermal conductivity of the entrapped air. Contributions from the molecular thermal conductivity of air, mass diffusion, and the eddy convection in the porous (frost) medium were considered in developing the analytical model. The contribution of eddy convection is assumed equal to the molecular thermal conductivity of air, based on work done by Biguria and Wenzel [34].

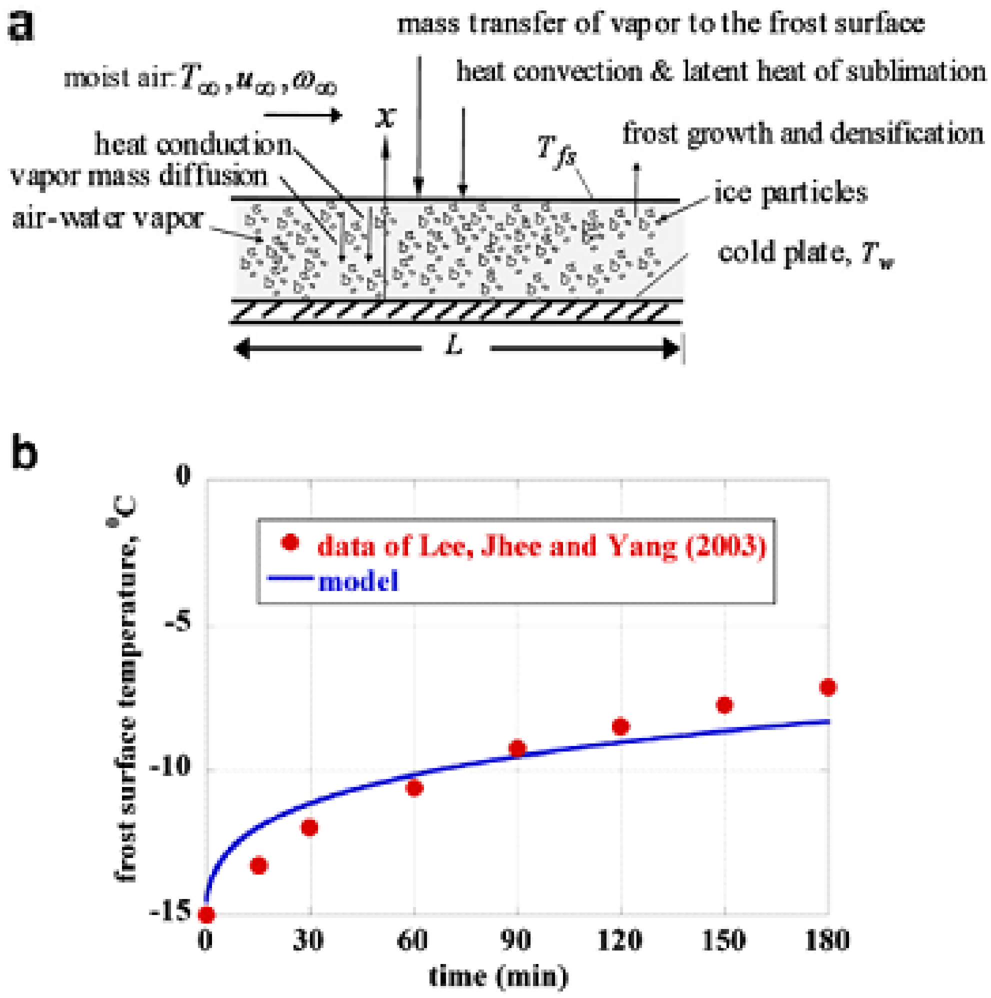

Figure 2-6 (a) Schematic representation of the problem domain and (b) comparison of experimental data and numerical calculations based on the numerical model developed by Kandula [31]

Cheikh *et al.* [30] developed a numerical model similar to that reported by Kandula [31]. It uses more realistic boundary conditions. The temperature boundary condition at the cold surface was kept fixed and at the frost surface was calculated using energy balance (heat flux). This heat flux basis sets the model apart from others that use saturation (or super-saturation, as Na [36] considered) temperature as a boundary condition. An empirical correlation was used to calculate the frost thermal conductivity. An initial frost density was chosen based on previous work by Jones and Parker [37]. The equations were discretized and solved by commercial software.

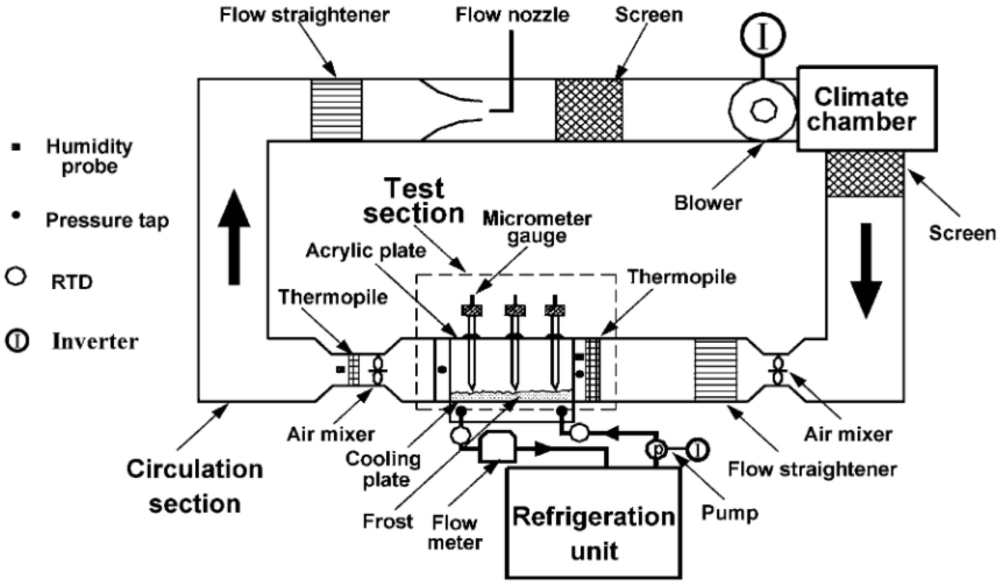

Figure 2-7 Experimental set-up used by Lee *et al.* [35] to investigate relation between heat and mass transfer for humid air flow over a cooled flat plate

Lee *et al.* [28] proposed a different method for estimating the heat and mass diffusivity relationship (*i.e.* Lewis number, Le) for humid air flow over a cooled flat plate. The Lewis number (Le) plays an important role in the prediction of heat and mass transfer from Chilton-Colburn analogy. Most commonly, it is considered as unity (for humid air flow over a cooled flat plate). However, a simplified correlation to estimate the Lewis number was proposed and detailed experiments [35] were performed to validate the correlation. The test setup of this experiment is shown in Figure 2-7. It consists of a refrigeration unit to cool a flat plate, a climate chamber to set humidity and temperature of the air before it flows over the plate, a test area where the thickness and temperatures are measured, and a blower (and associated parts) to control the flow rate. Based on the results of the experiment, Lee theorized that this correlation is much more accurate than the assumption of Le = 1.0.

In recent years, several studies have been performed on frost formation in cryogenic systems. Byun [38] studied frosting and fogging on a cryogenic vaporizer surface. Experiments were performed below -100 °C. Their simulations showed that frost density decreased further from the cold surface, however only average density was verified experimentally. Byun [39] did another similar study, finding the same density behavior, this time verified by through quantitative numerical analysis. It found that sublimation occurs when the frost surface temperature is near the cold surface temperature, resulting in low density deposition. Condensation-freezing occurs as the frost surface temperature warms (near -40 °C), resulting in higher density deposition. Qi [40] performed a CFD analysis on low temperature and low water-vapor content air on a cold surface. The analysis found that frost density and thickness both increase with water vapor content, from 10 ppm to 1000 ppm. Frost density has a stronger correlation to water vapor content, while frost thickness increased more mildly.

REFERENCES

[1] F.G. Kerry, Industrial Gas Handbook : Gas Separation and Purification, (2007)

[2] J.E. Hamak, Minerals Handbook, United States Geological Survey, 2015

[3] T.E. Rufford, K.I. Chan, S.H. Huang, E.F. May, A Review of Conventional and Emerging Process Technologies for the Recovery of Helium from Natural Gas, Adsorption Science & Technology, 32(1) (2014) 49-72

[4] M. Mehrpooya, A. Shafaei, Advanced exergy analysis of novel flash based Helium recovery from natural gas processes, Energy, 114 (2016) 64-83

[5] M. Alders, D. Winterhalder, M. Wessling, Helium recovery using membrane processes, Separation and Purification Technology, 189 (2017) 433-440

[6] M.P. Lozano, M. Gabal, J. Sesé, M.P. Pina, C. Rillo, Purification of Recovered Helium with Low level of Impurities: Evaluation of Two Different Methods, Physics Procedia, 67 (2015) 158-162

[7] C.A. Scholes, U.K. Ghosh, Review of Membranes for Helium Separation and Purification, Membranes (Basel), 7(1) (2017) 9

[8] A. Saberimoghaddam, V. Khebri, Design and construction of a helium purification system using cryogenic adsorption process, Iranian Journal of Chemical Engineering(IJChE), 15(1) (2018) 89-101

[9] J.G. Weisend II, Cryogenic Technology, in: Kirk-Othmer Encyclopedia of Chemical Technology, John Wiley & Sons, Hoboken, NJ, 2012, pp. 1-29

[10] M. Wright, Design and Development of a Helium Purifier, Old Dominion University, Norfolk, VA, 2009

[11] M.S. Yao, R.P. Wang, Z.Y. Liu, X.D. He, J. Li, The helium purification system of the HTR-10, Nuclear Engineering and Design, 218(1) (2002) 163 – 167

[12] V.P. Singh, D.M. Ruthven, Adsorption of moisture on molecular sieve adsorbents at low humidity, F84026, Canadian Fusion Fuels Technology Project, Canada, 1984

[13] D. Hatfield, F. Casagrande, I. Campisi, P. Gurd, M. Howell, D. Stout, H. Strong, D. Arenius, J. Creel, K. Dixon, V. Ganni, P. Knudsen, SNS Cryogenic Systems Commissioning, AIP Conference Proceedings, 823(1) (2006) 1436-1443

[14] S.A. Stern, F.S. DiPaolo, The Adsorption of Atmospheric Gases on Molecular Sieves at Low Pressures and Temperatures. The Effect of Preadsorbed Water, Journal of Vacuum Science and Technology, 4(6) (1967) 347-355

[15] S. Da-Ming, An experimental study of the adsorption characteristics of 13X molecular sieves, Journal of Physics E: Scientific Instruments, 22(3) (1989) 159-162

[16] S.C. Collins, Helium Purification Method and Apparatus, in, Cryogenic Technology, Inc., USA, 1970, pp. 19

[17] J.P. Dauvergne, D. Delikaris, F. Haug, S. Knoops, A helium freeze-out cleaner operating at atmospheric pressure, Cryogenics, 34 (1994) 135 – 138

[18] R.W. Wilson, H.R. Newsom, Helium: Its Extraction and Purification, Journal of Petroleum Technology, 20(04) (1968) 341-344

[19] A.E. Technology, Helium Gas Cryogenic Purifiers, in, South Holland, IL, 2021

[20] D. Kroll, Development of the mechanical design for a freeze-out purifier, Michigan State University, East Lansing, MI, 2020

[21] R. Hilz, Verschiedene Arten des Ausfrierens einer Komponente aus binären, strömenden Gasgemischen, VDI-Verlag, 1940

[22] H. Hausen, Bemessung und Gestaltung der im Gleichstrom und Gegenstrom arbeitenden Rekuperatoren, in: Wärmeübertragung im Gegenstrom, Gleichstrom und Kreuzstrom, Springer Berlin Heidelberg, Berlin, Heidelberg, 1950, pp. 148-170

[23] B.M. Bailey, Freeze Out Purification of Gases in Heat Exchangers, in, Springer US, Boston, MA, 1960, pp. 45-53

[24] R.B. Hinkley, J.C. Burke, F.E. Ruccia, R.P. Berthiaume, R.C. Reid, E.M. Drake, I.W. Dingwell, M.E. Weber, Contaminant Freeze-Out In Heat Exchangers. Volume II - Basic Investigation Of Contaminant Freeze-Out, ASD-TDR-63-508, United States Air Force Systems Command, Wright-Patterson Air Force Base, OH, 1963

[25] W. Woodside, Calculation of the thermal conductivity of porous media, Canadian Journal of Physics, 36(7) (1958) 815-823

[26] H.-M. Chang, J.L. Smith, Mass transfer of supersaturated contaminants in cryogenic helium heat exchangers, Int. J. Heat Mass Transfer, 33 (1990) 1299-1306

[27] M. Kandula, Frost growth and densification on a flat surface in laminar flow with variable humidity, International Communications in Heat and Mass Transfer, 39(8) (2012) 1030-1034

[28] K.-S. Lee, W.-S. Kim, T.-H. Lee, A one-dimensional model for frost formation on a cold flat surface, Int. J. Heat Mass Transfer, 40(18) (1997) 4359-4365

[29] K.-S. Lee, W.-S. Kim, The effects of design and operating factors on the frost growth and thermal performance of a flat plate fin-tube heat exchanger under the frosting condition, KSME International Journal, 13(12) (1999) 973-981

[30] A. El Cheikh, A. Jacobi, A mathematical model for frost growth and densification on flat surfaces, Int. J. Heat Mass Transfer, 77 (2014) 604-611

[31] M. Kandula, Frost growth and densification in laminar flow over flat surfaces, Int. J. Heat Mass Transfer, 54(15) (2011) 3719-3731

[32] J.D. Yonko, C.F. Sepsy, An investigation of the thermal conductivity of frost while forming on a flat horizontal plate, ASHRAE transactions, 73(2) (1967) 1.1-1.11

[33] M. Kandula, Effective thermal conductivity of frost considering mass diffusion and eddy convection, 1(4) (2010) 321-336

[34] G. Biguria, L.A. Wenzel, Measurement and Correlation of Water Frost Thermal Conductivity and Density, Industrial & Engineering Chemistry Fundamentals, 9(1) (1970) 129-138

[35] K.-S. Lee, S. Jhee, D.-K. Yang, Prediction of the frost formation on a cold flat surface, Int. J. Heat Mass Transfer, 46(20) (2003) 3789-3796

[36] B. Na, R.L. Webb, Mass transfer on and within a frost layer, Int. J. Heat Mass Transfer, 47(5) (2004) 899-911

[37] B.W. Jones, J.D. Parker, Frost Formation With Varying Environmental Parameters, J Heat Trans, 97(2) (1975) 255-259

[38] S. Byun, H. Jeong, D. R. Kim, Lee, K.-S., Modeling of frost growth and fog generation at ultra-low temperatures, Int. J. Heat Mass Transfer, 166 (2021) 120741

[39] S. Byun, et al., Frost modeling under cryogenic conditions, Int. J. Heat Mass Transfer, 161 (2020) 120250

[40] Y. Qi, et al. Mechanisms of trace water vapor frosting on a cryogenic surface in Nitrogen Gas Flow, Int. J. Heat Mass Transfer, 169 (2021) 120898

Chapter 3 : Performance Characterization of an Industrial Freeze-Out Helium Purifier

To understand and characterize the operating envelope and performance of a helium purification system, the commercially procured helium purifiers at the Facility for Rare Isotope Beams (FRIB) at Michigan State University (MSU) are considered. Although this system is not specifically designed for freeze out process, it is equipped to deal with type of contamination and is widely used in large scale cryogenic systems for particle accelerators at several national research facilities in the United States, and is representative of the present state of the art. There are four identical purifier systems available at FRIB. These purifiers are designed to purify up to 60 g/s (nominally at 13.0 bar) of helium. They can sustain inlet contaminations of up to several hundred ppm_v of nitrogen (air), but only a fraction of that in moisture. They use liquid nitrogen as the cooling medium for adsorption and moisture collection. The purifier components and operating mode is discussed in chapter 2, as well as briefly in the following section. The operating and regeneration procedure can be found in Appendix A. The performance characterization of this purifier is discussed in detail in the subsequent sections.

Several performance parameters for the industrial helium purifier will be measured. These are the following –

a) Liquid nitrogen (LN) consumption during nominal operating conditions

b) Frost collection capacity of purifier during nominal operating conditions and controlled operating conditions

c) Helium consumption (vent) during regeneration process (purifier blow-down)

d) Gaseous nitrogen consumption during regeneration process (purifier warm-up)[1]

The measurement/calculation procedure and resulting performance data from each of these tests are presented in the following sections.

3.1 Description of an Industrial Freeze-Out Helium Purifier

The industrial helium purifier has four main components, and several associated components for data collection and operation. The components are a heat exchanger used for freeze-out (HX-1), a heat exchanger used to recover the cooling from the nitrogen boil-off (HX-2), a nitrogen boiler heat exchanger utilizing liquid nitrogen to cool the helium close to 80K, and an adsorber bed to remove the components of air. The air collection capacity of the purifier was estimated, but this estimation showed that it would not be the limiting factor in purifier operation. The calculation showing this is in Appendix B. The focus of the testing is on heat exchanger 1 (HX-1). A schematic of the purifier is shown in Figure 3-1. HX-2 is a relatively small heat exchanger (UA of 0.05 kW/K compared with 1.21 kW/K for HX-1). HX-2 can be isolated from the system in order to send all the contaminated helium through HX-1. This results in the flow thermal capacity being approximately the same on both sides of HX-1, hereon described as HX-1 being 'balanced'.

---

[1] *The purifier utilizes gaseous nitrogen flow heated with electrical heater to warm-up the components for regeneration.*

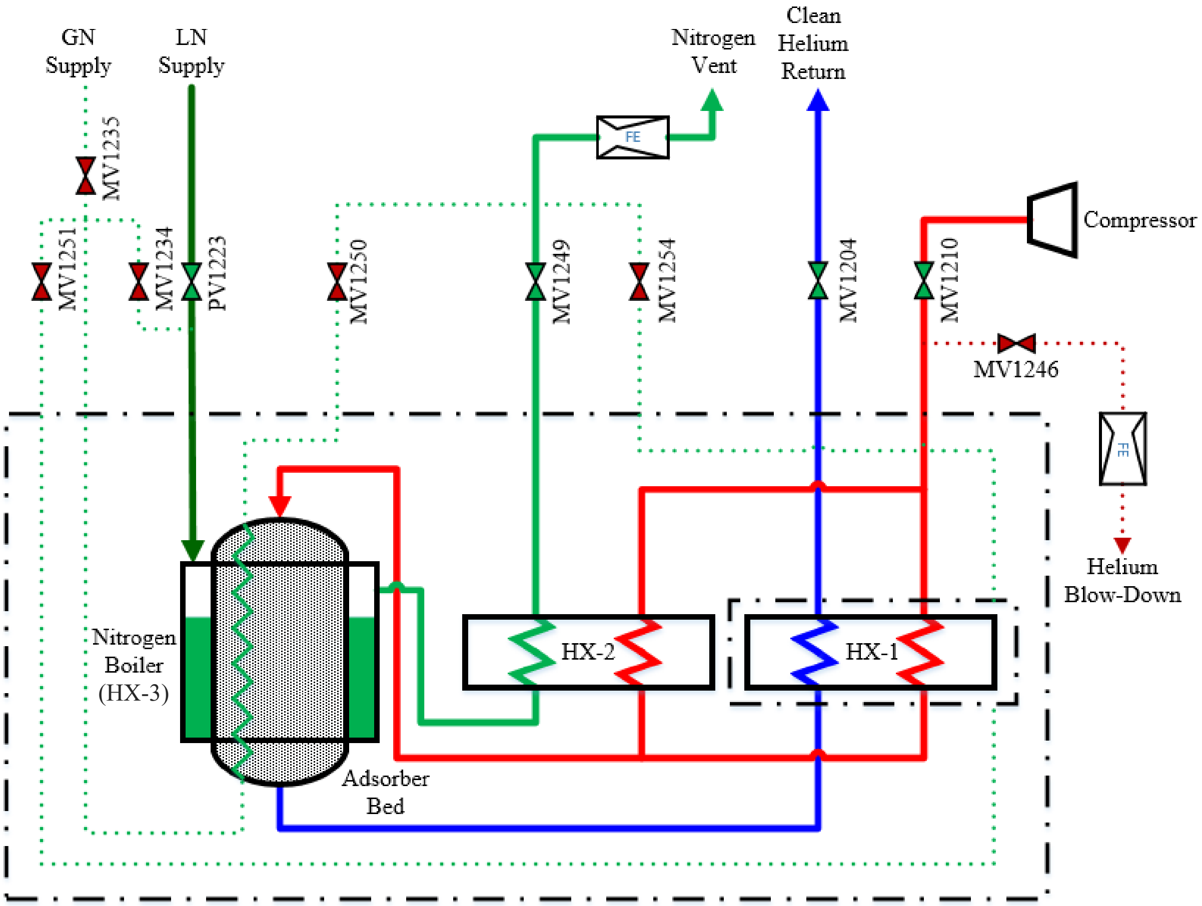

Figure 3-1 Schematic of FRIB purifier

Several auxiliary pieces of equipment were added to the purifier to study the influence of the various parameters, through several tests, which are discussed in this chapter. A sonic venturi was connected to the helium vent line to measure the amount of helium being vented during regeneration of the purifier. A classical venturi (Rosemount 3051 series differential pressure transmitter) flowmeter was connected to the nitrogen vent line. It measures the nitrogen flow rate leaving the purifier during operation, showing the liquid nitrogen utility usage. The liquid nitrogen (LN) consumption rate is an indication of the cooling required by the purifier and is directly related to the operating cost of the system. It also measures the nitrogen flow rate being used to warm the purifier during regeneration. There is a multi-component detector that is used to measure the instantaneous contamination level of water in the helium gas at the purifier inlet. There are pressure sensors measuring the pressure of the incoming helium (high side), clean helium (low side) return, nitrogen vent, and helium vent. Similarly, there are several temperature sensors throughout the purifier, measuring the important temperatures for the operation and characterization of the purifier.

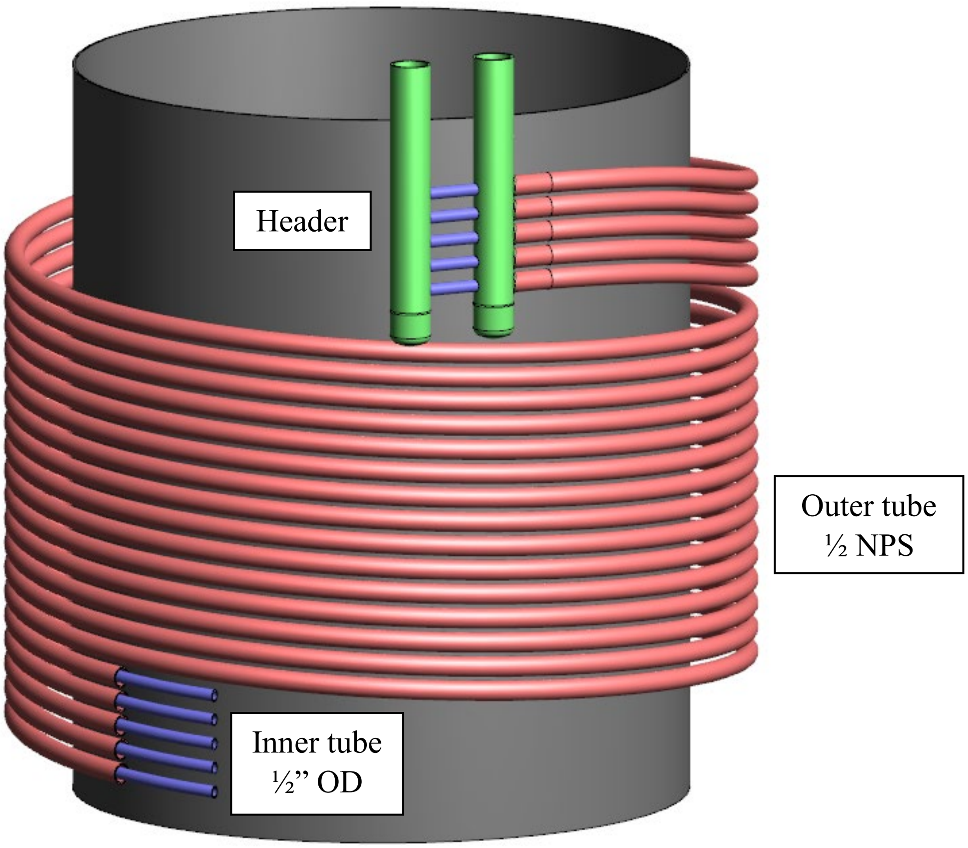

Figure 3-2 Simplified geometrical model of freeze-out heat exchanger

Heat exchanger 1 has 10 parallel passes of coaxial tube-in-tube geometry, coiled in a helix, as shown in Figure 3-2. The cold returning gas flows through the inner tubes (called the low side), while the contaminated gas flows through the annular space between the two coaxial tubes (called the high side). A header splits the gas flow into these 10 tubes.

Heat exchanger 1 has 10 parallel passes of coaxial tube-in-tube geometry, coiled in a helix, as shown in Figure 3-2. The cold returning gas flows through the inner tubes (called the low side), while the contaminated gas flows through the annular space between the two coaxial tubes (called the high side). A header splits the gas flow into these 10 tubes.

When the purifier has reached its contaminant capacity (typically for moisture first), the purifier must be regenerated to remove all the contaminants so it may be operated again. This includes blow down to atmospheric pressure, warm up using heated nitrogen to melt the frost, pump and backfill to remove the contaminants, and purge and cool down to prepare for operation.

3.2 Thermal-Hydraulic Characteristics of HX-1 during Steady-State Operation

A process model was developed to characterize purifier and heat exchanger properties and performance. It takes inputs of helium purifier inlet mass flow rate, pressure and temperature, HX-2 cold-end temperature difference, and nitrogen mass flow rate, pressure, and vent temperature. At a single point in time, it calculates all purifier temperatures, pressures, and mass flow rates (for unbalanced condition). It then uses these inputs and calculated values to calculate heat and mass transfer within the heat exchanger, temperature profile (cooling curve), UA profile, and NTU profile along the length of the heat exchanger.

Given average temperatures along the length, the Nusselt number in the annulus and the tube are calculated. De is Dean number, δ is the coiling ratio, and $B_{q,t}$ is the heat transfer correction factor for helical flow.

$$Nu_a = 0.027 De^{0.94} Pr^{0.69} \delta^{0.01} \tag{3.1}$$

$$Nu_t = 0.023 B_{q,t} Re_t^{0.8} Pr^{0.33} \tag{3.2}$$

The heat transfer coefficients are calculated as shown below, including a correction '*factor*', which was introduced to match the NTU with the test data for the steady state purifier heat exchanger, given the heat exchanger has no frost deposition. This factor is approximately 0.95 in order to match an NTU of approximately 16 for all test cases.

$$h_a = \frac{Nu * k_a}{d_{h,a}} * factor \qquad 3.3$$

$$h_t = \frac{Nu * k_t}{d_{h,t}} * factor \qquad 3.4$$

From these the heat transfer resistances are calculated. R_{frost} is calculated at each point along the length of the heat exchanger, based on the frost profile that is designated for that point in time.

$$R_{tube,cond} = \frac{d_{i,t} \ln\left(\frac{d_{o,t}}{d_{i,t}}\right)}{A_{s,t} k_{Cu}} \qquad 3.5$$

$$R_{tube} = \frac{1}{h_t A_{s,t}} \qquad 3.6$$

$$R_{annulus} = \frac{d_{i,t}}{d_{o,t} h_a A_{s,t}} \qquad 3.7$$

$$R_{frost} = \frac{d_{i,t} \ln\left(\frac{d_{frost}}{d_{o,t}}\right)}{A_{s,t} k_{frost}} \qquad 3.8$$

Where $A_{s,t}$ is the surface area of the inner tube. The UA for each unit length is calculated as such:

$$\Delta UA = (\Delta\%NTU) \sum \frac{1}{R_i} = (\Delta\%NTU) * \left[\frac{1}{R_{annulus}} + \frac{1}{R_{tube}} + \frac{1}{R_{tube,cond}} + \frac{1}{R_{frost}}\right] \qquad 3.9$$

Where $\Delta\%NTU$ is determined by an initial temperature profile using constant temperature ratio, in order to establish a discretization and initial properties at those points along the length of the heat exchanger. This new UA distribution along the length of the heat exchanger can be used to calculate the temperature profile. First, given the inlet stream temperatures and mass flow rates, the following equations are used to calculate the high side outlet temperature the heat exchanger. The low side outlet temperature is calculated using an energy balance.

$$T_{h,o} = T_{h,i} - \left(T_{h,i} - T_{l,i}\right)Z \tag{3.10}$$

$$Z = \frac{1 - e^{D}}{\frac{C_h}{C_l} - e^{D}} \tag{3.11}$$

$$D = UA\left[\frac{1}{C_h} - \frac{1}{C_l}\right] \tag{3.12}$$

If the heat exchanger has balanced flow capacities, the following equation is used instead.

$$T_{h,o} = T_{h,i} + \frac{-T_{h,i} + T_{l,i}}{\frac{C}{UA} + 1} \tag{3.13}$$

Then, starting from the warm end, the temperatures can be solved for along the length. For unbalanced flow, the high side outlet temperature is calculated by the following equations. The low side inlet temperature is then calculated by energy balance.

$$T_{h,o} = \frac{T_{h,i}\left[1 - Z - \frac{C_h}{C_l}Z\right] + ZT_{l,o}}{\left[1 - \frac{C_h}{C_l}Z\right]} \tag{3.14}$$

For balanced flow, the high side outlet temperature is calculated by equation 3.15. This version is simplified because $C_h = C_l$.

$$T_{h,o} = \frac{\left[\frac{C}{UA} - 1\right]T_{h,i} + T_{l,o}}{\left[\frac{C}{UA}\right]} \tag{3.15}$$

This method calculates a temperature profile based on an assigned frost deposition profile (or none). It can be calculated in the process model using the partial pressure curve with temperature or input directly from outside data. Figure 3-3 shows the cooling curves, NTU, and

UA at steady state with no frost for a balanced HX-1 and an unbalanced HX-1. The balanced case shows linear cooling curves, while the unbalanced case concave cooling curves which pinch at the cold end of the heat exchanger. NTU is slightly higher in the unbalanced case, as the minimum stream capacity decreased with the flow rate. However, UA is slightly lower in the unbalanced case, due to the heat exchanger being less effective with the unbalanced flow capacities. These curves are very important to establish and understand moving forward with this work. The temperature distribution effects the way frost deposits. It can shift where the frost deposits in the heat exchanger. NTU is the main performance parameter that is used to describe the overall performance as it degrades over time.

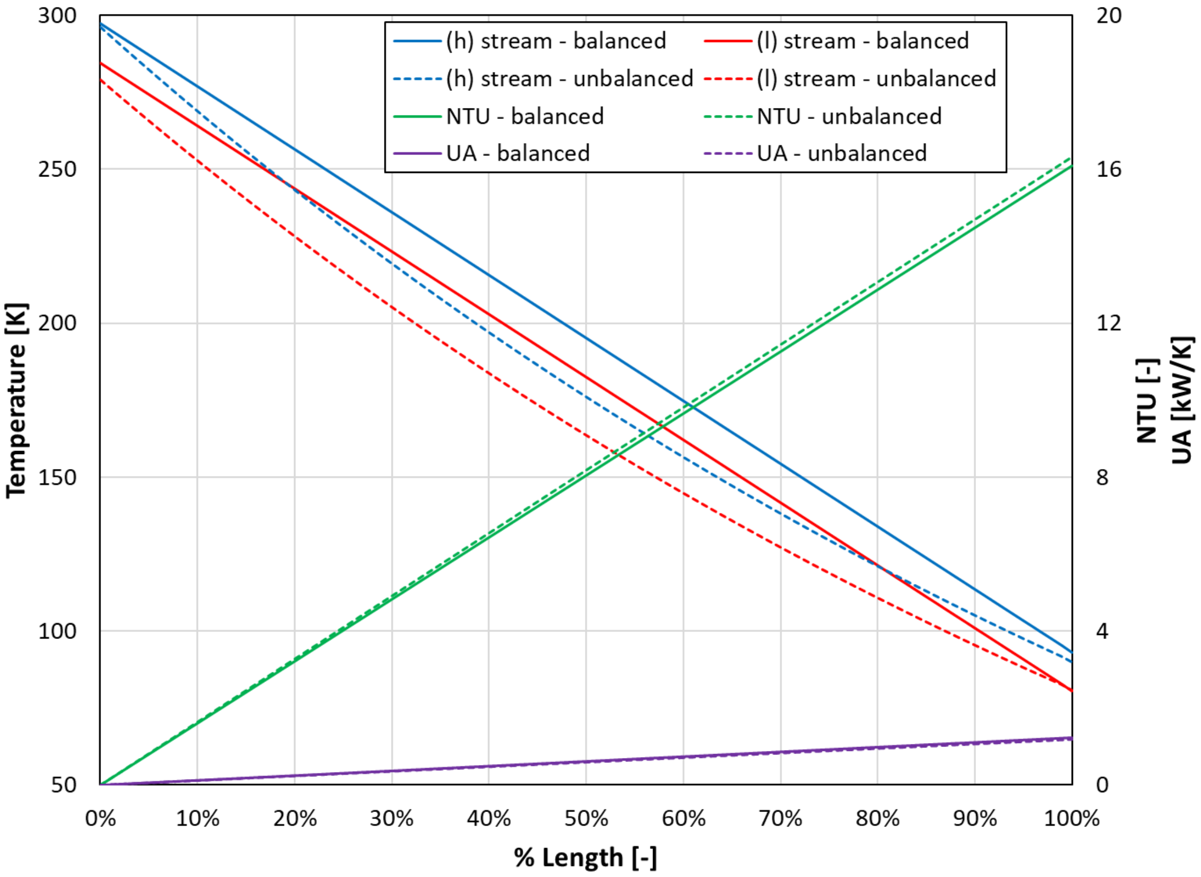

Figure 3-3 Cooling curve and NTU distribution with un-balanced (a) and balanced (b) flow under clean conditions

In order to get a baseline for liquid nitrogen consumption, it was measured during a nominal operating condition. The objective of this test was to quantify the nitrogen vapor that is vented during operation. Liquid nitrogen is introduced to the system as a cooling medium and is vented as vapor nitrogen after utilizing its refrigeration capacity. The liquid nitrogen (LN) consumption rate is an indication of the cooling required by the purifier and is directly related to the operating cost of the system.

A classical venturi tube was used to measure the vapor nitrogen flow rate leaving the purifier. Sizing calculations for the venturi is provided in Appendix B The following instrumentation will be used to measure the necessary process parameters required for calculating the vapor nitrogen flow rate –

- Upstream pressure: GE Unik 500 series pressure transmitter
- Upstream temperature: Lakeshore Platinum series resistance temperature detector
- Venturi pressure drop: Rosemount 3051 series differential pressure transmitter

The corresponding helium flow rate is measured using a similar setup (using venturi tube) at the purifier skid.

The tests yielded slightly different results for when HX-2 was isolated and when it was operating. When the extra cooling from the nitrogen boil-off was being utilized in HX-2, the nitrogen flow rate was measured to be 3.88 g/s on average for a helium flow of approximately 14.6 g/s at 13.8 bar. This calculation neglects the effects of flash on liquid nitrogen inlet, assuming nitrogen maintains the pressure measured at the vent. When HX-2 was isolated, balancing the helium flow rates in HX-1, the nitrogen flow rate was measured to be 5.26 g/s for a helium flow of approximately 14.2 g/s at 13.7 bar. This is because the refrigeration from the nitrogen vapor (from 80K to room temperature) is utilized for cooling and thus requires less liquid nitrogen for the unbalanced cases, which are more efficient from a nitrogen usage perspective.

3.3 Performance Degradation of HX-1 and Associated Frost Collection Capacity

Very little is known about the performance of the purifier heat exchanger under the frosting conditions that occur during operation. To study the effects of freeze-out on the heat exchanger, a series of tests were performed. The goal of these tests is to find the capacity for moisture collection under various conditions in order to better understand the driving forces that contribute to increased moisture capacity and operating time, as well as how these forces contribute to heat exchanger performance.

Tests were performed under two sets of conditions – one following a nominal operation of the purifier at FRIB (with variable moisture contamination at the inlet), and the second with a controlled injection of moisture into the purifier. The first test mimics the performance of the purifier under a practical condition, and the second in a controlled condition. The test data was analyzed to understand the influence of the various process parameters on the moisture collection capacity and operational efficiency.

3.3.1 *Measurement under Practical Operating Conditions (Variable Inlet Contamination)*

The first test was done during a period of maintenance on the FRIB refrigerator. During a nominal operation of the purifier the inlet contamination can vary widely depending on the helium being processed (whether from an equipment being commissioned, or make-up helium being added to the system). Moreover, the helium stream flow rate can vary widely. The moisture contamination level increased as the cryogenic components warmed up, releasing impurities, sending them to the purifier. Measurements under such variable (but practical) conditions are shown in Figure 3-4.

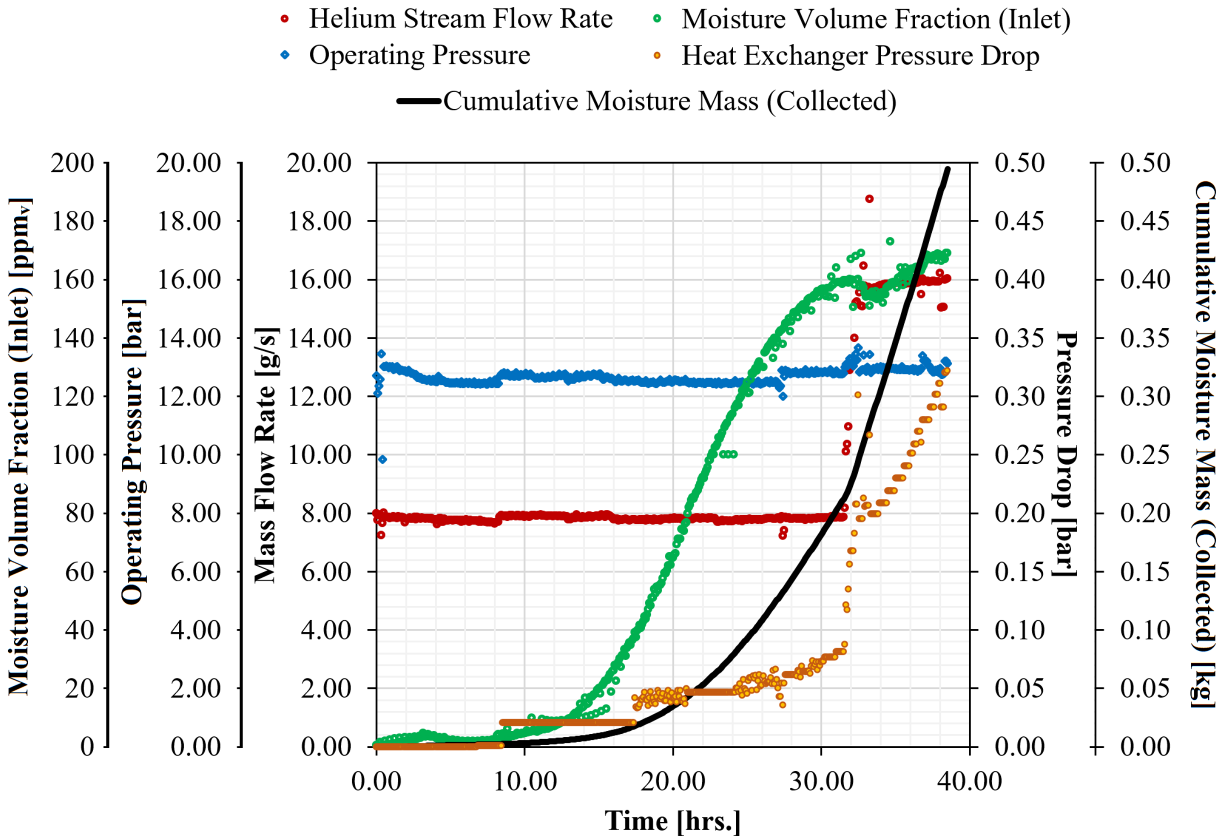

Figure 3-4 Measured high-side helium flow rate, moisture volume fraction, heat exchanger pressure-drop and corresponding estimated moisture mass collected over the operating period

For this test, the frost collection capacity of the purifier is measured using two different methods. The first is by integral sum of the moisture contamination measured at the inlet to the purifier. The inlet purity of the helium to the purification system is measured (and constantly monitored) using a digital hygrometer (Panametrics Dew.IQ) in ppm$_v$. The helium mass flow rate ($\dot{m}_{he}$) at the inlet to the purifier is measured using a venturi tube at the purifier skid. The moisture flow rate ($\dot{m}_w$) into the purifier is calculated using the equation below –

$$\dot{m}_w = w_w \dot{m}_{he} \tag{3.16}$$

Here, w_w is the mass fraction of the water vapor in the helium stream. The purifier is continued to be operated until the pressure drop in the heat exchanger (due to moisture collection) is elevated to a pre-determined level (typically above 0.25 bar). After this point, the pressure drop begins to rise exponentially, indicating that it is reaching blockage of flow. The total moisture collected to the purifier is then be calculated using an integral sum of the moisture contamination level during operation. One assumption commonly considered at this very low level of humidity (moisture) is the volume fraction of moisture is equal to the mole fraction. This assumption is based on ideal gas law in the dilute limit and is widely accepted in the industry [1] for this low level contamination.

The second method is gravimetric. The total moisture in its liquid form (water) is collected during regeneration of the purifier and is measured. As described in 3.1, the frost is melted during warm-up and removed during pump-downs. It is then collected in a cold trap, before being re-melted for measurement. The calculated (integral sum) and measured (gravimetric) moisture collected over the operating period is summarized in Table 3-1.

Table 3-1 Summary of frost collection measurement and estimation

Parameter	**Value**
Nominal operating pressure [bar]	13.0
High-side helium flow rate [g/s]	Variable
Moisture volume fraction at inlet [ppm_v]	Variable
Estimated amount of moisture collected (integrated sum) [kg]	0.50
Measured amount of moisture collected (gravimetric) [kg]	0.56
Maximum observed pressure drop [bar]	0.33
Total operating time [hr.]	38.5

Approximately 10% variation between the measured (gravimetric) and estimated (integrated sum) data is observed. This could be due to measurement errors and the resolution and accuracy limitations of the hygrometer.

3.3.2 *Development of Low-Level Moisture Generator*

A controlled contamination study is required to understand the influence of the various process parameters on the moisture collection process. Controlling contamination level and flow rate allows for isolation and better study of specific variables and their effects on frost deposition in the purifier heat exchanger. Equipment to achieve constant and controllable low-level contamination is not available commercially. As such, a low-level moisture generator was designed and fabricated. Tests were conducted at controlled inlet moisture contamination conditions were performed to estimate the moisture collection capacity of the purifier.

A schematic diagram of the moisture generator set-up is shown in Figure 3-5. The recovery compressor supplies clean helium to the moisture generator from helium gas storage tanks for this test. The moisture generator set-up uses two helium streams – one '*dry*' (moisture volume fraction < 0.1 ppm$_v$) and the other saturated with moisture. Balanced mixing of the two streams through two valves (MV112 and MV101) is used to achieve a target contamination (moisture) level (typically between 10 – 100 ppm$_v$). Helium bubbled through a sintered metal filter in a water-filled vessel generates the saturated helium stream. The vessel was filled with a more than sufficient amount of water (3-5 times the collected mass) before each test. The total flow rate and humidity (moisture volume fraction) of the contaminated (mixed) helium stream at the outlet of the moisture generator were measured by the digital hygrometer.

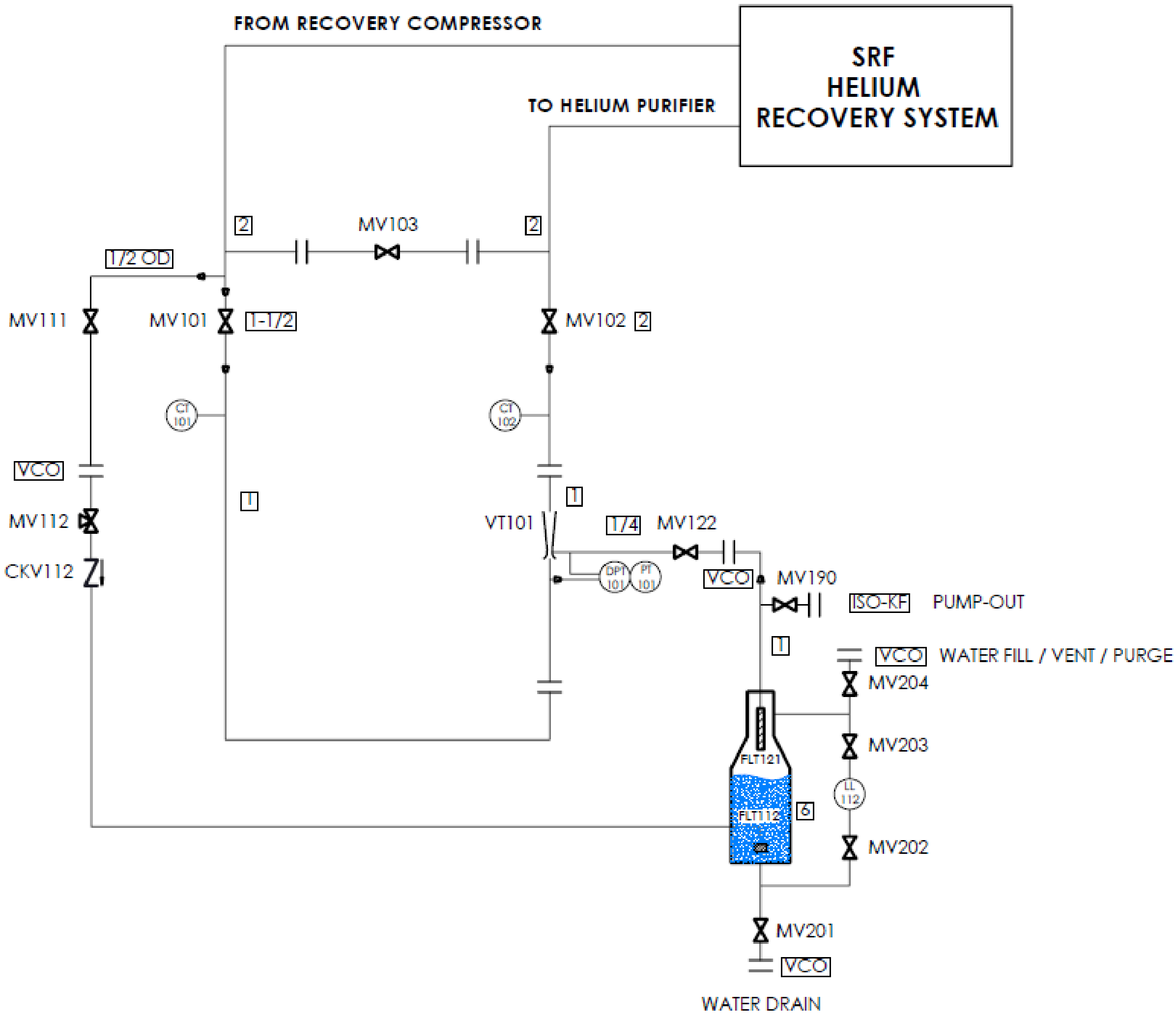

Figure 3-5 Schematic diagram of a constant low-level moisture generator set-up

The moisture generator water vessel, valves, and surrounding piping were designed as per ASME B31.3 and modeled in SolidWorks, as shown in Figure 3-6. The water vessel and surrounding piping were fabricated at FRIB. The valves (and their flow coefficients) were selected specifically to allow for generation of a desired range of low level moisture contamination, based on the relative flow rates through them. For MV101, a Swagelok SS-4MG-MH was chosen with a C_V of 0.03. With full flow through MV101 ($C_V = 0.16$), the moisture generator is designed to be capable of generating a contamination range of approximately 5-190 ppm_V. The design calculation assumes all of the helium coming out of the water vessel is completely saturated.

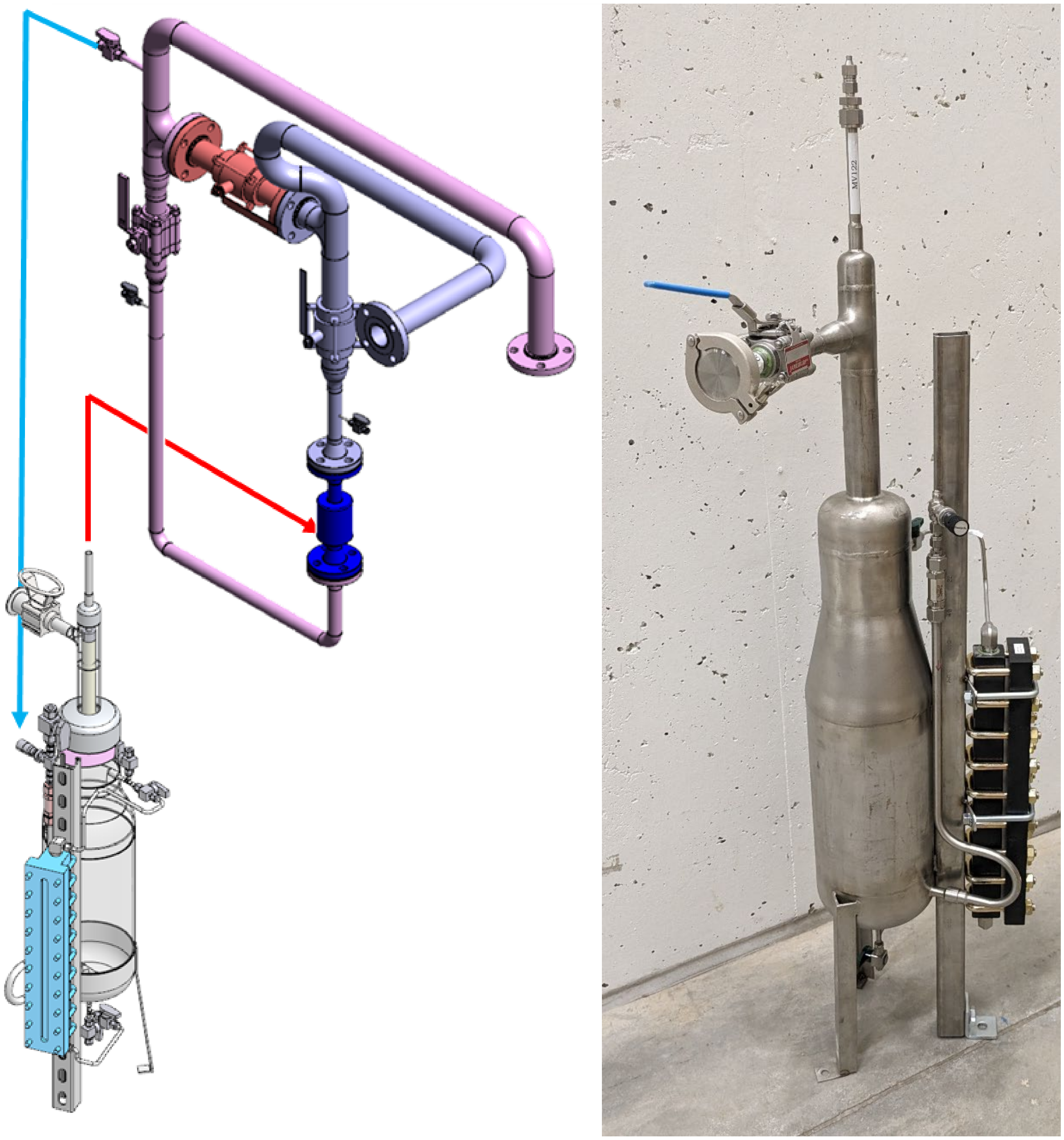

Figure 3-6 3D model and photo of the low level moisture generator

Figure 3-6 also shows the liquid level measurement port in blue on the 3D model and in black in the picture. It shows how much water is in the vessel during operation, and the depleted water in this vessel is the most reliable way of accounting for how much moisture is added to the helium stream. A graduation was attached, so that it can be followed and verified during the progression of the test. In order to convert this vertical measurement into a volume, a calibration of the graduation was performed, correlating the two. This was completed for volumes between 0.3 L and 6.5 L. A correlation between liquid level and volume was calculated using a linear trend line of the data, as shown in Figure 3-7. There is a gap in the middle of the range (150 mm to 180 mm) because the liquid level viewing port is split into two, with a metal frame in between.

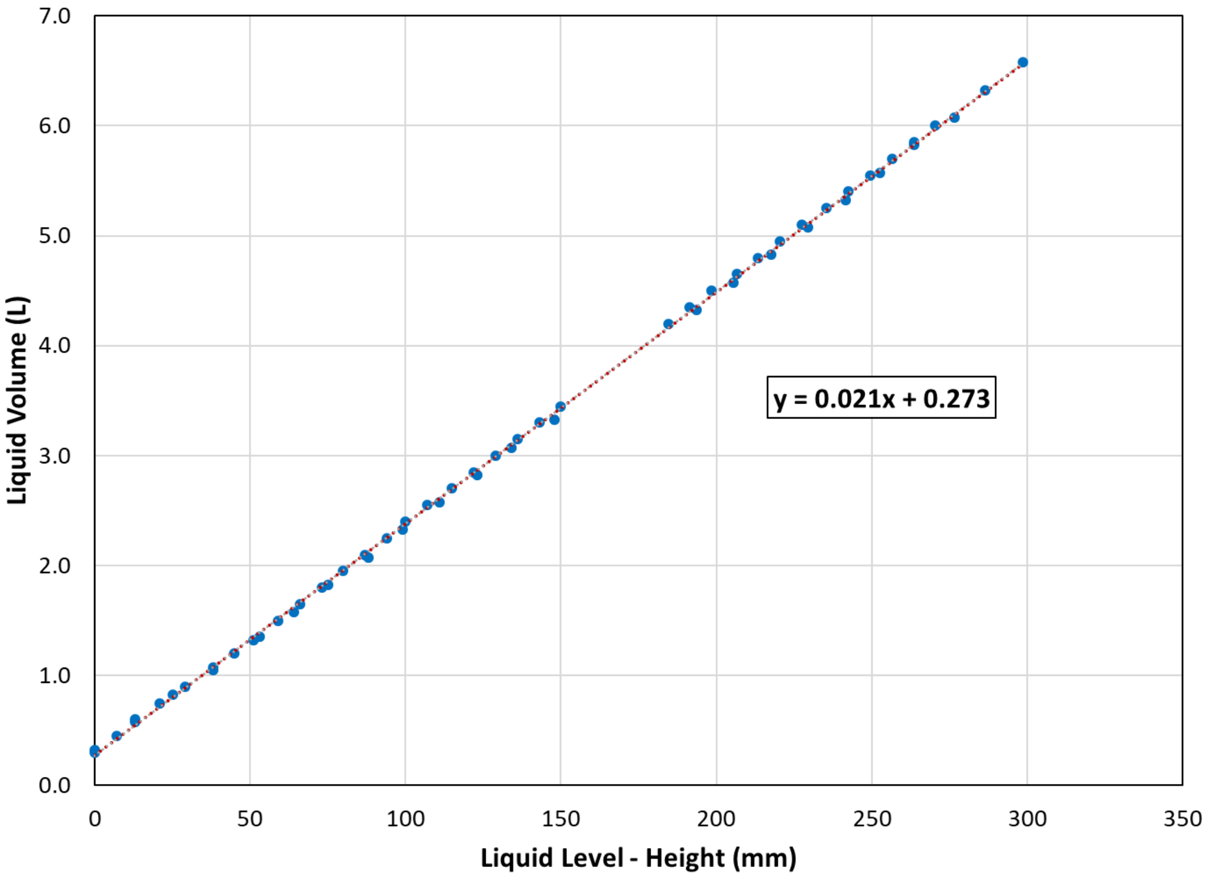

Figure 3-7 Liquid volume calibration with height

Initial testing of the low level moisture generator was performed using nitrogen gas, in order to show its effectiveness and stability. The objective of this test was to show that the moisture generator vessel was capable of generating saturated gas at a consistent level (given that the conditions are consistent) and to determine if the amount of water in the vessel impacted whether the gas comes out saturated. A dew point hygrometer was used to measure the moisture contamination level coming out of the vessel (saturated) during this test. The volume of water in the vessel was varied between 1.0 L and 7.0 L. The hygrometer consistently read approximately 56 C (+/- 1 C, corresponding to 18 ppm), with a slight increase in dew point below 1.5 L of water. The gas inlet tube sits at a height in the vessel equivalent to approximately 0.7 L of water, as the low water level is approached, the gas has very little water by which to be saturated before emerging from the surface. This results in insufficient saturation, as indicated by the dew point measurements. In order to avoid this with some room for error, it was determined that the water vessel should not be drained below 2.0 L during operation. Due to the expected purifier moisture capacity of 0.5 L from the nominal purifier test, the moisture generator water vessel was filled to 3.0 L at the beginning of each of the controlled tests.

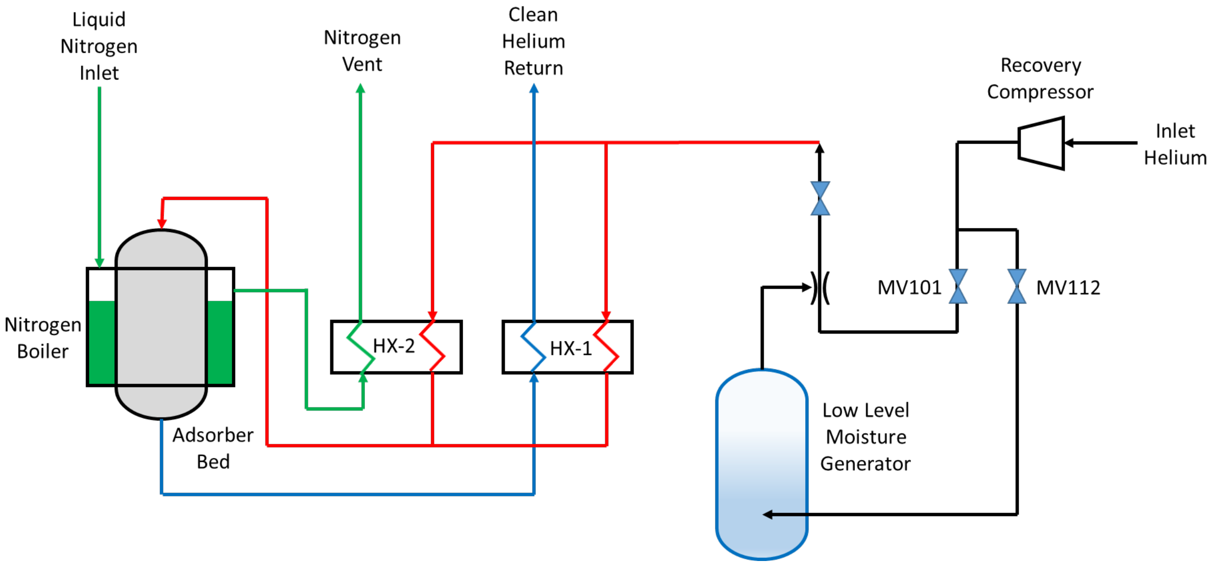

Figure 3-8 Schematic of purifier with test set-up

Figure 3-8 shows the overall flow path of the helium during the controlled testing. The recovery compressor supplies clean helium from gas storage tanks. The low level moisture generator used to inject the moisture-contaminated helium stream (with known inlet contamination) into the purifier. It takes a slip steam of the incoming helium and saturates in the water-filled vessel. This slip stream is recombined with the clean helium in a ratio that creates the desired moisture contamination level. The now contaminated helium is then purified, by way of moisture freeze-out in the purifier heat exchanger. The helium is then sent back to the helium gas storage tanks.

Moisture contamination level was calculated during testing with several methods. First is the liquid level measurement on the moisture generator itself to show how much water has left the vessel (and therefore entered the purifier). Second is the volume difference of water in the moisture generator water vessel between the beginning and end of the test. The vessel was filled with a specific and recorded volume of water at the beginning, and then drained at the end of the test. These two are the most direct measurements of the amount of water sent to the purifier, and so held as the most reliable. The water removed from the purifier during regeneration is also measured for verification. This measurement can introduce error due to water leaving with the helium when pumping down to very low pressures. The digital hygrometer mounted at the purifier inlet gives real time recorded data of the contamination level. However, while it can show gradient, it was shown to be consistently at odds with the liquid level measurement due its actual measuring accuracy limitations. This error was roughly consistent between tests and corrected in the data analysis, which is discussed in the following sections.

3.3.3 *Measurement under Controlled Operating Conditions*

With the use of the low-level moisture generator, the purifier was tested under controlled operating conditions. Four tests were performed, as described in Table 3-2. Two different contamination levels were tested (~30 ppm and ~ 60 ppm), both with balanced and unbalanced flow in HX-1. The helium mass flow rate was approximately 14 g/s, the inlet pressure was approximately 14 bar, and the starting pressure drop in the purifier was approximately 0.1 bar. Humidity level was chosen as an independent variable because it can shift where frost begins depositing by changing the partial pressure profile. A higher humidity will begin depositing at warmer temperatures. For example, 60 ppm of water vapor in helium will begin frosting at ~251 K, while 30 ppm will begin frosting at ~245 K. Flow imbalance was chosen as variable because it can shift where frost deposits in the heat exchanger by shifting the cooling curves (temperature profiles) in the heat exchanger.

Table 3-2 Test conditions (parameters)

Test #	ω_{in}	HX-1 Flow	$\dot{m}_l$	$\dot{m}_{HX-3,start}$	P_{inlet}	ΔP_{start}
	[ppm$_v$]	[-]	[g/s]	[g/s]	[bar]	[bar]
1	32.0	Balanced	14.9	0.00	14.3	0.10
2	32.1	Unbalanced	14.6	0.60	14.0	0.09
3	68.6	Balanced	14.2	0.00	14.3	0.10
4	58.3	Unbalanced	13.8	0.50	14.0	0.10

During testing, various temperatures along the flow/process path, the inlet pressure to the purifier, the pressure drop across the purifier, the inlet mass flow rate of helium, the mass flow rate of nitrogen leaving the vent, and the moisture content of the inlet helium were collected by a data logger. The temperatures were measured at the purifier inlet, HX-1 outlet, HX-2 outlet, N_2 boiler helium inlet, N_2 vent from HX-2, adsorber bed outlet, and purifier outlet. The first step in the data analysis was determining what data we can trust. These were largely determined by the physical location of the temperature sensors, mass and thermal energy balance and operational experience for analysis and especially HX-1. The following terminology will be used in this study. The high side of the heat exchangers is the side with contaminated helium, incoming to HX-1 at nearly 300

K at the warm end. The low side is the side with clean returning helium or nitrogen, incoming to HX-1 at nearly 80 K at the cold end.

The purifier inlet moisture content, as measured by the digital hygrometer, had two inaccuracies. First, there is a signal that repeats every ~15 minutes that was removed in post-processing. Second, the hygrometer appears to be understating the value by about 50%, based on the value measurement within the moisture generator water vessel. Therefore, the hygrometer is used as a reference and not for actual moisture value in the stream.

The nitrogen mass flow rate and temperature also had some consistently timed anomalous signals, however these were determined to be real data. The nitrogen boiler liquid level is controlled based on a maximum and minimum volume. When it reaches the minimum, it fills until it reaches the maximum. This batch-type process results in non-steady state instantaneous nitrogen measurements. When the nitrogen boiler fills, some of the nitrogen flashes (due to pressure changes across a valve upstream) to vapor. This vapor immediately travels through HX-2, increasing the mass flow rate through the nitrogen vent and decreasing the temperature due to the influx of cold gas. Since these spikes are due to flash and not interaction in the heat exchangers (as the components of interest), they were filtered out of the data. Based on an assumption that the pressure of the incoming liquid nitrogen is 1.0 bar, all the spikes in mass flow and temperature of nitrogen are due to flash across the valve, reducing the nitrogen from the supply pressure of 3.5 bar to 1.0 bar. They are therefore negated and filtered out of the dataset.

The heat in-leak in the purifier is also not known or measured. The design basis reported an ambient heat leak of 75 W. Based on vessel surface area (assuming exclusively radiation takes place), a theoretical estimate of 46 W was calculated. Based on these estimations, the heat in-leak was assumed to be 75 W (insignificant compared the HX thermal duty) for the data analysis. It is assumed that heat in-leak is constant for all tests. For the purposes of ease of calculation, it is assumed that all the heat in-leak occurs to the low side of HX-1.

The HX-1 inlet temperature measurements were assumed to be accurate because they lined up with what we expect at room temperature, and they were mostly unchanging throughout the tests. The HX-1 outlet temperature measurements were questioned, along with the nitrogen mass flow rate and vent temperature. This was because the low-side outlet decreased over time, but the high-side outlet did not increase. This signals that there is heat exchanger performance degradation, which we expect, but it was only captured by one temperature measurement. Increased nitrogen flow rate is also the result of heat exchanger degradation. In order to analyze which combination of measurements should be taken as accurate, 12 different cases were considered, with various combinations of trusting LN flow, high-side outlet temperature, low-side outlet temperature, and heat in-leak values. Various energy balances were used to recalculate the values that were assumed to incorrect in each case. These cases, and the resulting temperatures, energy balances, and heat exchanger performance metrics are shown in Appendix D. Through this analysis, it was determined that the nitrogen mass flow rate and temperature measurements were trustworthy. Because the heat exchanger high pressure cold end outlet temperatures weren’t capturing the performance degradation that was happening, the energy balances around the heat exchangers weren’t closing. In the cases in which the nitrogen flow rate was calculated, it was either decreasing over time (showing inverse performance degradation of HX-1) or were much lower than the measured values to start (which contradicts with operational experience and initial calculation estimates). Using the nitrogen flow rate and nitrogen vent temperature, the HX-1 high side outlet temperature was recalculated using an energy balance around the nitrogen boiler and the adsorber bed. The HX-1 low side temperature was calculated using this newly calculated temperature, the heat in-leak, and the energy stored in frost (which is extremely small) in an energy balance around HX-1.

For the unbalanced case, a few more energy balances are required, as there is no measurement for how much helium goes through HX-2. The same nitrogen boiler and adsorber bed balance is done to calculate the high side temperature at the inlet of the nitrogen boiler. However, there are two heat exchanger that contribute to this temperature. In order to calculate the helium mass flow rate going through HX-2, an energy balance around HX-2 is done. A temperature difference of 0.1 K at the cold end of HX-2 is assumed. The flow rate of nitrogen is significantly higher than that of helium in this heat exchanger. A sensitivity analysis on this temperature difference was performed, showing less than a 5% error in HX-1 NTU between 0.1 K and 50 K temperature difference, with that decreasing to less than 0.1% over the length of the test. It also showed less than 10% error in HX-2 helium flow rate, similarly decreasing over the length of the test. This sensitivity analysis shows that any error in the assumption of 0.1 K temperature difference is inconsequential in the overall analysis of the purifier. Now that the overall mass flow rate and mass flow rate through HX-2 are known, the mass flow rate through HX-1 is calculated using a mass balance around the mixing point. The same is done for the temperature of the HX-1 high side outlet using an energy balance around the mixing point. Finally, an energy balance around HX-1 is used to calculate the low side HX-1 outlet temperature.

Now that all the temperatures and mass flow rates are known, HX-1 can be analyzed, with the end goal being calculating its UA and NTU to show how its performance degrades over time. Energy balances are used to calculate the high-side and low-side duties. The log mean temperature difference is calculated based on the recalculated temperatures. The UA is then calculated as shown in equation 3.17.

$$UA = \frac{q_l}{\Delta T_{LM}} \quad 3.17$$

The stream capacities are then calculated as shown in equation 3.18 and 3.19. The minimum of these two is C_{min}.

$$C_h = \frac{q_h}{\Delta T_h} \quad 3.18$$

$$C_l = \frac{q_l}{\Delta T_l} \quad 3.19$$

Knowing UA and C_{min}, NTU can be calculated as such:

$$NTU = \frac{UA}{C_{min}} \quad 3.20$$

During the four tests, the purifier was operated under prescribed conditions in Table 3-2 until the pressure drop across the purifier reached approximately 0.6 bar. This signifies a point in the test at which the pressure drop is increasing exponentially, which means the purifier is almost plugged with frost.

Figure 3-9 shows the operating conditions throughout the duration of each of the four tests. Table 3-3 shows the major results of the tests. The mass collected during these tests is a direct function of the contamination level, the mass flow rate, and the time. Therefore, the 60 ppm cases took significantly less time. Test 1 (30 ppm, balanced) had the most mass collection, while the other 3 cases collected roughly the same amount, although test 2 (30 ppm, unbalanced) had the least mass collection. The 60 ppm tests had a more abrupt (exponential) pressure drop increase at the end of the tests, after staying mostly constant for most of the test. The 30 ppm tests had a more linear increase in pressure drop throughout the duration of the tests. The 60 ppm tests used more nitrogen toward the end of the tests than the 30 ppm tests, suggesting that the heat exchanger degraded more. The balanced cases used more nitrogen than the unbalanced cases, as they were not utilizing the nitrogen boil-off to cool the incoming helium.

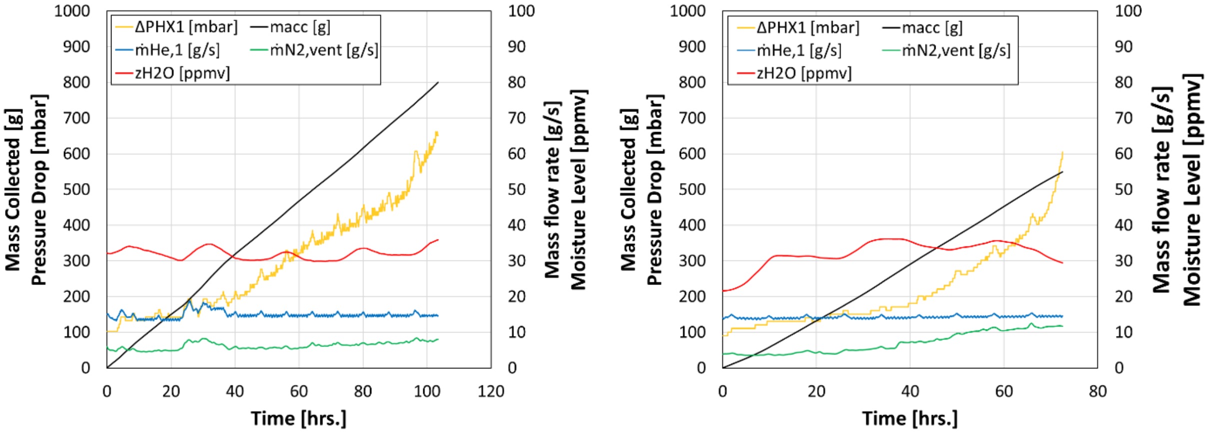

(a) Test 1 – 30 ppm balanced

(b) Test 2 – 30 ppm, unbalanced

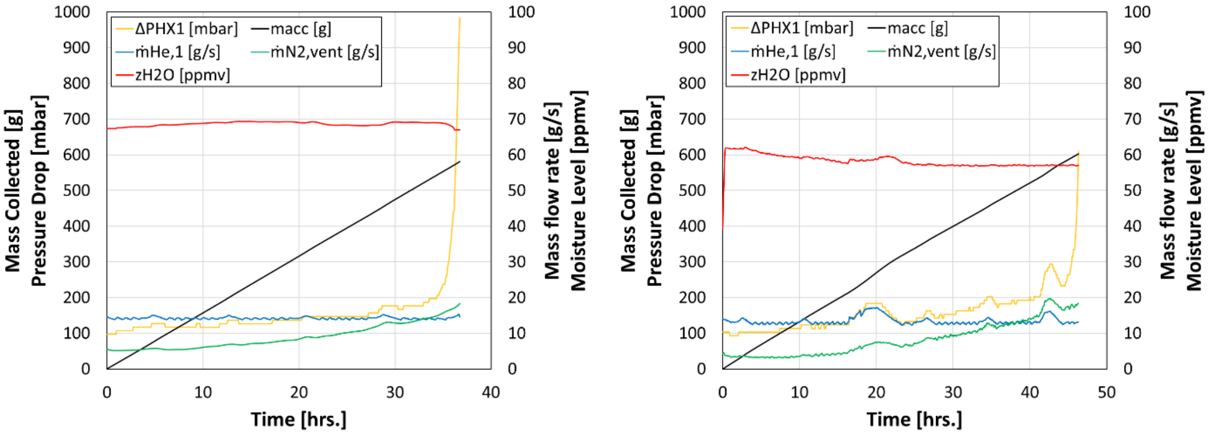

(c) Test 3 – 60 ppm balanced

(d) Test 4 – 60 ppm, unbalanced

Figure 3-9 Controlled test measured outputs for tests 1, 2, 3, and 4, including HX-1 pressure drop, HX-1 helium mass flow rate, purifier inlet ppm, mass of frost accumulated, and nitrogen vent flow rate in time

Table 3-3 Controlled test results

Test	Inlet Moisture	HX-1 Flow	Final NTU	Final ΔP	HX-1 Mass Collected	Time of Test
	[ppm$_v$]	[-]	[-]	[bar]	[g]	[hrs.]
1	32.0	Balanced	9.7	0.66	800	103.5
2	32.1	Unbalanced	5.8	0.61	538	71.4
3	68.6	Balanced	3.6	0.98	581	36.8
4	58.3	Unbalanced	3.2	0.61	591	46.3

Figure 3-10 and Figure 3-11 show the UAs and NTUs of the tests. All four tests started at approximately 16 NTU and 1140 W/K of UA. The 30 ppm tests had less NTU degradation than the 60 ppm tests. The balanced tests had less NTU degradation than the unbalanced tests (although this difference is minimal for the 60 ppm tests). Figure 3-12 and Figure 3-13 show the warm end and cold end temperature differences. At the beginning of the tests, the high side outlet was slightly colder in the unbalanced tests than the balanced tests. At the end of the tests, the low side outlet was colder and the high side outlet was warmer in the 60 ppm tests. The low side outlet was colder in the unbalanced cases than the balanced cases. The 30 ppm tests have much more variation between the balanced and unbalanced conditions than the 60 ppm tests.

In the unbalanced tests, the temperature differences on each end of the heat exchanger were different, but slowly converged as the helium flow rate through HX-2 decreased to near zero (~0.07 g/s). This was the case for both unbalanced cases. The HX-2 flow rate started at ~0.6 g/s, then decreased over time as HX-2 plugged with frost. The frost capacity of HX-2 is very small, approximately 12 grams.

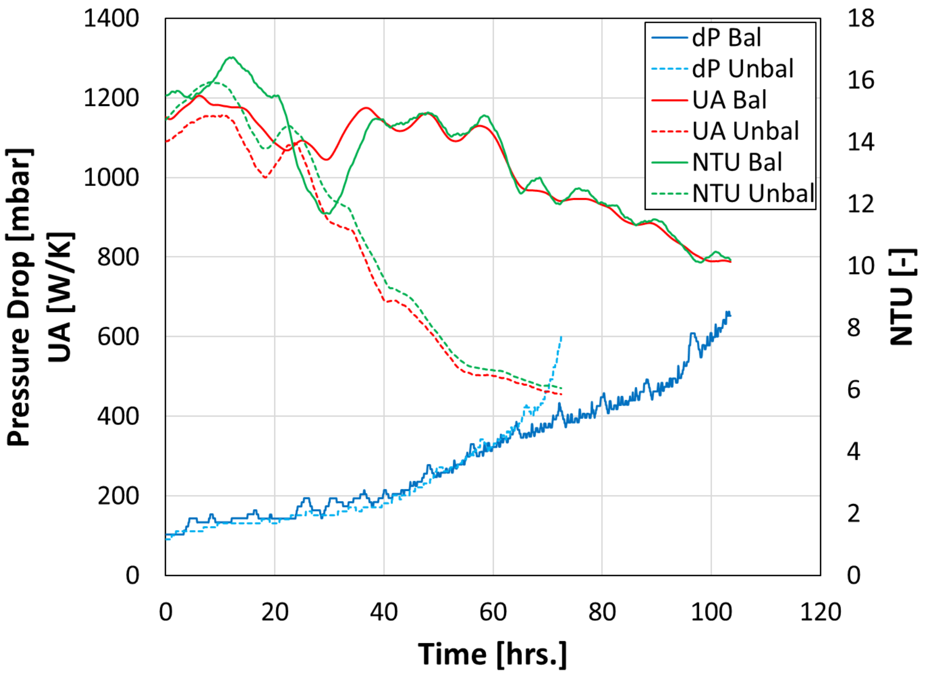

Figure 3-10 Controlled test heat exchanger characterization parameters for 30 ppm tests (tests 1 and 2)

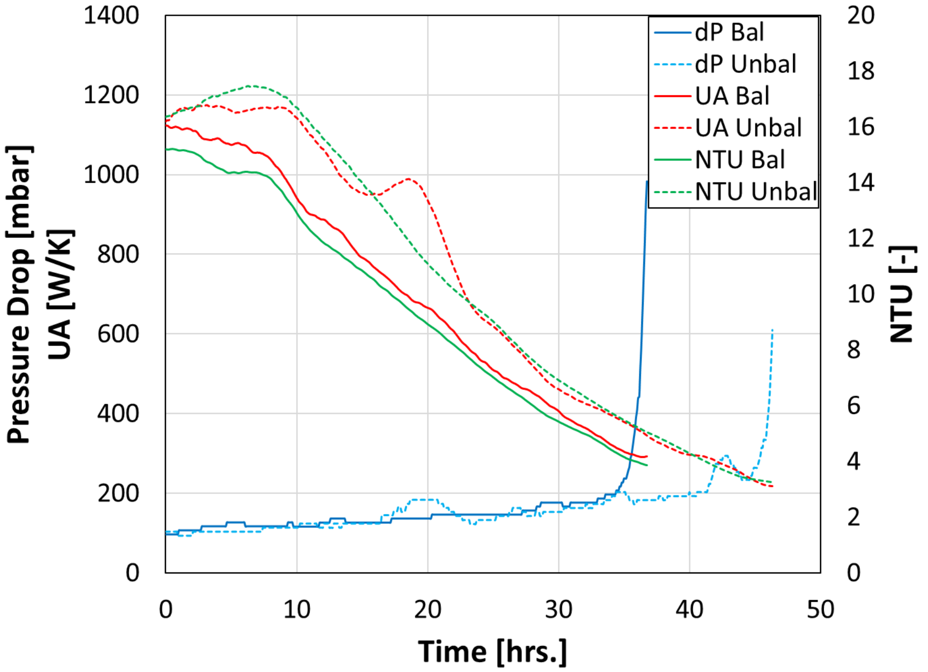

Figure 3-11 Controlled test heat exchanger characterization parameters for 60 ppm tests (tests 3 and 4)

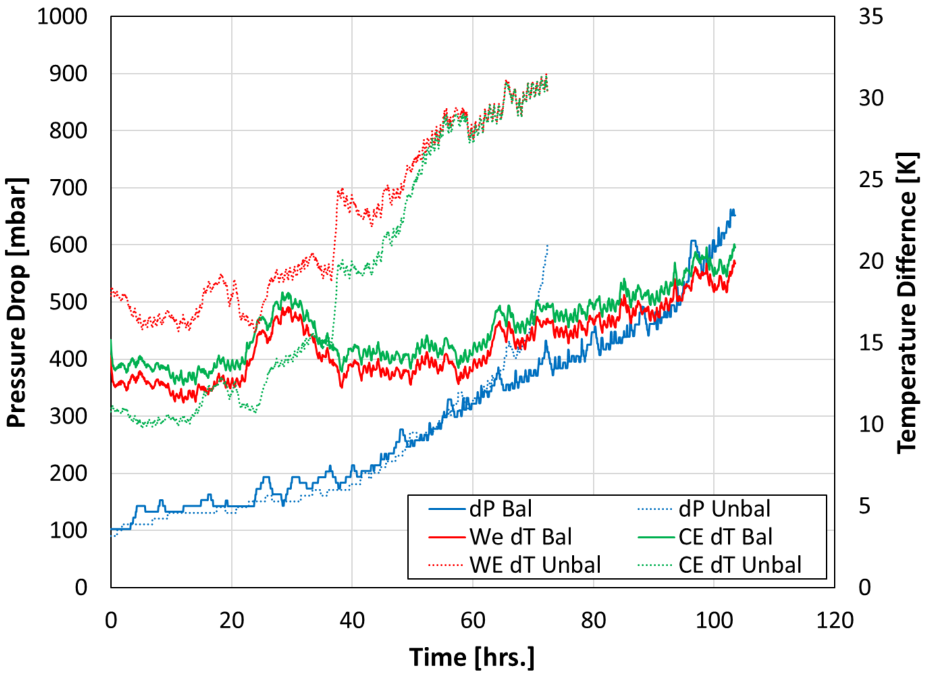

Figure 3-12 Controlled test heat exchanger differences for 30 ppm tests (tests 1 and 2)

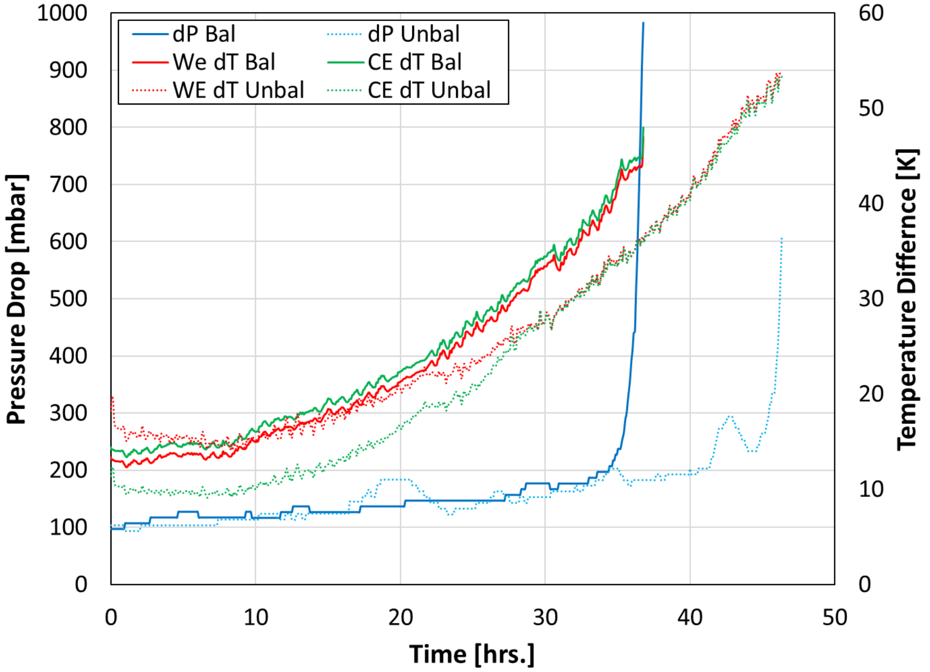

Figure 3-13 Controlled test heat exchanger temperature differences for 60 ppm (tests 3 and 4)

Figure 3-14 shows the pressure drop for all four tests normalized in time (t/t_f). It shows how the slope of the pressure drop vary between the tests. The 60 ppm tests show the same flat, then exponential curve. The 30 ppm tests show a more linear increase in pressure drop, with the 30 ppm balanced test being the most linear.

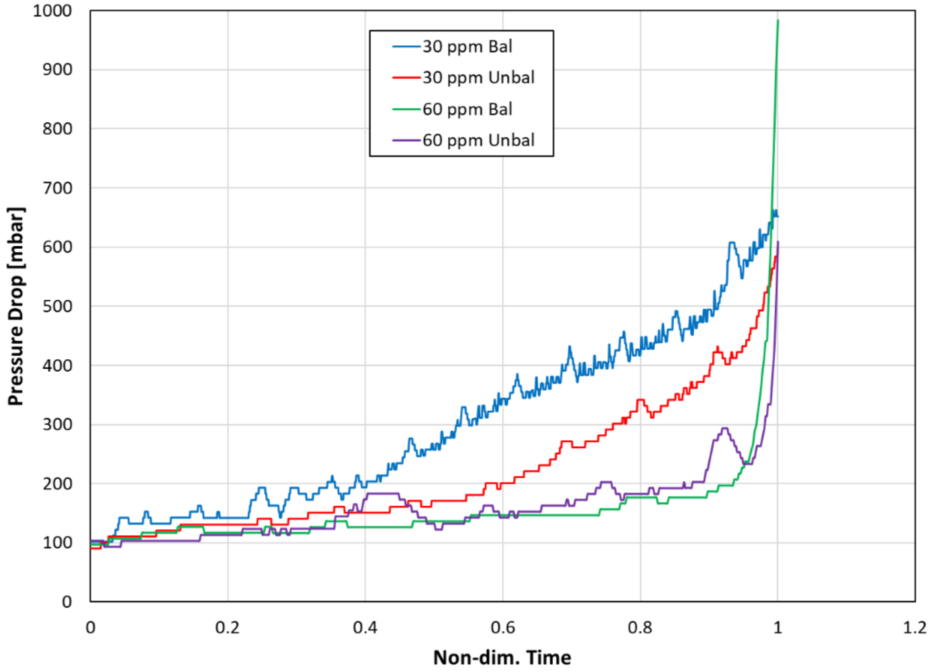

Figure 3-14 Pressure drop normalized for time

These observations lead to several hypotheses. First, the 30 ppm balanced test deposited frost more spread out throughout the heat exchanger, allowing for more area of frost deposition with less localized pressure drop. This means that the cooling curves in the heat exchanger shifted gradually over time, allowing frost to deposit over a larger heat exchanger area. Second, the 60 ppm cases are plugging with frost more locally. This is shown by the pressure drop rising rapidly and suddenly. The more spread out moisture deposition causes pressure drop to rise gradually (as opposed to abruptly), as it constricts more of the flow area of the annulus over time, but evenly throughout the tube, so as not to completely block flow.

The 30 ppm tests have much more variation between the balanced and unbalanced conditions than the 60 ppm tests because the lower real test value ppm (58 vs 68 ppm) in the balanced test counteracts the effect of the unbalanced heat exchanger. The partial pressure curve is nearer to the inlet for the 60 ppm tests, so it could be plugging with frost in the header when the cooling curve shifts toward the entrance to the heat exchanger over time.

The mechanical construction of the ten parallel tube sets in the heat exchanger makes a large difference on the flow distribution between the tubes and its impact on the heat exchanger performance. If the flow is not balanced between the tubes (biased by the header design), one tube may get more flow, resulting in it collecting more mass and plugging before the other tubes. If the flow is blocked in one of the tubes, the refrigeration from the low side going through that tube is wasted. The low side flow is practically constant in each tube throughout the duration of the test, although it may not be equal between tubes, as it experiences the same flow mal-distribution that the high side does. This flow blockage may cause frost to build up closer and closer to the header in that tube, due to cold temperatures reaching the header. Blockages in one tube would cause the mass flow rate in the other tubes to increase, taking on the additional flow. This would cause the cold end temperature difference in the remaining tubes to increase, while the warm end temperature difference decreases. This decrease in the warm end temperature difference results in the frost depositing closer to the cold end of the heat exchanger over time, shifting further as more tubes plug. Flow blockage in certain tubes causes the heat exchanger NTU to decrease greatly, as the low side flow is wasted. This effect can be seen in tests 2, 3, and 4, in which NTU dropped significantly, but gradually. In order to achieve this magnitude of NTU degradation, flow distribution must be affected. This effect is further investigated theoretically in chapter 5.

3.4 Regeneration of Purifier

During regeneration, the contaminant-laden helium inside the purifier is vented to the atmosphere. The total mass of helium lost during this process may not be insignificant. Moreover, additional helium is used (and vented) for clean-up of the purification system following the regeneration process. The helium usage during each regeneration of the purifier system can be theoretically estimated (based on the known internal volume of the purifier) and measured (during blow-down, using a flow meter). Each of these processes are discussed below.

3.4.1 *Estimation and Measurement of Helium Consumption during Regeneration (Blow-Down)*

During regeneration, the contaminant-laden helium inside the purifier is vented to the atmosphere. The total mass of helium lost during this process may not be insignificant. Moreover, additional helium is used (and vented) for clean-up of the purification system following the regeneration process. The helium usage during each regeneration of the purifier system can be theoretically estimated (based on the known internal volume of the purifier) and measured (during blow-down, using a flow meter). Each of these processes are discussed below.

The overall volume of the helium space is calculated based on the known dimensions of the purifier. These calculations are presented in the tables below.

Table 3-4 Calculation of gas volume in adsorber vessel

Parameter	**Value**
Shell OD [in.]	14.00
Shell thickness [in.]	0.18
Shell ID [in.]	13.64
Shell length [in.]	84.0
Empty volume [in.]	12274.3
Adsorbent volume [in^3]	6802.8
Gas (Helium) volume [in^3]	1841.1
Gas (Helium) volume [m^3]	0.030

Table 3-5 Calculation of gas (helium) volume in heat exchangers

	HX-1 (1)	HX-1 (2)	HX-2	HX-3
Tube OD [in.]	0.84	0.50	0.50	0.50
Tube thickness [in.]	0.065	0.049	0.065	0.065
Tube ID [in.]	0.71	0.402	0.37	0.37
Tube length / pass [ft.]	2000	2000	2500	2500
No. of passes	6	6	8	12
Total Tube-side volume [in^3]	4751.0	1523.1	2150.4	3225.6
Total Tube-side volume [m^3]	0.078	0.025	0.035	0.053

The total gas volume is calculated to be 13491.0 in^3 or 0.221 m^3. As mentioned earlier, the nominal operating pressure of the purifier is 13.0 bar and the system is blown down (vented) to approx. 1.0 bar. The mass lost in this process is estimated to be approx. 0.93 kg.

The helium used to flush the contaminants out of the purifier following the regeneration process is calculated using above calculated volume as well. Typically, four cycles of pump-down (to vacuum) and backfill (to approx. 0.5 bar) processes are carried out. The total helium used in this process is approx. 0.071 kg. The total amount of helium used per regeneration process is estimated to be approx. 1.0 kg.

The objective of this testing is to directly measure the helium usage during the regeneration process. A sonic nozzle was used to measure the amount of the helium vented during the regeneration (blow-down) process. The upstream pressure and temperature to the sonic nozzle was measured using a GE Unik 5000 series pressure transducer and a Lakeshore Platinum series resistance temperature detector (RTD). The mass flow rate through the sonic nozzle was calculated using the measured upstream pressure and temperature. The transient mass flow rate was calculated over the entire blow-down period to calculate the total mass vented. This information also provided the overall gas volume inside the purifier system. Sizing calculations for the sonic nozzle are provided in Appendix C. The result of the measurement was that the blow-down of the purifier during regeneration used 0.76 kg. This is an expected under measurement (compared to 0.93 kg estimated), because the test was stopped at 2.1 bar (instead of 1.0 bar like the estimation). This was to leave a positive pressure differential to the ambient air on the other side of the sonic nozzle.

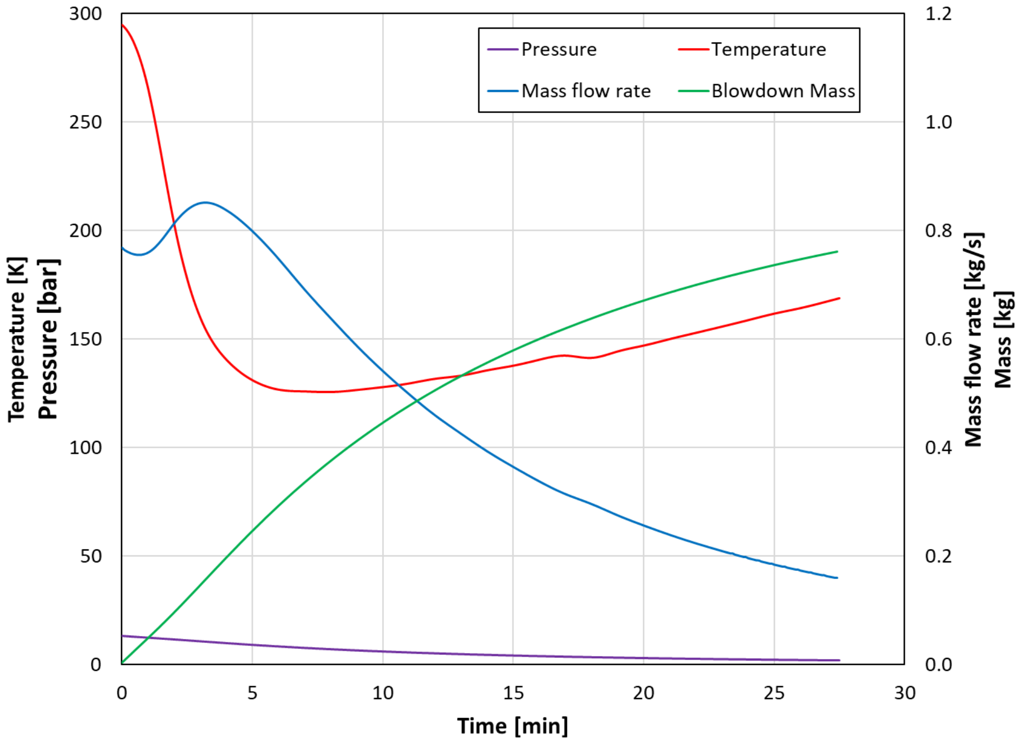

Figure 3-15 Measurement (mass flow, pressure, temperature, blowdown mass) vs. time (for blowdown)

3.4.2 *Measurement of the Nitrogen Usage during Regeneration*

Warm-up of the purifier following operation (and prior to regeneration) is carried out by circulating (open loop) gaseous nitrogen heated by an electrical heater. The gaseous nitrogen is supplied through the GN2 supply at MV1235 and leaves through the nitrogen vent (as seen in Figure 3-1), while the remaining helium in the purifier is stagnant. A classical venturi tube was used to measure the flow rate of the gaseous nitrogen (and corresponding warm-up rate of the purifier). Cumulative mass of the total nitrogen used was calculated by integrating the transient mass flow rate over the warm-up period. The instrumentation used for this measurement are the same as that described in Sec. 3.2. The total nitrogen mass used was 671.6 kg, averaging 8.69 g/s over 21.5 hours.

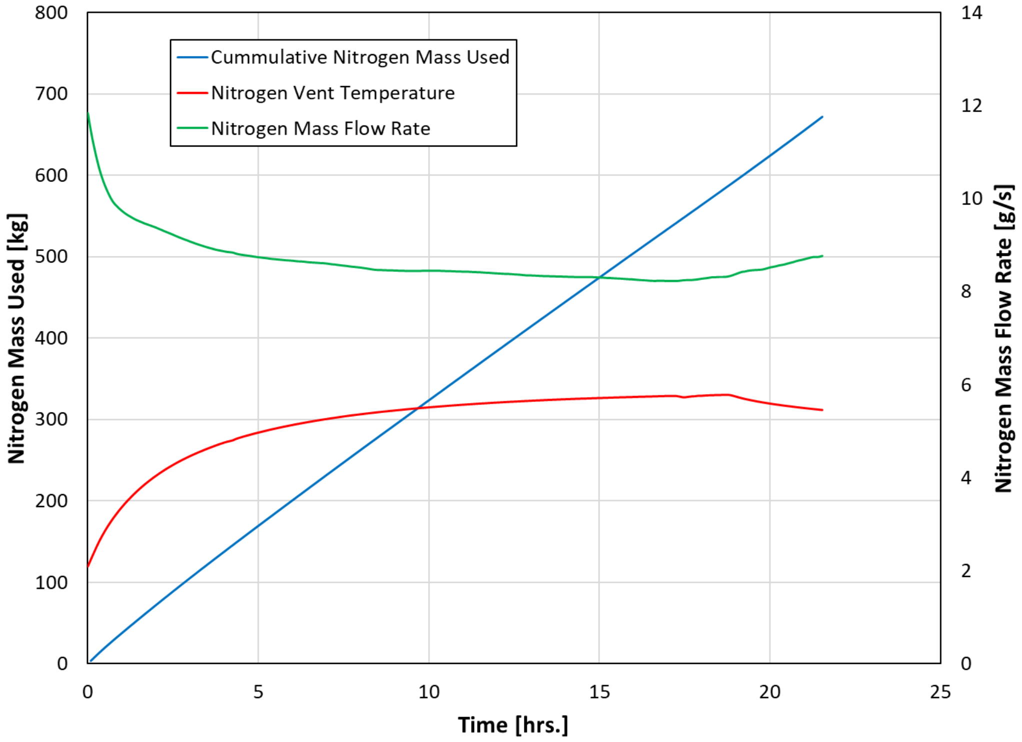

Figure 3-16 Measurement (mass flow, vented mass) vs time (for warm-up)

REFERENCES

[1] I.O.f. Standardization, Humidity - Part 1: Terms, definitions and formulae, in, 2002, pp. 28.

Chapter 4 : Modeling Frost Formation on an Iso-Thermal Surface

A transient zero-dimensional computational model was developed to simulate the formation of frost on an iso-thermal flat plate. The model calculates the heat and mass transfer of the system and estimates the properties of the frost. This model is validated using experimental data and numerical results from literature of high relative humidity air under atmospheric conditions. The model is used to study the effects of high pressure, carrier gas, absolute humidity, wall temperature difference, and reduced temperature differential on frost formation.

4.1 Problem Description

The developed model considers external flow of a specific humid carrier gas stream over a flat plate (ℓ = 0.1 m) maintained at a specific temperature (T_w). The inlet stream is a defined temperature (T_{amb}), and at a specific operating pressure (p), with a given value of absolute humidity (ω_i). The flow over the isothermal flat plate is characterized by the flow Reynolds number ($Re = \frac{\rho_i u_i\, l}{\mu}$). A schematic diagram of the model geometry is shown in Figure 4-1. The model inputs include carrier gas, inlet gas temperature, pressure, humidity, Reynolds number (flow velocity), and wall temperature.

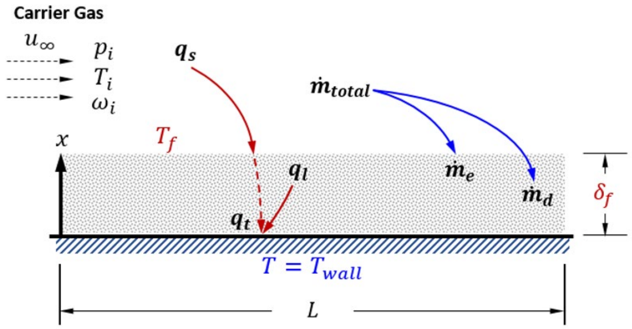

Figure 4-1 Schematic diagram of the model geometry and boundary conditions

4.2 Model Development

4.2.1 *Governing Equations*

Several assumptions are considered for the developed model. The frost growth is considered in the normal (to the flat plate) direction and is uniform (along the length of the plate). It considers that the gas stream has a constant mass flow rate, pressure, and absolute humidity. Frost density and thermal conductivity are assumed to be uniform across the thickness of the frost layer.

Mass and energy balances form the basis of the numerical model. For the problem geometry shown in Figure 4-1, these fundamental equations are –

$$\dot{m}_t = \frac{d}{dt}\left(x_f \rho_f\right) = \rho_f \frac{dx_f}{dt} + x_f \frac{d\rho_f}{dt} = \rho_i h_m (\omega_i - \omega_s) \qquad 4.1$$

$$q_t = h_c\left(T_i - T_f\right) + \rho_f \frac{\partial x_f}{\partial t} L_{sv} + \delta_f \frac{\partial \rho_f}{\partial t} L_{sv} \qquad 4.2$$

The mass balance (eqn 4.1) considers effusion ($\dot{m}_e = \rho_f \frac{dx_f}{dt}$) and diffusion ($\dot{m}_d = x_f \frac{d\rho_f}{dt}$) of gas into the frost layer. A frost density correlation [1], based on gas temperature and frost surface temperature is considered in this model. The energy balance (eqn 4.2) includes three terms, representing sensible heat from convection, latent heat going toward deposition, and latent heat going toward densification, respectively. The energy balance considering conduction through the frost layer is provided by the following –

$$q_{cond} = -k_f \frac{dT_f}{dx_f} = -h_c\left(T_i - T_f\right) - \rho_f L_{sv} \frac{dx_f}{dt} \qquad 4.3$$

The energy balance for an elemental frost thickness in the interior of the frost layer (considering latent heat transport from the moisture) can be expressed as –

$$k_f \frac{d^2 T_f}{dx_f^2} = -L_{sv} \frac{\dot{m}_d}{x_f} \qquad 4.4$$

The above equation can be integrated with appropriate boundary conditions (and using eqn. 4.3) to find the temperature distribution along the frost layer –

$$T_f = T_w + \left(\frac{x_f}{k_f}\right) h_c\left(T_i - T_f\right) + \frac{1}{2}\left(\frac{x_f L_{sv}}{k_f}\right)\left[\rho_i h_m(\omega_i - \omega_s) + \rho_f \frac{dx_f}{dt}\right] \tag{4.5}$$

The applicable thermal boundary and initial conditions for the frost layer are as follows –

$$T_f(t = 0) = T_w \tag{4.6a}$$

$$T_f(x = 0) = T_w \tag{4.6b}$$

$$T_f\left(x = x_f\right) = T_f \tag{4.6c}$$

The mass balance (eqn. 4.1), along with the correlation for density [1] and the frost surface temperature, are used to derive the equation for the frost layer growth –

$$\frac{dx_s}{dt} = \frac{h_m \rho_a (\omega_a - \omega_s) - \rho_f \frac{dx_s}{dt}}{x_s \frac{0.533\rho_{ice}}{T_m * 6}\left(2 + \frac{T_{fs}}{T_m}\right)^{\frac{-5}{6}}\left(2 + \frac{T_a}{T_m}\right)^{\frac{1}{3}}\left[\frac{h_c}{k_f}\left(T_a - T_{fs}\right) + \frac{\rho_f L_{sv}}{k_f}\frac{dx_s}{dt}\right]} \tag{4.7}$$

Several correlations exist for estimating the frost properties (density and thermal conductivity). Frost thermal conductivity is commonly correlated as a function of only the frost density. Kandula [2] developed a semi-empirical model taking into consideration the effect of carrier gas (k_a), mass diffusion (k_d), and eddy convection (k_c) within the porous layer. This correlation has been used in the present model –

$$\frac{k_f}{k_{adc}} = 1 - \sqrt{1 - \psi} + \frac{2\sqrt{1 - \psi}}{1 - \zeta B}\left[\frac{(1 - \zeta)B}{(1 - \zeta B)^2}\ln\left(\frac{1}{\zeta B}\right) - \frac{B + 1}{2} - \frac{B - 1}{1 - \zeta B}\right] \tag{4.8}$$

$$k_{adc} = k_a + k_d + k_c \tag{4.9}$$

Here, ψ is frost porosity, ζ is the ratio of gas thermal conductivity to ice thermal conductivity, and B is the shape factor related to porosity. The mass diffusivity of the frost within the carrier gas is calculated using the correlation developed by Fuller et al. [3] –

$$D = \frac{T_f^{1.75}\left(\frac{1}{M_{CG}} - \frac{1}{M_f}\right)^{\frac{1}{2}}}{p_i\left(V_{CG}^{\frac{1}{3}} + V_f^{\frac{1}{3}}\right)^2} \qquad 4.10$$

Here V_{CG} and V_f are constants defined for the carrier gas (air, helium, hydrogen, *etc.*) and water vapor. The latent heat of formation of frost (L_{sv}) was obtained from a correlation based on the frost temperature in Fahrenheit [4] –

$$L_{sv} = \{-0.1083\,T_f + 2833\}\frac{kJ}{kg} \qquad 4.11$$

The thermal conductivity of ice is calculated based on the frost temperature from Dietenberger [5]. The solid-vapor saturation pressure was calculated using a correlation developed by Wexler [6]. For a given Reynolds number over the flat plate of finite length, the convective heat transfer coefficient was obtained from the correlation for Nusselt number for laminar flow over a flat plate. The convective mass transfer coefficient was obtained based on the Chilton-Colburn analogy between heat and mass transfer, which is found to be applicable under frosting conditions [7]. A Lewis number of unity (Le = 1.0) is assumed [8] for verification of the model with air as the carrier gas. The saturation concentration of moisture in the carrier gas at the frost surface, including the effect of compressibility, is calculated by –

$$\omega_s(T) = \frac{M_f}{M_{CG}}\frac{Z_f}{Z_f}\frac{p_{vs}(T)}{p_t - p_{vs}(T)} \qquad 4.12$$

Here p_{vs} is the saturation vapor pressure based on the correlation from Mago and Sherif [4]. Details regarding the overall model are discussed by Kandula [9]. Several non-dimensional parameters are considered to characterize the results obtained from the model. These are the non-dimensional frost surface temperature (θ) and the frost porosity (ψ). They are defined as follows -

$$\theta = \frac{T_f - T_w}{T_m - T_w} \qquad 4.13$$

$$\psi = \frac{1 - \rho_f/\rho_{ice}}{\frac{\rho_{cg}}{\rho_{ice}}} \qquad 4.14$$

4.2.2 *Numerical Methods*

The frost layer growth and frost surface temperature are obtained by numerically integrating eqn. 4.7 in conjunction with eqn. 4.5. A flowchart describing the overall solution procedure is shown in Figure 4-2. To start the calculation, initial guesses for the frost layer height ($x_f = 10^{-5}\ m$) and the frost surface temperature ($T_f = T_w$) are considered at the initial time (t = 0.0 sec). The equation describing the frost surface temperature (eqn. 4.5) is implicit in nature. An iterative solution scheme using the Bi-section method is used to solve for this temperature and the frost growth rate (eqn. 4.7) simultaneously. Once a solution is achieved, the solved frost surface temperature is used to calculate the frost properties and the growth rate. The frost growth rate is integrated over time to calculate the frost layer height at the next time step ($t + \Delta t$). For a given ambient condition (carrier gas, absolute humidity, etc.) and wall temperature, the non-dimensional frost surface temperature has a limiting value (θ_{max}). Above this value the frost surface temperature will be greater than the corresponding solid-vapor saturation temperature of moisture in the gas stream, and the frost accretion will stop. Mathematically, the limiting value of the non-dimensional frost surface temperature is given by –

$$\theta_{max} = \frac{T_s(\omega_i) - T_w}{T_m - T_w} \qquad 4.15$$

For the brevity of the computations, the time integrations were carried out until the non-dimensional frost surface temperature reaches 95% of this limiting value. Variable time steps are used for the calculations. A sensitivity analysis was performed on time step, property evaluation routines, and saturation vapor pressure over ice correlations. CoolProp [10] was used to calculate thermal fluid properties required for the model.

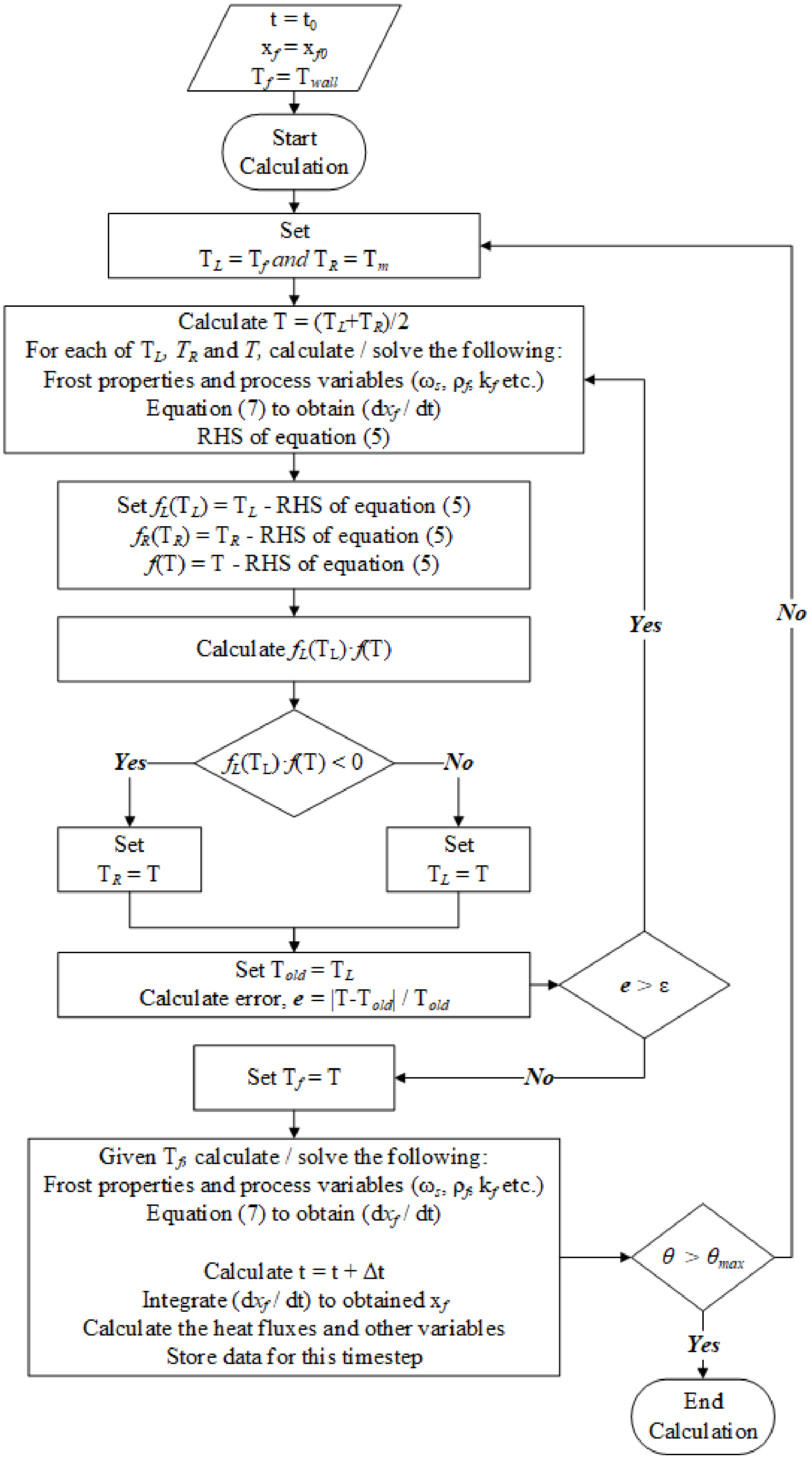

Figure 4-2 Flowchart of the numerical solution algorithm

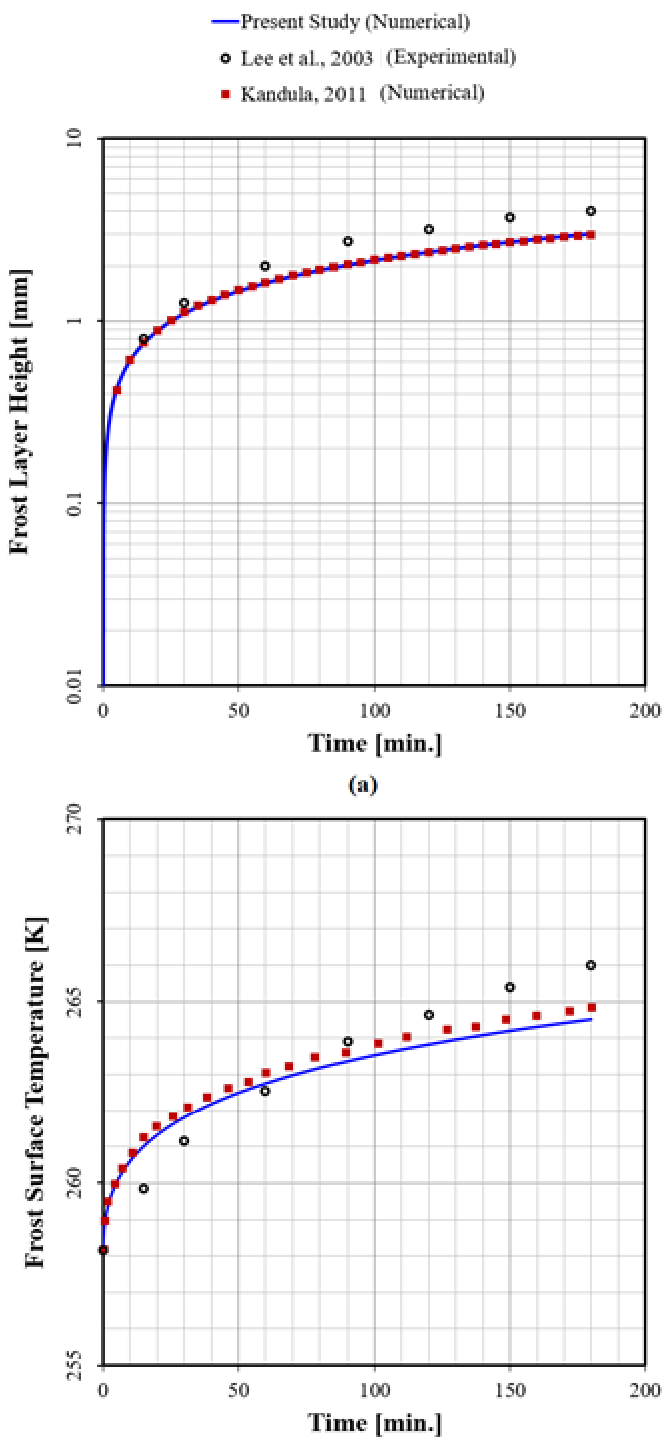

(a)

(b)

Figure 4-3 Comparison of calculated and measured [9, 11] (a) transient frost layer height and (b) frost surface temperature with humid air stream ($p_i = 1.0$ bar, $T_i = 288.2$ K, $T_w = 258.2$ K, $\omega_i = 0.00633$ kg/kg$_{air}$, and $u_i = 2.5$ m/s)

4.3 Model Validation

The developed computational model is validated using data available from the literature [9, 11]. Figure 4-3 shows the transient frost formation (layer height) and surface temperature on a flat plate of 0.3 m length. A comparison of the calculated values and those obtained numerically by Kandula [9] is presented in Figure 4-3. For the case compared, the carrier gas is air (at ambient pressure, and 288.2 K temperature) is flowing over the flat plate maintained at 258.2 K. The flow velocity is 2.5 m/s (Re = 5.6×10^4), and has an absolute humidity of 0.00633 kg/kg_{air}. A frost density correlation developed by Kandula [9] was used, as it is valid for these operating conditions, whereas Byun's correlation [1] is valid for the cryogenic conditions that are the interest of study. The calculations show very good match with the experimental data in the literature, validating the accuracy of the model. At present, experimental data for frost accretion at elevated pressures and cryogenic surface temperatures are not available. Hence, the model couldn't be validated using these conditions.

4.4 Results and Discussion

12 different cases are simulated in the present study with the model described in Sec. 4.3. These cases are listed in Table 4-1. The dynamics of the frost formation and densification has been investigated with changing operating pressure of the carrier gas stream (Cases 1-4), wall temperature difference as defined in equation 4.16 (Cases 1, 5, 6), reduced temperature differential ($\overline{\Delta T}$) defined as the ratio between wall temperature difference and ambient temperature difference as defined in equation 4.16 (Cases 1, 7, 8), absolute humidity (Cases 1, 9, 10), and the carrier gas itself (Cases 1, 11, 12).

$$\Delta T_{red} = \frac{\Delta T_{wall}}{\Delta T_{amb}} = \frac{T_{sat} - T_{wall}}{T_{amb} - T_{sat}} \qquad 4.16$$

Table 4-1 List of cases with corresponding simulation parameters

Case No.	**P [bar]**	**Carrier Gas**	ppm_v [ppm_v]	ΔT_{wall} [K]	ΔT_{red} [-]
1	12	*Helium*	50	1.0	1.0
2	15	*Helium*	50	1.0	1.0
3	9	*Helium*	50	1.0	1.0
4	6	*Helium*	50	1.0	1.0
5	12	*Helium*	50	0.5	1.0
6	12	*Helium*	50	2.0	1.0
7	12	*Helium*	50	1.0	0.5
8	12	*Helium*	50	1.0	2.0
9	12	*Helium*	10	1.0	1.0
10	12	*Helium*	100	1.0	1.0
11	12	*Nitrogen*	50	1.0	1.0
12	12	*Hydrogen*	50	1.0	1.0

For this study, the reduced temperature differential is used as this ratio of temperature differences. Saturation temperature is a dependent variable calculated from the absolute humidity and effected by the carrier gas and its pressure. The wall temperature and ambient gas temperature are calculated from calculated based on the reduced temperature differential and the wall temperature difference, using equation 4.16. The wall temperature difference can be framed as the sensible temperature difference, and therefore the driver of mass transfer. The ambient temperature difference can be framed as the sensible temperature difference, which has a large impact on heat transfer and how the cooling provided by the wall is used. Three different carrier gas streams are considered. These are helium, nitrogen, and hydrogen. The inlet gas stream temperature is equal to the ambient temperature.

Figure 4-4 represents the transient frost deposition (layer height) and the frost surface temperature for Case 1. The asymptotic behavior of the frost layer height and the non-dimensional frost surface temperature can be observed in these plots. The temperature asymptotically approaches θ_{max}, beyond which direct freeze-out from the gas stream into frost (ice) is not feasible. For this reason, the calculation is carried out until the non-dimensional frost surface temperature reaches 95% of θ_{max}. For this case, the time required to approach this limiting value is in excess of 14,000 hours, and approx. 5.6 mm of frost has been deposited on the flat plate.

To freeze-out low levels of moisture from the carrier gas, a significant amount of energy is spent on cooling the gas just from the ambient temperature to its corresponding solid-vapor saturation temperature. The latent heat flux is considerably lower due the minute amount of moisture being frozen. The effect of different parameters on the frost accretion and densification dynamics is discussed in Sec. 4.4.1-4.4.5. The total frost deposited on the (cold) wall is calculated by integrating eqn. 1 over the total simulated time and is given by –

$$m'' = \int_0^{t_f} \dot{m}_t dt \qquad 4.17$$

Table 4-2 describes how each impacted variable (left column) is affected by an increase in the studied variable (top row). ↑ is increase, ↑→ is slight increase, ↑↑ is large increase, and → is no change (opposite for decreases). It shows the effects of increasing each variable on saturation temperature, stopping condition, absolute humidity difference, heat transfer coefficient, mass transfer coefficient, total simulation time, maximum frost thickness, maximum mass deposited, and frost density.

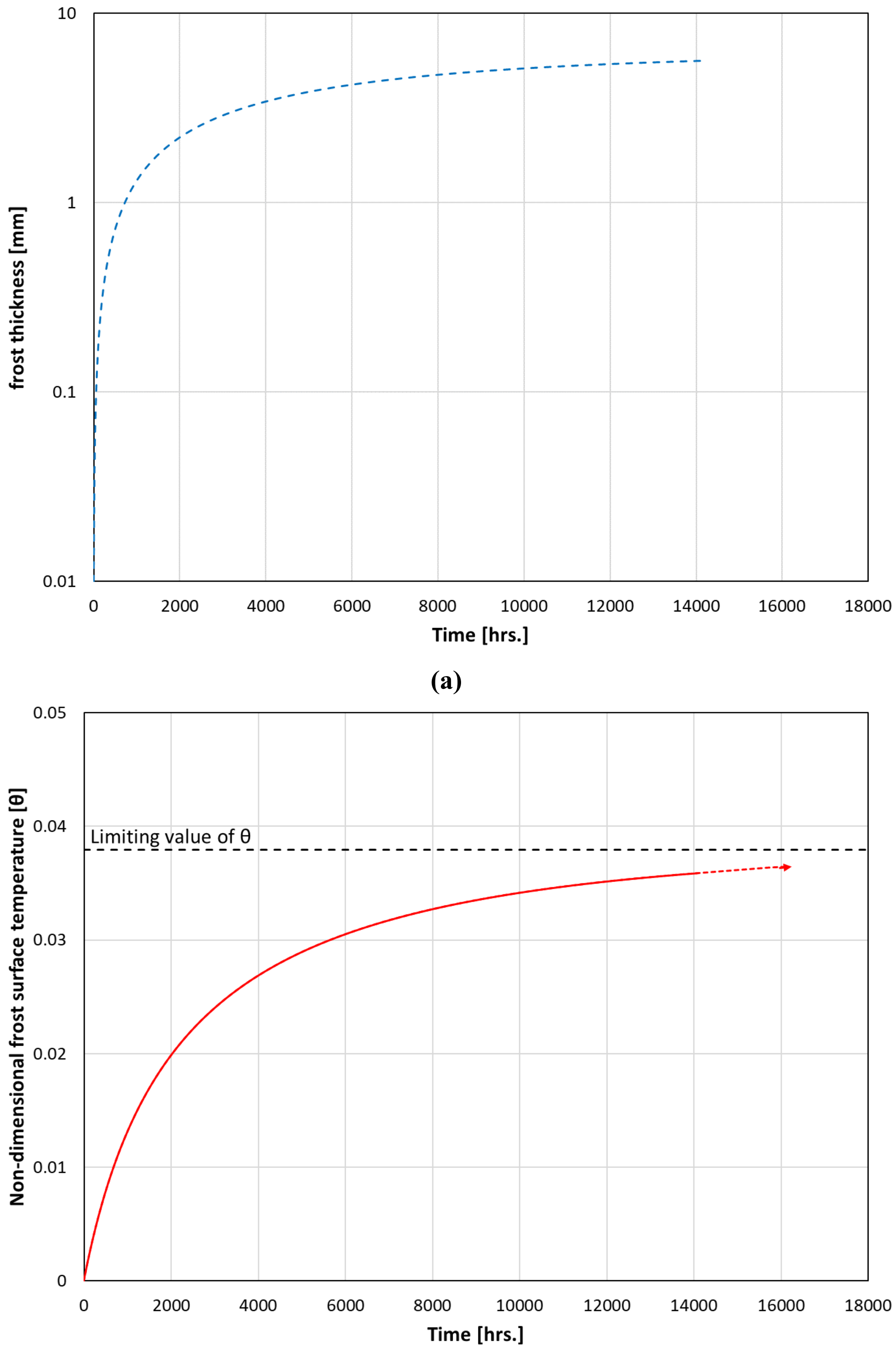

(a)

(b)

Figure 4-4 Transient variation of (a) frost layer height and (b) non-dimensional frost surface temperature for case 1

Table 4-2 Effects of studied variables on selected parameters

Studied Variable	Pressure ↑	ΔT_{wall} ↑	ΔT_{red} ↑	Humidity ↑	Carrier Gas Molecular Weight ↑
T_{sat}	↑	→	→	↑	→↓
θ_{max}	↑	↑	→	↑	→
$\Delta\omega$	↓	↑	→	↑	↓
h_c	→	→	→	→	↓
h_m	↓	→	→	↑→	↓
time	↑	↓↓	↑↑	↓↓	↑
x_f	→	→	↑	→	↑
m_f	↑→	↑→	↑	↑→	↑
ρ_f	↑→	→	→	↑→	→

4.4.1 *Effect of Operating Pressure*

A change in gas pressure affects several factors, including the saturation vapor pressure and most fluid properties. This in turn impacts Reynolds number (Re), and therefore heat and mass transfer coefficients. The diffusion coefficient decreases with increased pressure, which would decrease mass transfer rate. Figure 4-6 shows that the saturation temperature (and therefore wall temperature; it is calculated via the reduced temperature differential, which is held constant) is much higher at elevated pressures due to increased partial pressure. The partial pressure increases because inlet absolutely humidity is held constant (see Figure 4-6), not relative humidity. For a given difference between saturation temperature and wall temperature, this decreases the sensible temperature gradient, slowing down heat transfer, the driver of the entire freeze-out process. This slower rate of frost accretion can be seen in Figure 4-5, however there is slightly more total frost at the end. This is caused by the ending condition. Because the wall temperature is higher at higher pressures, the θ_{max} value is higher. Therefore, the calculation will reach its ending condition much later, allowing more time for mass transfer. This extra time overwhelms the effect of the reduced mass transfer rate. With all these effects combined, the overall frost layer height and frost accumulation are observed to increase as operating pressure of the carrier gas is increased. A higher gas pressure slightly increases frost thickness, has little effect on the rate of frost deposition, increases the frost surface temperature, and has little effect on the absolute humidity difference.

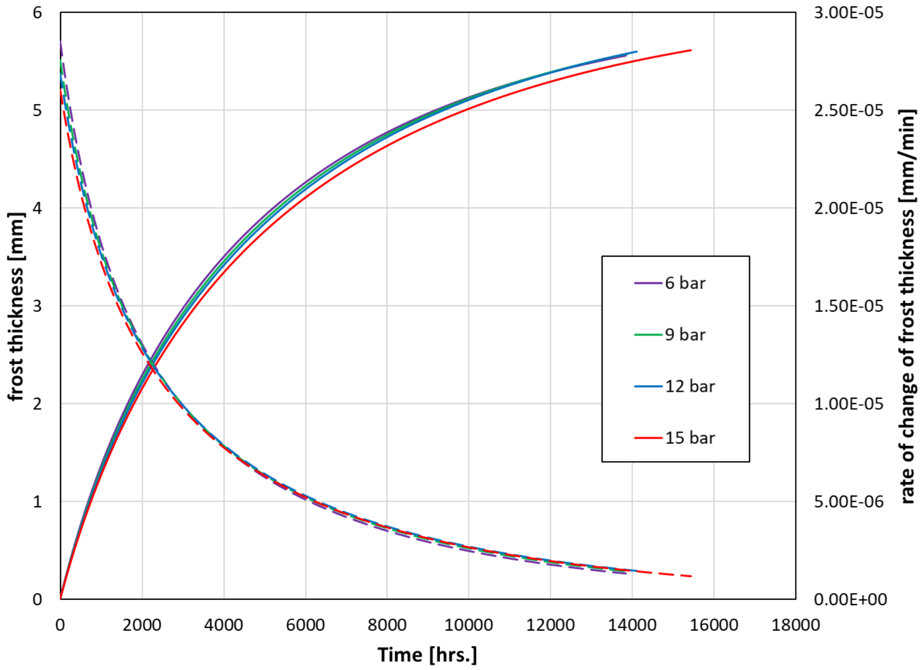

Figure 4-5 Transient variation of frost thickness (solid lines) and rate of change of frost thickness (rate of frost deposition) (dashed lines) with variation in operating pressure

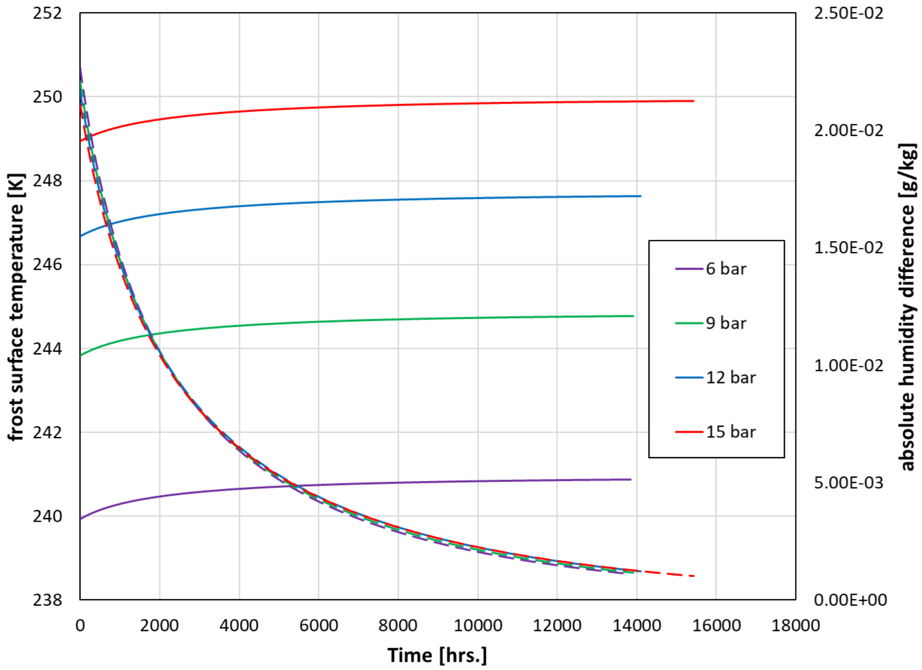

Figure 4-6 Transient variation of frost surface temperature (solid lines) and absolute humidity difference (dashed lines) with variation in operating pressure

4.4.2 *Effect of Wall Temperature Difference*

The temperature difference between the wall and the saturation condition (ΔT_{wall}) is the main driving force of heat transfer. This increases the absolute humidity difference, the main driving force of mass transfer (see Figure 4-8). This produces the increased rate of change of frost thickness with increasing temperature difference seen in Figure 4-7. However, as seen in Figure 4-8, the maximum permissible frost surface temperature remains the same because the saturation condition is not affected. This results in the magnitude of the temperature difference affecting the rate of frost deposition, but not the total amount deposited. Therefore, the larger wall temperature difference takes less time to reach its asymptote. A wall temperature difference has no effect on frost thickness, increases the rate of frost deposition, has no effect on the final frost surface temperature, and increases the absolute humidity difference.

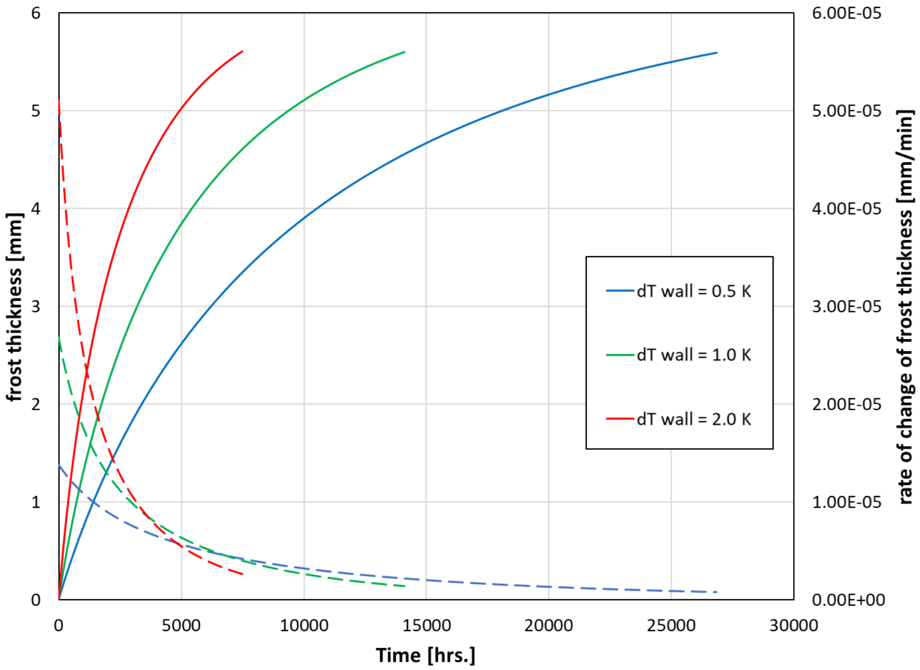

Figure 4-7 Variation of frost thickness (solid lines) and rate of change of frost thickness (dashed lines) with variation in wall temperature difference

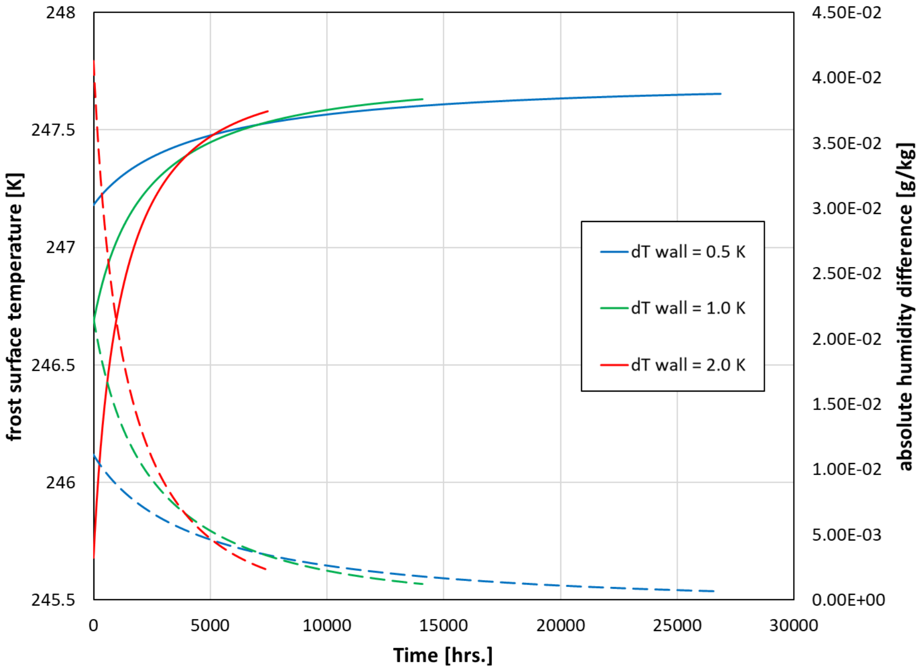

Figure 4-8 Variation of frost surface temperature (solid lines) and absolute humidity difference (dashed lines) with variation in wall temperature difference

4.4.3 *Effect of Reduced Temperature Differential*

The reduced temperature differential, defined as the ratio of the wall temperature difference to the ambient temperature difference, is effectively the ratio between the boundaries of latent and sensible heat. Thus, it has a large impact on how the available cooling is used. Because the initial conditions are the same for each case, the saturation temperature and ending frost temperature are the same (Figure 4-10). However, because when the reduced temperature differential is larger, less cooling must be used on sensible heat, more may be used on latent heat. As Figure 4-9 shows, this increases the maximum thickness of the frost layer greatly. The ratio of wall temperature difference to ambient temperature difference, or reduced temperature differential, affects the total frost deposition, but not the rate. A higher reduced temperature differential increases frost thickness, has little effect on the rate of frost deposition, has no effect on the final frost surface temperature, and has no effect on the initial absolute humidity difference.

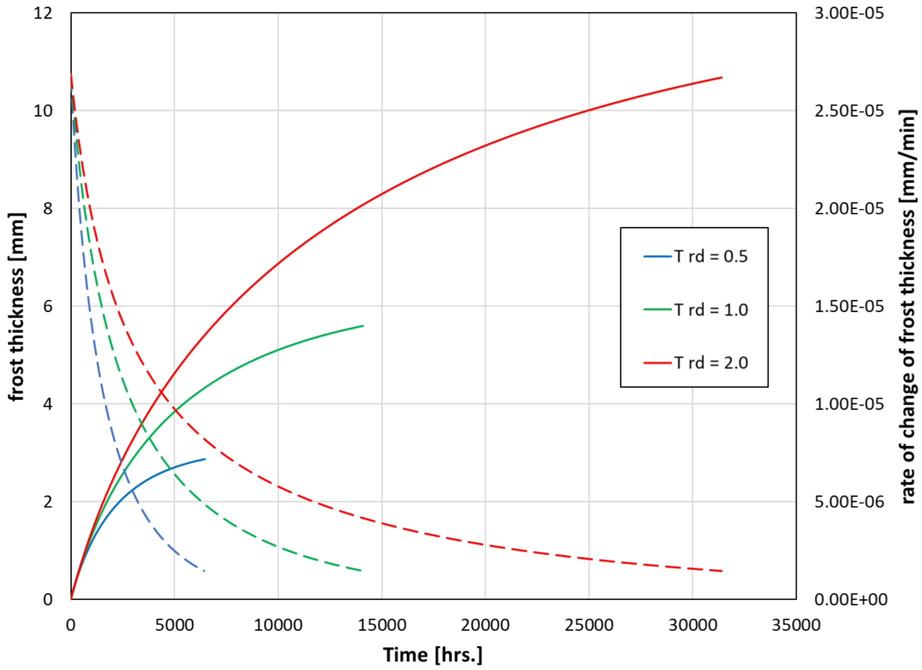

Figure 4-9 Variation in frost thickness (solid lines) and rate of change of frost thickness (dashed lines) with variation in reduced temperature differential

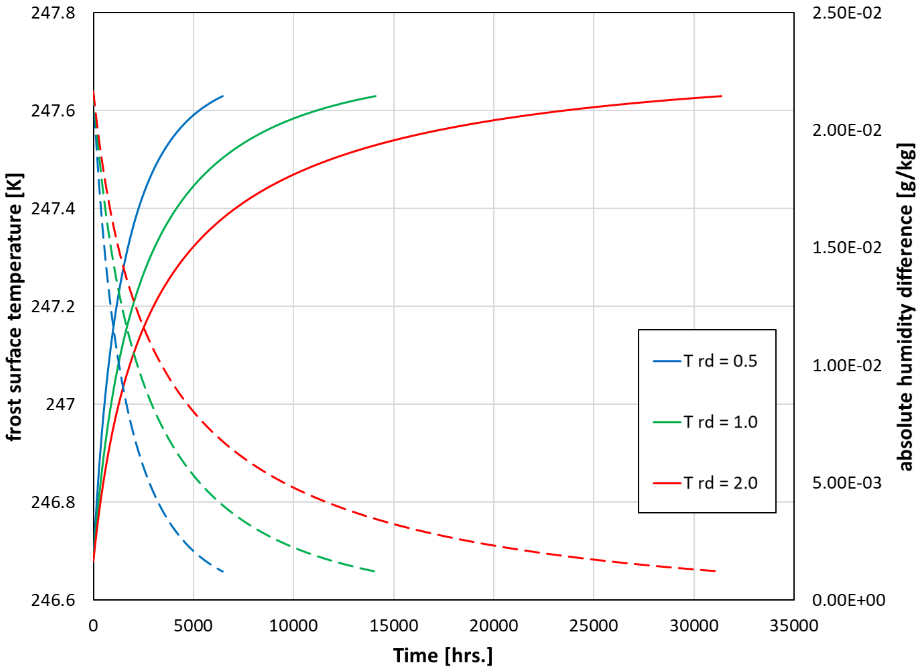

Figure 4-10 Variation in frost surface temperature (solid lines) and absolute humidity difference (dashed lines) with variation in reduced temperature differential

4.4.4 *Effect of Absolute Humidity*

Absolute humidity hugely changes the temperature ranges the system works in, through defining the saturation temperature. Between 10 and 100 ppm, the saturation temperature ranges from 232 K to 255 K. Higher saturation temperature results (Figure 4-12) in higher absolute humidity difference, the driving force of mass transfer rate. The mass transfer coefficient also moderately increases due to the saturation condition. This results in a significantly increased rate of change of frost thickness, seen in Figure 4-11. Like the wall temperature difference, because the reduced temperature differential is the same, maximum frost thickness has very little change between cases. There is a small variation in maximum frost thickness, with it increasing with absolute humidity. Because the frost thickness changes little between cases, and the frost deposition rate increases greatly with increased humidity, it takes much less time to reach the end condition when humidity is increased. Humidity was the only factor that had any impact on the frost density, with higher humidity increasing it slightly. A higher absolute humidity slightly increases frost thickness, increases the rate of frost deposition, increases the frost surface temperature, and increases the absolute humidity difference.

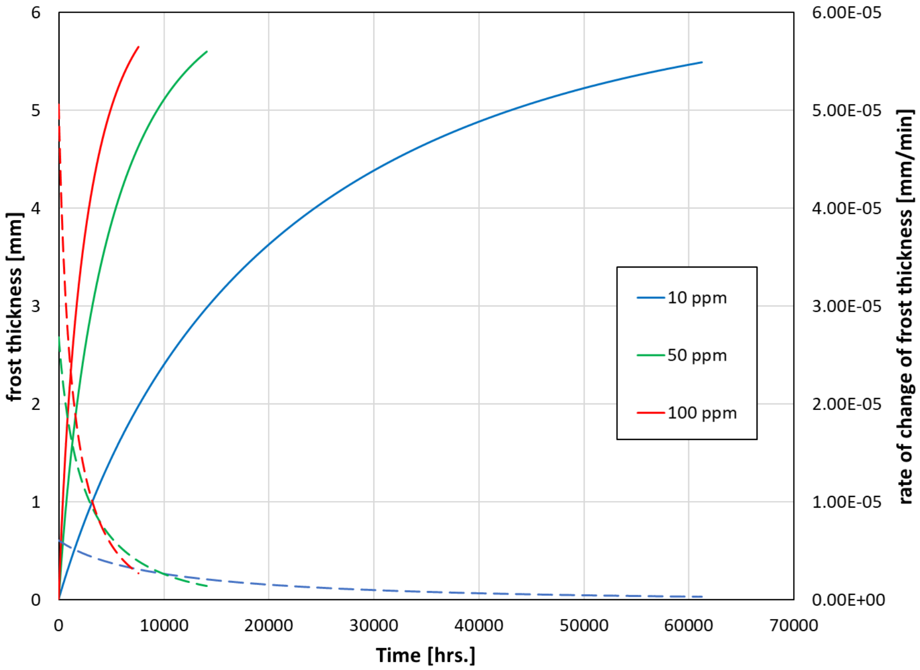

5

Figure 4-11 Variation in frost thickness (solid lines) and rate of change of frost thickness (dashed lines) with variation in absolute humidity

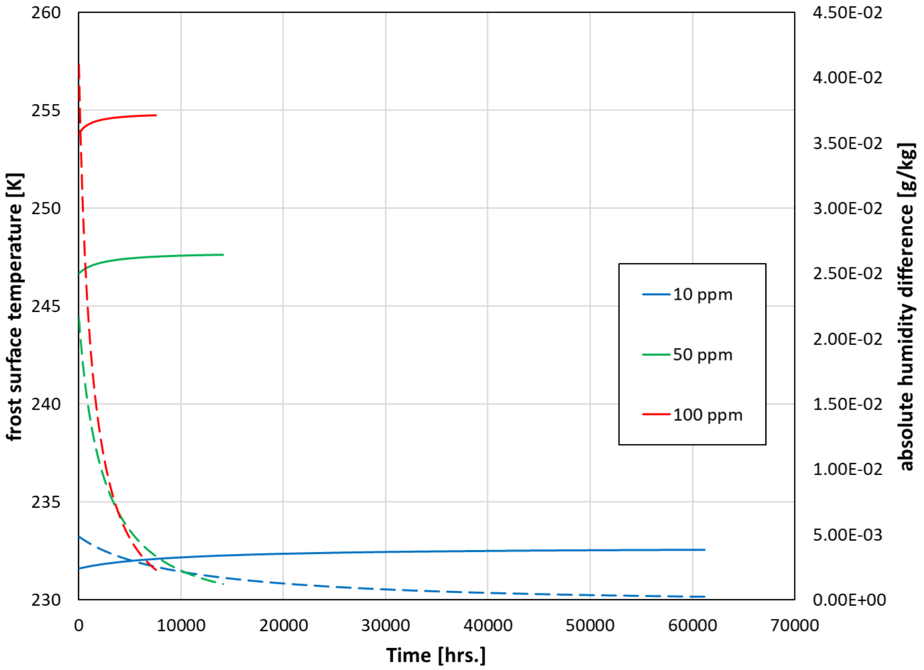

Figure 4-12 Variation in frost surface temperature (solid lines) and absolute humidity difference (dashed lines) with variation in absolute humidity

4.4.5 *Effect of Carrier Gas*

The carrier gas thermo-physical properties affect Reynolds number, which in turn affects heat transfer coefficient and mass transfer coefficient. The mass diffusivity of moisture in the carrier gas stream has a significant impact on the mass transfer, as well as the heat transfer. The absolute humidity (ωi) is held constant for each of the cases. However, the solid-vapor saturation humidity ratio (ωs) is variable as it is dependent on the molecular weight of the carrier gas (eqn. 4.12). Due to this change, the saturation temperature that lines up with those humidities is roughly equal. As seen in Figure 4-14, the frost surface temperature ending points are not significantly different. The larger effect comes in the heat and mass transfer coefficients. They are both significantly lower for higher molecular weight gases. This reduces the rate of frost deposition and absolute humidity difference. It takes far longer to reach equilibrium, due to the lessened heat transfer coefficient increasing the maximum frost thickness. A higher carrier gas molecular weight increases frost thickness, decreases the rate of frost deposition, decreases the final frost surface temperature, and decreases the absolute humidity difference.

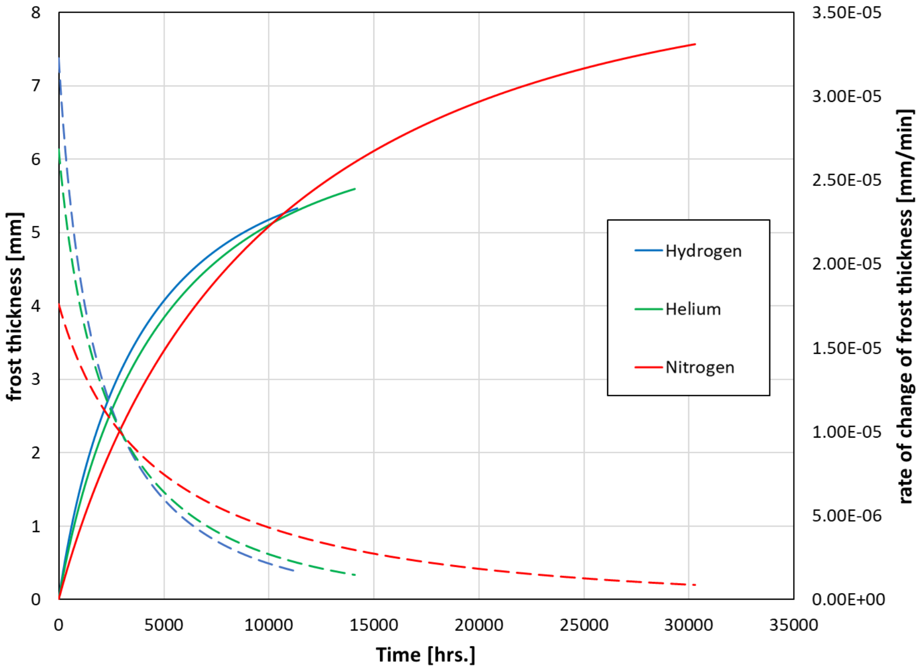

Figure 4-13 Variation in frost thickness (solid lines) and rate of change of frost thickness (dashed lines) with variation in carrier gas

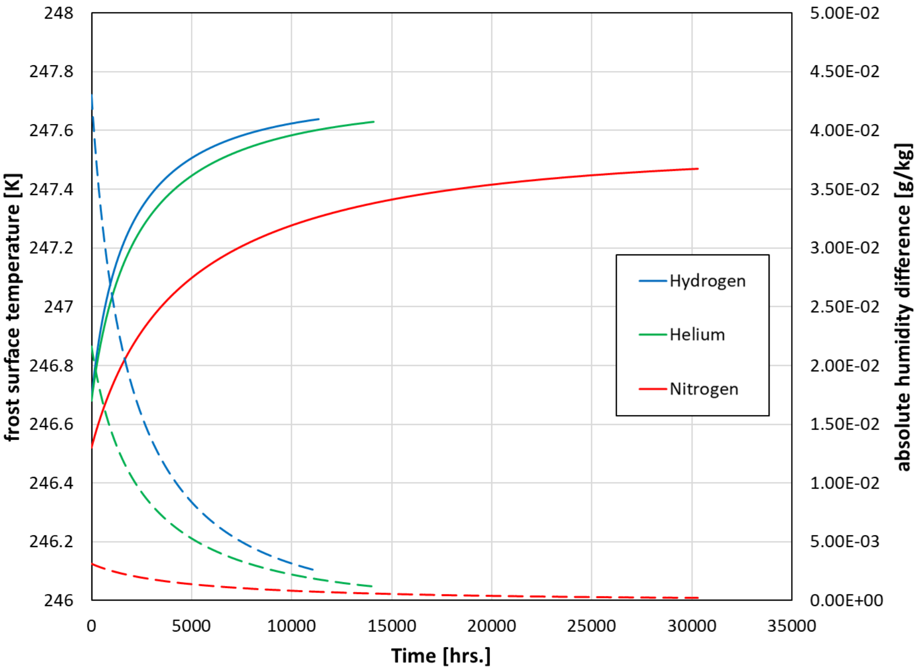

Figure 4-14 Variation in frost surface temperature (solid lines) and absolute humidity difference (dashed lines) with variation in carrier gas

4.4.6 *Effect of Estimation of Frost Accretion*

At the stopping condition of the model, there is very little frost deposition, so conductive heat transfer through the frost layer will be nearly equal to convective heat transfer through the carrier gas at the end of the simulation, as shown in equation 4.18.

$$h_c(T_a - T_{fs}) = k_f \frac{dT_{fs}}{dx} \qquad 4.18$$

$$x_f = \frac{k_f}{h_c} \frac{(T_{fs} - T_{wall})}{(T_{amb} - T_{fs})} \qquad 4.19$$

This can be used to estimate the frost thickness without simulating at all. Figure 4-15 shows this the results of this estimation for the cases studied in this sections 4.4.1-4.4.5. In equation 4-19, the ratio of temperatures is close to the definition of reduced temperature differential (see equation 4-16). The difference is that T_{fs} (at the end of the simulation) replaces T_{sat}. These values are very close to each other, but the simulation stops when it reaches the value of T_{fs} in equation 4.19, which is defined as 95% of the way between T_{wall} and T_{sat}. This slight change helps to estimate the frost thickness that the simulation will predict. If the simulation was ran for unlimited time, or one wanted the real maximum value of frost thickness, T_{sat} would be used instead.

The estimation of final frost thickness fits the simulation data within 0.5% error for all cases, as seen in Figure 4-15. This is useful for showing that the simulation matches with assumed condition at equilibrium. However, this estimation has some limitations. It only predicts the maximum frost thickness for an external flow system. It cannot predict transient results or the amount of time it takes to reach the maximum thickness. Also, a real system (heat exchanger) will never reach the maximum frost thickness, as the frost surface temperature will never reach the saturation temperature. Fukada et al. [12] developed another simplified correlation, which was observed to be valid for only one carrier gas. This correlation can be used when density is changing significantly, but this is not the case for these studies.

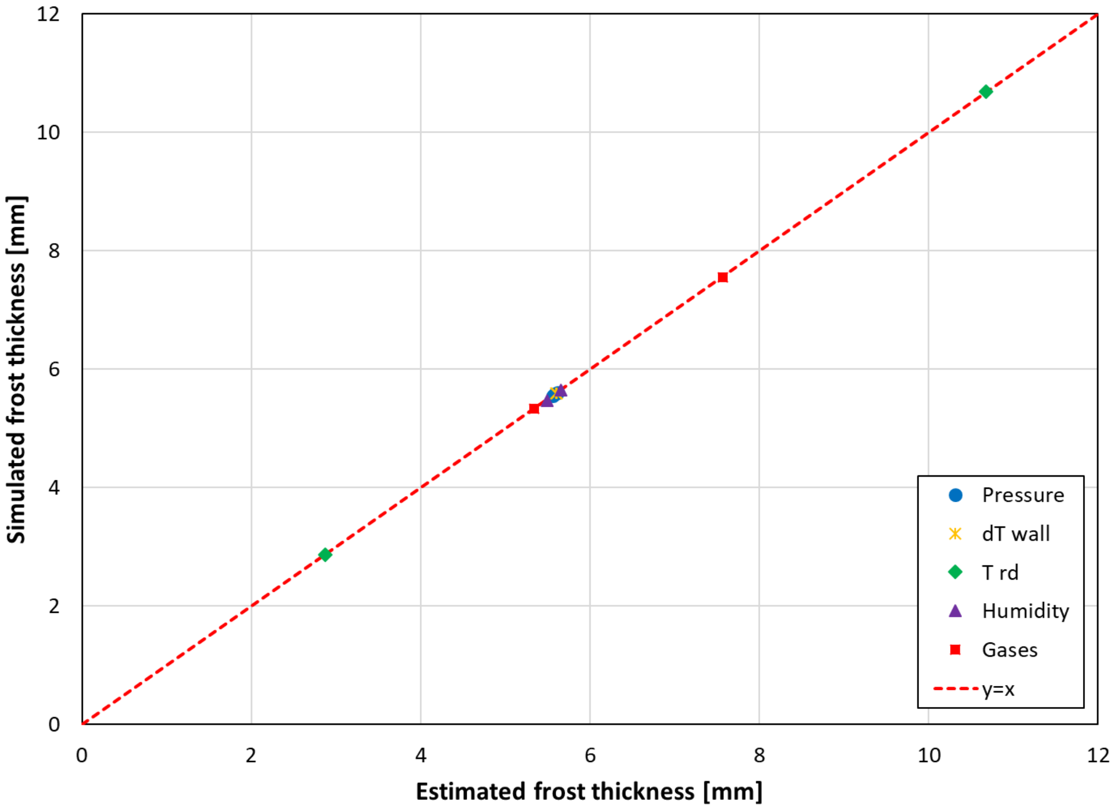

Figure 4-15 Estimated frost thickness vs numerically calculated frost thickness

4.5 Summary

A transient volume averaged computational model is developed to predict the formation and densification of frost over a flat plat with different carrier gases at elevated pressures. A parametric study is carried out with the developed model to predict the effects of pressure, wall temperature difference, reduced temperature differential, absolute humidity, and different carrier gases on the frost formation dynamics. Table 4-3 summarizes the effects of increasing each of these studied factors. An important takeaway from this study is that the temperature difference between the wall and the saturation condition has an impact on the frost deposition rate, but not the final frost thickness. The ratio of wall temperature difference to ambient temperature difference (reduce temperature differential) has the opposite effect, impacting final frost thickness, but not frost deposition rate. This has implications on how controlling the temperature difference within a purifier heat exchanger may affect its capacity and operation time.

A method of estimating the final frost thickness is discussed. Using the equality of conduction heat transfer through the frost layer and convection heat transfer through the gas at the stopping condition, the final frost thickness can be estimated. This estimation showed very close (<1% error) matching with the simulation results. If frost thickness is the only desired output, this estimation is useful and saves computation time relative to the simulation.

The simplified model is developed with the intent to gather a first approximation for the frost accretion characteristics. In chapter 5, this model will be converted to handle internal flow over a complex heat exchanger geometry in one-dimension.

Table 4-3 Summary of effects on increasing studied variables

Variable	Total frost collected	Frost thickness	Frost deposition rate	Frost surface temperature	Absolute humidity difference
Pressure	↑→	↑→	→	↑	→
Wall temperature difference	↑→	→	↑	→	↑
Reduced temperature differential	↑	↑	→	→	→
Absolute humidity	↑→	↑→	↑	↑	↑
Carrier gas molecular weight	↑	↑	↓	↓	↓

REFERENCES

[1] S. Byun, et al. Frost modeling under cryogenic conditions, Int. J. Heat Mass Transfer, 161 (2020) 120250

[2] M. Kandula, Frost growth and densification in laminar flow over flat surfaces, Int. J. Heat Mass Transfer, 54(15) (2011) 3719-3731

[3] E. Fuller, P. Schettler, C. Gidding, A new method for prediction of binary gas-phase diffusion coefficients. Vacuum, 16(10) (1966) 551

[4] Mago, Pedro, and S Sherif. “Frost Formation and Heat Transfer on a Cold Surface in Ice Fog.” 42nd AIAA Aerospace Sciences Meeting and Exhibit, (2004)

[5] M.A. Dietenberger, Generalized correlation of the water frost thermal conductivity, Int. J. Heat Mass Transfer 26 (4) (1983) 607–619

[6] A. Wexler, Vapor Pressure Formulation for Ice, Journal of Research of the National Bureau of Standards Section a-Physics and Chemistry, 81(1) (1977) 5-20

[7] D.L. O'Neal, D.R. Tree. “A Review of Frost Formation in Simple Geometries.” ASHRAE, (1985)

[8] K.-S. Lee, W.-S. Kim, T.-H. Lee, A one-dimensional model for frost formation on a cold flat surface, Int. J. Heat Mass Transfer, 40(18) (1997) 4359-4365

[9] M. Kandula, Frost growth and densification in laminar flow over flat surfaces, Int. J. Heat Mass Transfer, 54(15) (2011) 3719-3731

[10] I. H. Bell, J. Wronkski, S. Quoilin, V. Lemort, Pure and Pseudo-pure Fluid Thermophysical Property Evaluation and the Open-Source Thermophysical Property Library CoolProp

[11] K.-S. Lee, W.-S. Kim, The effects of design and operating factors on the frost growth and thermal performance of a flat plate fin-tube heat exchanger under the frosting condition, KSME International Journal, 13(12) (2003) 973-981

[12] S. Fukada, H. Tsuru, M. Nishikawa, Frost formation under different gaseous atmospheres, Journal of Chemical Engineering of Japan, (1995) 28(6), 732–737

Chapter 5 : Modeling Frost Formation in a Heat Exchanger

After establishing the frost formation model on a simple geometry, the model was extended to a purifier heat exchanger geometry (HX-1) tested and analyzed in chapter 3. It involves the same heat and mass transfer basis, with several key changes made to better simulate the purifier heat exchanger system. The key changes are extending the model to be one-dimensional (rather than zero-dimensional), have varying wall temperature along its length, and simulate internal flow.

This model is used to study the effect of two input parameters to the heat exchanger, helium humidity (low level moisture contamination levels) and heat exchanger flow balance.

5.1 Problem Description

The developed model considers humid helium gas flow in a heat exchanger. The iso-thermal surface model was zero-dimensional, being that it occurs at a point and all frost growth was calculated as a scalar, with an average value for frost properties. In extending this model to a heat exchanger, it becomes one-dimensional in heat exchanger length. The heat exchanger length is discretized and each segment of length is treated like a zero-dimensional calculation. This allows for the wall temperature to vary along the heat exchanger length, as determined by a calculated low side gas temperature. The model takes in helium at ~300 K at the heat exchanger inlet to the high (impure helium supply) side and helium at ~80 K at the heat exchanger inlet to the low (pure helium return) side.

The heat exchanger of interest is the test heat exchanger from chapter 3. It contains ten sets of two concentric tubes coiled to form a purifier heat exchanger. The tubes are joined at supply and return headers as shown in Figure 5-1, which, at the warm end of the heat exchanger, splits the incoming high side (dirty, higher temperature and pressure) helium into 10 tubes (there are two of the units shown in the Figure 5-1, each splitting the flow into 5 tubes) and merges the flow from the 10 low side (clean) helium tubes. At the cold end, the same type of headers are used for the inverse purpose to return low side flow (clean, lower temperature, which provides the cooling to the high side flow and lower pressure). As described in chapter 3, the high side flow is in the annular space between the tubes, so this being where the frost deposits make it the main focus of the modelling. This model simulates only one of the tubes, multiplying the mass collection by 10 to describe the full heat exchanger collection capacity. This has some shortcomings that are discussed in the following sections.

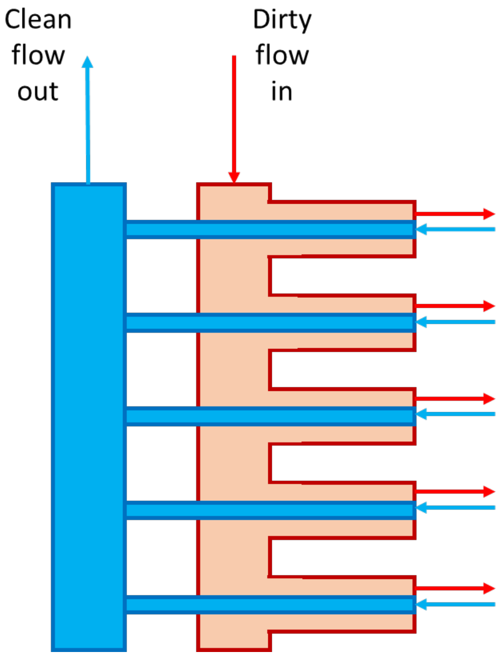

Figure 5-1 Schematic of HX showing header arrangement

5.2 Model Development

The critical changes from the zero-dimensional model are a length dimension, internal flow (heat exchanger channel), and variable wall temperature (along the length). The heat exchanger is discretized along the length. Each length segment is calculated as an individual point calculation with a finite length as described in the zero-dimensional model in chapter 4.

The calculation is carried out by taking in input parameters and initial values, then calculating the temperature profiles. The temperatures are used as inputs to the frost deposition calculation, outputing frost properties. The pressure drop in the annulus, considering frost deposition is calculated until the calculated value reaches an assigned value of 0.6 bar, determined from the testing. The calculation is treated as a marching scheme, marching in length from the warm end to the cold end of the heat exchanger, then stepping forward in time and repeating.

Each length step takes in an inlet helium humidity, existing frost height, frost temperature, fluid temperature, and wall temperature. A new frost height, frost temperature, and outlet helium humidity are calculated. The difference between the inlet and outlet helium humidity is calculated based on the mass of frost deposited during that time-step. The outlet helium humidity is then taken as the inlet to the next length step.

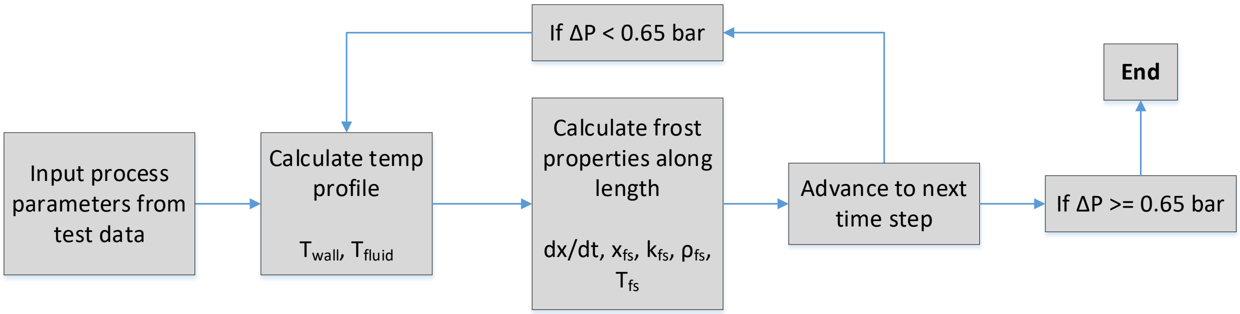

Figure 5-2 Flowchart of the numerical solution algorithm

Constant density was assumed for these 1D calculations. At high pressures and low temperatures, the frost forms as a sheath, rather than as dendrites [1]. This assumption is further reinforced by the results on Byun's [2] density correlation used in several of the calculations in chapter 4. There was very little variation in density in the range studied (which are broader than the range studied in this chapter), between 180-200 kg/m3. Byun established this in cryogenic temperatures with nitrogen as the carrier gas. This calculation (like the zero-dimensional model) also assumes constant frost properties within the frost layer at a given length and time step. The average frost density in helium gas was estimated to be 86-135 kg/m^3, as calculated from test data mass measurements and a frost deposition profile that follows the partial pressure saturation curve at initial conditions and this value looks reasonable for helium. The model was run with several different constant density values within this range for each of the test cases from chapter 3. The top end of this range (135 kg/m^3) fit most closely with the test data, so this constant value was chosen for this study. This is within the range seen in previous studies on air systems as well [2-5], including Byun's correlation discussed above.

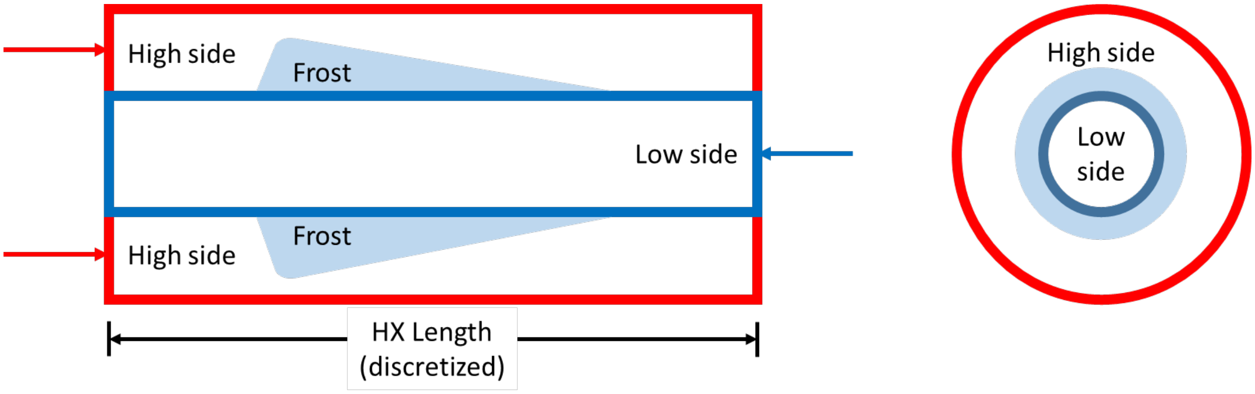

Figure 5-3 Schematic of model geometry

The tube-in-tube geometry has two distinct hydraulic diameters [6], both including frost height, as shown in Figure 5-3. The hydraulic diameter for flow uses both tube surfaces as the wetted perimeter.

$$d_h = D_{inner} - \left(d_{outer} + 2x_f\right) \tag{5.1}$$

D_{inner} is the inner diameter of the outer tube, d_{outer} is the outer diameter of the inner tube, and x_f is the frost thickness. The hydraulic diameter for heat transfer uses only the inner tube surface as the wetted perimeter.

$$d_{h,HT} = \frac{D_{inner}^2 - \left(d_{outer} + 2x_f\right)^2}{d_{outer} + 2x_f} \tag{5.2}$$

The Reynolds number is calculated by its definition, but the critical Reynolds number is calculated using a coiling factor [7].

$$Re_c = 20{,}000\delta^{0.32} \tag{5.3}$$

The geometry affects the heat transfer through the Nusselt number. A correlation for Nusselt number using Dean number and a coiling factor (δ) is used [7, 8].

$$Nu_{ann} = 0.027De^{0.94}Pr^{0.69}\delta^{0.01} \tag{5.4}$$

The subsequently calculated convective heat transfer coefficient tends to increase exponentially when the frost height gets near to the outer tube due to its strong dependence on Reynolds number. This is unrealistic, however, so the convective heat transfer coefficient is capped at 500 W/m^2K.

In mass transfer models in literature [2-4], a Lewis number of one for the calculation of the mass transfer coefficient is often assumed, which was proven approximately true in air systems at low pressure [3]. Based on preliminary calculations using the definition of Lewis number, this is not the case for this helium system. Therefore, the physical definition of Lewis number was used when calculating the mass transfer coefficient. A maximum of 0.024 m/s was used for mass transfer coefficient for the same reason as the convective heat transfer coefficient.

The high and low side temperatures along the heat exchanger were calculated using equations derived from [9]. The temperatures at the inlet to both streams are defined as inputs. The temperatures and frost properties (thickness, temperature, thermal conductivity) for the previous time step are used to calculate the UA and NTU for the current time step (for the first time step, it is assumed that UA and NTU are evenly distributed along the length). The resistances for the convection through the annulus, frost layer, conduction through the inner tube, and the convection through the inner tube are calculated in cylindrical coordinates at each length step. For the test heat exchanger, the heat transfer coefficients for the annulus and the tube are corrected before being used in the resistance equations in order to match the NTU for the clean HX from the test data. An NTU of approximately 16 derived from the test for the balanced case with a clean HX was used as the benchmark. To fit the test data, a correction factor of 0.957 was used to correct the heat transfer coefficients, as shown below for the annular example.

$$h_{ann} = \frac{Nu * k_{ann}}{d_{h,ann}} * 0.957 \tag{5.5}$$

The overall heat transfer coefficient is calculated at each length step by the sum of the inverse of the resistances. Δ%NTU is the percentage of the NTU that occurs within this length step, with the same going for ΔUA.

$$\Delta UA = (\Delta\%NTU)\sum\frac{1}{R_i} = (\Delta\%NTU) * \left[\frac{1}{R_{fs}} + \frac{1}{R_{annulus}} + \frac{1}{R_{tube}} + \frac{1}{R_{tube,cond}}\right] \tag{5.6}$$

ΔNTU is then calculated using C_{min}. From here, the ΔNTU and ΔUA can be summed to find the totals for the entire heat exchanger. Now the actual outlet temperatures at the current time step can be calculated. ‘l’ denotes the low side of the HX, ‘h’ denotes the high side of the HX, ‘i’ denotes the inlet of that stream, and ‘o’ denotes the outlet of that stream. Because of its countercurrent nature, $T_{h,i}$ and $T_{l,o}$ are at the warm end of the HX. The following equations were used to calculate the outlet temperature of the high side, with an energy balance being used to calculate the outlet temperature of the low side.

$$T_{h,o} = T_{h,i} - \left(T_{h,i} - T_{l,i}\right)\frac{1 - e^{D}}{\frac{C_h}{C_l} - e^{D}} \tag{5.7}$$

$$D = UA\left[\frac{1}{C_h} - \frac{1}{C_l}\right] \tag{5.8}$$

$$Z = \frac{1 - e^D}{\frac{C_h}{C_l} - e^D} \qquad 5.9$$

Once the outlet temperatures are calculated, the temperatures can be calculated at each length step based on a variation of the same equation, marching from the warm end to the cold end. The outlet temperature of the high side and the inlet temperature of the low side are known. The inlet temperature of the high side is calculated using the equation below and the outlet temperature of the low side is calculated by energy balance. The subscripts here denote the relative local positions, with respect to the length step of interest.

$$T_{h,o} = \frac{T_{h,i}\left[1 - Z - \frac{C_h}{C_l}Z\right] + ZT_{l,o}}{\left[1 - \frac{C_h}{C_l}Z\right]} \qquad 5.10$$

The previous equations assume that the thermal capacities of the high and low side streams are unequal. If they are equal, the equations change a bit.

$$T_{h,o} = T_{h,i} - \frac{T_{h,i} - T_{l,i}}{\frac{C}{UA} + 1} \qquad 5.11$$

$$T_{h,o} = \frac{\left[\frac{C}{UA} - 1\right]T_{h,i} + T_{l,o}}{\left[\frac{C}{UA}\right]} \qquad 5.12$$

The temperature profiles are then used to calculate the frost thickness and properties as described in chapter 4.

5.3 Validation of Model

The model was validated using test data, first at clean conditions. Given the heat transfer coefficient correction, the NTU matches the test data at approximately 16. The inlet and outlet temperatures were also matched within 1.0%. After the clean conditions were matched, the dirty conditions were compared, as well as transient results. The model was run using test data inputs (fluid temperature, humidity, pressure, mass flow rate) until the pressure drop approximately matched the test data at the end of the test (650 mbar). It can be noted that test 3 ran until the pressure drop was 980 mbar, but due to the exponential nature of pressure drop at the end of the tests, this was only less than five minutes past when it reached 650 mbar. The results at the end condition of the simulation are shown in Figure 5-4 through 5-7. The largest difference seen between the simulation cases is the frost distribution profile between balanced and unbalanced cases. The unbalanced case have a narrower peak and deposit a bit more mass toward the warm end of the HX. As seen in Table 5-1, only test 1 matched closely to the mass collected. The model did not match the test NTU data. The simulation does not degrade nearly as much as the test does. They both begin at 16 NTU, but the simulation ends at 13.9 NTU while the test ends at 9.7 NTU. A similar mismatch is found in the outlet temperatures (mismatch of ~8 K instead of < 1 K at clean condition). This can be explained by an assumption of the model that does not reflect the real operating process. This leads to a major hypothesis. Flow distribution between the tubes has a dominant effect on heat exchanger performance and frost collection capacity.

Table 5-1 Test and model results at the end condition

Test #	ω_{in}	HX-1 Flow	$m_{collected}$		NTU		ΔP_{HX-1}	
	[ppm$_v$]	[-]	[g]		[-]		[mbar]	
			test	model	test	model	test	model
1	32.0	Balanced	800	777	9.7	13.9	660	650
2	32.1	Unbalanced	538	761	5.8	14.0	610	650
3	68.6	Balanced	581	784	3.6	14.1	980	650
4	58.3	Unbalanced	591	742	3.2	14.3	610	650

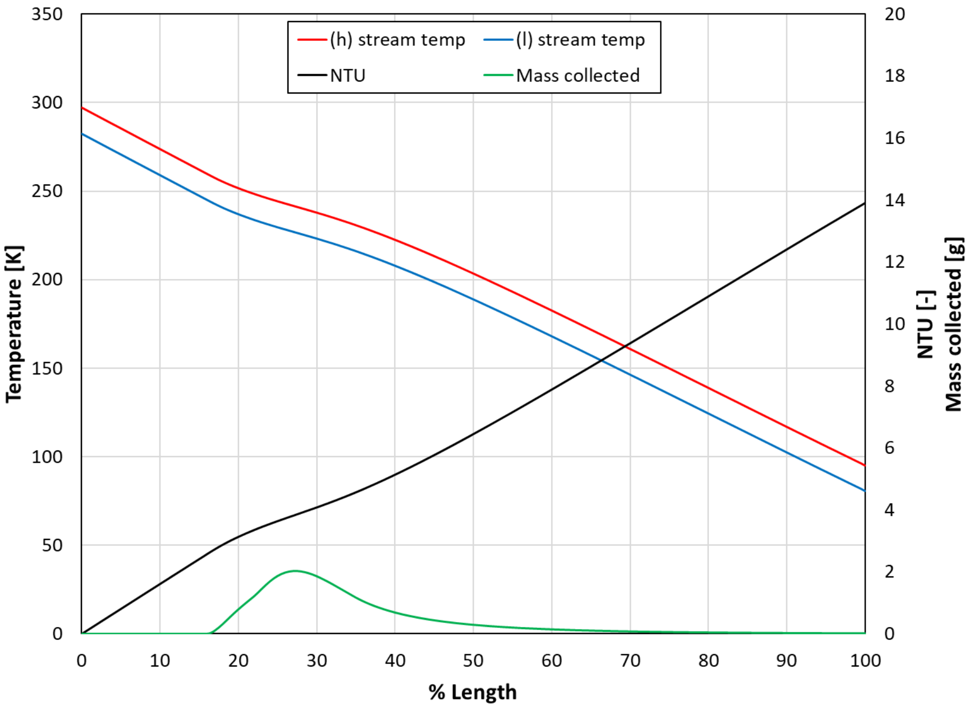

Figure 5-4 Test validation case: 32.0 ppm, balanced HX-1

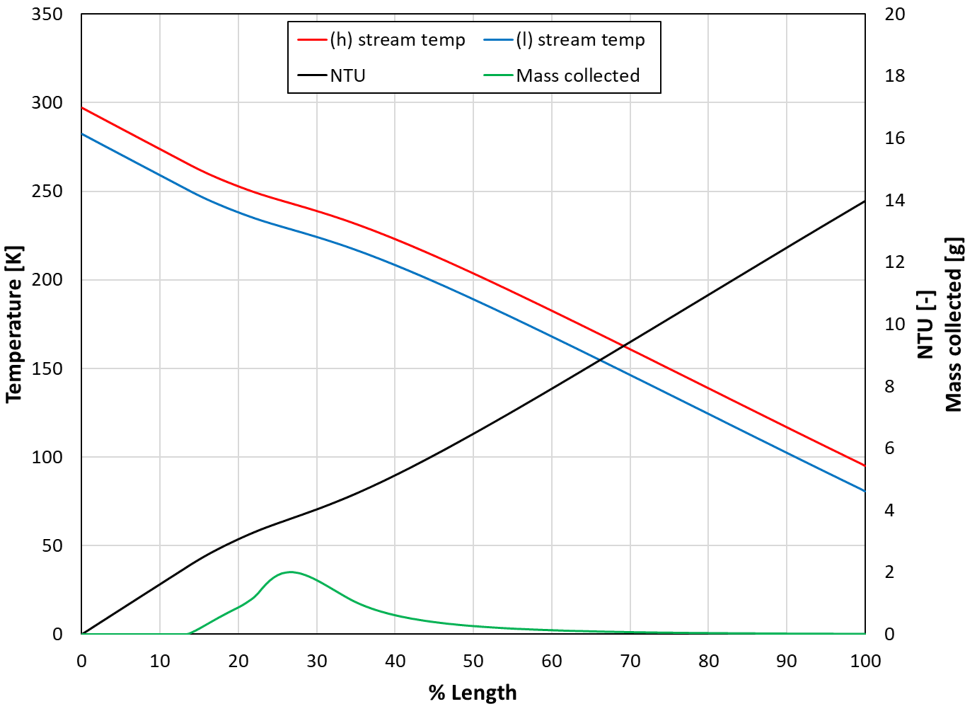

Figure 5-5 Test validation case: 32.1 ppm, unbalanced HX-1

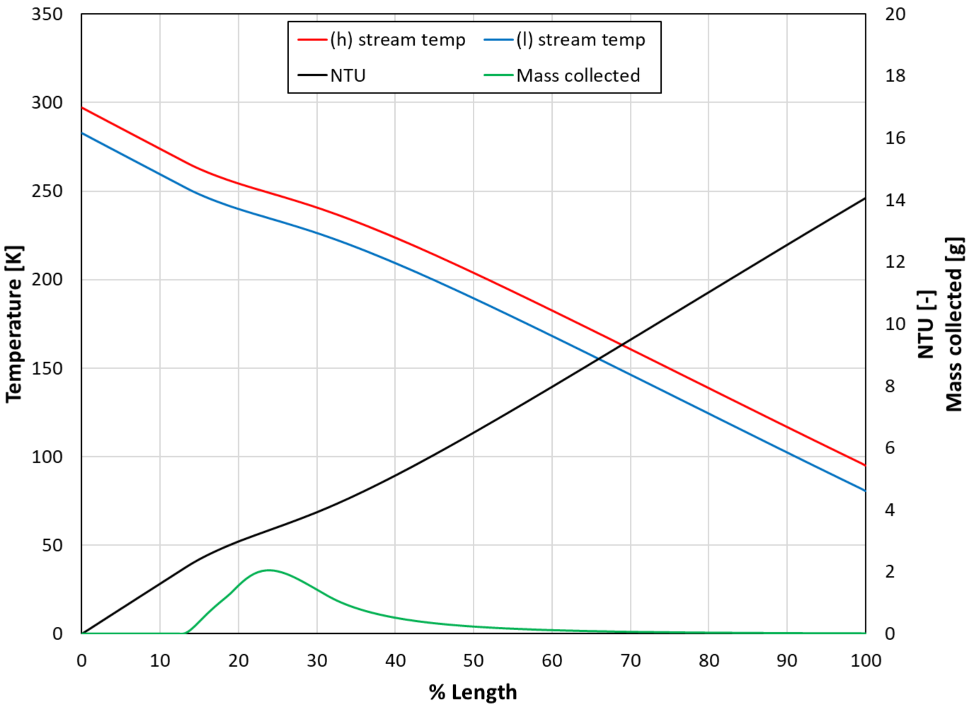

Figure 5-6 Test validation case: 68.6 ppm, balanced HX-1

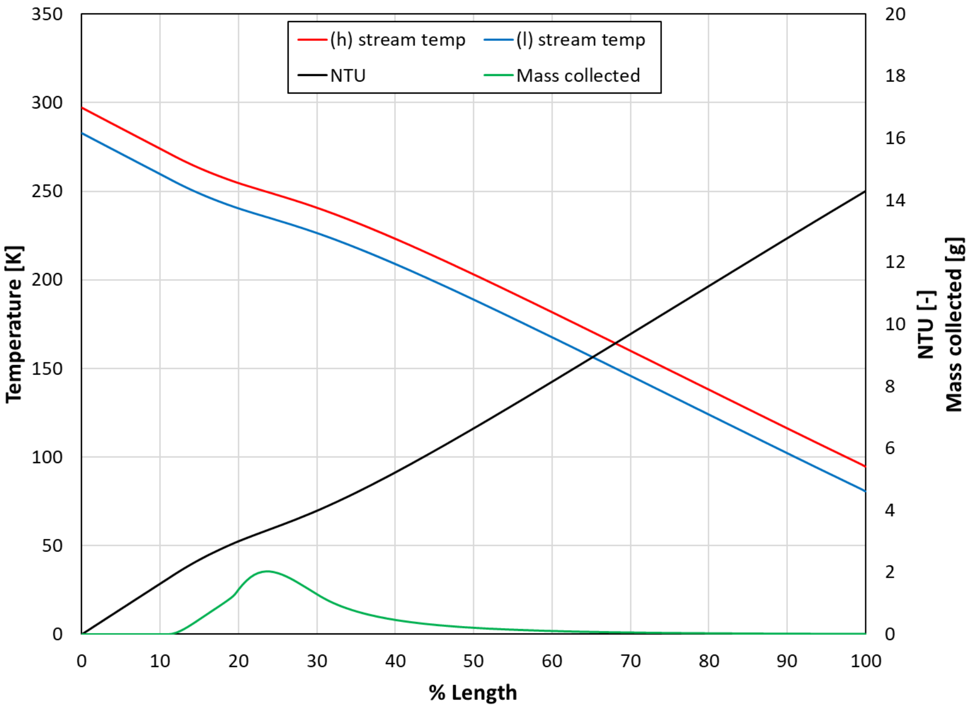

Figure 5-7 Test validation case: 58.3 ppm, unbalanced HX-1

At close examination, the difference in the test data to the model can be attributed to the flow mal-distribution resulting from the header design. The model assumes equal high and low side flow in all ten tubes for the entire test duration. However, this is not realistic, as the high side flow in the ten tubes slightly vary from top to the bottom of the header. This slight difference can have a large impact on frost deposition and cooling curves, potentially blocking the flow in certain tubes sooner than the others. This results in uneven mass flow through the annulus, as some tubes have more deposition restricting the flow, with no change in the total mass going through the low side each tubes. This actual flow mal-distribution reduces the effective UA and NTU’s much more than the model prediction, which did not account for this effect. This is discussed in more detail in the following section, as the simulation results explain the effects.

The transient test data is compared with the transient simulation results in Figure 5-8 through Figure 5-11. Here it can be seen further that only test 1 matches the mass collected as well as the time to reach the maximum pressure drop. The other simulations ran for approximately the same length of (simulation) time before reaching the maximum pressure drop. This further enforces the idea that there is another significant factor at play impacting the maximum frost deposition and heat exchanger degradation and causing the heat exchanger to plug and lose effectiveness earlier than expected. The aforementioned hypothesis of flow distribution will be analyzed further using this model in the coming sections.

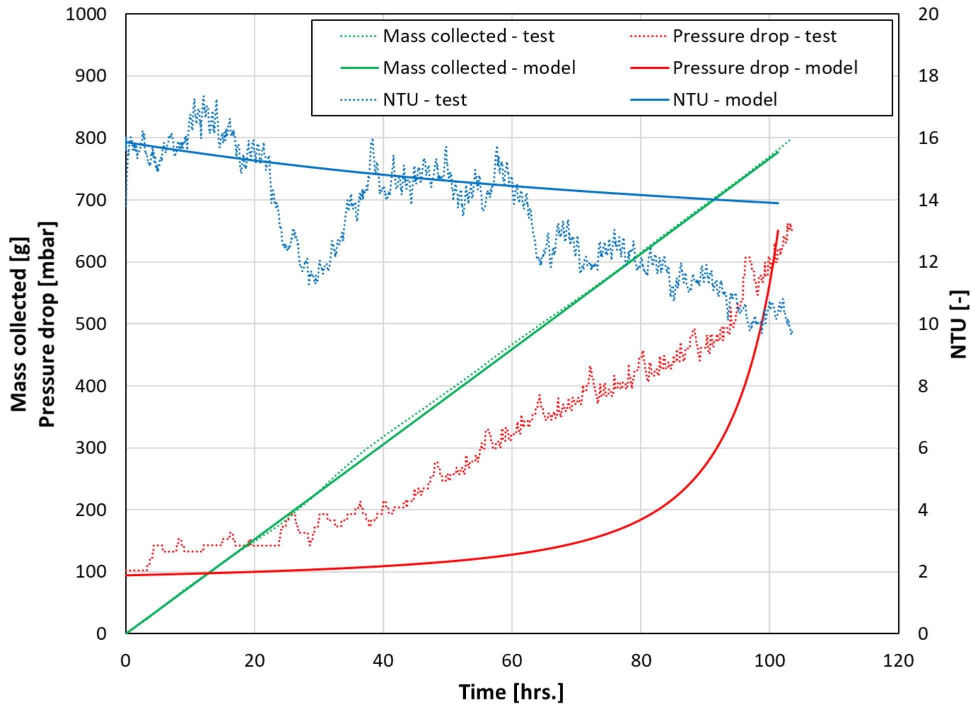

Figure 5-8 Transient NTU, frost mass, and pressure drop for test 1 comparison with model

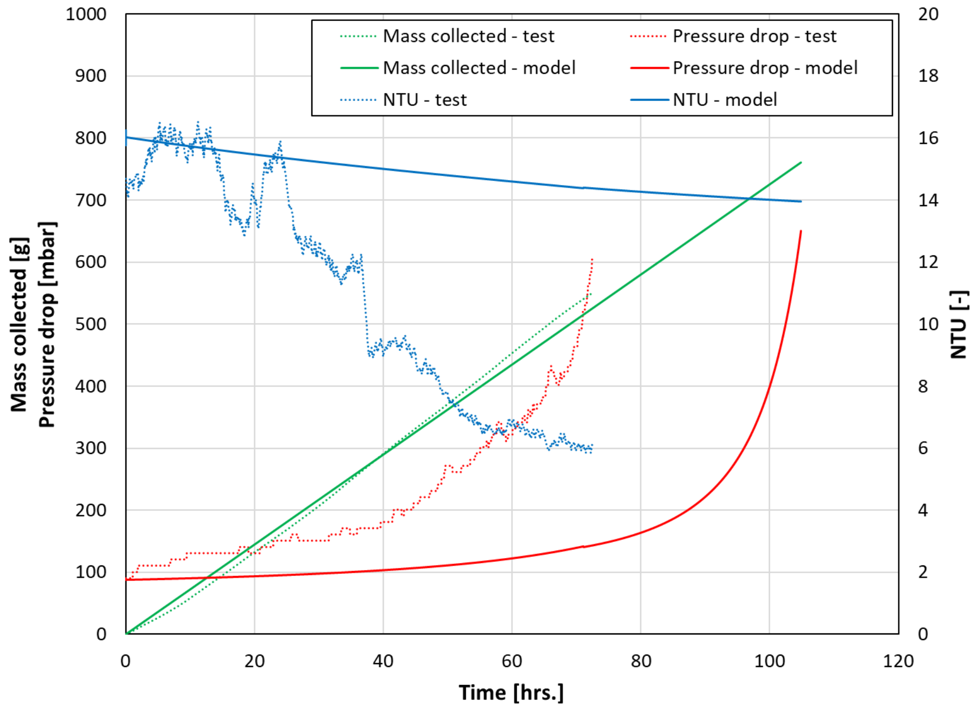

Figure 5-9 Transient NTU, frost mass, and pressure drop for test 2 comparison with model

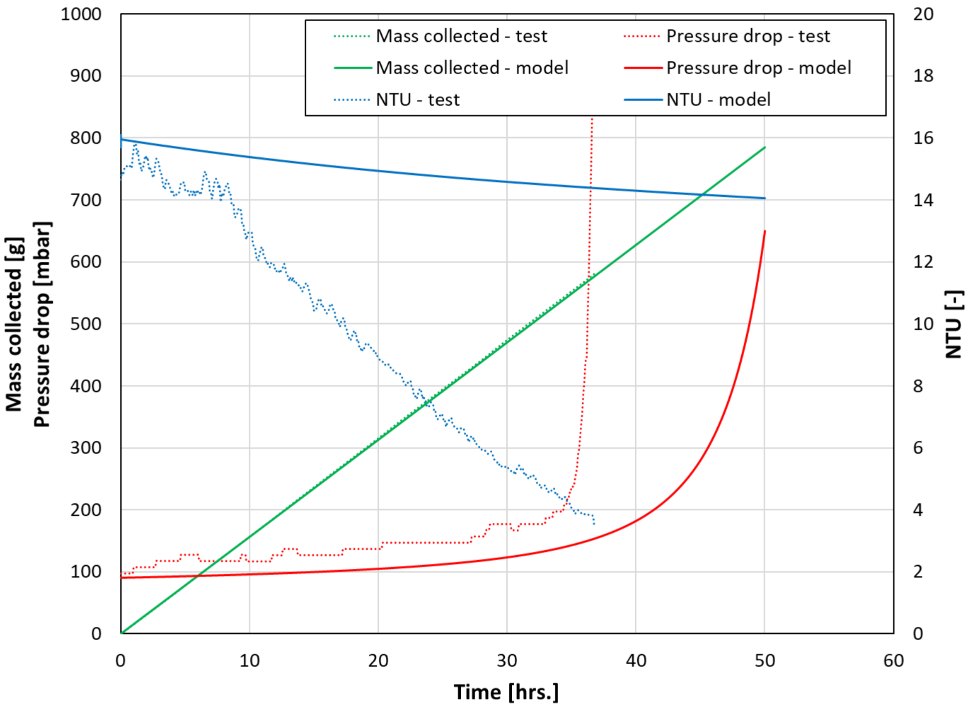

Figure 5-10 Transient NTU, frost mass, and pressure drop for test 3 comparison with model

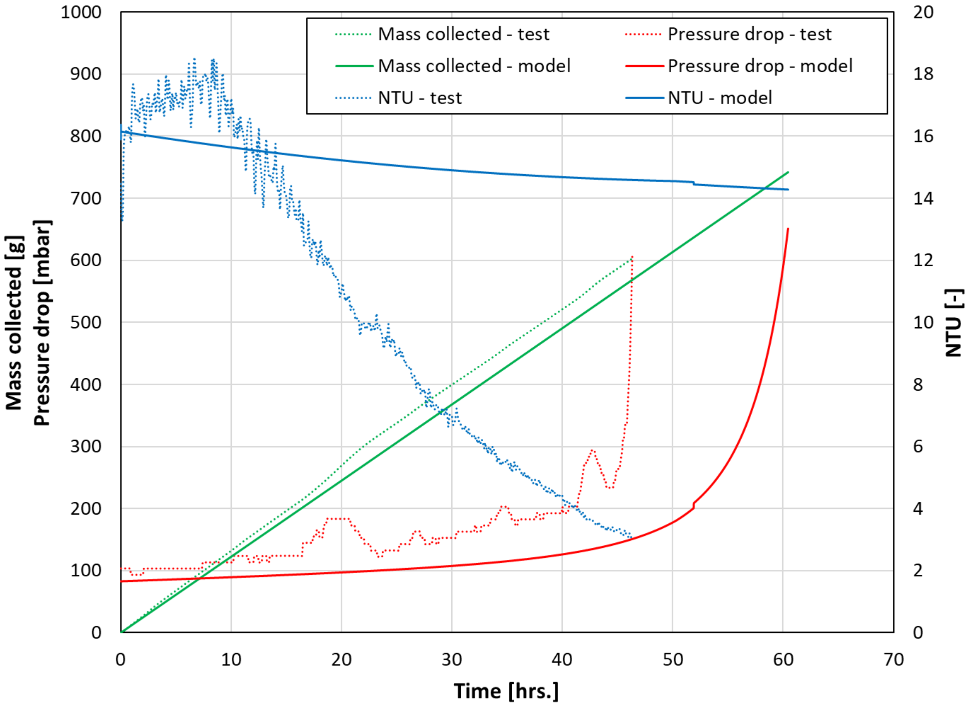

Figure 5-11 Transient NTU, frost mass, and pressure drop for test 4 comparison with model

5.4 Effect of Flow Imbalance on Heat Exchanger Cooling Curves and Associated Frost Formation

Flow imbalance has a great impact on the heat exchanger cooling curves and associated frost formation. The model is used to investigate this in detail in this section. In Figure 5-12, the unbalanced case has a mass flow through the high side 20% less than that through the low side. This 20% difference in mass flow is intentionally larger than that from the test cases to better illustrate the effects at play. All other inputs are held constant between the cases.

First, the unbalanced case deposits frost much closer to the warm end (inlet), by approximately 16% of the length of the HX. This is caused by the shift in the cooling curves due energy balance between high and low side flows. In the balanced case, the temperature difference shows little deviation between the warm end and the cold end. In the unbalanced case, the flow disparity causes the cooling curve to pinch at the cold end and open at the warm end. There is more flow through the low side, which causes the high side to closely approach the returning low side temperature (causing the pinch) and low side flow to leave the warm end at a colder temperature.

The frost deposition is also slightly more localized and results in a slightly higher frost height at the end condition. This is due to the larger temperature difference in the frost deposition range. Temperature difference is the driving force of all heat and mass transfer, so more mass deposits when this is larger temperature difference driver.

Flow imbalance is a broader factor for the real heat exchanger as well. During testing, the flow imbalance was intentionally manipulated for the purposes of using all the available cooling provided by the liquid nitrogen. However, due to the header geometry mentioned before, the flow distribution is not exactly equal between the 10 tubes, even in the balanced case. As shown in Figure 5-12, if there is less flow through a particular annular channel, the frost deposition can shift toward the header. If the flow imbalance reaches a level like that shown in the plot, the frost can start to deposit near the warm end of the heat exchanger. If it shifts even more, it could deposit in the header, blocking flow considerably. This is the hypothesis for why the NTU degrades so much more in the unbalanced tests than expected, and more than the balanced tests.

Two additional simulation cases were run to investigate how frost deposits when the flow imbalance is changing over time. This represents cases in which the high side flow distribution between tubes changes over time as certain tubes plug (increasing pressure drop in those tubes), causing more high side flow to go through other less plugged tubes whereas the low side return flow remains equal in all the tubes.

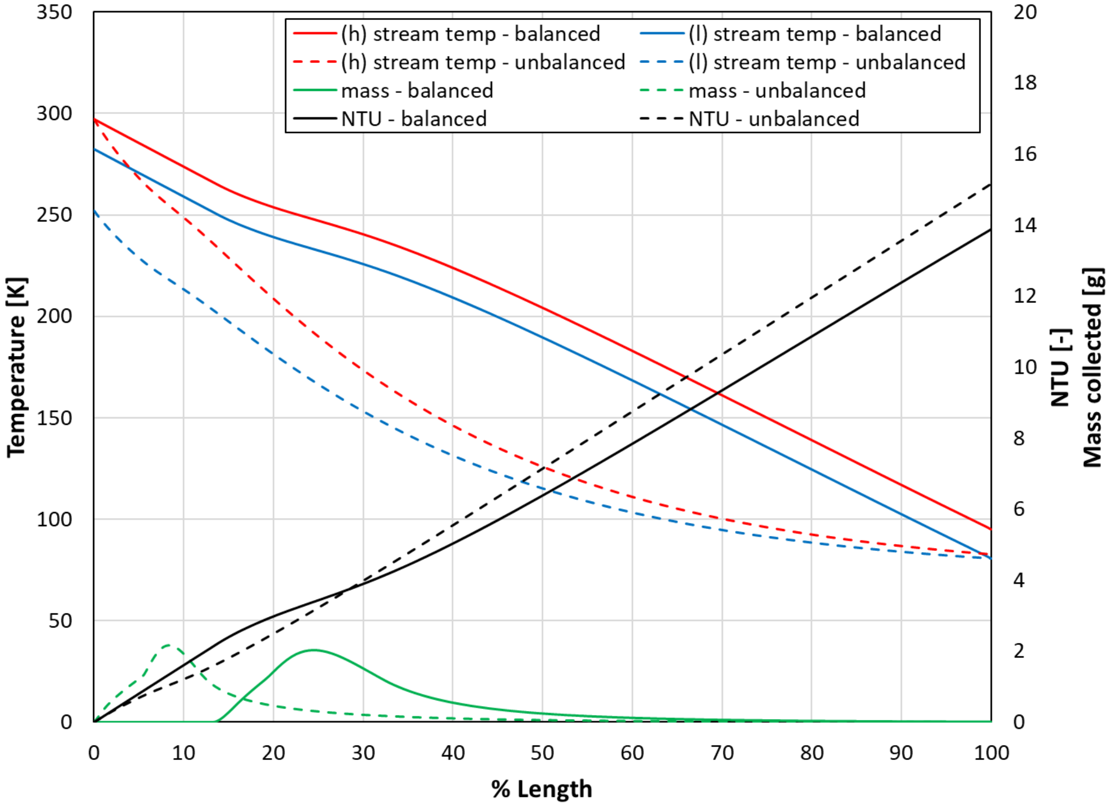

Figure 5-12 Model calculated NTU, cooling curves, and frost mass distribution for the 60 ppm balanced and unbalanced cases

Figure 5-13 shows a case in which the flow starts balanced and shifts to having more flow through the high side. By the end of this simulation, the cooling curves pinch at the warm end, shifting the region of frost deposition (where saturation conditions occur) toward the cold end. The shift of the cooling curves in this direction over time results in the region of frost deposition to shift toward the cold end over time. This causes much more mass to deposit, because the frost doesn't reach a height that causes a significant pressure drop until much later than in the constant mass flow cases. As a result of these effects, this simulation case deposits much more overall frost mass (1512 g). This study explains the strong influence of the cooling curves on the total amount of frost collection in a cycle.

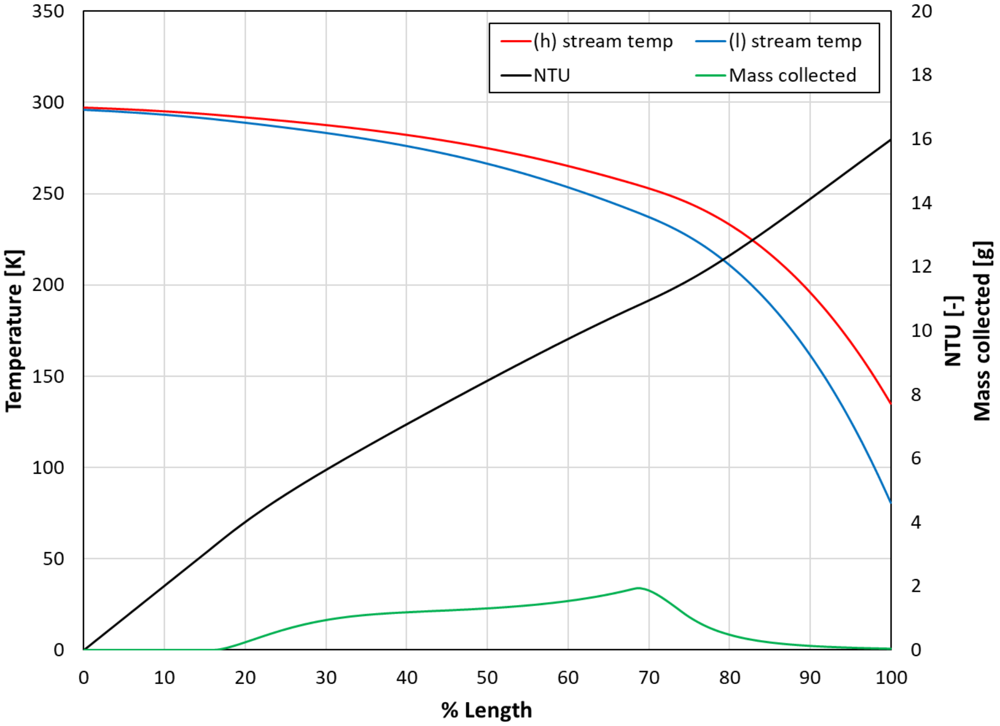

Figure 5-13 Model results for thermal capacity ratio shifting from 1 to 1.2

Figure 5-14 shows a case in which the starts balanced and shifts to having less flow through the high side. With more relative mass flow through the low side, the cooling curves shift over time to pinching at the cold end. This extends the frost deposition range slightly. However, it doesn't have much room to shift, as it's already close to the warm end. The deposition also deposits more locally at a given time (like the unbalanced test case, which has lower high side flow like this one), so the frost height will be higher. This increases the pressure drop, stopping the simulation sooner, resulting in less mass accumulation. These effects work against each other, with the effect of local deposition (increased pressure drop) being more dominant to cause less mass to be deposited in this case than the balanced flow case (685 g). This mass is between the results for balanced flow (785 g) and a ratio of 0.8 (567 g), the end points of this case.

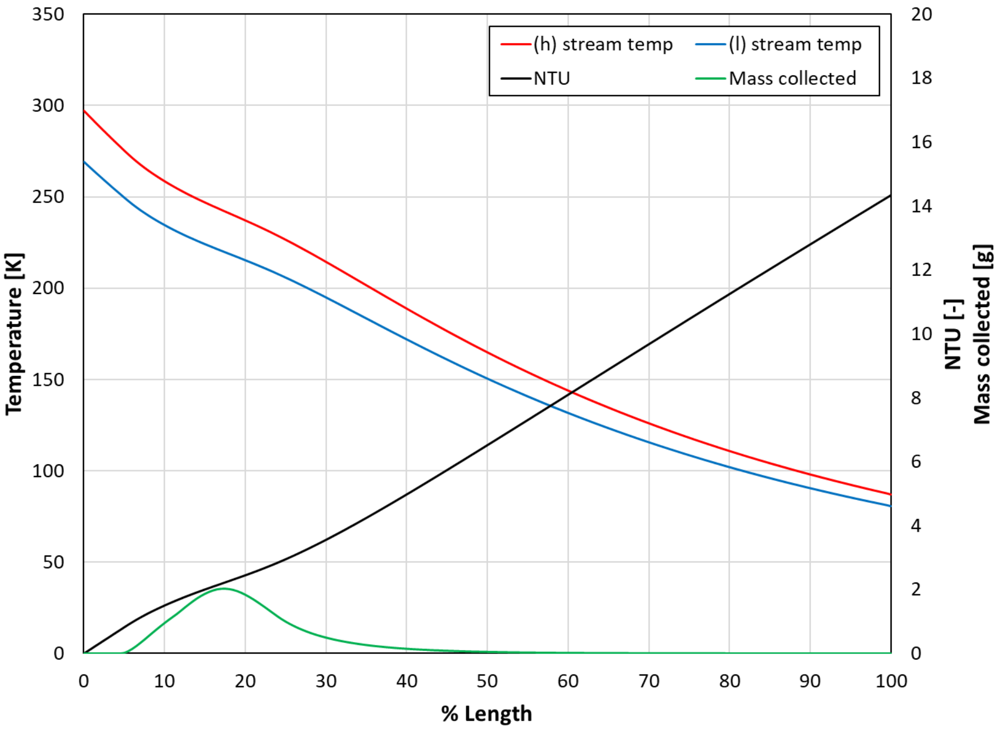

Figure 5-14 Model results for thermal capacity ratio shifting from 1 to 0.8

5.5 Effect of Inlet Moisture Contamination Level and Associated Frost Formation

Inlet moisture contamination level has an effect on the frost formation. The partial pressure profile and the associated saturation temperature change as the inlet moisture contamination changes. The two cases discussed are 30 ppm and 60 ppm, for the both the balanced HX flow (Figure 5-15) and the unbalanced HX flow (Figure 5-16). Inlet contamination has a minimal impact on the cooling curves, as the only difference is a slight shift in frost deposition location. Both cases result in the same final NTU, with the distribution slightly shifted along the length.

The point of peak frost deposition shifted approximately 6% of the length of the heat exchanger between 30 and 60 ppm of moisture in the helium stream. This shift is reduced when the flow is unbalanced, to approximately 2%. The temperature gradients are steeper in the frost deposition range, so the saturation temperature difference effect is lessened.

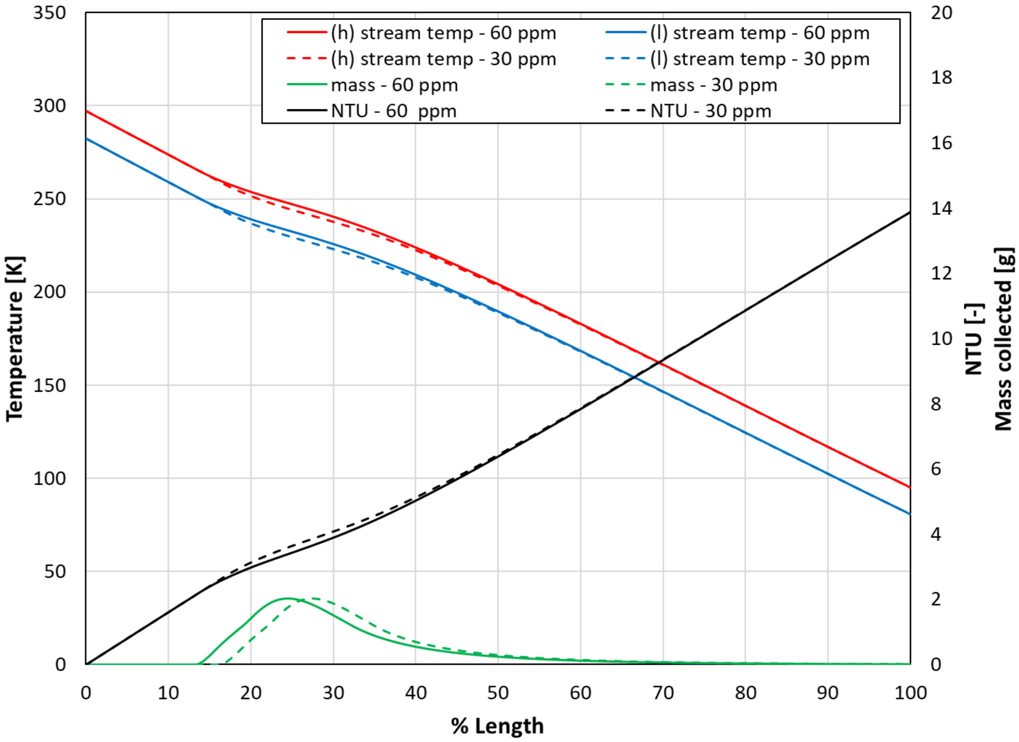

Figure 5-15 Model calculated NTU, cooling curves, and frost mass distribution for the balanced, 30 ppm and 60 ppm cases

Comparing all 4 cases in Figure 5-15 and Figure 5-16, the frost deposition is closer to the warm end when the inlet moisture contamination is higher and/or the mass flow is unbalanced. The frost deposition is closer to the cold end when the inlet moisture contamination is lower and the mass flow is balanced. When the deposition shifts toward the warm end, the header may have frost deposit in it, blocking parts of it, causing severe degradation in NTU. This is what happens in the test data for both the unbalanced cases and the 60 ppm cases (to a lesser degree). When certain tubes get plugged, the remainder of the mass flow is distributed into the remaining open unplugged tubes. This results in the opposite effect to the original flow imbalance. When the high side flow is greater than the low side flow in a given tube, the cooling curve shifts to open at the cold end, pinching at the warm end. This results in frost depositing nearer to the cold end, which increases the area available to collected frost. This actually increases the frost collection capacity of these tubes, while the other tubes are not collecting frost. The combination of this effective increase in frost collection capacity in some tubes and complete plugging of others work against each other to determine the overall frost collection capacity for each case; but less mass collection than the balanced flow case.

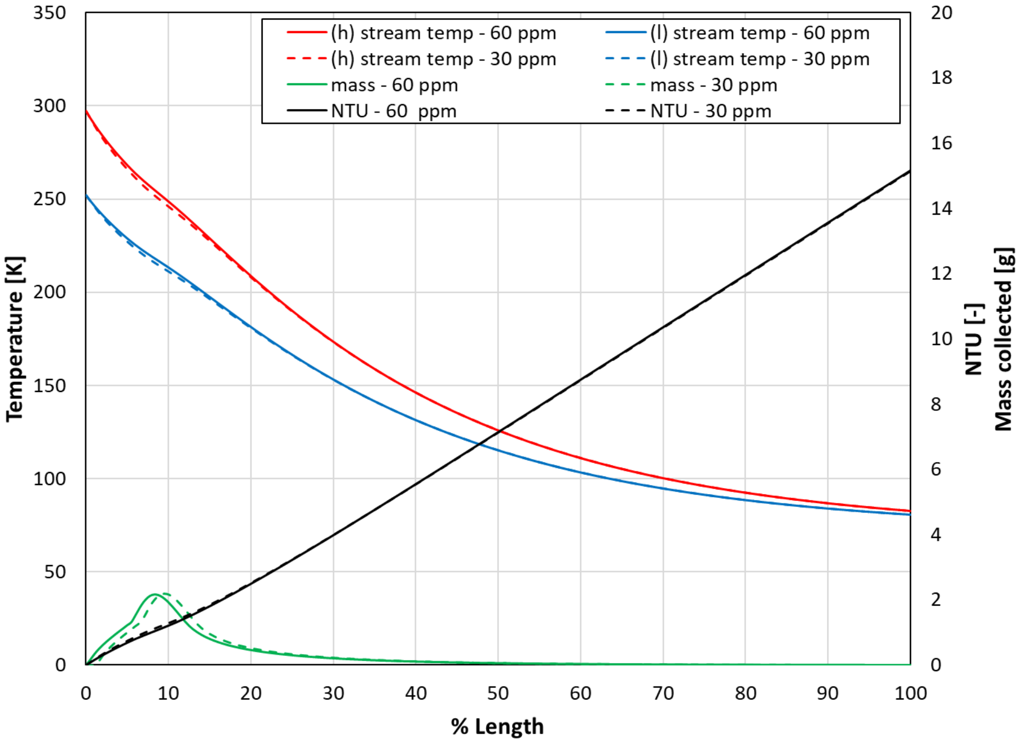

Figure 5-16 Model calculated NTU, cooling curves, and frost mass distribution for the unbalanced, 30 ppm and 60 ppm cases

5.6 Summary

A transient, one-dimensional, heat and mass transfer model was developed for a tube-in-tube heat exchanger. Critically, it calculates gas cooling curves, heat exchanger NTU, frost deposition, and frost properties. The mass transfer model was validated for a 30 ppm balanced case. The effects of inlet moisture contamination level and heat exchanger flow imbalance were discussed. It was found that lower ppm and a more balanced heat exchanger result in frost deposition shifted toward the cold end, collecting more moisture. Crucially, this shift is away from the header that splits flow into the tubes at the warm end. It was hypothesized that the header causes flow mal-distribution, resulting in certain tubes having more high side flow than others. This flow mal-distribution can cause tubes with less high side flow to frost nearer to the header, eventually causing frosting in the header. It can also cause tubes with more high side flow to plug sooner because of increased mass deposition close to the inlet header. This plugging reduces the number of available tubes and causes more severe imbalance, resulting in large degradation of heat exchanger performance by the metric of NTU. Transient control of the flow imbalance is discussed for its potential to shift the frosting zone of the heat exchanger over time. When the high side flow is increased by 20% over the duration of operational period, this shifting can greatly increase the estimated capacity of the heat exchanger, from 785 g to 1512 g. The freeze-out heat exchanger design discussed in chapter 6 is developed to eliminate/ minimize the flow distribution issues discussed here and observed in the test purifier heat exchanger.

REFERENCES

[1] T. Kobayashi, On the habit of snow crystals artificially produced at low pressures, Journal of Meteorological Society of Japan, 36 (5) (1958) 193-208

[2] S. Byun, et al. Frost modeling under cryogenic conditions, Int. J. Heat Mass Transfer, 161 (2020) 120250

[3] M. Kandula, Frost growth and densification in laminar flow over flat surfaces, Int. J. Heat Mass Transfer, 54(15) (2011) 3719-3731

[4] M. Kandula, Frost growth and densification on a flat surface in laminar flow with variable humidity, International Communications in Heat and Mass Transfer, 39(8) (2012) 1030-1034

[5] R. Le Gall, et al., Modelling of frost growth and densification, Int. J. Heat Mass Transfer, 40 (13) (1997) 3177-3187

[6] V. Kumar, et al., Pressure drop and heat transfer study in tube-in-tube helical heat exchanger, Chemical Engineering Science, 61 (13) (2006) 4403-4416

[7] S. Garimella, et al., Experimental investigation of heat transfer in coiled annular ducts, J. Heat Transfer, 110(2) (1988) 329-336

[8] D. Majidi, et al., Experimental studies of heat transfer of air in double-pipe heat exchanger, Applied Thermal Engineering, 133 (2018) 276-282

[9] W. F. Stoecker, Design of Thermal Systems, McGraw-Hill (1971)

Chapter 6 : Design and Analysis of a Cryogenic Freeze-Out Heat Exchanger

Materials in this chapter are an extension of the work reported in [1]. Inderscience retains copyright of that paper.

6.1 Problem Description

Considering the design and performance characterization of the existing industrial helium purification systems available commercially, and operational shortcomings discussed in previous chapters, the conceptual design of a novel freeze-out helium purifier is proposed. The mechanical design and configuration of the design is based on Kroll [2]. The main shortcomings of the purifier discussed in chapter 5 are large nitrogen usage (due to inefficient heat exchange and for the regeneration process), suboptimal design for freeze-out (manifesting as significant NTU degradation over time and frost blockages due to flow mal-distribution long before expected capacity is reached, and excess helium wastage during regeneration process). It uses contamination (moisture) freeze-out in a coiled finned tube heat exchanger followed by cryogenic adsorption (at 80 K) to remove air (nitrogen and oxygen). Liquid nitrogen is used in the purifier as the primary coolant. The major focuses of the proposed design are to maximize the moisture collection capacity of the freeze-out heat exchanger to maximize the operating period of the purifier (time between regenerations), while minimizing the overall utility (liquid nitrogen, helium and electricity) consumption. This chapter discusses the major details of the proposed purifier design - including process flow, component design, and modes of operation. It also optimizes the design of the heat exchanger for minimum exergy use, by modifying the number of helium tube passes, mandrel diameter, and total heat exchanger surface area. Lastly, the effects of fin density and mandrel diameter on frost deposition and heat exchanger performance are analyzed and compared to a commercially available system.

6.1.1 *Purification Process*

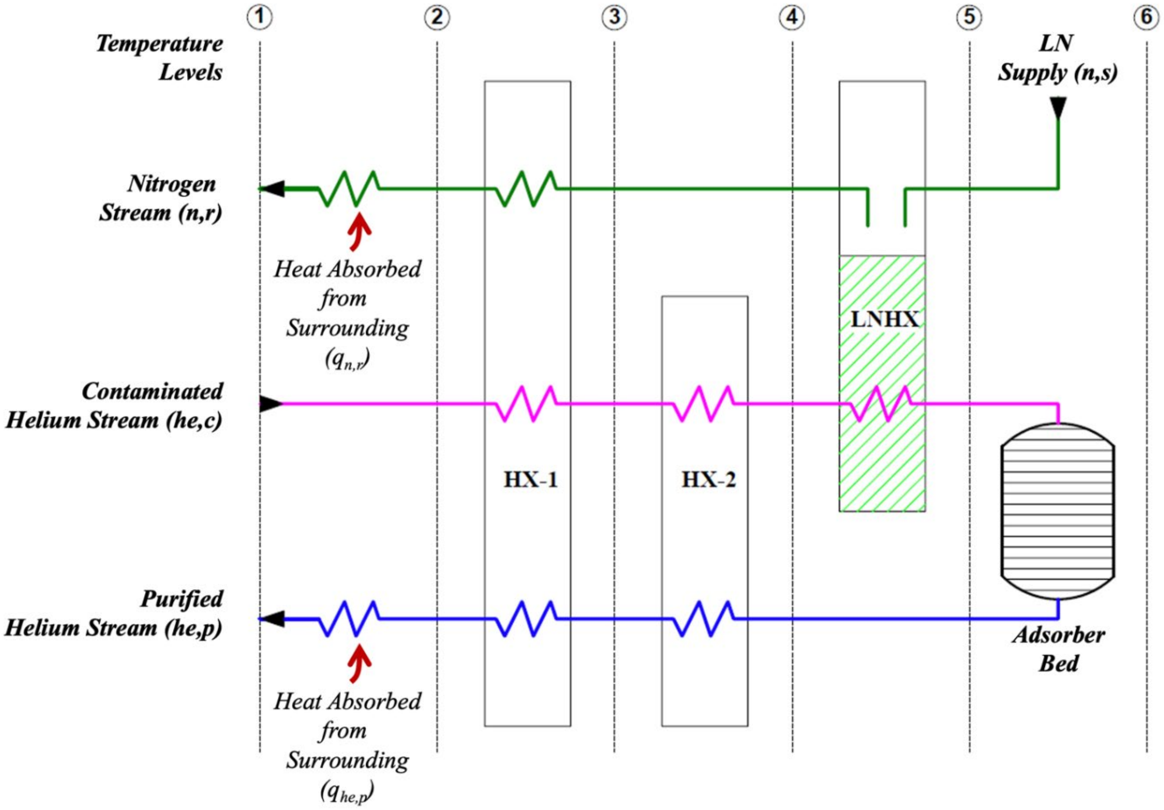

Figure 6-1 Simplified flow diagram of the freeze-out purification system

A simplified flow diagram of the freeze-out helium purifier considered in this study is shown in Figure 6-1. The temperature levels ($j = 1\ to\ 6$) shown represent the changes in stream temperatures within the purification system. There are four process streams within this helium purifier: namely, a contaminated helium stream, a purified helium stream, a liquid nitrogen supply stream, and a saturated / vapor nitrogen stream. These are denoted by the subscripts, (*he,c)*, (*he,p)*, (*n,s)*, and (*n,r)* respectively. An external compressor pressurizes the contaminated helium stream (*he,c*) and circulates it through the purification system, but is outside the scope of this project. The purification system consists of heat exchangers HX-1 and HX-2, a liquid nitrogen (LN) vessel (with associated cooling coils), and an activated carbon bed, cooled by the LN, for low-level air removal.

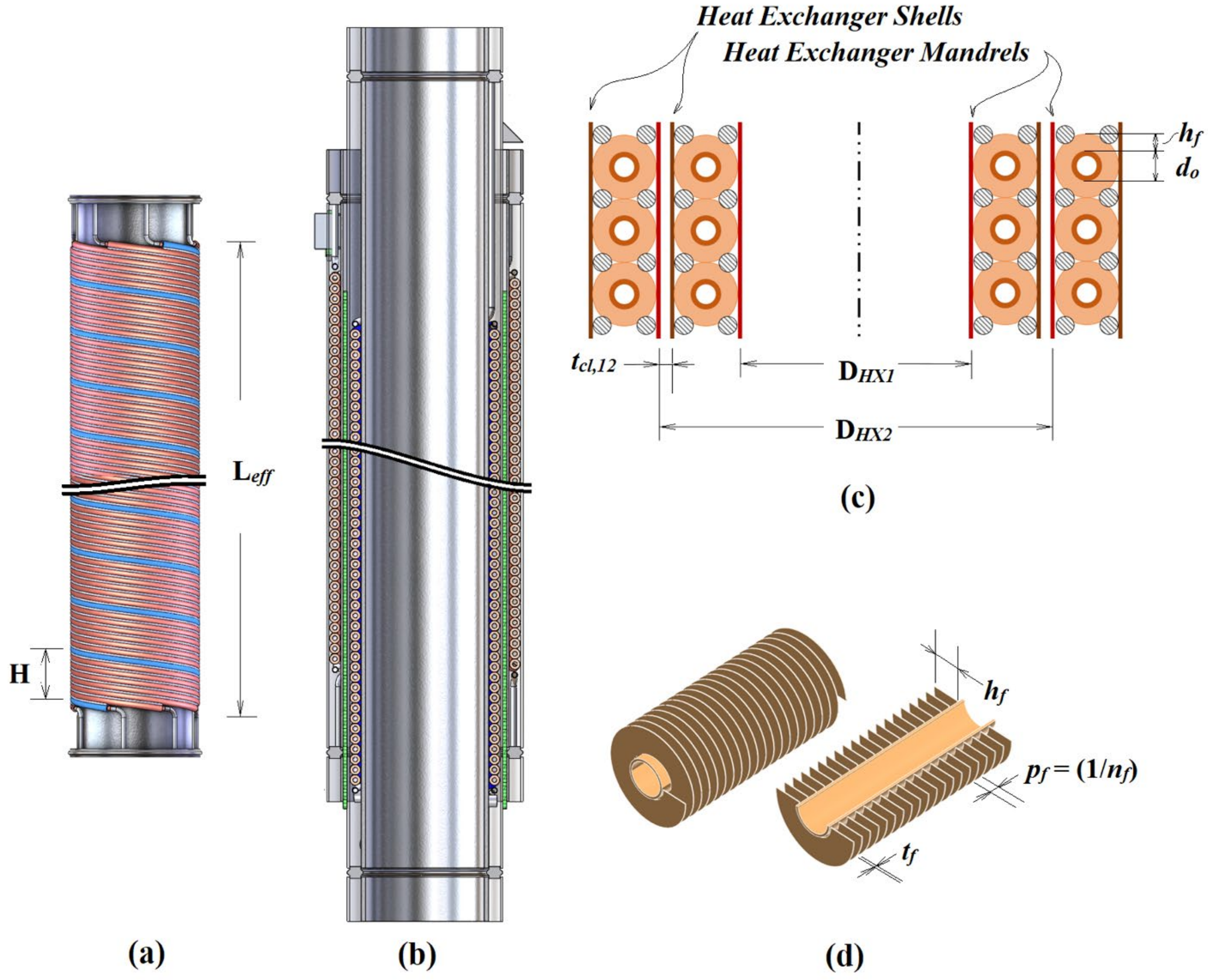

Figure 6-2 Schematic representation of (a) HX-1 showing parallel finned-tube passes (blue line represents one single pass of helically wound finned-tube), (b) overall heat exchanger assembly cross-section showing HX-2 nested inside HX-1 (c) cross-section of freeze

Multi-pass, helically coiled, finned-tube heat exchangers (HX-1 and HX-2) are considered in this study. Detailed schematic views of the freeze-out heat exchanger design considered in this study are shown in Figure 6-2. For heat exchanger geometrical compactness and to aid the moisture removal process during regeneration of the purifier, the heat exchange process is split into two parts, HX-1 and HX-2. Each heat exchanger consists of a mandrel (diameter, D) with helically wound parallel finned tube passes wrapped over it (refer to Figure 6-2 (a)). The contaminated helium stream (*he,c*) flows over the finned tubing, providing ample surface area for frost deposition. This flow is confined by a cylindrical shell mounted over the mandrel and helically wound finned-tube assembly. Additionally, there is a sealing rope which directs the gas flow over the fins by filling in any gaps between cylindrical tubes. Within the heat exchangers, the contaminated helium stream (*he,c*) is cooled by the purified helium stream (*he,p*) and saturated nitrogen vapor stream (*n,r*) from the LN vessel flowing through the finned-tubes. Coiled finned-tube type heat exchangers are relatively simple in construction, while providing a relatively large surface area per unit volume (high compactness) and mechanical flexibility to resist stresses developed from frost deposition on the heat exchanger surfaces and for the regeneration thermal cycles. In addition, they are less susceptible to flow mal-distribution resulting from flow blockage due to ice buildup. The axial design of the shell-side distributes the flow evenly, including inherent adjustments during operation to affirm this more even distribution.

HX-2 is nested physically within HX-1 (refer to Figure 6-2 (b) and Figure 6-2 (c)) and is designed to act solely as a (partial) refrigeration recovery heat exchanger. HX-1 is primarily designed to capture the frost. The entire heat exchanger sub-assembly (HX-1 and HX-2) is mounted vertically in the helium purifier in such a way that the contaminated helium stream enters the bottom of HX-1 and leaves at the top, then going over to the top of HX-2 and leaving at the bottom. In this way, during regeneration (warm-up), the moisture will flow towards the more contaminated section of HX-1 and is assisted by gravity.

The contaminated helium stream (*he,c*) coming out of HX-2 is further cooled using helically-wound tube coils (LNHX) submerged in liquid nitrogen. The rest of the contaminants (*i.e.*, constituents of air) are removed by the (LN cooled) activated carbon adsorber bed. The purified helium stream (*he,p,2*) and the nitrogen stream (*n,r,2*) coming out of the warm end of HX-1 is cooler than the contaminated helium stream (*he,c,2*) going in to HX-1 (due to the ineffectiveness of the heat exchanger), creating a temperature difference at the warm end. The heat absorbed from the surrounding to raise these stream temperatures to the ambient temperature (*i.e.* 300 K) is given by $q_{he,p}$ and $q_{n,r}$ respectively. There are heat dissipation terms, as the purifier outputs and helium input are assumed to be 300 K. All these heat exchange to the surrounding is accounted for in the exergy analysis of the purifier system and thus contribute to the overall exergetic efficiency of the system. Further details on the mechanical design of this helium purifier construction is discussed in [2].

Table 6-1 List of process parameters considered in this study

Parameter	**Value**	**Unit**
Helium mass flow rate, $\dot{m}_{he}$	30.0	g/s
Contaminated stream inlet pressure, $p_{he,c,1}$	10.0	bar
Nitrogen stream outlet pressure, $p_{n,s,1}$	1.05	bar
Purified helium stream outlet temperature, $T_{he,p,1}$	300.0	K
Contaminated helium stream inlet temperature, $T_{he,c,1}$	300.0	K
Vapor nitrogen stream outlet temperature, $T_{n,r,1}$	300.0	K
Inlet volume fraction of moisture in Contaminated Stream, $\dot{v}_{H2O,in}$	10.0	ppm_v
Amount of moisture (frost) collected, m_f	1.0	kg

The objective of this study is to find the exergetically optimum design parameters, consisting of the number of parallel coiled finned-tube passes, N_p and mandrel diameter, D, for both heat exchangers (HX-1 and HX-2), with a constant total shell-side surface area ($A_{S,S}$), a specific finned-tube element, and under a given range of process conditions. The process conditions considered for this study are provided in Table 6-1. The subscripts refer to the stream and temperature levels following the convention described earlier in this section. Note that the temperatures listed at 300 K are all at level one in Figure 6-1. This is an assumption of the analysis, accounting for heat dissipation through warm (300 K atmosphere) piping.

6.2 Development of a Process Model for Freeze-Out Helium Purifier

6.2.1 *Geometrical Modeling of the Heat Exchanger*

The thermal and hydrodynamic model of the freeze-out heat exchanger is developed considering helium as a perfect ideal gas (*i.e.*, constant specific heat), and following the methodology described by Yuksek [3]. Table 6-2 lists all the geometrical parameter values for the finned-tube element that is considered in this study. These dimensions are also described in Figure 6-2 (c) and Figure 6-2 (d).

Table 6-2 List of geometrical parameters for finned tubing considered in this study (values in parentheses are in US customary units)

Parameter	**Value**	**Unit**
Tube outside diameter, d_o	12.7 (0.500)	mm (*in.*)
Tube thickness, t_t	1.25 (0.049)	mm (*in.*)
Fin height, h_f	4.78 (0.188)	mm (*in.*)
Fin thickness, t_f	0.51 (0.020)	mm (*in.*)
Fin density, n_f	0.472 (12)	fins/mm (*fins/in.*)

Considering the finned-tube geometry provided in Table 6-2, heat exchanger geometrical parameters are calculated for a given total (HX-1 and HX-2) shell-side surface area ($A_{S,S}$). The number of parallel coiled finned-tube passes in HX-2 is given by $N_{p,HX2}$. This is one of the variables for the exergetic optimization problem. Number of parallel coiled finned-tube passes in HX-1 ($N_{p,HX1}$) is obtained from the following equation -

$$N_{p,HX1} = N_{p,HX2} + N_{p,N} \tag{6.1}$$

Here, $N_{p,N}$ is the number of parallel finned-tube passes for vapor nitrogen stream (HX-1 only, HX-2 does not have finned-tube passes for a vapor nitrogen stream, refer to Figure 6-1). The stream capacity of the vapor nitrogen stream is significantly less than that for the helium stream as specific heat at constant pressure, c_p for gaseous helium is approx. five times higher than that for vapor nitrogen. Also, the helium flow rate is significantly greater than that for vapor nitrogen. Altogether, the refrigeration capacity of the vapor nitrogen stream is insignificant compared to of the purified helium stream and hence, $N_{p,N}$ is kept constant ($N_{p,N} = 2$) in this study (enough to avoid any significant frictional pressure losses in the tubing).

The mandrel outside diameter in HX-2 is given by D_{HX2}. This is the other variable for the exergetic optimization problem. The mandrel outside diameter of HX-1 (D_{HX1}) is obtained from the following equation -

$$D_{HX1} = D_{HX2} + 2\left(t_{HX1} + t_{HX2} + t_{cl,12} + d_f\right) \tag{6.2}$$

Here, the mandrel shell thicknesses for both heat exchangers (t_{HX1} and t_{HX2}) are considered to be schedule 10S [4]. Standard engineering dimensions corresponding to each of the mandrel diameter considered in this study are provided in Sec. 4 (Table 6-3). The parameter $t_{cl,12}$ refers to the radial clearance between the two heat exchangers (including HX-1 shell thickness and the clearance for vacuum insulation between the two heat exchangers). Considering practical fabrication clearances and spacing for multi-layered insulation (MLI) to avoid radiation heat in-leak (from HX-1 to HX-2), a constant value of 0.375 in. (approx. 9.52 mm) is considered for $t_{cl,12}$. The finned-tube diameter (d_f) calculated from the following equation -

$$d_f = d_o + 2h_f \tag{6.3}$$

Each finned-tube pass in the heat exchangers forms a helix with a helix height $H = d_f N_p$ (Here, N_p is the corresponding number of finned-tube passes in the heat exchanger) and helix length per turn, $L = \sqrt{H^2 + C^2}$. Here, C is the helix circumference and for the finned-tube wrapping, it is given by $\pi\left[D + d_f\right]$, where D is the corresponding mandrel outside diameter of the heat exchanger. The effective axial length of each exchanger (refer to Figure 6-2 (a)) is then calculated from the following equation –

$$L_{eff} = N_t H + d_f\left(N_p - 1\right) \tag{6.4}$$

Here, N_t is the total number of helix turns for each finned-tube pass with $N_t = (L/L_t)$ and L_t is the total length of finned-tube for each finned-tube pass. Effective length of both heat-exchangers are considered the same (*i.e.*, $L_{eff,HX1} = L_{eff,HX2}$) to keep the heat exchanger assembly compact. The total number of finned-tube turns for each heat exchanger (HX-1 or HX-2) can be calculated from $N_{tt} = (L_{eff}/d_f)$.

The shell-side average surface area in each heat exchanger is calculated using the total number of finned-tube turns in the heat exchanger, the mean coil diameter $\left[D + d_f\right]$, and the finned-tube element geometry. It is given by –

$$A_{S,S,HX} = \pi^2 N_{tt}\left[D + d_f\right] d_o \left[1 + 2n_f h_f \left(1 + \frac{h_f}{d_o}\right)\right] \tag{6.5}$$

The total length of finned-tube for each finned-tube pass in each heat exchanger (L_t) is calculated using equations 6.4 and 6.5, for specified values of the total heat exchanger shell-side surface area $\left(A_{S,S} = A_{S,S,HX1} + A_{S,S,HX2}\right)$, HX-2 mandrel diameter (D_{HX2}) and number of parallel coiled finned-tube passes ($N_{p,HX2}$). The shell-side free-flow cross-sectional area is calculated using:

$$A_{S,c} = 2\pi\left[D + d_f\right]h_f\left(1 - n_f t_f\right) \qquad 6.6$$

The shell-side hydraulic diameter is given by $d_{S,h} = \frac{4A_{S,c}}{(A_{S,S,HX/L_{eff}})}$.

The tube side average surface area (total) in each heat exchanger is calculated using:

$$A_{t,S} = N_{tt}\pi^2\left[D + d_f\right](d_o - 2t_t) \qquad 6.7$$

And the tube side free-flow cross-sectional area (total) in each heat exchanger is calculated using:

$$A_{t,C} = N_p \frac{\pi}{4}(d_o - 2t_t)^2 \qquad 6.8$$

6.2.2 *Heat Transfer Model*

For each heat exchanger (HX-1 and HX-2), the net thermal ratings (UA) are calculated using the following equation –

$$(UA) = \left[\frac{1}{\sum h_t A_{t,S}} + \frac{\ln\left({}^{d_o}/_{d_i}\right)}{2\pi N_p L_t k_t} + \frac{1}{\eta_o h_S A_{S,S,HX}}\right]^{-1} \qquad 6.9$$

Here, h_t and h_S are the tube-side and shell-side convective heat transfer coefficients in the heat exchangers respectively, k_t is the thermal conductivity of the tube material (*copper*), and d_i is the tube inside diameter. The fin efficiency (η_o) is calculated following [5] for circular / helical fins.

For helically wound coiled finned-tube heat exchangers, the tube-side heat transfer coefficient (h_t) and pressure drop (Δp_t) are obtained following Gupta *et al.* [6].

$$h_t = \frac{Nu_t \cdot k_f}{d_i} \tag{6.10}$$

$$Nu_t = \begin{cases} 4.36B_{q,t}; Re_t < 3000 \\ 0.023B_{q,t}{Re_t}^{0.8}Pr^{0.33}; Re_t \geq 3000 \end{cases} \tag{6.11}$$

$$\Delta p_t = 4f_t \cdot \left(\frac{L_t}{d_i}\right) \cdot \left(\frac{G_t^2}{2\rho}\right) \tag{6.12}$$

$$f_t = \begin{cases} \left(\frac{16}{Re_t}\right)B_{p,t}; Re_t < 3000 \\ 0.071B_{p,t}{Re_t}^{-0.23}; Re_t \geq 3000 \end{cases} \tag{6.13}$$

Here, G_t is the tube-side mass flux ($G_t = \dot{m}/A_{t,C}$), Re_t is the tube-side flow Reynolds number ($Re_t = G_t d_i/\mu$), $B_{q,t}$ and $B_{p,t}$ are the heat transfer and pressure drop correction factors for Dean vortices [7-9] and are given by –

$$B_{q,t} = 1 + 3.6\left[1 - \frac{d_i}{D + d_f}\right]\left(\frac{d_i}{D + d_f}\right)^{0.8} \tag{6.14}$$

$$B_{p,t} = 1 + 7.5\left(\frac{d_i}{D + d_f}\right) \tag{6.15}$$

The shell-side heat transfer coefficient (h_S) and pressure drop ($\Delta p_{S,h}$) are calculated following Howard *et al.* [10].

$$h_S = \frac{Nu_S \cdot k_f}{d_{S,h}} \tag{6.16}$$

$$j_S = \begin{cases} 0.4019 \cdot {Re_S}^{-0.5393} \cdot \lambda_f^{0.057}; Re_S < 3000 \\ 0.0584 \cdot {Re_S}^{-0.3044} \cdot \lambda_f^{0.057}; Re_S \geq 3000 \end{cases} \tag{6.17}$$

$$\Delta p_{S,h} = 4f_S \cdot \left(\frac{L_{eff}}{d_{S,h}}\right) \cdot \left(\frac{G_S^2}{2\rho}\right) \tag{6.18}$$

$$f_S = \begin{cases} 0.6094 \cdot {Re_S}^{-0.6017} \cdot \lambda_f^{0.758}; Re_S < 2000 \\ 0.0139 \cdot {Re_S}^{-0.1009} \cdot \lambda_f^{0.758}; Re_S \geq 2000 \end{cases} \tag{6.19}$$

Here, G_S is the shell-side mass flux ($G_S = \dot{m}/A_{S,c,min}$), Re_S is the shell-side flow Reynolds number ($Re_S = G_S d_{S,h}/\mu$), j_S is the shell-side Colburn factor ($Nu_S/Re_S \cdot \mathrm{Pr}$) and λ_f is a fin geometry factor $\left[h_f/\left(p_f - t_f\right)\right]$. ρ and μ are the fluid density and viscosity evaluated at the mean fluid temperatures.

The heat exchanger total NTU is calculated using $NTU = UA/C_{min}$. Here, C_{min} is the minimum of the stream capacity ($\dot{m}c_p$) of the heat exchanger fluid streams. The heat exchanger NTU per turn is calculated from $NTU_t = NTU/N_{tt}$. The heat exchanger effectiveness per turn is calculated using the following equation [3] –

$$\varepsilon_t = \begin{cases} \dfrac{1}{C_r}\left[1 - e^{-C_r\left(1-e^{-NTU_t}\right)}\right]; \text{when tube stream capacity is minimum.} \\ 1 - e^{-\frac{1}{C_r}\left(1-e^{-C_r NTU_t}\right)};\ \text{when shell stream capacity is minimum.} \end{cases} \tag{6.20}$$

Here, $C_r = C_{min}/C_{max}$. For helically wound coiled finned-tube heat exchangers, the effectiveness correction factor, Y (for multiple tube passes) and the overall heat exchanger effectiveness, ε are given by [3, 11] –

$$Y = \frac{1 - \varepsilon_t}{1 - C_r \varepsilon_t} \tag{6.21}$$

$$\varepsilon = \frac{1 - Y^{N_{tt}}}{1 - C_r Y^{N_{tt}}} \tag{6.22}$$

Shell-side stream outlet temperature ($T_{he,c,j}$) for both the heat exchangers are calculated from their respective effectiveness, using the following –

$$T_{he,c,j+1} = T_{he,c,j} - \varepsilon \cdot \left(\frac{C_{min}}{C_S}\right) \cdot \left(T_{he,c,j} - T_{he,p,j+1}\right) \tag{6.23}$$

For the sake of simplicity of the model, tube-side outlet temperature of vapor nitrogen stream (HX-1) is considered to be equal of that for the purified helium stream (*i.e.* $T_{n,r,2} = T_{he,p,2}$). The tube-side stream outlet temperature ($T_{he,p,2}$) for HX-1 is obtained by a control volume energy balance equation around the heat exchanger. However, this equation is implicit in $T_{he,p,2}$ and hence solved by iterative process. Since both heat exchangers are connected in series – process conditions (pressure and temperature) from one are affected by the other. Hence, the overall assembly process is also solved by iteration (successive substitution).

The temperature distributions within the heat exchangers are calculated using the stream inlet / outlet temperatures, following [11]. Each heat exchanger (HX-1 and HX-2) is sub-divided into a specific number of sections (M) of equal NTU $(\Delta NTU = NTU_{HX}/M)$. The shell-side temperature distribution is estimated with an (assumed) equal temperature ratio (T_r) profile across the sub-divisions. Here the temperature ratio, T_r is given by –

$$T_r = \left(\frac{T_{he,c,j}}{T_{he,c,j+1}}\right)^{-\frac{1}{M}} \qquad 6.24$$

The shell-side temperature at any point $(i + 1)$ within the heat exchanger is calculated using $T_{he,c,i+1} = T_{he,c,i}T_r$. Here, the index i refers to intra heat exchanger temperature levels (of sub-divisions), while j is the index for inter component temperature levels in the purification system. The tube-side unknown temperature is then sequentially solved (from $i = 1 \; to \; M$) using control volume energy balance for each sub-division. The pressure drop across each stream (shell-side and tube-side) is assumed to be equally distributed.

This temperature profile is used as an initial estimate. From here, the temperature profile along the length of the heat exchanger is calculated using the method outlined in section 5.2 using an iteratively guessed and corrected outlet temperature of the HX-1 high side, incorporating resistances through the tubes, fluids, and frost. These two methods are iteratively solved until the temperatures and NTUs match. The frost deposition profile was similarly assumed to follow the partial pressure curve as defined in chapter 5.

6.2.3 *Mass Transfer Model*

Frost accretion on the finned tube (shell-side) surface is a complex phenomenon, and is affected by several process parameters (*e.g.* process fluid, operating pressure, moisture mass fraction) [12-14]. For the initial exergetic optimization, the frost accretion and associated pressure drop is approximated considering the following assumptions –

(a) Frost is deposited only at the crevice between two circular fins (see Figure 6-3), as a porous layer with variable volume fraction (α_f) along the axial length of the heat exchanger.

(b) The frost layer thickness is uniform along the axial length of the heat exchanger and is equal to $(p_f - t_f)$, *i.e.*, the gap between two successive fins.

(c) The frost volume fraction (α_f) is a function of the local mass transfer rate at the (shell-side) surface of the heat exchanger.

(d) The mass transfer (from contaminated helium stream to the shell-side heat exchanger surface) coefficient follows Chilton-Colburn analogy with a calculated Lewis number.

(e) The quantity of moisture in the contaminated helium stream is significantly low, such that the moisture mass fraction (w) and the absolute humidity (ω) are practically the same. These two parameters are used interchangeably in this paper.

(f) The frost accretion / mass transfer takes place only if the contaminated helium stream becomes super-saturated in moisture, *i.e.*, if the localized moisture mass fraction in the contaminated helium stream (ω_i) becomes greater than the saturated mass fraction at the local shell-side temperature $(\omega_{sat,i})$.

The total (shell-side) volume available within HX-1 for frost accretion can be calculated from the following equation –

$$V_{S,f} = N_p \cdot \left(\frac{\pi}{4}\right) \cdot \left(d_f^2 - d_o^2\right)\left(1 - n_f t_f\right) L_t \qquad 6.25$$

At the inlet to HX-1 (contaminated helium stream, he, c), the mass fraction and the mass flow rate of the moisture is given by –

$$\omega_{in,1} = 1 - \frac{1}{\left(\frac{M_{H2O}}{M_{He}}\right) \cdot \left(\frac{v_{H2O,in}}{10^6}\right) + 1} \tag{6.26}$$

$$\dot{m}_{H2O,in,1} = \dot{m}_{he}\omega_{in,1} \tag{6.27}$$

Here, $v_{H2O,in}$ is the volume fraction of moisture (ppm$_v$) at HX-1 inlet. M_{H2O} and M_{He} are the molecular weights of moisture (water) and process gas (helium) respectively. For the i^{th} sub-division within HX-1, the mass transfer rate and localized moisture fraction are calculated from the following set of equations –

$$\omega_{sat,i} = \left(\frac{M_{H2O}}{M_{He}}\right) \cdot \frac{1}{Z_i} \cdot \left(\frac{p_{v,sat,i}}{p_i - p_{v,sat,i}}\right) \tag{6.28}$$

$$\dot{m}_{H2O,in,i} = \dot{m}_{H2O,out,i-1} \tag{6.29}$$

$$\dot{m}_{f,i} = \begin{cases} \rho_{He,i} \cdot \left(dA_{S,S,HX1}\right) \cdot h_{m,i} \cdot \left(\omega_{in,i} - \omega_{sat,i}\right); \; \left(\omega_{in,i} - \omega_{sat,i}\right) > 0 \\ 0; \; \left(\omega_{in,i} - \omega_{sat,i}\right) \leq 0 \end{cases} \tag{6.30}$$

$$\dot{m}_{H2O,out,i} = \dot{m}_{H2O,in,i} - \dot{m}_{f,i} \tag{6.31}$$

$$\omega_{out,i} = \frac{\dot{m}_{H2O,out,i}}{\dot{m}_{he}} \tag{6.32}$$

$$\omega_{in,i+1} = \omega_{out,i} \tag{6.33}$$

Here, Z, p and ρ_{He} are the localized compressibility factor, pressure and density for the process gas (helium) at the sub-division conditions. $p_{v,sat}$ is the solid-vapor saturation pressure for moisture (water) evaluated at the local contaminated helium stream temperature $\left(T_{he,c,i}\right)$. It is obtained from the correlation provided by Wexler [15]. $dA_{S,S,HX1}$ refers to the differential (shell-side) surface area of the sub-division. h_m is the localized mass transfer coefficient given by $(Sh \cdot D/d_{S,h})$. Sh is the Sherwood number obtained from Chilton-Colburn analogy and D is the binary diffusion coefficient of helium-moisture mixture. It is calculated following Fuller *et al.* [16].

Per the assumptions stated earlier, the volume fraction of the frost deposited is directly proportional to the localized rate of mass transfer. It is calculated based on equation 6.34.

$$\alpha_{f,i} = C \cdot \frac{\dot{m}_{f,i}}{\max\limits_{1 \le i \le M} \left| \dot{m}_{f,i} \right|} \tag{6.34}$$

Here, C is a constant that governs the total (frost) mass accumulation. For a total required (frost) mass of m_f, the value of C can be calculated from –

$$C = \frac{m_f}{\left[\frac{1}{NTU_{HX1}} \int_{i=1}^{i=M} \alpha_{f,i} dNTU \right] \cdot V_{S,f} \cdot \rho_{ice}} \tag{6.35}$$

Here, ρ_{ice} is the density of solid ice (917 kg/m^3) [12]. The corresponding pressure drop due to moisture accretion ($\Delta p_{S,f,i}$) in each sub-division is calculated from the Ergun equation [17, 18].

$$\Delta p_{S,f,i} = \left\{ \frac{180 \mu_i u_{s,i}}{d_p^2} \cdot \frac{\left(1 - \varphi_{f,i}\right)^2}{\varphi_{f,i}^3} + \frac{3.6 \rho_{He,i} u_s^2}{d_p} \cdot \frac{\left(1 - \varphi_{f,i}\right)}{\varphi_{f,i}^3} \right\} \cdot dl \tag{6.36}$$

Here, μ is the dynamic viscosity of the process gas (helium), $\varphi_{f,i}$ is the localized frost porosity and is equal to $(1 - \alpha_{f,i})$, u_s is the superficial flow velocity through the frost layer and d_p is the equivalent frost (particle) diameter. According to Libbrecht [19], frost accretion from dilute gas mixture and at cryogenic temperatures typically exhibit hexagonal shaped crystals. Cheikh and Jacobi [14] found the side of these hexagon varies from 0.2 – 0.5 mm. Hexagon with a side of 0.2 mm is assumed in this study, and the mean frost diameter is calculated following [18]. The total pressure drop in the shell-side of HX-1 is calculated from –

$$\Delta p_S = \Delta p_{S,h} + \sum_{i=1}^{i=M} \Delta p_{S,f,i} \tag{6.37}$$

For the study of the effects of fin density and mandrel diameter on heat exchanger performance and frost deposition, the frost deposition profile was assumed to be non-porous (with constant density) and follow the partial pressure curve as defined in chapter 5 (especially for comparison with test/simulation results).

6.2.4 *Liquid Nitrogen Vessel, Cooling Coils, and Adsorber Bed*

The liquid nitrogen vessel (LNHX, refers to Figure 6-1), consists of 10 parallel passes of helically coiled tubing ($d_{o,LN} = 12.7\,mm, d_{i,LN} = 10.9\,mm$) submerged in a bath of liquid nitrogen. The contaminated helium stream (*he,c*) coming out of HX-2 flows through the helically coiled tubing and is further cooled by the surrounding liquid nitrogen bath. The tube-side pressure drop and heat transfer coefficient of these cooling coils are calculated using Eqn. 6.10-6.15. The shell-side heat transfer coefficient is calculated using Kutateladze correlation for boiling heat transfer in liquid nitrogen [20]. The overall heat transfer coefficient is calculated using Eqn. 6.9. The outlet temperature of the contaminated helium stream from the cooling coils is calculated based on $\in -NTU$ equations.

The adsorber bed is considered to be maintained at a constant temperature (equal to the saturation temperature of the liquid nitrogen). The adsorber bed pressure drop is calculated from Ergun equation [17] with coconut shell activated carbon adsorbent. Based on the mechanical design of the adsorber bed and associated thermal intercepts, an external heat leak (q_{ex}) of approx. 200 W has to be absorbed in to the liquid nitrogen bath. The steady-state liquid nitrogen flow is based on the following energy balance equation –

$$\dot{m}_{LN} = \frac{q_{LNHX} + q_{ex}}{\{h_{in,LN} - h_{sat}(p_{LN})\}} \tag{6.38}$$

Here, q_{LNHX} is the duty of the cooling coils, $h_{in,LN}$ is the supply enthalpy of the liquid nitrogen stream (assumed to be equal to saturated liquid enthalpy of nitrogen at 1.50 bar) and h_{sat} is the saturated liquid enthalpy of nitrogen at the LN vessel pressure (p_{LN}). The LN vessel pressure is obtained from the pressure drop (HX-1 tube-side for vapor nitrogen stream), and a vent pressure of 1.05 bar.

6.3 Effect of Design Parameters

6.3.1 *Initial Design of Reference Geometry*

A preliminary $\in -NTU$ analysis was carried out to achieve a minimum design heat exchanger effectiveness of 90%. For a given value of total shell-side surface area of the freeze-out heat exchanger, there are two parameters that are varied to find the optimal design, which is defined as the design which leads to minimal exergetic irreversibility. These are the number of parallel coiled finned-tube passes in HX-2 $(N_{p,HX2})$ and HX-2 mandrel outside diameter (D_{HX2}). The rest of the geometrical parameters are either held constant (refer to the parameters listed in Table 6-2) or are calculated from the optimization parameters mentioned above. Moreover, the total freeze-out heat exchanger shell-side surface area (HX-1 and HX-2 combined, $A_{S,S}$) is varied to investigate its effect on the optimized design. In total, 210 different designs are considered and analyzed using the process cycle model developed. Independent optimization parameters considered for these cases are listed in Table 6-3. The results from the process cycle analysis are discussed in the following sections.

A heat exchanger geometry with a total heat exchanger (HX-1 and HX-2) shell-side surface area $(A_{S,S})$ of 50 m^2, HX-2 mandrel diameter (D_{HX2}) of 10 NPS (273.1 mm) and 7 parallel coiled finned-tube passes $(N_{p,HX2})$ in HX-2 is arbitrarily selected from Table 6-3. This configuration is referred to as the *reference geometry* in the present and subsequent sections of this chapter.

Detailed thermal-hydraulic and exergetic analysis of the freeze-out purification system with the *reference geometry* is presented in this section.

The effective length (L_{eff}) of the heat exchangers with the *reference geometry* is approx. 1.90 m. The shell-side surface area $(A_{S,S,HX})$ for HX-1 and HX-2 are approx. 28.3 m^2 and 21.7 m^2 respectively. The total shell-side volume available for frost accretion $(V_{S,f})$ is approx. 0.018 m^3.

Table 6-3 List of parameters and corresponding values considered for the optimization

Optimization Parameters	***Values***
Total shell-side surface area of freeze-out heat exchanger (HX-1 and HX-2), $A_{S,S}$ [m^2]	42.5, 45, 50, 55, 57.5
Number of parallel coiled finned-tube passes in HX-2, $N_{p,HX2}$ [-]	4, 5, 6, 7, 8, 9, 10
HX-2 Mandrel outside diameter, D_{HX2} [NPS (mm)]	6 (168.3) 8 (219.1) 10 (273.1) 12 (304.8) 14 (355.6) 16 (406.4)

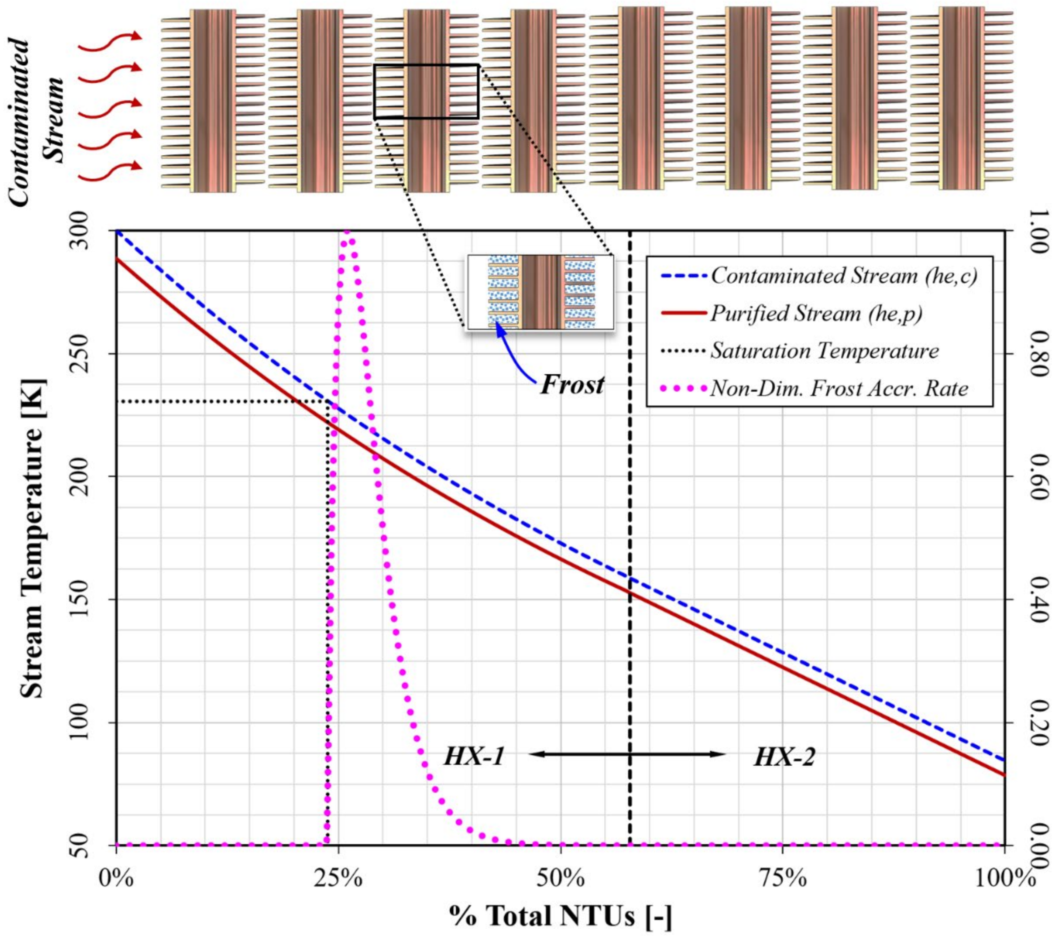

Figure 6-3 Calculated stream temperatures and non-dimensional frost accretion rate as a function of the total heat exchanger NTU fraction, with the reference geometry and the process conditions listed in Table 6-1; the assumed frost accretion volume is shown in the accompanying schematic

Calculated stream temperature profiles in HX-1 and HX-2, with the *reference geometry* and as a function of the total heat exchanger NTU fraction are shown in Figure 6-3. The process conditions corresponding to this figure are listed in Table 6-1. For both HX-1 and HX-2, the flow cross-sectional area is constant along the longitudinal axis (effective length, L_{eff}) of the heat exchangers. Hence, the fractional NTU (percent fraction of total NTU) is directly proportional to the length of the heat exchangers and can be used to represent the stream temperature profiles (as shown in Figure 6-3). The localized variation of the non-dimensional frost accretion rate ($\dot{m}_f/\dot{m}_{f,max}$) as obtained from Eqn. 6.30, and the solid-vapor saturation temperature of water (corresponding to the inlet moisture volume fraction) are also shown in this figure. It is observed that the frost accretion is localized to HX-1 and instead of being uniformly distributed over the coiled finned-tubes, it is highly localized.

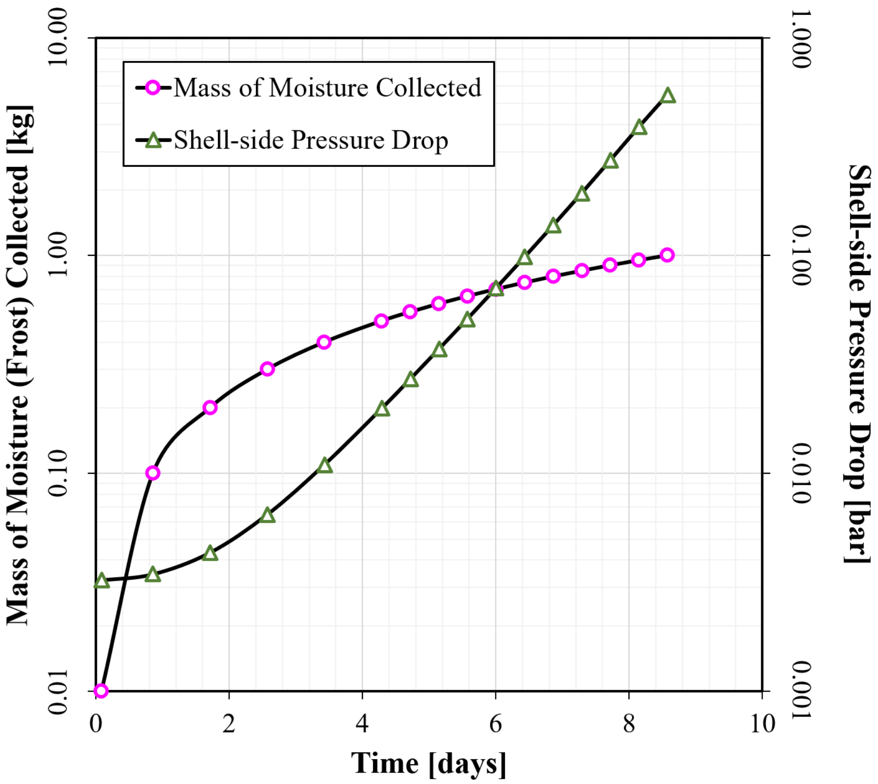

Figure 6-4 Temporal variation of total frost (mass) accumulation and corresponding HX-1 shell-side pressure drop, with the reference geometry

The localized accretion of frost over the heat exchanger shell-side flow is responsible for significantly larger frictional pressure drop in the shell-side of the heat exchanger (HX-1). The overall shell-side pressure drop can be obtained for different quantities of frost accumulation by solving Eqn. 6.34-6.36. For the process conditions listed in Table 6-1, the temporal variation of the total frost (mass) accumulation and the corresponding the shell-side pressure drop in HX-1 is shown in Figure 6-4. At the specified inlet moisture volume fraction, it takes approx. 8.5 days to accumulate 1.0 kg of frost, and the corresponding pressure drop in HX-1 is approx. 0.65 bar. This is considerably higher compared to the initial (*no-frost*) pressure drop of approx. 3.0 mbar.

The overall exergy consumption / utilization in this purification system with the *reference geometry* is shown in Figure 6-5 as Grassmann diagrams. Figure 6-5 (a) shows the total exergy input and output to and from the purification system. The overall exergetic efficiency of the purifier with the *reference geometry,* under the process conditions listed in Table 6-1 is found to be approx. 87.7%. It should be noted that; in a practical system – majority of the exergy losses (typically over 70%) are from the compressor used to pressurize and circulate the contaminated helium stream. However, it is not within the scope of the present study, and the performance parameters discussed (*e.g.*, exergetic efficiency, irreversibilities) are only for the purifier cold box system.

Figure 6-5 (b) shows the distribution of the purifier cold box exergy losses (irreversibilities). For the case discussed, HX-1 irrevesibility was found to be the largest contributor to the total. Exergy losses due to the frictional pressure drop in HX-1 shell side is a function of time (with frost accretion). For the steady-state analysis, a time averaged shell-side pressure drop is calculated following –

$$\Delta\bar{p}_{S,HX1} = \frac{1}{t_o}\int_{t=0}^{t=t_o} \Delta p_{S,HX1}\,dt \qquad 6.39$$

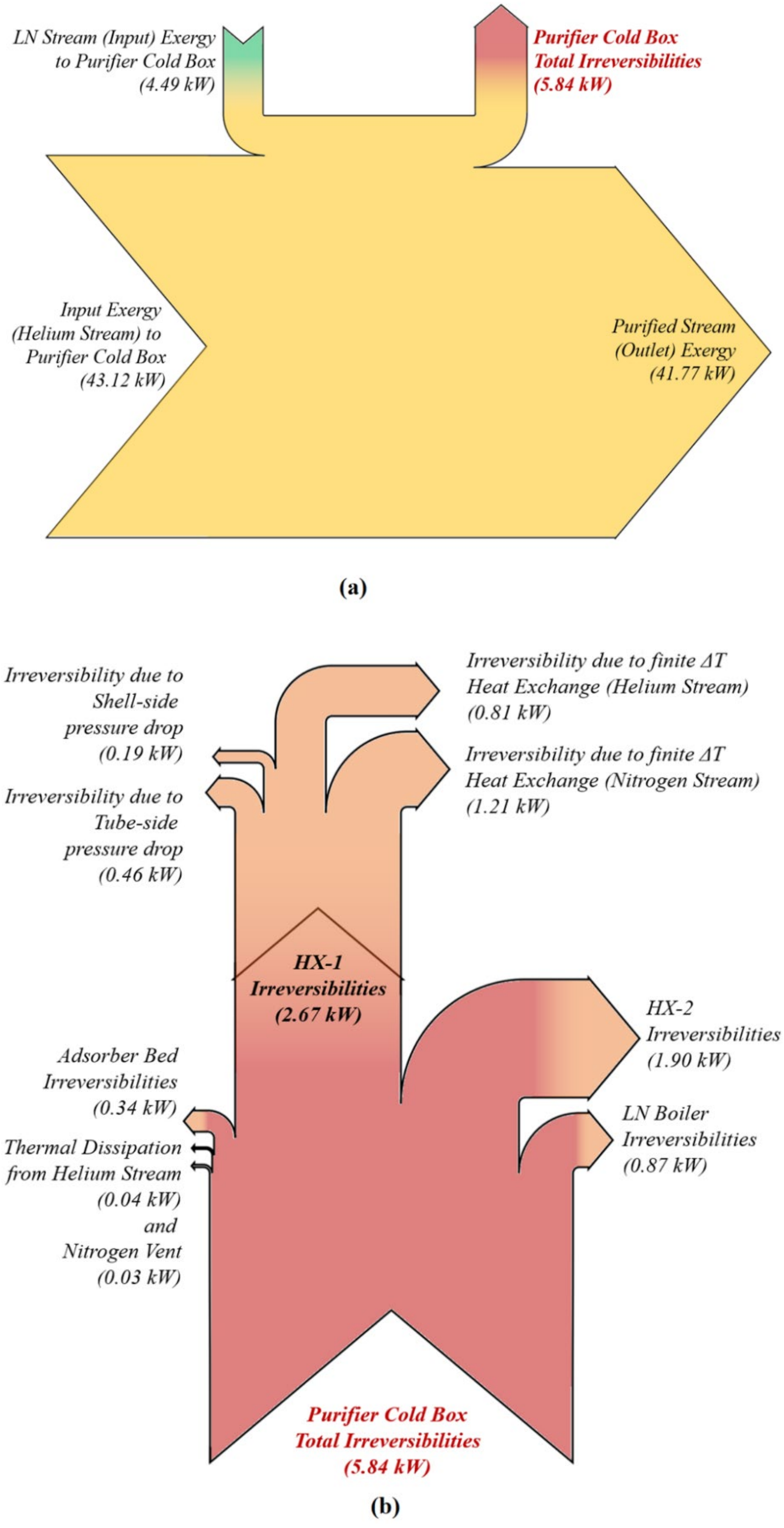

Figure 6-5 Grassmann diagrams of (a) total exergy flow and (b) distribution of exergy losses in the purifier cold box, with the reference geometry

A significant portion of the HX-1 irreversibility is observed to be due to the heat exchange between the vapor nitrogen stream (*n,r*) and the contaminated helium stream (*he,c*). This is primarily due to the larger temperature differential between the two streams. For both heat exchangers, the primary contributor to the exergy losses is due to heat exchange (*i.e.*, ineffectiveness of heat exchangers). This is also evident from Figure 6-5 (a) – as the LN stream (input) exergy is supplied to overcome the ineffectiveness of the heat exchange processes, and it is almost equal to the total irreversibility of the purifier cold box (*i.e.*, exergy losses due to frictional pressure drop is relatively smaller).

6.3.1.1 *Effect of Variation of Geometrical Parameters*

Thermal-hydraulic and exergy analysis for different values of HX-2 mandrel diameter (D_{HX2}), and no. of parallel tube-side passes ($N_{p,HX2}$) (as listed in Table 6-3), with a total heat exchanger shell-side surface area ($A_{S,S}$) of 50 m^2 were carried out first. Comparative performance analysis of these different geometries is discussed in this section.

The effective length (L_{eff}) of the heat exchangers (HX-1 and HX-2) is observed to be proportional to HX-2 mandrel diameter (D_{HX2}) only, for a given shell-side surface area. This dependency is also true for the shell-side surface area ratio of the two heat exchangers. The variation of the heat exchanger effective length (L_{eff}), and the shell-side surface area ratio ($A_{S,S,HX1}/A_{S,S,HX2}$) as a function of HX-2 mandrel diameter (D_{HX2}) is shown in Figure 6-6.

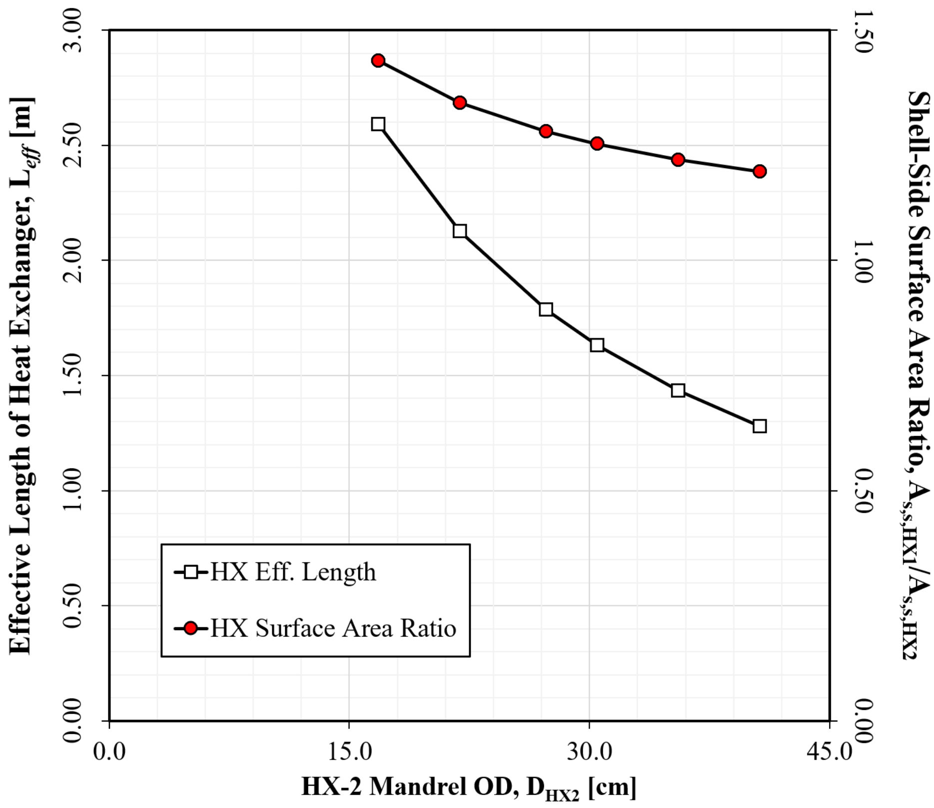

Figure 6-6 Variation of the heat exchanger effective length and the shell-side surface area ratio as a function of HX-2 mandrel diameter, with a total shell-side surface area of 50 m^2

Variation of the total irreversibility of the purifier cold box (I_{CBX}) as functions of the geometrical parameters ($N_{p,HX2}$ and D_{HX2}) with $A_{S,S} = 50\, m^2$ is shown in Figure 6-7. It is observed that there exists a combination of HX-2 mandrel diameter (D_{HX2}) and no. of parallel tube-side passes ($N_{p,HX2}$) in the range studied – for which the total purifier cold box irreversibility is minimum. This happens to be the *reference geometry* ($N_{p,HX2} = 7,\ D_{HX2} = 10\, NPS/273.1\, mm$) discussed in Sec. 5.1. It is also observed that the total purifier cold box irreversibility is maximum (in the range studied) for the minimum HX-2 mandrel diameter (D_{HX2}) and parallel tube-side passes ($N_{p,HX2}$).

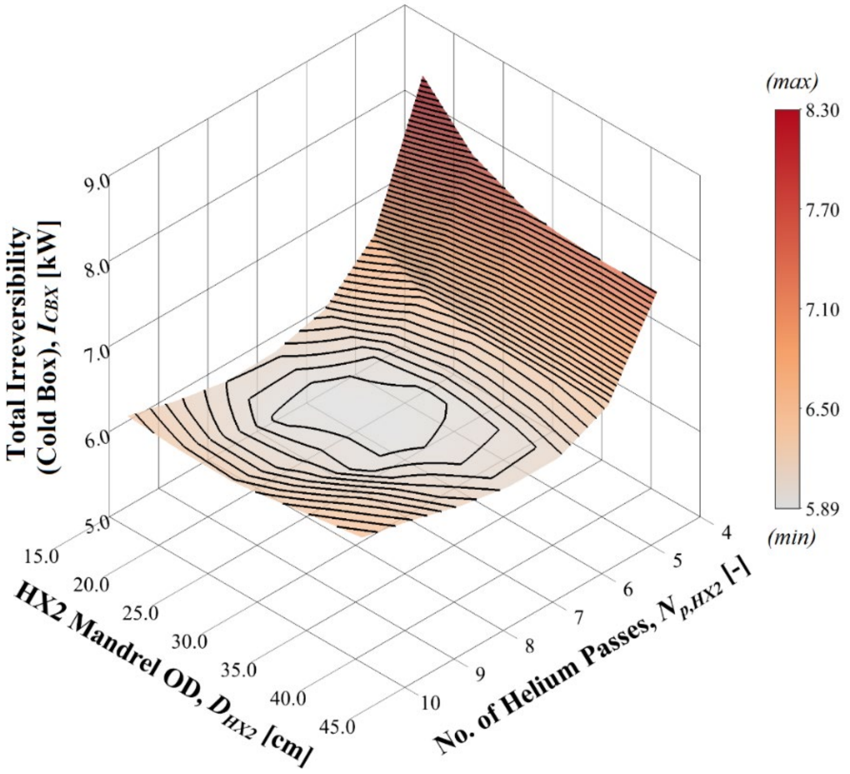

Figure 6-7 Variation of the total purifier cold box irreversibility as functions of the HX-2 mandrel diameter and no. of parallel tube-side passes, with $A_{S,S} = 50\ m^2$

Figure 6-8 presents the variation of the total heat exchanger (HX-1 and HX-2) NTU as a function of HX-2 mandrel diameter (D_{HX2}), with a total shell-side surface area ($A_{S,S}$) of 50 m^2. The combined NTU is observed to be varied within a range from approx. 21 to 38. It exhibits an inversely proportional relationship to both variable geometrical parameters. As $N_{p,HX2}$ is increased, the overall length of each finned tube pass decreases and the heat exchanger effectiveness (ε) is reduced. As D_{HX2} increases, both the effective length (L_{eff}) of the heat exchanger and the heat exchanger aspect ratio (L_{eff}/D_{HX2}) decreases (with a specific surface area). This causes a reduction in the heat exchanger effectiveness as well.

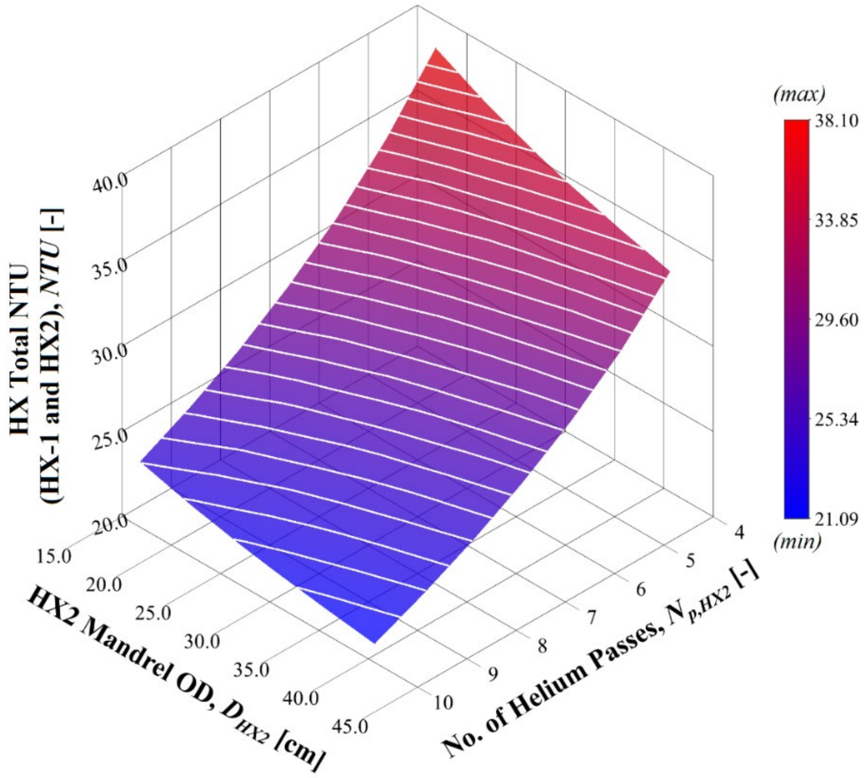

Figure 6-8 Variation of the total heat exchanger (HX-1 and HX-2) NTU as a function of HX-2 mandrel diameter, with a total shell-side surface area of 50 m^2

Figure 6-9 presents the variation of HX-1 irreversibility (I_{HX1}). as functions of the HX-2 mandrel diameter (D_{HX2}) and no. of parallel tube-side passes ($N_{p,HX2}$), with $A_{S,S} = 50\ m^2$. It shows that the HX-1 irreversibility follows the same general trend to the total purifier cold box irreversibility (see Figure 6-7). In both cases (Figure 6-7 and Figure 6-9), the maximum irreversibility is exhibited for the geometry with minimum $N_{p,HX2}$ and D_{HX2}. To understand this behavior, variation of HX-1 irreversibility is further decomposed into the component due to frictional pressure drop ($I_{HX1}^{\Delta p}$) and that due to finite temperature difference heat exchange ($I_{HX1}^{\Delta T}$) [21]. Variation of these components as function of the HX-2 mandrel diameter (D_{HX2}) and number of parallel tube-side passes $\left(N_{p,HX2}\right)$, with $A_{s,s} = 50m^2$ are shown in Figure 6-10a and Figure 6-10b, respectively.

The overall variation of HX-1 irreversibility (and by extension – the total purifier cold box irreversibility) can be explained in terms of the heat exchanger geometrical aspect ratio (L_{eff}/D_{HX2}). The overall pressure drop (both shell-side and tube-side) is directly proportional to this parameter. The heat exchanger effectiveness (ε) is also proportional to this parameter. For the geometry with minimum $N_{p,HX2}$, the tube-side pressure drops are very high (due to longer overall finned tube lengths to accommodate the same shell-side surface area) and vice versa. For the geometry with minimum D_{HX2}, the shell-side pressure drops are higher (due to the longer aspect ratio) and vice versa. But, the heat exchangers become highly effective with longer aspect ratio and irreversibility due to finite temperature heat exchange $(I_{HX1}^{\Delta T})$ is minimized (see Figure 6-10b). In general, the mean value of $I_{HX1}^{\Delta T}$ is greater. But it shows less numerical variance with varying $N_{p,HX2}$ and D_{HX2}. However, $I_{HX1}^{\Delta p}$ exhibits a strong dependence on these geometrical parameters. This is a result of the frost accretion process. Accumulation of the frost layer inhibits flow, increasing the shell-side pressure drop (see Figure 6-4). The overall pressure drop in HX-1 is also higher (compared to that in HX-2) due to the relatively warmer operating temperature (approx. 300-180 K). The algebraic combination of these two components $(I_{HX1}^{\Delta p}, I_{HX1}^{\Delta T})$ brings the minimum HX-1 irreversibility towards a point with relatively shorter aspect ratio.

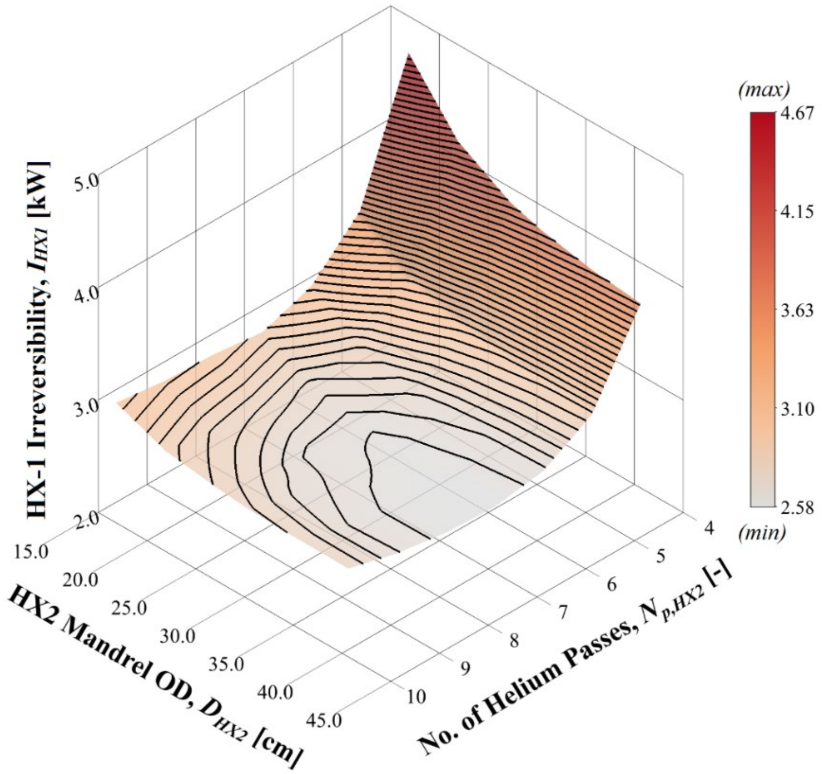

Figure 6-9 Variation of the HX-1 irreversibility as functions of the HX-2 mandrel diameter and no. of parallel tube-side passes, with $A_{S,S} = 50\ m^2$

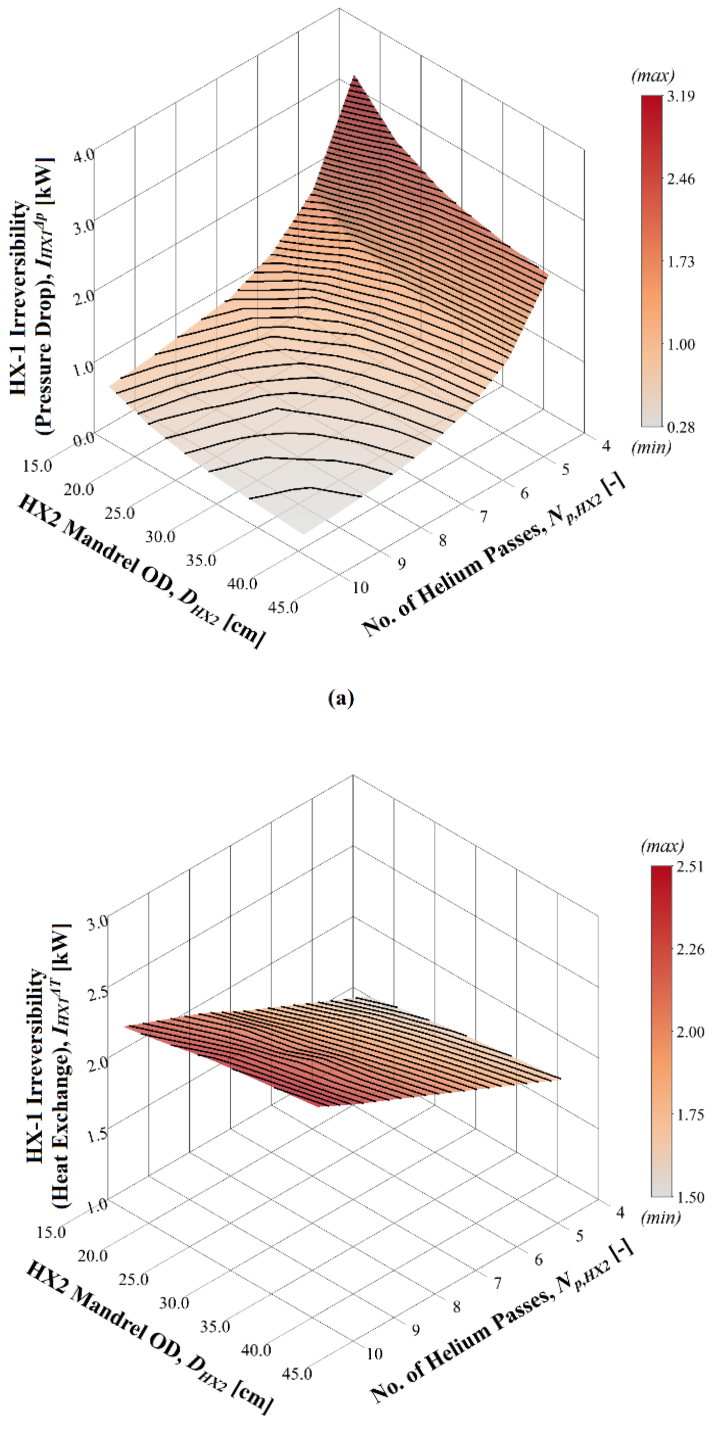

(a)

(b)

Figure 6-10 Variation of (a) frictional pressure loss component, and (b) finite temperature difference heat exchange component of HX-1 irreversibility as functions of the HX-2 mandrel diameter and no. of parallel tube-side passes, with $A_{S,S} = 50\ m^2$

Variation of HX-2 irreversibility with the two variable geometrical parameters ($N_{p,HX2}$ and D_{HX2}) with constant surface area is shown in Figure 6-11. The frictional pressure loss component ($I_{HX2}^{\Delta p}$) of the HX-2 irreversibility is found to be insignificant as there are no frost accretion in this heat exchanger (see Figure 6-3). The effective density of the contaminated helium stream is also greater (with relatively cooler operating temperatures) and the frictional pressure losses are not prominent. However, HX-2 operating temperature being cooler and cryogenic (approx. 180-80 K), even the slightest ineffectiveness in this heat exchanger has a significant effect on the overall irreversibility (as observed from Figure 6-11). Due to this factor, the minimum HX-2 irreversibility is found towards a point with longer aspect ratio. The overall purifier cold box irreversibility (I_{CBX}) is primarily an algebraic combination of these two (I_{HX1} and I_{HX2}). The design for the rest of the components is kept constant for this study and they have minimal impact on the variation of the total irreversibility. The minimum purifier cold box irreversibility is found at a point which neither corresponds to the longer nor the shorter aspect ratio for these heat exchangers (in the range studied).

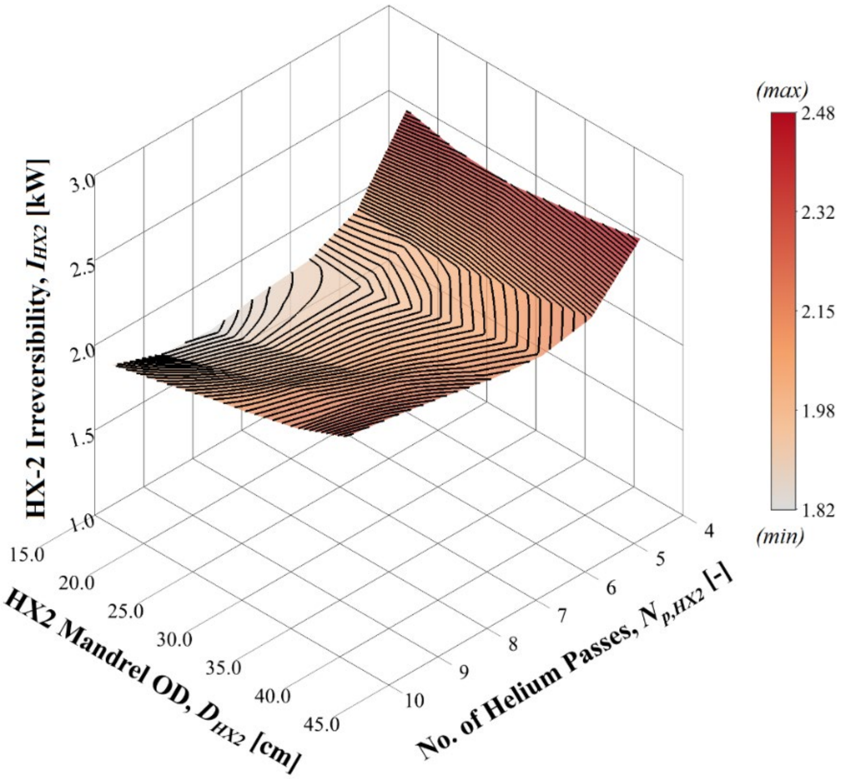

Figure 6-11 Variation of the HX-2 irreversibility as functions of the HX-2 mandrel diameter and no. of parallel tube-side passes, with $A_{S,S} = 50\ m^2$

6.3.1.2 *Effect of Variation of Shell-Side Surface Area*

The effect of variation of the total shell-side surface area ($A_{S,S}$) on the irreversibility of the purifier cold box was also studied. A shell-side surface area of $A_{S,S} = 50\ m^2$ has been used in the *reference geometry*. Four additional shell-side surface areas ($A_{S,S} = 42.5, 45, 55, 57.5\ m^2$) were considered for this study. Figure 6-12 (a and b) shows the variation of the total purifier cold box irreversibility as a function of the variable geometrical parameters ($N_{p,HX2}$ and D_{HX2}) for shell-side surface area of 42.5 m^2 and 57.5 m^2 respectively.

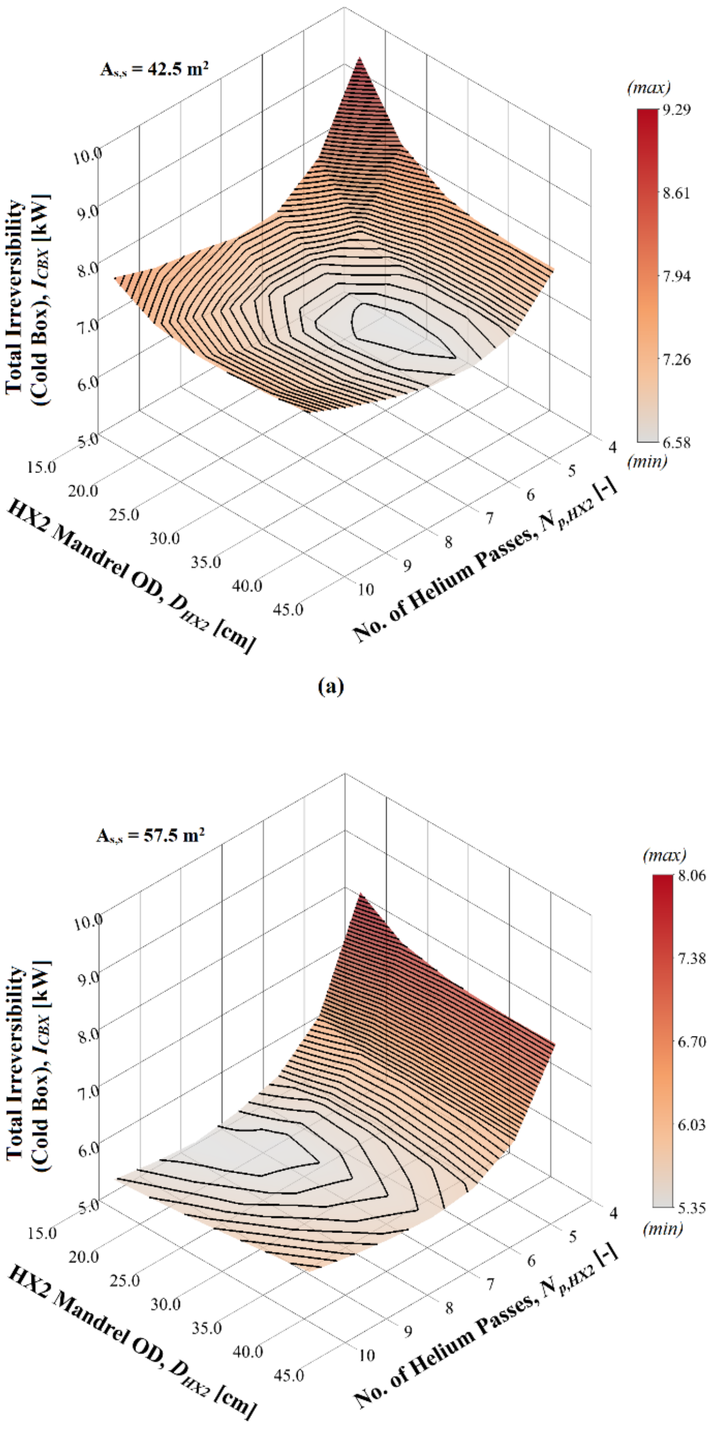

(a)

(b)

Figure 6-12 Variation of the total purifier cold box irreversibility as functions of the HX-2 mandrel diameter and no. of parallel tube-side passes, with (a) $A_{S,S} = 42.5\ m^2$ and (b) $A_{S,S} = 57.5\ m^2$

It is observed that, as the heat exchanger shell-side surface area ($A_{S,S}$) is increased, the heat exchanger effective length (L_{eff}) increases for the same combination of $N_{p,HX2}$ and D_{HX2}. This increases the frictional pressure loss component of the irreversibility, but even greatly reduces the finite temperature difference heat exchange component of the irreversibility. With increasing shell-side surface area for the heat exchangers, the optimal geometry (*i.e.*, one with minimum exergy losses) has increased no. of parallel tube-side passes ($N_{p,HX2}$) and a smaller HX-2 mandrel diameter (D_{HX2}).

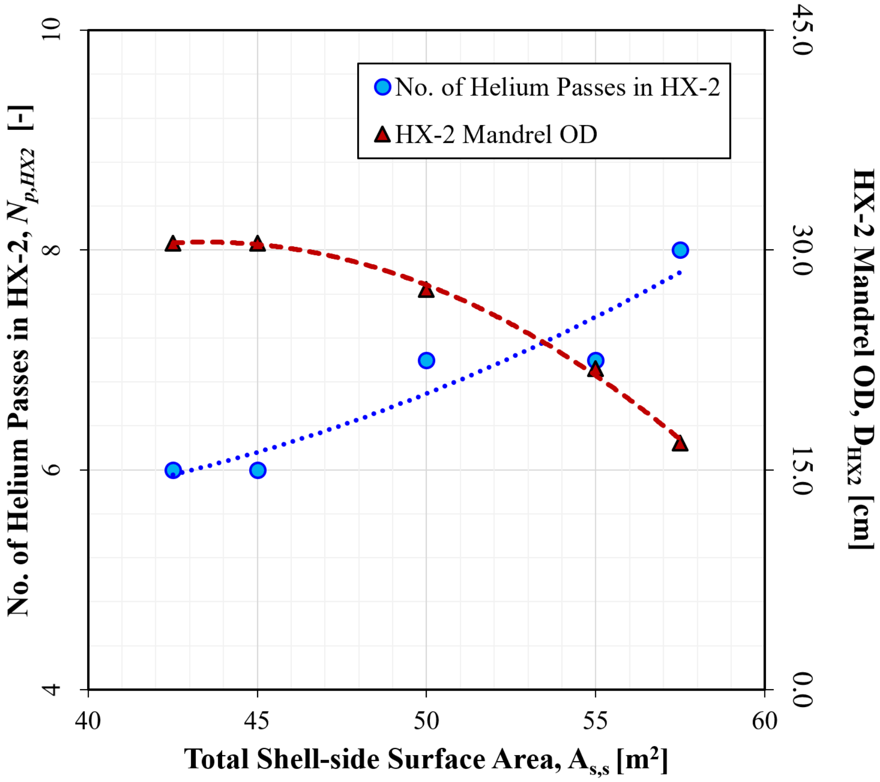

Figure 6-13 Variation of the optimal geometrical parameter combination with changing heat exchanger shell-side surface area

Figure 6-13 shows the variation of the optimal (*i.e.*, one with minimum exergy losses) geometrical parameter combination with changing heat exchanger shell-side surface area ($A_{S,S}$). As the shell-side surface area increases, the pressure drop due to frost accumulation decreases (larger available volume for the same frost mass accumulation over time). This reduces the irreversibility due to the shell-side pressure drop. Hence, the frictional pressure loss component of the irreversibility is dominated by the tube-side pressure losses. A greater no. of parallel tube-side passes tends to reduce the tube-side pressure losses. These effects combined, drives up the optimal $N_{p,HX2}$ with increasing shell-side surface area. Reducing the HX-2 mandrel diameter yields a much longer aspect ratio (L_{eff}/D_{HX2}) for the heat exchangers. This in turn greatly reduces the finite temperature heat exchange component of the irreversibility and the optimal D_{HX2} decreases with increasing shell-side surface area.

6.3.1.3 *Practical Considerations for Design*

Results discussed in Sec. 5.2 and 5.3 are solely from a theoretical aspect with the constraints provided in Table 6-1 and Table 6-2. However, in practice there are several additional constraints that may need to be considered. One of these constraints is geometrical. The effective length (L_{eff}) of the heat exchanger is a proportional function of the mandrel diameter (D_{HX2}) for a given shell-side surface area (see Figure 6-6). Based on size limitations of components and availability of space, there might be additional constraints on this length. Another important practical consideration for the heat exchanger design is the shell-side surface area distribution between HX-1 and HX-2. Since, HX-1 has the larger mandrel by design – the ratio ($A_{S,S,HX1}/A_{S,S,HX2}$) will always be greater than 1.0. A much larger HX-1 shell-side surface area would provide greater capacity for moisture accumulation. From that aspect, a smaller mandrel diameter (for a given shell-side surface area) may be desired. However, as discussed in Sec. 5.2, a smaller mandrel diameter would also yield a greater shell-side pressure drop in general. In this study, a time-averaged shell-side pressure drop is considered (Sec. 5.1) for the exergy analysis. But from the aspect of equipment operation and safety, a significantly larger shell-side pressure drop in the heat exchanger may not be desired even though it is transient. The maximum shell-side pressure drop (transient) in HX-1 variation for the cases studied with $A_{S,S} = 50\ m^2$ is shown in Figure 6-14. From this figure, it is also observed that increasing the no. of parallel tube-side passes ($N_{p,HX2}$) can also amplify the shell-side pressure drop as frost is collected. With $N_{p,HX2} = 4$, the heat exchanger effective length is longer and the frost is captured (relatively) uniformly over the length of the heat exchanger. Hence, the shell-side pressure drop remains relatively lower. On the other hand, with $N_{p,HX2} = 10$, the heat exchanger effective length is shorter and the frost is accretion is highly localized, thereby increasing the shell-side pressure drop significantly.

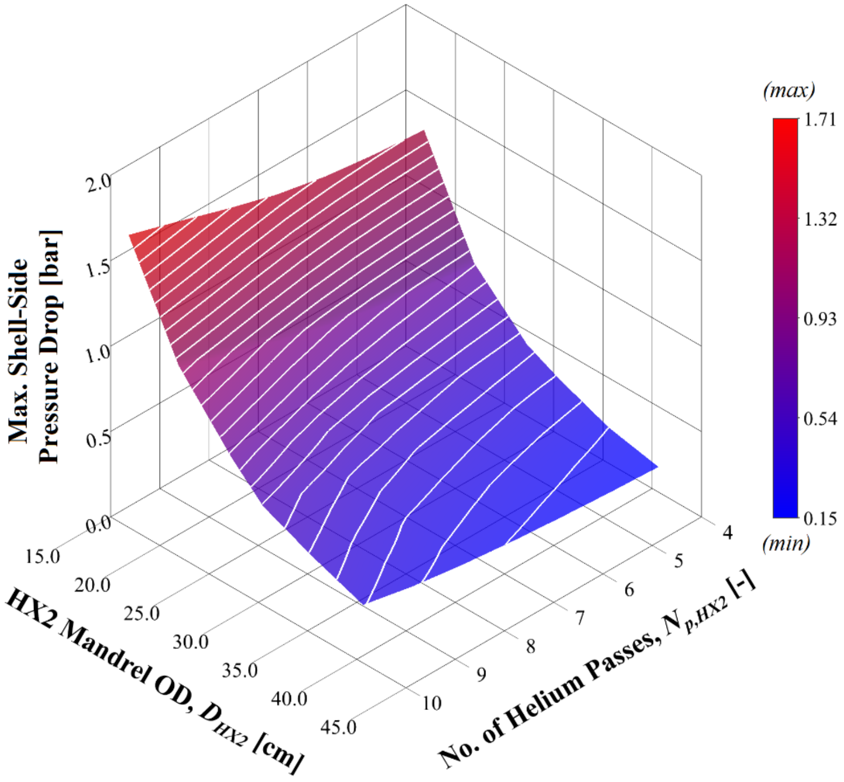

Figure 6-14 Variation of the maximum shell-side pressure drop in HX-1 as functions of the HX-2 mandrel diameter and no. of parallel tube-side passes, with $A_{S,S} = 50\ m^2$

Another practical consideration is the cost of operation. These costs come from the irreversibility (exergy losses) in the purifier. These losses have to be made up for by some input. The first loss is the irreversibility due to temperature difference, which for the optimal design case is 4.49 kW. This is caused by heat in-leaks and heat transfer resistance in the heat exchangers. The flow coming out of the heat exchanger is cooled down to the desired temperature in a liquid nitrogen bath. The amount of liquid nitrogen that boils off is the utility that makes up for the temperature difference in the purifier heat exchangers. The efficiency of liquefaction is typically ~37% [22]. This results in requiring 12.14 kW to recover these losses. The second loss is irreversibility due to pressure drop, which for the optimal design case is 1.35 kW. This is caused by friction in the flow path and greatly increased by frost accumulation. This flow is re-pressurized by a recovery compressor before entering the liquefaction cycle. The irreversibility is recovered by this compressor at its isothermal efficiency, which is typically ~45%. Given this efficiency, the total power needed to replace the irreversibility due to pressure drop is 3.00 kW. The total power needed to recover all irreversibilities in the purifier is 15.14 kW and the major part is for the liquid nitrogen.

This section establishes the exergetically optimal freeze-out heat exchanger, assuming a simplified frost deposition. For the process and design constraints considered, the optimized heat exchanger is found have a HX-2 mandrel diameter of 10 NPS (273.1 mm), and a 7 parallel helium tube passes, with a total heat exchanger shell-side surface area of 50.0 m^2. The next sections will focus on the heat exchanger performance and frost deposition, especially in comparison to the commercially available purifier tested and analyzed in chapters 3 and 5, respectively.

6.3.2 *Effect of Fin Density on Heat Exchanger Performance*

The effect of fin density on HX-1 performance and frost deposition over the course of the operation period were estimated using the process model. Fin density of HX-1 was chosen because it is a large difference in the design between this purifier and the commercial purifier discussed in chapters 3 and 5. It has no fins (tube-in-tube geometry), significantly reducing the surface area for heat exchange, but increasing the volume available for frost deposition. The test case used for comparison with this study is the 30 ppm base with a balanced heat exchanger. For the purposes of this study, HX-2 was held at a constant geometry, with 12 fins/in, to maintain maximum heat exchange where there is no frost deposition. The design of the purifier and its regeneration procedure relies on there being no frost in HX-2. It is important to note that for the comparison to the commercially available purifier, the entirety of the heat exchanger is potentially capable of collecting frost. In the finned-tube heat exchanger, only HX-1 is available to collect frost. This means that the NTU, surface area, and notably open volumes listed for the commercially available purifier is for the entire temperature range (300-80 K), whereas in the finned-tube purifier, they are only for HX-1, which spans from 300 K to between 222 and 147 K, depending on the geometry chosen. It was decided to compare HX-1 to the entire heat exchanger for the purposes of comparing frosting capabilities. HX-2 has a constant geometry between cases, with approximately 17.2 NTU, and no direct impact on nitrogen usage.

Table 6-4 lists the geometries studied, and the results of each at the beginning of the operating period, as well as the commercial purifier test data for reference. The test case chosen for comparison has 30 ppm moisture and an unbalanced heat exchanger. This case was chosen because the nitrogen usage is least when the heat exchanger is unbalanced, giving the most generous comparison. The mass of frost listed is assuming the cooling curves never shift, this is the maximum that could be collected. All cases were calculated using 14 in HX-1 mandrel OD.

The largest effects of increasing fin density is an increase in heat exchanger surface area and a decrease in open volume available for frost deposition. With more heat exchanger surface area, there will be more efficient heat exchange. This has two main impacts. First, less nitrogen usage. The function of the nitrogen is to make up for any temperature difference at the cold end of the heat exchanger, so a warmer high side outlet from HX-1 will result in more nitrogen usage. The second impact is temperatures being cooler result in the frost being deposited in a narrower range in HX-1. This reduces the capacity of the heat exchanger. When the fins are less dense (2 and 4 fins/in), the temperature gets so warm that the frosting temperature range extends to HX-2, resulting in frost depositing in HX-2, an unfavorable outcome. The more open volume available (with fewer fins), the more room there is for frost. This increases the maximum potential frost thickness and frost capacity of the heat exchanger by having more physical space.

The impacts of the heat exchanger surface area and open volume work against each other. With fewer fins, more mass can deposit, but heat exchange is less efficient resulting in more nitrogen usage (although notably still less than the commercial purifier with the exception of 2 fins/in). With 2 and 4 fins/in, this is taken to the extreme of depositing frost outside of HX-1. This is unacceptable. Therefore, 6 fins/in in the minimum fin density to maintain all the frost in HX-1. With more fins, less mass can deposit, but heat exchange is more efficient and less nitrogen is used.

It appears that with 6 fins/in, the mass deposited is approximately equal to or greater than most of the test cases, while maintaining the design condition of keeping the frost within HX-1, and keeping the design objective of using less nitrogen.

Table 6-4 Fin density study results, with commercial purifier test data

Fins/in	$A_{ss,\ total}$ [in^2]	V_{open} [in^3]	m_{frost} [g]	NTU [-]	$T_{ho,HX\text{-}1}$ [K]	$\dot{m}_{N2}$ [g/s]
Commercial purifier	18910	2399	549	15.9	N/A	4.01
2	11715	1311	851	7.2	222.2	4.14
4	17756	1256	926	11.4	189.9	3.70
6	23798	1201	627	14.8	171.1	3.33
8	29839	1147	451	17.4	159.8	3.09
10	35880	1092	342	19.3	152.6	2.94
12	41922	1038	272	20.8	147.8	2.83

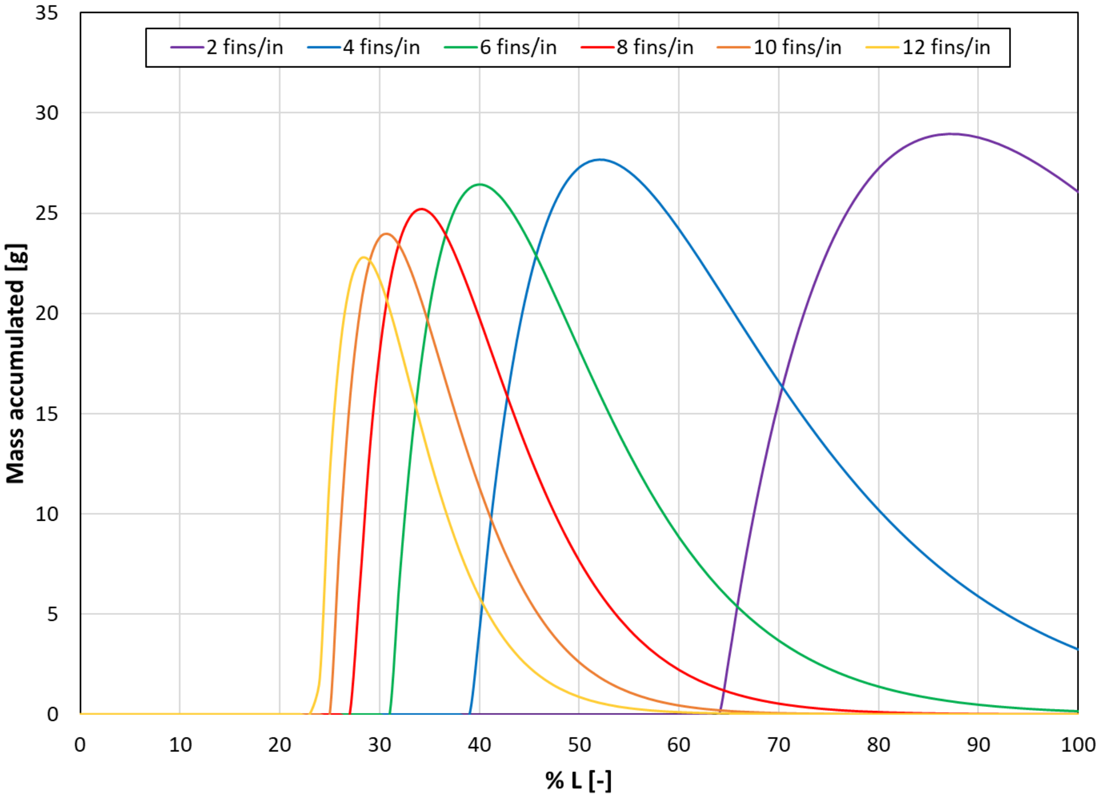

Figure 6-15 Fin density effect on frost deposition profile

Figure 6-15 shows the frost deposition profiles of the fin density cases. It illustrates how 2 and 4 fins/in continue depositing frost beyond HX-1, in HX-2. It also illustrates how the temperatures (shown for 2 and 12 fins/in in Figure 6-16) impact the frost deposition profile. A certain surface area in the heat exchanger is required to provide efficient enough heat exchange to keep the frost in HX-1.

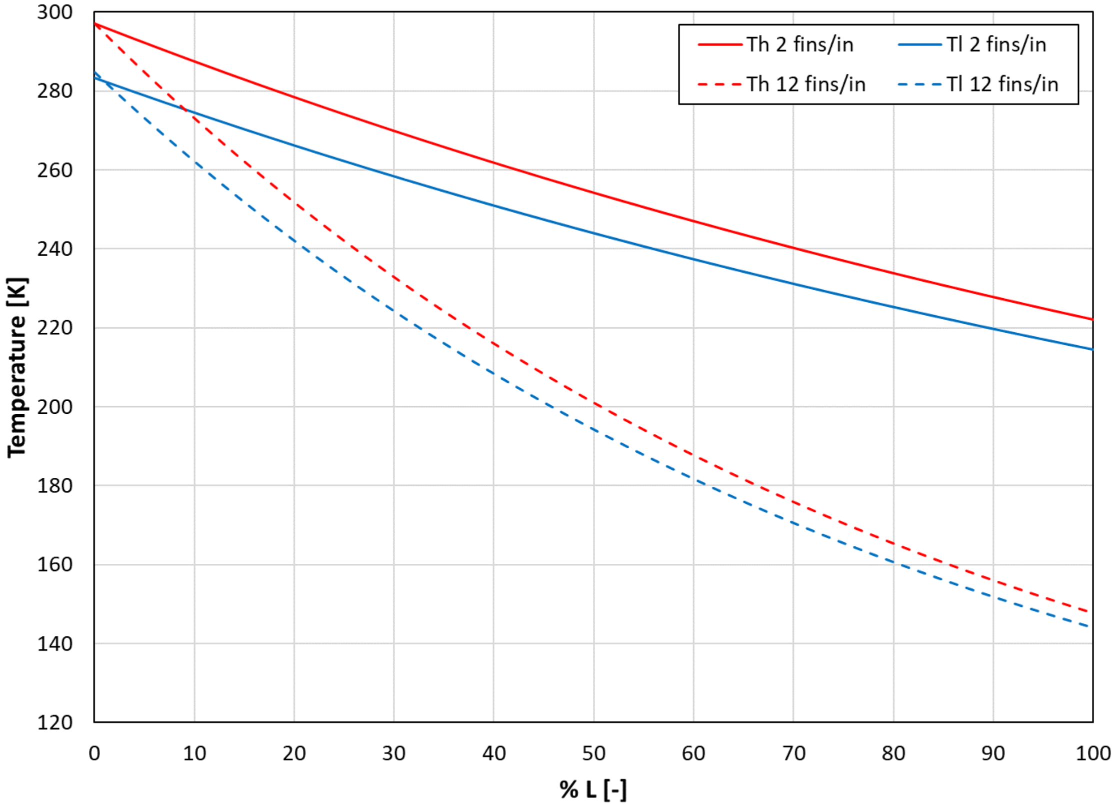

Figure 6-16 Fin density effect on heat exchanger cooling curves

The previous results shown were at the initial condition, assuming no shift in cooling curves. Table 6-5 shows the results at 3 points throughout the operational period of the purifier: the beginning, when it reaches 50% of the maximum frost thickness, and the end (100% of maximum frost thickness). The crucial results from this table are the way NTU and nitrogen flow rate change over time, as frost deposits. This is especially important in comparison to the commercial purifier. Each geometry shows that even as NTU degrades with frost accretion over time, the nitrogen mass flow rate required to maintain the purifier does not increase nearly as much as the commercial purifier. The commercial purifier nearly triples its nitrogen usage by the end of the test, while the freeze-out purifier increases its nitrogen usage by 28% at most. This shows that the separate of the cooling of the helium into two heat exchangers, one for frost collection and one exclusively for further cooling, greatly reduces the nitrogen usage during operation. The second heat exchanger can be designed optimally for efficient heat exchange, with no regard for frosting, allowing it to compensate when the effectiveness of HX-1 is reduced by frost.

The full effect of the transient increases in nitrogen usage are shown in Table 6-5 as well, in the total mass of nitrogen used during the 72 hour operating period. This further illustrates the impact of the large increase in nitrogen usage that the commercial purifier requires as its effectiveness decreases. The case of 6 fins/in, which is the closest in frost mass capacity to the commercial purifier, suggests that the finned-tube heat exchanger will use approximately half as much nitrogen as the commercial purifier.

Table 6-5 Transient calculations for heat exchanger performance with varied fin density

Fins/in	% max. x_{fs}	m_{frost} [g]	NTU [-]	$\dot{m}_{N2}$ [g/s]	m_{N2} [kg]
Commercial purifier	0	0	15.91	4.01	1831
	50	259	11.60	5.54	
	100	549	6.10	11.64	
2	0	0	7.17	4.15	1272
	50	304	2.49	5.09	
	100	475	1.51	5.30	
4	0	0	11.44	3.70	1094
	50	439	6.42	4.26	
	100	907	4.37	4.66	
6	0	0	14.84	3.33	911
	50	313	11.24	3.48	
	100	595	9.17	3.76	
8	0	0	17.38	3.09	810
	50	205	15.30	3.10	
	100	440	13.42	3.20	
10	0	0	19.32	2.95	767
	50	170	17.88	2.96	
	100	340	16.64	2.97	
12	0	0	20.75	2.77	718
	50	136	19.79	2.77	
	100	273	18.92	2.78	

Figure 6-17 shows the full transient data from the commercial purifier test case compared with the freeze-out purifier with 6 fins/in. It shows that even when the NTUs decrease by approximately 40% by the end of the test, the nitrogen flow rate only increases by approximately 13% in this case. Again, the variation in NTU at the beginning of the test data is due to the heat exchanger taking a few hours to reach steady state upon beginning operation. The real beginning NTUs are approximately 15.9, as can be seen in Figure 6-17 in which it increases at first.

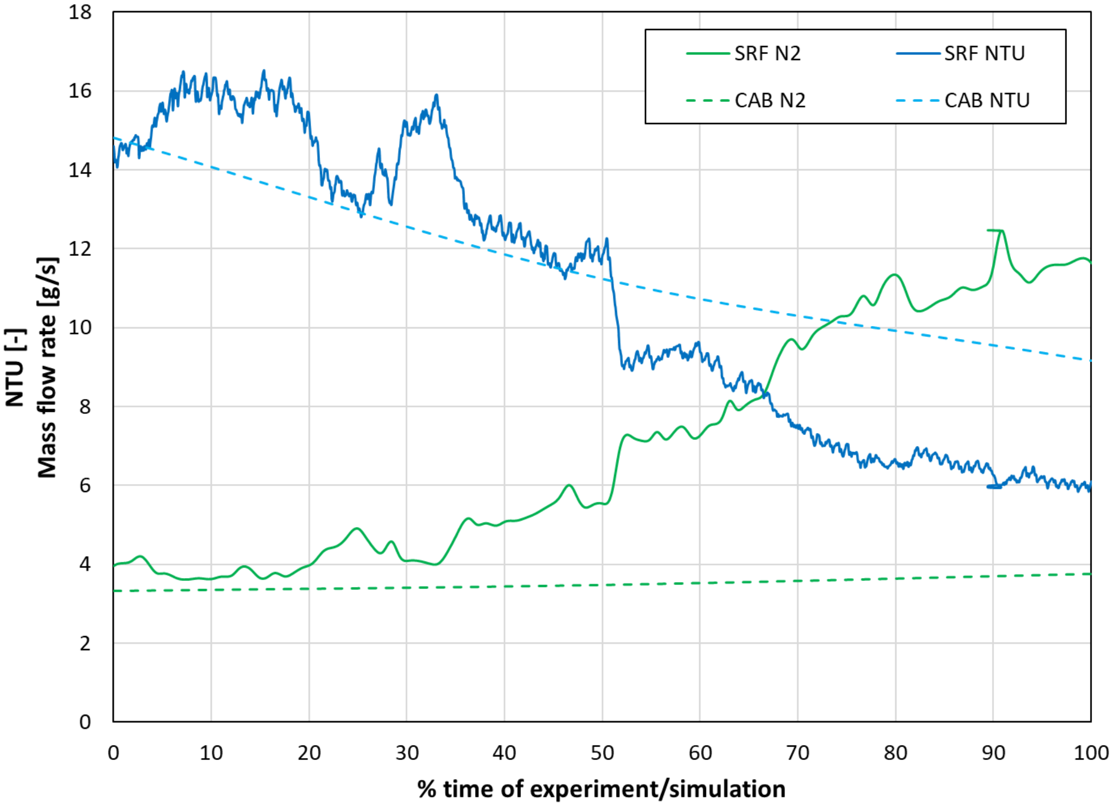

Figure 6-17 Freeze-out heat exchanger NTU and N2 usage compared with commercial purifier test data

There is the possibility that a variable fin density throughout HX-1 could be optimal. Using a higher fin density in the non-frosting regions and a lower fin density in the frosting regions would have some advantages over the constant fin density design. This design concept takes advantage of two observations of the above study. First, increased heat transfer from higher fin density lowers utility (liquid nitrogen) usage, while decreasing frost capacity. Second, increased open area from lower fin density increases frost capacity, while increasing nitrogen usage. This combination would allow for more effective heat transfer where no frost is collected, and increased frost capacity where that is useful, making use of the benefits of both high and low fin densities. For example, there could be 12 fins/in for the first 20% of the length of the heat exchanger, then 6 fins/in for the remainder of the length of HX-1. This would gain the benefit of having the capacity of the uniform 6 fins/in case, while reducing the nitrogen usage slightly due to more efficient heat transfer in the first 20% of the length.

However, this design concept has a few downsides. First, helium inlet conditions can vary during purifier operation, so the points at which frosting will occur may shift, widening the potential frosting region of the heat exchanger. Flow rate and humidity may vary depending on how the purifier is being used (regular helium clean-up during refrigerator operation vs. equipment commissioning or cool-down), changing the temperature at which frosting begins (based on the partial pressure). Although it may still provide benefits, it extends the region of the heat exchanger that would require the low fin density for increased frost capacity. Second, using variable fin density would require additional welding between tubes of different fin densities. These added connections increase the chance for structural damage and leakages due to thermal cycling that occurs when warming up and cooling down the purifier during regeneration. The additional capacity and/or lessened nitrogen usage is not worth the structural complications that this design concept introduces. Thus, a constant fin density is more practical.

6.3.3 *Effect of Mandrel Diameter on Heat Exchanger Performance*

The effect of mandrel diameter was also studied to show how a heat exchange axial length impacts the performance. All three cases were calculated using 12 fins/in. In this case, due to the way the heat exchanger was designed, HX-2 does change with HX-1 in this study. HX-2 mandrel OD maintains a difference of 3.75 in smaller than the HX-1 mandrel OD.

Because the tube length was held constant, the surface area and open volume don't vary. Only the axial length and diameter vary. This results in smaller variations in heat exchanger performance. A larger mandrel OD results in a slightly wider frost profile and slightly more nitrogen usage. In all three cases, the nitrogen usage over time barely changed. Although the 10 in case changed the most, it was still only an increase of less than 4%.

Table 6-6 Mandrel diameter study results

Mandrel OD [in]	$A_{ss,\ total}$ [in^2]	V_{open} [in^3]	m_{frost} [g]	NTU [-]	$T_{ho,HX\text{-}1}$ [K]	$\dot{m}_{N2}$ [g/s]
10	41922	1038	261	21.5	145.3	2.63
14	41922	1038	272	20.8	144.5	2.77
18	41922	1038	284	20.3	144.4	2.82

From a practical design standpoint, decreasing mandrel OD makes heat exchanger longer. Maintaining equal surface area, the HX-1 with a 10 in OD mandrel is 90.0 in long, the HX-1 with a 14 in OD mandrel is 67.7 in long, and the HX-1 with an 18 in OD mandrel is 54.6 in long. This is a significant change in the length of the heat exchanger and therefore a significant change in the required length of the entire cold box. Depending on the space limitations of system in which it is installed, this length could be a limiting factor.

The commercial purifier is estimated (in Chapter 3) to use ~0.76-1.0 kg of helium during regeneration. Based on a similar estimation, the reference geometry for the finned-tube heat exchanger purifier will use a total of approximately 0.68 kg of helium during regeneration, with

0.64 kg being vented during blow-down and 0.04 kg being used for pump and backfills (evacuation of remaining moisture using helium). This is a significant reduction from the commercial purifier. Another aspect of regeneration is warm up. The commercial purifier achieves this by pumping heated (~350 K) nitrogen gas through the nitrogen circuit and spaces around the heat exchangers (evacuated during operation). It uses an electric heater to heat the nitrogen gas from 300 K to 350 K. The nitrogen usage during this was measured to be 6.67 g/s for 34.8 hours, for a total usage of 836 kg total. During this time, the heater uses a total of 14.51 kWh. The finned tube heat exchanger purifier circulates helium with an electric heater to warm up the purifier. This saves all the gaseous nitrogen that the commercial purifier uses. It is anticipated to use less power as well because it heats the purifier more directly through the main helium circuit, instead of the smaller nitrogen circuit.

6.4 Summary

This chapter discussed the influence of the various deign parameters on the performance and a proposed design for a freeze-out purifier, focusing on the freeze-out heat exchanger. A process model was developed to study the heat exchanger, from an exergy standpoint and a heat and mass transfer standpoint. An initial exergy irreversibility minimization was done to find a good reference point for further study. This examined the effects of mandrel diameter, number of tube passes, and heat exchanger surface area. The minimum irreversibility was found to be with a 10 NPS HX-2 mandrel diameter (14 in HX-1 mandrel OD), 7 helium tube passes, and a heat exchanger shell-side surface area of 50 m^2.

Using this reference geometry, a study of certain geometrical factors was done with a focus on heat exchanger performance and mass collection capacity. The geometrical parameters that were varied were finned-tube fin density and HX-1 mandrel diameter. Denser fins results in more heat transfer surface area, reducing nitrogen usage and increasing NTUs in the heat exchanger. It also results in decreased open volume for frost to accumulate, so the frost capacity is decreased. With too few fins (<6 fins/in), the heat exchange suffers to a point that frost begins accumulating in HX-2. The heat exchanger is not designed to collect frost in HX-2, so HX-1 must have at least 6 fins/in. Less dense fins also results in increased nitrogen usage. There is some possibility for the use of variable fin density along the length of the heat exchanger, but structural design considerations may outweigh the benefit of decreasing nitrogen usage.

Mandrel diameter had a minimal impact on mass capacity and heat exchange. A smaller diameter results in more NTUs and less nitrogen usage, but less mass collected. However, all of the effects are minimal relative to the effect of fin density.

This study compared the fin density cases to test data from the commercial purifier tested in chapter 3. When directly comparing the highest capacity case (within the design condition) of 6 fins/in to the test data, it was estimated the finned-tube heat exchanger collects slightly more frost, while using significantly less nitrogen. The finned-tube heat exchanger also has a significant design advantage of less effect on flow distribution due to the axial flow on the shell side. The shell-side flow is not split into 10 tubes like the commercial purifier. The design inherently re-distributes the flow as needed during transient operation, so no local flow imbalances can proliferate, as described in chapter 5. This also significantly reduces variability in the capacity of the purifier.

Of additional note is that the finned-tube design does not have built-in capability to use imbalanced flow, like was studied in the commercial purifier. A minor modification can be made to the piping of the purifier to allow for less low-side flow, creating an imbalance of more contaminated high-side flow than low-side flow, by flowing some of the low-side flow through a bypass circuit. This is the opposite imbalance that the commercial purifier can achieve (it can only provide equal or less high-side flow), but this was shown to be the more advantageous imbalance (see Figure 5-13). The finned-tube design can achieve a similar manipulation of cooling curves to that achieved by the flow imbalance in the commercial purifier by manipulating the liquid nitrogen flow into the purifier. If the nitrogen flow is increased, the heat exchanger will cool the contaminated helium more in HX-1, resulting in the frosting region shifting toward the warm end of the heat exchanger. Beginning the operation with increased nitrogen flow and decreasing it over time could increase the capacity of the heat exchanger by shifting the frosting region toward the cold end over time, taking advantage of the effect studied in the one-dimensional transient model and shown in Figure 5-13.

Overall, the finned-tube heat exchanger is shown to use less nitrogen (especially as frost deposits), while collecting at least as much frost as the commercial purifier (for the 6 fins/in design). It also uses less helium and no nitrogen gas during regeneration. By reducing the fin density of HX-1 compared with the originally proposed design, the freeze-out purifier can very efficiently collect moisture while minimizing utility usage.

REFERENCES

[1] D. Kroll, N. Hasan, Exergetic design and analysis of a freeze-out heat exchanger for helium purification, Int. J. Exergy, 45(3/4) (2024) 236-256

[2] D. Kroll, N. Hasan, V. Ganni, A. Fila, A. Engeda, Freeze-out purifier for helium refrigeration system applications, IOP Conference Series: Materials Science and Engineering, 755 (2020) 012056

[3] E. Yuksek, Capacity Improvement of a Small-Scale Cryogenic System Using Exergy Analysis, Old Dominion University, 2009

[4] ASME, ASME Standard B36.19M - Stainless Steel Pipe, in, ASME, New York, NY, 2018, pp. 18

[5] W. Rohsenow, J. Hartnett, Y. Cho, Handbook of heat transfer, McGraw-Hill, New York, 1998

[6] P.K. Gupta, P.K. Kush, A. Tiwari, Design and optimization of coil finned-tube heat exchangers for cryogenic applications, Cryogenics, 47(5) (2007) 322-332

[7] W.R. Dean, Note on the motion of fluid in a curved pipe, The London, Edinburgh, and Dublin Philosophical Magazine and Journal of Science, 4(20) (1927) 208-223

[8] C.E. Kalb, J.D. Seader, Heat and mass transfer phenomena for viscous flow in curved circular tubes, Int. J. Heat Mass Transfer, 15(4) (1972) 801-817

[9] S.A. Berger, L. Talbot, L.S. Yao, Flow in Curved Pipes, Annual Review of Fluid Mechanics, 15(1) (1983) 461-512

[10] J. Howard, N. Hasan, P. Knudsen, Thermal-Hydraulic Characterization of Shell-Side Flow in a Cryogenic Coiled Finned-Tube Heat Exchanger, J Heat Trans, (2021)

[11] P.N. Knudsen, Testing and analysis of an exergetically efficient 4 K to 2 K helium heat exchanger, Old Dominion University, Norfolk, VA, 2016

[12] M. Kandula, Frost growth and densification in laminar flow over flat surfaces, Int. J. Heat Mass Transfer, 54(15) (2011) 3719-3731

[13] K.-S. Lee, S. Jhee, D.-K. Yang, Prediction of the frost formation on a cold flat surface, Int. J. Heat Mass Transfer, 46(20) (2003) 3789-3796

[14] A. El Cheikh, A. Jacobi, A mathematical model for frost growth and densification on flat surfaces, Int. J. Heat Mass Transfer, 77 (2014) 604-611

[15] A. Wexler, Vapor Pressure Formulation for Ice, Journal of Research of the National Bureau of Standards Section a-Physics and Chemistry, 81(1) (1977) 5-20

[16] E.N. Fuller, P.D. Schettler, J.C. Giddings, New method for prediction of binary gas-phase diffusion coefficients, Industrial & Engineering Chemistry, 58(5) (1966) 18-27

[17] S. Ergun, A.A. Orning, Fluid Flow through Randomly Packed Columns and Fluidized Beds, Industrial & Engineering Chemistry, 41(6) (1949) 1179-1184

[18] J. Comiti, M. Renaud, A new model for determining mean structure parameters of fixed beds from pressure drop measurements: application to beds packed with parallelepipedal particles, Chemical Engineering Science, 44(7) (1989) 1539-1545

[19] K. Libbrecht, Snow Crystals : A Case Study in Spontaneous Structure Formation, Princeton University Press, Princeton, NJ, 2022

[20] S.S. Kutateladze, Boiling heat transfer, Int. J. Heat Mass Transfer, 4 (1961) 31-45

[21] T.J. Kotas, Exergy analysis of simple processes, in: T.J. Kotas (Ed.) The Exergy Method of Thermal Plant Analysis, Butterworth-Heinemann, 1985, pp. 99-161

[22] J. Franz, A.C. Ordonez, Cryogenic heat engines made using electrocaloric capacitors, American Physical Society, Texas Section Fall Meeting (2001)

Chapter 7 : Summary

7.1 Overall Summary

The overall objective of this research was to develop an improved understanding of frost deposition in a freeze-out heat exchanger for helium purification applications. This objective was undertaken due to a lack of understanding of such systems in the literature and the shortcomings of alternative methods of purification, such as adsorption using molecular sieve beds. Commercially available freeze-out purifiers require large amount of liquid nitrogen and utility use and moisture collection are not well understood.

The objectives of this research are to understand the effects of process parameters such as pressure, fluid to wall temperature difference, contamination level, etc. on the performance of helium purifiers for the purpose of making operational improvements to existing purifiers and improving the design of future purifiers. The goal is to study how to increase frost capacity, increase operational cycle time, decrease utility usage per unit capacity (per gram collected), and effectively use the available heat exchanger surface area. New design improvements including choice of type of heat exchanger, reduced effect of flow mal-distribution due to frost deposition, heat exchanger surface area, compactness, and efficient utility usage contribute to a design that has a higher capability to operate efficiently.

In the interest of these objectives, several tasks were undertaken. First, an existing commercially available helium purifier was tested and characterized. The heat exchanger in the purifier was used as a freeze-out heat exchanger for removal of moisture. Liquid nitrogen consumption was tested during nominal operation to establish a baseline for utility usage. The purifier was then tested under practical conditions to establish a baseline capacity expectation. In order to better study how inlet conditions impact purifier performance, testing was then done under controlled operating conditions. This involved the design and fabrication of a custom low-level moisture contaminant generator to ensure constant amounts of moisture entering the purifier. The tests studied the effects of both inlet contamination level (ppm_v) and heat capacity ratio (by way of balancing and unbalancing the flow in the heat exchanger). Lastly, for a complete understanding of the purifier, the air collection capacity via adsorption was estimated and the helium and nitrogen usage during regeneration were tested.

The first step in modeling frost formation in a purifier heat exchanger was establishing an understanding of how frost forms in a simplified geometry on an iso-thermal surface. This model was developed and validated using test results in literature for air systems, then expanded to study how purifier-like conditions impact these results. The conditions studied were gas pressure, low level absolute humidity, wall temperature difference, reduced temperature differential, and carrier gas (including helium). The effects of each variable on frost accretion and heat transfer were studied, and a correlation was developed to describe the behavior.

Now that an understanding of frost formation in a simplified system has been established, it was extended to model heat exchange along the length of a heat exchanger with a tube-in-tube geometry (like the previously tested model). The model predicts heat exchanger performance, outlet temperatures, and frost formation profile. This model was validated using the test data gathered on the commercially available purifier. A hypothesis was formed as to why, in several cases, the test data did not match the model results. That hypothesis was that flow mal-distribution was causing variation in frost formation between the 10 tube pairs in the heat exchanger, resulting in some tubes plugging before others, significantly reducing the effectiveness of the heat exchanger. In light of this, the imbalance of flow in the heat exchanger was studied in depth using the model. This included transient variation of the degree of imbalance. The effect of moisture contamination level was also studied.

In the above sections, an existing helium purifier was studied and characterized. The last task of this research was to study a recently proposed design of a helium freeze-out purifier, to compare with the existing purifier. This purifier design uses a coiled finned-tube heat exchanger, with the intention of improving frost capacity and reducing utility usage. First, a process model was developed to predict the performance of the purifier, using information learned from the studies done on the commercially available purifier. Then, the effect of design parameters on exergetic efficiency, frost capacity and distribution, and heat exchanger effectiveness were investigated. Recommendations were made for design decisions on this purifier in relation to the effectiveness of the existing purifier.

7.2 Specific Conclusions and Impact of Findings

7.2.1 *Performance Characterization of an Industrial Freeze-Out Helium Purifier*

An industrial freeze-out helium purifier was tested during operation and regeneration. The nitrogen usage during regeneration was measured to be approximately 671.6 kg, average 8.69 g/s over 21.5 hours. The helium consumed during regeneration was estimated and measured to be approximately 1.0 kg. The nitrogen usage during nominal operation was 3.88 g/s when utilizing the nitrogen boil-off in HX-2 (unbalanced HX-1), and 5.26 g/s when not utilizing HX-2 (balanced HX-1). The frost collection capacity of the purifier was tested during nominal operating conditions (uncontrolled ppm) and found to be approximately 500-560 g.

In order to test under controlled conditions, a low-level moisture generator was developed and was shown to be capable of generating a controllable low-level moisture contamination of 5-190 ppm. This equipment was designed and fabricated for this testing. Using this equipment, the industrial purifier was tested under four different conditions, with ~30 and ~60 ppm, and a balanced and unbalanced HX-1 flow. It was found that the purifier had a moisture collection capacity of ~530-600 g, with one exception. At 30 ppm with a balanced HX-1, it collected 800 g. This was hypothesized that flow mal-distribution caused frosting at different rates in different tubes (of the 10 tube pairs) within the heat exchanger. When one tube becomes plugged with frost before others, the cold flow in that tube is not used for cooling the incoming contaminated flow, as the contaminated flow is channeled through the remaining nine open tubes. The cold flow that reaches the warm end as a result of this causes frosting in the header. This hypothesis is supported by the sharp increase in pressure drop at the end of the test. It would also explain the sharp drop in NTU the heat exchanger experiences, far more than expected by evenly distributed frosting. The 60 ppm cases experienced this more extremely because, due to the partial pressure vs temperature curve in the heat exchanger, the frosting occurs closer to the warm end. The unbalanced cases also experience more effects from flow mal-distribution because they resulted in more localized frost distribution, shown by the sharp increases in pressure drop at the end of the test. Flow mal-distribution was explored further in later chapters.

The heat exchanger started at approximately 16 NTU. Over time it reduced to 3-10 NTU, depending on the test. The 30 ppm tests had less NTU degradation than the 60 ppm tests. The balanced tests had less NTU degradation than the unbalanced tests. More NTU degradation results in more nitrogen usage, making up for the increased temperature difference in the heat exchange process. The pressure drop had an abrupt (exponential) increase at the end of the 60 ppm tests, after staying mostly constant for most of the test. The 30 ppm tests had a more linear increase in pressure drop throughout their durations. For the unbalanced cases, the helium flow rate through

HX-2 decreased to nearly zero after a period of time, due to HX-2 plugging with frost much sooner than HX-1, despite its small flow rate (<5% of total helium flow).

7.2.2 *Modeling and Estimation of Frost Formation on an Iso-Thermal Surface*

The zero-dimensional computational model was validated using experimental data of a system of air at atmospheric pressure. The validated model was used to study the effects of carrier gas, high pressure, low temperature, and low-level humidity on frost formation on an iso-thermal flat plate. It was observed through these calculations that frost thickness increased very slightly when pressure increased, did not change when wall temperature difference increased, increased when reduced temperature differential increased, increased slightly when absolute humidity increased, and increased when carrier gas molecular weight increased. Table 4-3 shows the impact of these important factors for frost accretion.

An increase in pressure increases the saturation temperature, from which the ambient and wall temperatures are calculated. This slightly increases the final frost thickness. An increase in pressure also decreases diffusivity and increases partial pressure, which decreases the sensible temperature difference. This slightly slows the rate of frost deposition. This combination of factors result in high pressures requiring more time to deposit very similar (slightly large) amounts of frost.

An increase in wall temperature difference increases the absolute humidity difference, the main driving force of mass transfer and increases the rate of frost deposition. The maximum frost thickness is unchanged, as the saturation condition is unaffected. This results in larger wall temperature difference depositing the same amount of frost in a shorter period of time.

An increase in reduced temperature differential has no impact on the frost deposition rate. This suggests that the wall temperature difference is the only temperature that matters for frost deposition rate. The ratio has no impact. The wall temperature difference is held constant, but the ambient temperature difference is decreasing. The mass transfer rate is driven by the wall temperature difference, so it isn't changing. Because the saturation temperature is constant, the maximum frost thickness is driven by the ambient temperature difference. When the ambient temperature difference is smaller, more cooling can be used to deposit frost. This increases the final frost thickness.

An increase in absolute humidity increases the frost deposition rate by increasing the amount of mass that flows over the cold plate, which increases the absolute humidity difference. The maximum frost thickness does not change because the wall temperature difference is constant. Absolute humidity is the only factor that was studied to have an impact on frost density, increasing it as humidity increases.

Carrier gas molecular weight effects the solid-vapor saturation humidity ratio. This is the main driving force of the frost accretion. Heat and mass transfer coefficients are both significantly lower for higher molecular weight gases. This reduces the rate of frost deposition and absolute humidity difference. The lower heat transfer coefficient causes the maximum frost thickness to be higher with larger carrier gas molecular weight.

A method of estimating final frost thickness was developed, by using the heat transfer conditions at the stopping condition. At the end of the simulation, the conduction heat transfer through the frost layer is equal to the convection heat transfer through the carrier gas. The estimation was shown to be accurate within 0.5% of the simulation result. Because all the required inputs can be calculated at the initial condition, this method can be used to predict frost thickness without carrying out the complex simulation that the model uses.

7.2.3 *Modeling and Estimation of Frost Formation on Heat Exchanger Surfaces*

The one-dimensional transient model for frost formation on a heat exchanger surface was validated using test data from the industrial helium freeze-out purifier. Specifically, it was validated using the 30 ppm balanced test (within 2% error). The other tests did not line up with the model's predictions, instead over-predicting frost collection. Because this model calculates the physics of one tube with a set flow rate, unaffected by the header and flow mal-distribution, this is expected assuming flow mal-distribution in the real system. Furthering this narrative, the model severely under predicted the NTU degradation in every case, but more so in the unbalanced and 60 ppm cases. The model predicts more localized frost deposition in the unbalanced cases, the effects of which were observed in the tests.

The effects of flow imbalance were studied further, with exaggerated conditions to distinguish the differences more starkly. In a sufficiently unbalanced heat exchanger at 60 ppm, frost deposition can deposit closer to warm end. As the operational time progresses, this could result in the header being cooled to a point where frost begins forming in it, before even reaching the tubes. This would cause the exponential increase in pressure drop observed in the testing. With the localized deposition caused by unbalanced flow, if it doesn't reach the header, frost will still plug the flow in the tubes in which it is unbalanced.

It was studied what happens when the flow imbalance changes over time. First, when the flow starts balanced and shifts to having more flow through the high side. In a static flow calculation, the cooling curves shift the frost toward the warm end as frost adds more heat transfer resistance. When the high side flow increases, this effect is counteracted by the cooling curves pinching at the warm end. This causes the frosting region of the heat exchanger to shift toward the cold end. This shift causes a significant increase in the frost capacity of the heat exchanger, from

785 g to 1512 g. Second, when the flow starts balanced and shifts to having less flow through the high side. The cooling curves shift over time to pinching at the cold end. This pushes the frost formation toward the warm end, increasing the potential region of frost collection over time. This effect is counteracted by the deposition happening more locally because of the steeper cooling curves in the frosting region. This results in 685 g being deposited, less than balanced flow, but more than a 0.8 ratio, the end point of this case.

It was observed that within the range studied, the ppm level of contamination had less of an effect than flow imbalance. Still, higher ppm causes frosting nearer to the warm end of the heat exchanger. It can contribute, along with flow imbalance toward frost being deposited nearer to the warm end and therefore the header.

The influence of various design parameters on the performance of a proposed freeze-out purifier was studied. It uses a coiled finned-tube design with contaminated flow on the shell-side to minimize the issue of flow mal-distribution the commercially available purifier has. An initial exergy irreversibility maximization was done, studying the effects of heat exchanger mandrel diameter, number of helium tube passes, and heat exchanger shell-side surface area. Total irreversibility showed minimums within the ranges of the three variables studied. The minimum irreversibility was found to be with a 10 NPS HX-2 mandrel diameter (14 in HX-1 mandrel OD), 7 helium tube passes, and a heat exchanger shell-side surface area of 50 m^2.

The optimization showed the impacts of those design parameters on many sources of irreversibility in the purifier and its heat exchanger. The total irreversibility of the purifier cold box increased greatly with fewer than 6 helium passes, due to increases in pressure drop from less flow area. This increase overwhelmed the decrease that was seen in irreversibility due to temperature difference, as a longer flow path results in more efficient heat exchange (more NTUs).

Increasing the area resulted in moving the optimal design toward a smaller mandrel diameter and more helium passes. This is due to less need for a longer heat exchanger to increase efficiency of heat exchange, so decreasing pressure drop further was beneficial. There are also some practical aspects to consider in design. Designing HX-1 shell side surface area to be much larger than HX-2 shell side surface area allows for more space in HX-1 for frost formation, increasing its potential collection capacity. This can be done by making the mandrel diameter smaller. However, a smaller mandrel diameter results in a higher pressure drop in the heat exchanger.

Following the establishment of an exergetically optimal design point, the effects of fin density in the finned-tube and mandrel diameter on heat exchanger frost capacity and performance were studied. Mandrel diameter had a minimal impact, relative to the impact of fin density, on mass capacity and heat exchange. Increased fin density means more surface area in the heat exchanger, allowing for much more efficient heat exchange, which results in less nitrogen usage. It also decreases the open volume in the heat exchanger, reducing frost capacity. Additionally, the more efficient heat exchange means steeper cooling curves (more temperature change per unit length), which narrows the length in which frost deposition can occur. This further reduces the frost capacity. Decreased fin density means less surface rea in the heat exchanger, making for less efficient heat exchange, which results in more nitrogen usage.

Notably, only 2 fins/in showed more nitrogen usage than the commercial purifier at the beginning of an operating period (4.15 g/s vs 4.01 g/s). However, even 2 fins/in used significantly less nitrogen over the course of an operating period than the commercial purifier (1272 kg vs 1831 kg). This is due to the NTUs of the heat exchanger reducing much less because the flow remains distributed evenly in the shell-side. Additionally, because this analysis is comparing HX-1 to the entire commercial purifier's heat exchanger, HX-2 can efficiently cool the helium down further without any degradation due to frost. This dampens the effect of the reduced NTUs in HX-1 on the overall nitrogen usage.

Any less than 6 fins/in reduces the heat exchange to a point where the frost deposits in both HX-1 and HX-2. HX-2 is not designed to collect frost, so this scenario is to be avoided. Therefore, 6 fins/in is recommended as a minimum. With 6 fins/in, HX-1 can collect over 600 g of frost (the average capacity of the commercial purifier). This design also uses approximately half of the nitrogen that the commercial purifier does in an equal operating period. There is potential for the use of variable fins throughout HX-1, to maximize heat exchange where there is no frost and maximize frost capacity in the frosting region. However, this presents additional design challenges due to weaknesses in brazed joints caused by thermal cycling.

This design can also take advantage of the imbalance studied in the commercial purifier in two ways. First, a slight modification to the piping can be made to allow bypass of low-side flow around the heat exchanger. Second, the liquid nitrogen flow rate can be manipulated to shift the cooling curves and therefore the frosting region, especially in a transient manner so as to shift the frosting region over time, increasing the capacity.

Additionally, it was shown that the proposed purifier design is estimated to use less helium during regeneration (0.68 kg vs 0.76-1.0 kg). The commercial purifier uses ~836 kg of heated nitrogen to warm it up during regeneration, whereas the proposed purifier design circulates ambient warm helium (300 K) through the purifier to warm it up, wasting no additional gas. All of this shows that the proposed purifier design can collect as much, or nearly as much, frost while reducing nitrogen usage significantly over the course of an equal operating period. Based on this analysis, if the objective is to reduce utility usage (especially liquid nitrogen usage), the proposed finned-tube purifier design is recommended as a significant improvement to the commercially available tube-in-tube purifier design.

7.3 Future Work and Recommendations

The stated scope provided many useful and novel insights into the inner workings of helium freeze-out purification. There were several observations made during these studies that provide opportunities for further inquiry outside the scope of this dissertation.

7.3.1 *Testing at Low ppm*

There are several sources of contamination in a helium liquefaction system. Commissioning new equipment typically results in 30+ ppm. Helium from a vendor (4.7 standard) is supplied with 30 ppm. The tests done in this dissertation were done at these levels of contamination. However, there are other sources that result in lower levels of contamination. Air can leak into sub-atmospheric helium systems during operation. Residual gases can desorb from non-metallic components slowly over many years of operation. Both of these sources typically cause 5-10 ppm of contaminants. Testing in this range would be beneficial to understand another common condition the purifier undergoes. It was observed in the testing that was done that lower ppm resulted in more collection capacity, likely due to it depositing toward the cold end of the heat exchanger. This allows more time avoiding the issues caused by the frosting in the header at the warm end (from flow mal-distribution). It would also diminish the increase in temperature difference within the heat exchanger, reducing the NTUs. This would reduce nitrogen usage during the duration of the operating period. Testing at lower ppm would also give a more complete picture of the impact ppm has on frosting in this heat exchanger.

7.3.2 *Model Frost Density*

The frost models discussed in this dissertation use a variety of methods for calculating density. The zero-dimensional model uses a correlation by Byun [1]. The one-dimensional model uses a constant value, validated by the testing and Byun's correlation, used in the tested conditions. Obviously, these are all educated estimations, checked that they are in the correct range, but not capturing the entirety of the density behavior in the frost. Specifically, because these estimations are relatively constant, they do not capture densification of frost, only deposition. For this reason, expanding the modeling to include two phases (solid ice and gaseous helium) within the frost layer density calculation would be useful. This expansion would calculate frost density, thermal conductivity, and other thermal properties. This type of calculation has been studied in simple conditions (like those used to validate the model in chapter 4) by Cheikh [2], using a seeding parameter for frost growth and a tortuosity parameter for flow through the porous frost layer. This calculation would be designed for the conditions in a helium purifier. If this densification effect is significant, it could increase the capacity of a purifier that makes use of it by several times. While perhaps not practical for repeated calculations from a computation time standpoint, such a model could be used to develop new correlations for frost density, thermal conductivity, and pressure drop for use in the frost models.

7.3.3 *Extension of the 1D Model to Include Flow Mal-Distribution*

A major outcome of the studies on the commercially available purifier in chapters 3 and 5 was that flow mal-distribution severely limits the frost collection capacity of the purifier and impacts the heat exchanger efficiency. This flow mal-distribution is caused by likely predictable physical behavior of the gas in the header. The model currently only models one tube-in-tube pair. If the heat exchanger model is extended to include all 10 tubes and the header, this flow mal-distribution may be predicted, making the model accurately predictive for all inlet conditions (ppm and imbalance).

7.3.4 *Develop a Correlation to Extend the Purifier Operation Time and Capacity by Adjusting the Flow Imbalance*

The observed effect of the flow mal-distribution can be used to extend the operating time and capacity of the commercial purifier. It was shown in chapter 5 that the flow imbalance in a single tube can be manipulated to increase the frost capacity. A correlation based on the measured pressure drop can be used as a guide to adjust the HX-1 flow capacity balance. This would be adjust directly by adjusting the HX-2 isolation valve position and liquid nitrogen use and thus manipulating the cooling curves to use more of the HX-1 surface area for freeze-out. A similar correlation can be developed for the finned-tube heat exchanger, adjusting liquid nitrogen use to shift the cooling curves. By having the returning helium bypass the heat exchanger, the flow imbalance can be manipulated. Through this flow imbalance, the cooling curves and frost profile can be adjusted over the operating period, as theorized in Figure 5-13 and Figure 5-14. Extending the frost profile may allow for the design to include a larger fin density, which in turn would reduce nitrogen usage, perhaps counteracting the decreased heat exchanger effectiveness from the flow capacity imbalance. This would be controlled by monitoring the temperature at the HX-1 outlet and the pressure drop in the heat exchanger. Through these methods, the surface area of the heat exchanger could be more fully utilized for frost accretion, increasing its frost capacity extending its operating period.

REFERENCES

[1] S. Byun, et al. Frost modeling under cryogenic conditions, Int. J. Heat Mass Transfer, 161 (2020) 120250

[2] A. El Cheikh, A. Jacobi, A mathematical model for frost growth and densification on flat surfaces, Int. J. Heat Mass Transfer, 77 (2014) 604-611

APPENDIX A: COMMERCIAL PURIFIER MODES OF OPERATION

Purification Mode

The general operating principle in this mode has been discussed in section 2.2. The supply helium flow pressure drop in the heat exchanger (for moisture collection capacity) and/or the nitrogen contamination level in the return helium indicated by the arc cell (adsorber bed capacity for air collection capacity) indicate the saturation conditions of the purifier. The purifier requires regeneration and is switched to the regeneration mode once it has reached the moisture or air capacity limit. Based on calculated estimates, the moisture capacity is the much more stringent condition.

Regeneration Mode

Regeneration of the purifier is performed to take out the contaminants from the purifier system and to restore to its design contamination collection capacity. The overall regeneration process can be sub-divided into the following segments -

a) *Isolation* – The purifier skid is isolated. Helium flow is diverted to another purifier while this unit regenerated.

b) *Helium Blow-down* – The purifier system is depressurized via a vent to release the potentially contaminated helium in the system. The pressure is reduced to approximately 2.0 bar. This leaves the system at positive pressure, helping with warm-up.

c) *System Warm-up* – The liquid nitrogen supply to the boiler vessel is turned off. Gaseous nitrogen is flowed through the nitrogen boiler, HX-2, and a (previously) vacuum space around HX-1. An electric heater warms up the gaseous nitrogen to approximately 350 K. The nitrogen is vented after flowing through these components.

d) *Contamination Removal* – Both air (oxygen and nitrogen) and moisture (in the form of water vapor) are removed from the system using several evacuation and back-fill cycles. The purifier is evacuated using a vacuum pump and consecutively back-filled with clean helium. The moisture is collected for measurement using a cold (liquid nitrogen) trap. The cycle is carried out several times (typically 3-4 times) until the cold trap doesn’t register any moisture contamination from the evacuation process (determined by pressure falling sufficiently low during evacuation, approximately 50 mbar).

e) *Purge and Cool-down* – Clean helium is circulated through the purifier as in purification mode. The liquid nitrogen supply to the boiler vessel is turned back on. The clean helium circulation is carried out until the desired temperature distribution across the purifier is attained. At this point the purifier is prepared for purification mode.

APPENDIX B: ESTIMATION OF AIR COLLECTION CAPACITY DURING NOMINAL OPERATION

Adsorption potential of different common adsorbent materials (activated charcoal, silica etc.) is a developed topic and theoretical calculation of the holding capacity for these adsorbents can be fairly accurate. This can be estimated from the overall effective mass of the adsorbent material, as well as geometry of the adsorber bed. Once this design information is obtained, the (air) holding capacity of the adsorber bed (using activated charcoal in this case) can be calculated using the method outlined in [1]. The input parameters and the calculated parameters for the purifier are presented in Table D-1. This capacity was found to be 4.34 kg, with the bed lasting for 23.95 days of operation. Nearly 24 days is far above the expected (and tested) operating time for the heat exchanger used for freeze-out. This shows that in this system, the air collection isn't the critical capacity, because it is much larger than the heat exchanger. Therefore, while required for purifier design, the air capacity is not considered further in this study.

Table B-1 Estimation of the air holding capacity of the activated charcoal adsorber bed

Parameter	**Variable**	**Value**	**[Unit]**
Helium mass flow rate	$\dot{m}$	30	[g/s]
Inlet volume fraction of air (N_2)	$V_{(N2)}$	10.0	[ppm_v]
Flow pressure	p	13.00	[*bar*]
Mass fraction of Air	$w_{(N2)}$	69.98	[ppm_w]
Mass fraction of Air		7.0E-05	[--]
Mass fraction of helium	$w_{(He)}$	1.00	[--]
Molecular weight of air (N_2)	$M_{(H2O)}$	28.01	[*g/mol*]
Molecular weight of helium	$M_{(He)}$	4.00	[*g/mol*]

Table B-1 (cont'd)

Parameter	**Variable**	**Value**	**[Unit]**
Molecular weight of mixture	M	4.00	[*g/mol*]
Adsorber bed temperature	T_{bed}	80	[K]
Specific gas constant for air (N_2)	R	0.297	[kJ/kg-K]
Saturation pressure of Nitrogen at bed temperature	p_s	1.38	[bar]
Adsorption potential	$(\varepsilon_{ij})_{eq}$	220.01	[kJ/kg]
Volumetric loading for BPL carbon	*n*	12.00	[cm^3/100g of adsorbent]
Mass of air (N2) adsorbed per unit mass of adsorbent	*w*	0.097	[g_{N2}/g_C]
Effective bed length	L_{bed}	64.5	[in.]
Effective bed diameter	d_{bed}	12.39	[in.]
Bed Gap for LN Cooler	$d_{bed,o}$	0	[in.]
Ratio of length to equivalent equil. Section	ξ	0.8	[-]
Effective volume of adsorbent	V_{bed}	0.102	[m^3]
Effective density of adsorbent	ρ_C	440	[g/l]
Total mass of Adsorbent	m_c	44.86	[kg]
Total mass of air adsorbed	m_{N2}	4.34	[kg]
Break-through time	t_B	23.95	[days]

APPENDIX C: DESIGN CALCULATIONS FOR TESTING EQUIPMENT

Table C-1 Classical venturi design calculations

	Real Gas	*Real Gas*	*Ideal Gas*		
FID	11	11	11	[-]	*Fluid ID #*
MW	4.003	4.003	4.003	[g/mol]	*Molecular weight*
p_1	1.010	1.010	1.01	[atm]	*Pressure (upstream)*
T_1	176.00	153.00	176.0	[K]	*Temperature (upstream)*
ρ_1	0.276	0.317	0.280	[kg/m^3]	*Density (upstream)*
Z_1	1.001	1.001	1.000	[-]	*Compressibility (upstream)*
μ_1	13.90	12.67	13.90	[mPa-s]	*Viscosity (upstream)*
k_1	1.668	1.668	1.667	[-]	*Isentropic exponent (upstream)*
De	-0.186%	-0.215%	-0.186%	[in/in]	*Thermal expansion*
D	1.682	1.682	1.682	[in]	*Upstream pipe inside diameter*
d	0.670	0.670	0.670	[in]	*Throat diameter*
A_t	0.351	0.351	0.351	[in^2]	*Throat area at process condition*
β	0.3983	0.3983	0.3983	[-]	*Ratio of throat to upstream pipe ID*
β^4	0.02518	0.02518	0.02518	[-]	
C_d	0.984	0.984	0.984	[-]	*Coefficent of discharge*
C	2.26E-04	2.26E-04	2.26E-04	[m^2]	$= C_d \cdot A_t [m^2] / (1-b^4)^{1/2}$

Calculate 'w', given 'Dp':

w	1.9	15.0	1.9	[g/s]	*Mass flow rate*
Re_D	4.02E+03	3.54E+04	4.04E+03	[-]	*Reynold's number*
Δp	0.50	30.00	0.50	[in. H_2O]	*Differential pressure*
x	0.0012	0.0729	0.0012	[-]	*Pressure drop ratio*
Y_1	0.9994	0.9653	0.9994	[-]	*Expansion factor (upstream)*
K	34.9	33.7	35.1	(atm-in.H_2O/K)$^{1/2}$]	

Table C-2 Sonic venturi design

Venturi Info:			
d	0.0440	[in]	*Throat Diameter*
D	0.402	[in]	*Pipe Diameter*
β	0.10945274	[--]	*Ratio of Throat to Pipe Diameter*
A_t	9.810E-07	[m^2]	*Throat Area*
C_d	0.9894	[--]	*Coeffcient of Discharge (ISO 5167 Sec. 10.1.5.2)*
C_{dc}	0.9930	[--]	*Coefficient of Discharge for Critical Flow (Based on CFD Simulations)*

Venturi Inlet Temperature		**Inlet Pressure**		**Outlet Pressure**		**Pressure Ratio**	**Specific Heat Ratio**	**Critical Pressure Ratio**	**Inlet Density (HX)**	**Compressibility Factor**	**Expansibility Factor**	**Critical Flow Function**	**Mass Flow Rate**	**Time to vent**	**Time to vent**
T_{vi}		**P_i**		**P_o**		**P_R**	**γ**	**$P_R\|_c$**	**ρ_i**	**Z**	**Y**	**C_i^***	**m**	**s**	**min**
[°C]	*[K]*	*[psig]*	*[atm]*	*[psig]*	*[atm]*	*[--]*	*[--]*	*[--]*	*[kg/m^3]*	*[--]*	*[--]*	*[--]*	*[g/s]*		
25.0	298.2	205.00	14.95	0.00	1.00	0.07	1.665	0.4874	2.43	1.01	N/A	0.726	1.356	737.2	12.29

APPENDIX D: ENERGY BALANCE ANALYSIS METHODS

Table D-1 Energy balance analysis for cases 1 and 2, detailed below

1. Measured Temperatures					2. Using LN flow, calculate $T_{h1,3}$				
Hours		**1**	**20**	**37**	**Hours**		**1**	**20**	**37**
$P_{HX, in}$	[bar]	13.56	13.60	14.21	$P_{HX, in}$	[bar]	13.56	13.60	14.21
ΔP_{HX}	[bar]	0.0974	0.1370	0.9868	ΔP_{HX}	[bar]	0.0974	0.1370	0.9868
$P_{purifier, out}$	[bar]	13.46	13.46	13.23	$P_{purifier, out}$	[bar]	13.46	13.46	13.23
$P_{N2,vent}$	[bar]	1.007	1.007	1.017	$P_{N2,vent}$	[bar]	1.007	1.007	1.017
$\dot{m}$	[g/s]	14.01	14.02	14.12	$\dot{m}$	[g/s]	14.01	14.02	14.12
$\dot{m}_{N2,vent}$	[g/s]	6.35	8.19	17.80	$\dot{m}_{N2,vent}$	[g/s]	6.35	8.19	17.80
$T_{h1,2}$	[K]	296.4	296.7	296.5	$T_{h1,2}$	[K]	296.4	296.7	296.5
$T_{h1,3}$	[K]	93.5	84.7	85.0	$T_{h1,3}$	[K]	97.2	101.5	127.1
$T_{l,3}$	[K]	80.5	80.6	82.7	$T_{l,3}$	[K]	80.5	80.6	82.7
$T_{l,2}$	[K]	285.8	269.2	232.2	$T_{l,2}$	[K]	285.8	269.2	232.2
$T_{N,2}$	[K]	88.0	84.3	84.1	$T_{N,2}$	[K]	88.0	84.3	84.1
$T_{N,5}$	[K]	78.0	78.0	78.0	$T_{N,5}$	[K]	78.0	78.0	78.0
$h_{N,2}$	[kJ/kg]	89	85	85	$h_{N,2}$	[kJ/kg]	89	85	85
$h_{N,5}$	[kJ/kg]	-96	-96	-96	$h_{N,5}$	[kJ/kg]	-96	-96	-96
$h_{h1,2}$	[kJ/kg]	1549	1550	1550	$h_{h1,2}$	[kJ/kg]	1549	1550	1550
$h_{h1,3}$	[kJ/kg]	494	448	449	$h_{h1,3}$	[kJ/kg]	510	532	665
$h_{l,3}$	[kJ/kg]	426	426	437	$h_{l,3}$	[kJ/kg]	426	426	437
$h_{l,2}$	[kJ/kg]	1494	1408	1216	$h_{l,2}$	[kJ/kg]	1494	1408	1216
$q_{HX1,h}$	[kW]	14.78	15.46	15.54	$q_{HX1,h}$	[kW]	14.56	14.28	12.49
$q_{HX1,l}$	[kW]	14.96	13.76	10.99	$q_{HX1,l}$	[kW]	14.96	13.76	10.99
Δq_{HX1}	[kW]	0.19	-1.70	-4.54	Δq_{HX1}	[kW]	0.41	-0.52	-1.50
ε_q	[-]	1.2%	-12.3%	-41.3%	ε_q	[-]	2.7%	-3.8%	-13.6%
$q_{N,He}$	[kW]	0.96	0.30	0.17	$q_{N,He}$	[kW]	1.18	1.48	3.22
$q_{N,N}$	[kW]	1.18	1.48	3.22	$q_{N,N}$	[kW]	1.18	1.48	3.22
q_{HL}	[kW]	0.040	0.040	0.040	q_{HL}	[kW]	0.040	0.040	0.040
ΔT_h	[K]	203	212	212	ΔT_h	[K]	199	195	169
ΔT_l	[K]	205	189	150	ΔT_l	[K]	205	189	150
ΔT_{hot}	[K]	10.6	27.4	64.3	ΔT_{hot}	[K]	10.6	27.4	64.3
ΔT_{cold}	[K]	13.1	4.1	2.3	ΔT_{cold}	[K]	16.7	20.9	44.4
C_h	[kW/K]	0.0729	0.0729	0.0734	C_h	[kW/K]	0.0731	0.0731	0.0737
C_l	[kW/K]	0.0729	0.0730	0.0735	C_l	[kW/K]	0.0729	0.0730	0.0735
C_{max}	[kW/K]	0.0729	0.0730	0.0735	C_{max}	[kW/K]	0.0731	0.0731	0.0737
C_{min}	[kW/K]	0.0729	0.0729	0.0734	C_{min}	[kW/K]	0.0729	0.0730	0.0735
C_r	[-]	0.9996	0.9997	0.9994	C_r	[-]	0.9974	0.9974	0.9971
ΔT_{LM}	[-]	11.78	12.29	18.65	ΔT_{LM}	[-]	13.40	24.01	53.74
UA	[-]	1.271	1.119	0.589	UA	[-]	1.117	0.573	0.205
NTU	[-]	17.44	15.35	8.03	NTU	[-]	15.32	7.86	2.78
ε	[-]	94.59%	93.90%	88.94%	ε	[-]	93.99%	88.81%	73.65%
E-bal	[kW]	-0.37	0.56	1.54	E-bal	[kW]	-0.37	0.56	1.54

Table D-2 Energy balance analysis for cases 3 and 4, detailed below

3. Using LN flow and q_{HL}, calculate $T_{h1,3}$				
Hours		**1**	**20**	**37**
$P_{HX, in}$	[bar]	13.56	13.60	14.21
ΔP_{HX}	[bar]	0.0974	0.1370	0.9868
$P_{purifier, out}$	[bar]	13.46	13.46	13.23
$P_{N2,vent}$	[bar]	1.007	1.007	1.017
$\dot{m}$	[g/s]	14.01	14.02	14.12
$\dot{m}_{N2,vent}$	[g/s]	6.35	8.19	17.80
$T_{h1,2}$	[K]	296.4	296.7	296.5
$T_{h1,3}$	[K]	96.6	100.9	126.5
$T_{l,3}$	[K]	80.5	80.6	82.7
$T_{l,2}$	[K]	285.8	269.2	232.2
$T_{N,2}$	[K]	88.0	84.3	84.1
$T_{N,5}$	[K]	78.0	78.0	78.0
$h_{N,2}$	[kJ/kg]	89	85	85
$h_{N,5}$	[kJ/kg]	-96	-96	-96
$h_{h1,2}$	[kJ/kg]	1549	1550	1550
$h_{h1,3}$	[kJ/kg]	507	529	662
$h_{l,3}$	[kJ/kg]	426	426	437
$h_{l,2}$	[kJ/kg]	1494	1408	1216
$q_{HX1,h}$	[kW]	14.60	14.32	12.53
$q_{HX1,l}$	[kW]	14.96	13.76	10.99
Δq_{HX1}	[kW]	0.37	-0.56	-1.54
ε_q	[-]	2.4%	-4.0%	-14.0%
$q_{N,He}$	[kW]	1.14	1.44	3.18
$q_{N,N}$	[kW]	1.18	1.48	3.22
q_{HL}	[kW]	0.040	0.040	0.040
ΔT_h	[K]	200	196	170
ΔT_l	[K]	205	189	150
ΔT_{hot}	[K]	10.6	27.4	64.3
ΔT_{cold}	[K]	16.1	20.3	43.9
C_h	[kW/K]	0.0731	0.0731	0.0737
C_l	[kW/K]	0.0729	0.0730	0.0735
C_{max}	[kW/K]	0.0731	0.0731	0.0737
C_{min}	[kW/K]	0.0729	0.0730	0.0735
C_r	[-]	0.9974	0.9974	0.9971
ΔT_{LM}	[-]	13.16	23.71	53.43
UA	[-]	1.137	0.580	0.206
NTU	[-]	15.60	7.96	2.80
ε	[-]	94.09%	88.94%	73.76%
E-bal	[kW]	-0.37	0.56	1.54

4. Using boiler E-bal, calculate LN flow				
Hours		**1**	**20**	**37**
$P_{HX, in}$	[bar]	13.56	13.60	14.21
ΔP_{HX}	[bar]	0.0974	0.1370	0.9868
$P_{purifier, out}$	[bar]	13.46	13.46	13.23
$P_{N2,vent}$	[bar]	1.007	1.007	1.017
$\dot{m}$	[g/s]	14.01	14.02	14.12
$\dot{m}_{N2,vent}$	[g/s]	5.16	1.67	0.95
$T_{h1,2}$	[K]	296.4	296.7	296.5
$T_{h1,3}$	[K]	93.5	84.7	85.0
$T_{l,3}$	[K]	80.5	80.6	82.7
$T_{l,2}$	[K]	285.8	269.2	232.2
$T_{N,2}$	[K]	88.0	84.3	84.1
$T_{N,5}$	[K]	78.0	78.0	78.0
$h_{N,2}$	[kJ/kg]	89	85	85
$h_{N,5}$	[kJ/kg]	-96	-96	-96
$h_{h1,2}$	[kJ/kg]	1549	1550	1550
$h_{h1,3}$	[kJ/kg]	494	448	449
$h_{l,3}$	[kJ/kg]	426	426	437
$h_{l,2}$	[kJ/kg]	1494	1408	1216
$q_{HX1,h}$	[kW]	14.78	15.46	15.54
$q_{HX1,l}$	[kW]	14.96	13.76	10.99
Δq_{HX1}	[kW]	0.19	-1.70	-4.54
ε_q	[-]	1.2%	-12.3%	-41.3%
$q_{N,He}$	[kW]	0.96	0.30	0.17
$q_{N,N}$	[kW]	0.96	0.30	0.17
q_{HL}	[kW]	0.040	0.040	0.040
ΔT_h	[K]	203	212	212
ΔT_l	[K]	205	189	150
ΔT_{hot}	[K]	10.6	27.4	64.3
ΔT_{cold}	[K]	13.1	4.1	2.3
C_h	[kW/K]	0.0729	0.0729	0.0734
C_l	[kW/K]	0.0729	0.0730	0.0735
C_{max}	[kW/K]	0.0729	0.0730	0.0735
C_{min}	[kW/K]	0.0729	0.0729	0.0734
C_r	[-]	0.9996	0.9997	0.9994
ΔT_{LM}	[-]	11.78	12.29	18.65
UA	[-]	1.271	1.119	0.589
NTU	[-]	17.44	15.35	8.03
ε	[-]	94.59%	93.90%	88.94%
E-bal	[kW]	-0.15	1.74	4.58

Table D-3 Energy balance analysis for cases 5 and 6, detailed below

5. Using overall E-bal, calculate LN flow				
Hours		**1**	**20**	**37**
$P_{HX, in}$	[bar]	13.56	13.60	14.21
ΔP_{HX}	[bar]	0.0974	0.1370	0.9868
$P_{purifier, out}$	[bar]	13.46	13.46	13.23
$P_{N2,vent}$	[bar]	1.007	1.007	1.017
$\dot{m}$	[g/s]	14.01	14.02	14.12
$\dot{m}_{N2,vent}$	[g/s]	3.37	10.23	25.26
$T_{h1,2}$	[K]	296.4	296.7	296.5
$T_{h1,3}$	[K]	93.5	84.7	85.0
$T_{l,3}$	[K]	80.5	80.6	82.7
$T_{l,2}$	[K]	287.8	271.2	234.2
$T_{N,2}$	[K]	88.0	84.3	84.1
$T_{N,5}$	[K]	78.0	78.0	78.0
$h_{N,2}$	[kJ/kg]	89	85	85
$h_{N,5}$	[kJ/kg]	-96	-96	-96
$h_{h1,2}$	[kJ/kg]	1549	1550	1550
$h_{h1,3}$	[kJ/kg]	494	448	449
$h_{l,3}$	[kJ/kg]	426	426	437
$h_{l,2}$	[kJ/kg]	1504	1418	1226
$q_{HX1,h}$	[kW]	14.78	15.46	15.54
$q_{HX1,l}$	[kW]	15.11	13.91	11.14
Δq_{HX1}	[kW]	0.33	-1.55	-4.40
ε_q	[-]	2.2%	-11.2%	-39.5%
$q_{N,He}$	[kW]	0.96	0.30	0.17
$q_{N,N}$	[kW]	0.62	1.85	4.57
q_{HL}	[kW]	0.00	0.00	0.00
ΔT_h	[K]	203	212	212
ΔT_l	[K]	207	191	152
ΔT_{hot}	[K]	8.6	25.4	62.3
ΔT_{cold}	[K]	13.1	4.1	2.3
C_h	[kW/K]	0.0729	0.0729	0.0734
C_l	[kW/K]	0.0729	0.0730	0.0735
C_{max}	[kW/K]	0.0729	0.0730	0.0735
C_{min}	[kW/K]	0.0729	0.0729	0.0734
C_r	[-]	0.9996	0.9997	0.9994
ΔT_{LM}	[-]	10.66	11.71	18.22
UA	[-]	1.417	1.188	0.611
NTU	[-]	19.45	16.29	8.32
ε	[-]	95.13%	94.23%	89.30%
E-bal	[kW]	0.00	0.00	0.00

6. Using HX energy balance, calculate $T_{l,2}$				
Hours		**1**	**20**	**37**
$P_{HX, in}$	[bar]	13.56	13.60	14.21
ΔP_{HX}	[bar]	0.0974	0.1370	0.9868
$P_{purifier, out}$	[bar]	13.46	13.46	13.23
$P_{N2,vent}$	[bar]	1.007	1.007	1.017
$\dot{m}$	[g/s]	14.01	14.02	14.12
$\dot{m}_{N2,vent}$	[g/s]	6.35	8.19	17.80
$T_{h1,2}$	[K]	296.4	296.7	296.5
$T_{h1,3}$	[K]	93.5	84.7	85.0
$T_{l,3}$	[K]	80.5	80.6	82.7
$T_{l,2}$	[K]	284.1	293.4	295.1
$T_{N,2}$	[K]	88.0	84.3	84.1
$T_{N,5}$	[K]	78.0	78.0	78.0
$h_{N,2}$	[kJ/kg]	89	85	85
$h_{N,5}$	[kJ/kg]	-96	-96	-96
$h_{h1,2}$	[kJ/kg]	1549	1550	1550
$h_{h1,3}$	[kJ/kg]	494	448	449
$h_{l,3}$	[kJ/kg]	426	426	437
$h_{l,2}$	[kJ/kg]	1480	1529	1537
$q_{HX1,h}$	[kW]	14.78	15.46	15.54
$q_{HX1,l}$	[kW]	14.78	15.46	15.54
Δq_{HX1}	[kW]	0.00	0.00	0.00
ε_q	[-]	0.0%	0.0%	0.0%
$q_{N,He}$	[kW]	0.96	0.30	0.17
$q_{N,N}$	[kW]	1.18	1.48	3.22
q_{HL}	[kW]	0.00	0.00	0.00
ΔT_h	[K]	203	212	212
ΔT_l	[K]	204	213	212
ΔT_{hot}	[K]	12.3	3.3	1.5
ΔT_{cold}	[K]	13.1	4.1	2.3
C_h	[kW/K]	0.0729	0.0729	0.0734
C_l	[kW/K]	0.0726	0.0727	0.0731
C_{max}	[kW/K]	0.0729	0.0729	0.0734
C_{min}	[kW/K]	0.0726	0.0727	0.0731
C_r	[-]	0.9962	0.9961	0.9961
ΔT_{LM}	[-]	12.67	3.69	1.87
UA	[-]	1.167	4.192	8.317
NTU	[-]	16.07	57.70	113.70
ε	[-]	94.31%	98.48%	99.31%
E-bal	[kW]	-0.22	-1.18	-3.05

Table D-4 Energy balance analysis for cases 7 and 8, detailed below

7. Using overall energy balance, calc $T_{l,2}$					8. Vary LN flow to match $T_{l,2}$ (goal seek)				
Hours		**1**	**20**	**37**	**Hours**		**1**	**20**	**37**
$P_{HX, in}$	[bar]	13.56	13.60	14.21	$P_{HX, in}$	[bar]	13.56	13.60	14.21
ΔP_{HX}	[bar]	0.0974	0.1370	0.9868	ΔP_{HX}	[bar]	0.0974	0.1370	0.9868
$P_{purifier, out}$	[bar]	13.46	13.46	13.23	$P_{purifier, out}$	[bar]	13.46	13.46	13.23
$P_{N2,vent}$	[bar]	1.007	1.007	1.017	$P_{N2,vent}$	[bar]	1.007	1.007	1.017
$\dot{m}$	[g/s]	14.01	14.02	14.12	$\dot{m}$	[g/s]	14.01	14.02	14.12
$\dot{m}_{N2,vent}$	[g/s]	6.35	8.19	17.80	$\dot{m}_{N2,vent}$	[g/s]	4.49	11.38	26.43
$T_{h1,2}$	[K]	296.4	296.7	296.5	$T_{h1,2}$	[K]	296.4	296.7	296.5
$T_{h1,3}$	[K]	93.5	84.7	85.0	$T_{h1,3}$	[K]	92.4	109.4	148.4
$T_{l,3}$	[K]	80.5	80.6	82.7	$T_{l,3}$	[K]	80.5	80.6	82.7
$T_{l,2}$	[K]	281.1	277.1	253.5	$T_{l,2}$	[K]	285.8	269.2	232.2
$T_{N,2}$	[K]	88.0	84.3	84.1	$T_{N,2}$	[K]	88.0	84.3	84.1
$T_{N,5}$	[K]	78.0	78.0	78.0	$T_{N,5}$	[K]	78.0	78.0	78.0
$h_{N,2}$	[kJ/kg]	89	85	85	$h_{N,2}$	[kJ/kg]	89	85	85
$h_{N,5}$	[kJ/kg]	-96	-96	-96	$h_{N,5}$	[kJ/kg]	-96	-96	-96
$h_{h1,2}$	[kJ/kg]	1549	1550	1550	$h_{h1,2}$	[kJ/kg]	1549	1550	1550
$h_{h1,3}$	[kJ/kg]	494	448	449	$h_{h1,3}$	[kJ/kg]	485	573	776
$h_{l,3}$	[kJ/kg]	426	426	437	$h_{l,3}$	[kJ/kg]	426	426	437
$h_{l,2}$	[kJ/kg]	1465	1444	1322	$h_{l,2}$	[kJ/kg]	1489	1403	1211
$q_{HX1,h}$	[kW]	14.78	15.46	15.54	$q_{HX1,h}$	[kW]	14.90	13.70	10.93
$q_{HX1,l}$	[kW]	14.56	14.28	12.49	$q_{HX1,l}$	[kW]	14.90	13.70	10.93
Δq_{HX1}	[kW]	-0.22	-1.18	-3.05	Δq_{HX1}	[kW]	0.00	0.00	0.00
ε_q	[-]	-1.5%	-8.3%	-24.4%	ε_q	[-]	0.0%	0.0%	0.0%
$q_{N,He}$	[kW]	0.96	0.30	0.17	$q_{N,He}$	[kW]	0.83	2.06	4.78
$q_{N,N}$	[kW]	1.18	1.48	3.22	$q_{N,N}$	[kW]	0.83	2.06	4.78
q_{HL}	[kW]	0.00	0.00	0.00	q_{HL}	[kW]	0.00	0.00	0.00
ΔT_h	[K]	203	212	212	ΔT_h	[K]	204	187	148
ΔT_l	[K]	201	197	171	ΔT_l	[K]	205	189	150
ΔT_{hot}	[K]	15.3	19.5	43.0	ΔT_{hot}	[K]	10.6	27.5	64.3
ΔT_{cold}	[K]	13.1	4.1	2.3	ΔT_{cold}	[K]	11.9	28.8	65.7
C_h	[kW/K]	0.0729	0.0729	0.0734	C_h	[kW/K]	0.0731	0.0732	0.0738
C_l	[kW/K]	0.0726	0.0726	0.0731	C_l	[kW/K]	0.0726	0.0726	0.0731
C_{max}	[kW/K]	0.0729	0.0729	0.0734	C_{max}	[kW/K]	0.0731	0.0732	0.0738
C_{min}	[kW/K]	0.0726	0.0726	0.0731	C_{min}	[kW/K]	0.0726	0.0726	0.0731
C_r	[-]	0.9962	0.9959	0.9955	C_r	[-]	0.9934	0.9928	0.9908
ΔT_{LM}	[-]	14.15	9.89	13.94	ΔT_{LM}	[-]	11.25	28.13	65.02
UA	[-]	1.029	1.443	0.896	UA	[-]	1.325	0.487	0.168
NTU	[-]	14.17	19.87	12.26	NTU	[-]	18.26	6.70	2.30
ε	[-]	93.58%	95.39%	92.65%	ε	[-]	95.10%	87.29%	69.92%
E-bal	[kW]	0.00	0.00	0.00	E-bal	[kW]	0.00	0.00	0.00

Table D-5 Energy balance analysis for cases 8.1 and 9, detailed below

8.1 Using Tl,2, calculate LN flow				
Hours		**1**	**20**	**37**
$P_{HX, in}$	[bar]	13.56	13.60	14.21
ΔP_{HX}	[bar]	0.0974	0.1370	0.9868
$P_{purifier, out}$	[bar]	13.46	13.46	13.23
$P_{N2,vent}$	[bar]	1.007	1.007	1.017
$\dot{m}$	[g/s]	14.01	14.02	14.12
$\dot{m}_{N2,vent}$	[g/s]	3.86	10.04	23.68
$T_{h1,2}$	[K]	296.4	296.7	296.5
$T_{h1,3}$	[K]	91.6	108.6	147.6
$T_{l,3}$	[K]	80.5	80.6	82.7
$T_{l,2}$	[K]	285.8	269.2	232.2
$T_{N,2}$	[K]	88.0	84.3	84.1
$T_{N,5}$	[K]	78.0	78.0	78.0
$h_{N,2}$	[kJ/kg]	89	85	85
$h_{N,4}$	[kJ/kg]	77	77	77
$h_{N,5}$	[kJ/kg]	-122	-122	-122
$h_{h1,2}$	[kJ/kg]	1549	1550	1550
$h_{h1,3}$	[kJ/kg]	481	569	771
$h_{l,3}$	[kJ/kg]	426	426	437
$h_{l,2}$	[kJ/kg]	1494	1408	1215
$q_{HX1,h}$	[kW]	14.96	13.76	10.99
$q_{HX1,l}$	[kW]	14.96	13.76	10.99
Δq_{HX1}	[kW]	0.00	0.00	0.00
ε_q	[-]	0.0%	0.0%	0.0%
$q_{N,He}$	[kW]	0.77	2.00	4.72
$q_{N,N}$	[kW]	0.77	2.00	4.72
q_{HL}	[kW]	0.00	0.00	0.00
ΔT_h	[K]	205	188	149
ΔT_l	[K]	205	189	150
ΔT_{hot}	[K]	10.6	27.5	64.3
ΔT_{cold}	[K]	11.1	28.0	64.9
C_h	[kW/K]	0.0731	0.0732	0.0738
C_l	[kW/K]	0.0729	0.0730	0.0735
C_{max}	[kW/K]	0.0731	0.0732	0.0738
C_{min}	[kW/K]	0.0729	0.0730	0.0735
C_r	[-]	0.9975	0.9972	0.9962
ΔT_{LM}	[-]	10.84	27.71	64.61
UA	[-]	1.381	0.496	0.170
NTU	[-]	18.95	6.80	2.31
ε	[-]	95.10%	87.29%	69.92%
E-bal	[kW]	0.00	0.00	0.00

9. Using LN flow, calculate $T_{h1,3}$ and $T_{l,2}$				
Hours		**1**	**20**	**37**
$P_{HX, in}$	[bar]	13.56	13.60	14.21
ΔP_{HX}	[bar]	0.0974	0.1370	0.9868
$P_{purifier, out}$	[bar]	13.46	13.46	13.23
$P_{N2,vent}$	[bar]	1.007	1.007	1.017
$\dot{m}$	[g/s]	14.01	14.02	14.12
$\dot{m}_{N2,vent}$	[g/s]	6.35	8.19	17.80
$T_{h1,2}$	[K]	296.4	296.7	296.5
$T_{h1,3}$	[K]	96.1	100.6	125.3
$T_{l,3}$	[K]	80.5	80.6	82.7
$T_{l,2}$	[K]	282.1	278.0	255.3
$T_{N,2}$	[K]	88.0	84.3	84.1
$T_{N,5}$	[K]	78.0	78.0	78.0
$h_{N,2}$	[kJ/kg]	89	85	85
$h_{N,4}$	[kJ/kg]	77	77	77
$h_{N,5}$	[kJ/kg]	-96	-96	-96
$h_{h1,2}$	[kJ/kg]	1549	1550	1550
$h_{h1,3}$	[kJ/kg]	504	528	656
$h_{l,3}$	[kJ/kg]	426	426	437
$h_{l,2}$	[kJ/kg]	1470	1449	1331
$q_{HX1,h}$	[kW]	14.63	14.34	12.62
$q_{HX1,l}$	[kW]	14.63	14.34	12.62
Δq_{HX1}	[kW]	0.00	0.00	0.00
ε_q	[-]	0.0%	0.0%	0.0%
$q_{N,He}$	[kW]	1.10	1.42	3.08
$q_{N,N}$	[kW]	1.10	1.42	3.08
q_{HL}	[kW]	0.00	0.00	0.00
ΔT_h	[K]	200	196	171
ΔT_l	[K]	202	197	173
ΔT_{hot}	[K]	14.3	18.6	41.2
ΔT_{cold}	[K]	15.6	20.0	42.6
C_h	[kW/K]	0.0731	0.0731	0.0737
C_l	[kW/K]	0.0726	0.0726	0.0731
C_{max}	[kW/K]	0.0731	0.0731	0.0737
C_{min}	[kW/K]	0.0726	0.0726	0.0731
C_r	[-]	0.9932	0.9931	0.9920
ΔT_{LM}	[-]	14.95	19.30	41.90
UA	[-]	0.979	0.743	0.301
NTU	[-]	13.49	10.23	4.12
ε	[-]	93.39%	91.38%	80.73%
E-bal	[kW]	0.00	0.00	0.00

Table D-6 Energy balance analysis for cases 10 and 11, detailed below

10. Vary LN flow to calc $T_{h1,3}$ and equalize HX1 E-bal					11. Using overall energy balance, calc $T_{l,2}$ and $T_{h1,3}$				
Hours		**1**	**20**	**37**	**Hours**		**1**	**20**	**37**
$P_{HX, in}$	[bar]	13.56	13.60	14.21	$P_{HX, in}$	[bar]	13.56	13.60	14.21
ΔP_{HX}	[bar]	0.0974	0.1370	0.9868	ΔP_{HX}	[bar]	0.0974	0.1370	0.9868
$P_{purifier, out}$	[bar]	13.46	13.46	13.23	$P_{purifier, out}$	[bar]	13.46	13.46	13.23
$P_{N2,vent}$	[bar]	1.007	1.007	1.017	$P_{N2,vent}$	[bar]	1.007	1.007	1.017
$\dot{m}$	[g/s]	14.01	14.02	14.12	$\dot{m}$	[g/s]	14.01	14.02	14.12
$\dot{m}_{N2,vent}$	[g/s]	0.30	0.79	1.85	$\dot{m}_{N2,vent}$	[g/s]	6.35	8.19	17.80
$T_{h1,2}$	[K]	296.4	296.7	296.5	$T_{h1,2}$	[K]	296.4	296.7	296.5
$T_{h1,3}$	[K]	91.6	108.6	147.5	$T_{h1,3}$	[K]	97.2	101.5	127.1
$T_{l,3}$	[K]	80.5	80.6	82.7	$T_{l,3}$	[K]	80.5	80.6	82.7
$T_{l,2}$	[K]	285.8	269.2	232.2	$T_{l,2}$	[K]	281.1	277.1	253.5
$T_{N,2}$	[K]	88.0	84.3	84.1	$T_{N,2}$	[K]	88.0	84.3	84.1
$T_{N,5}$	[K]	78.0	78.0	78.0	$T_{N,5}$	[K]	78.0	78.0	78.0
$h_{N,2}$	[kJ/kg]	89	85	85	$h_{N,2}$	[kJ/kg]	89	85	85
$h_{N,5}$	[kJ/kg]	-96	-96	-96	$h_{N,5}$	[kJ/kg]	-96	-96	-96
$h_{h1,2}$	[kJ/kg]	1549	1550	1550	$h_{h1,2}$	[kJ/kg]	1549	1550	1550
$h_{h1,3}$	[kJ/kg]	481	569	771	$h_{h1,3}$	[kJ/kg]	510	532	665
$h_{l,3}$	[kJ/kg]	426	426	437	$h_{l,3}$	[kJ/kg]	426	426	437
$h_{l,2}$	[kJ/kg]	1494	1408	1216	$h_{l,2}$	[kJ/kg]	1465	1444	1322
$q_{HX1,h}$	[kW]	14.96	13.76	10.99	$q_{HX1,h}$	[kW]	14.56	14.28	12.49
$q_{HX1,l}$	[kW]	14.96	13.76	10.99	$q_{HX1,l}$	[kW]	14.56	14.28	12.49
Δq_{HX1}	[kW]	0.00	0.00	0.00	Δq_{HX1}	[kW]	0.00	0.00	0.00
ε_q	[-]	0.0%	0.0%	0.0%	ε_q	[-]	0.0%	0.0%	0.0%
$q_{N,He}$	[kW]	0.77	2.00	4.72	$q_{N,He}$	[kW]	1.18	1.48	3.22
$q_{N,N}$	[kW]	0.05	0.14	0.33	$q_{N,N}$	[kW]	1.18	1.48	3.22
q_{HL}	[kW]	0.00	0.00	0.00	q_{HL}	[kW]	0.00	0.00	0.00
ΔT_h	[K]	205	188	149	ΔT_h	[K]	199	195	169
ΔT_l	[K]	205	189	150	ΔT_l	[K]	201	197	171
ΔT_{hot}	[K]	10.6	27.4	64.3	ΔT_{hot}	[K]	15.3	19.5	43.0
ΔT_{cold}	[K]	11.1	28.0	64.8	ΔT_{cold}	[K]	16.7	20.9	44.4
C_h	[kW/K]	0.0731	0.0732	0.0738	C_h	[kW/K]	0.0731	0.0731	0.0737
C_l	[kW/K]	0.0729	0.0730	0.0735	C_l	[kW/K]	0.0726	0.0726	0.0731
C_{max}	[kW/K]	0.0731	0.0732	0.0738	C_{max}	[kW/K]	0.0731	0.0731	0.0737
C_{min}	[kW/K]	0.0729	0.0730	0.0735	C_{min}	[kW/K]	0.0726	0.0726	0.0731
C_r	[-]	0.9975	0.9973	0.9964	C_r	[-]	0.9932	0.9931	0.9919
ΔT_{LM}	[-]	10.84	27.70	64.56	ΔT_{LM}	[-]	15.98	20.18	43.72
UA	[-]	1.381	0.497	0.170	**UA**	[-]	0.911	0.707	0.286
NTU	[-]	18.94	6.81	2.32	**NTU**	[-]	12.55	9.74	3.91
ε	[-]	95.10%	87.30%	69.94%	ε	[-]	92.91%	90.97%	79.88%
E-bal	[kW]	0.72	1.86	4.38	**E-bal**	[kW]	0.00	0.00	0.00

REFERENCES

[1] D. Kroll, Development of the mechanical design for a freeze-out purifier, Michigan State University, East Lansing, MI, 2020.